Development of Ultra High Strength Steels for Engineering Applications

A Dissertation Submitted
in the fulfillment of the requirements
for the degree of

Doctor of Philosophy

Submitted by

Shivraj Singh Kasana
Regd. No. 951512001

Under the guidance of

Dr. O. P. Pandey
Senior Professor,
SPMS, TIET, Patiala

THAPAR INSTITUTE
OF ENGINEERING & TECHNOLOGY
(Deemed to be University)

School of Physics and Materials Science
Thapar Institute of Engineering and Technology
(Deemed to be University), Patiala
June, 2021

CERTIFICATE

Certify that the work presented in the thesis entitled "**Development of Ultra High Strength Steels for Engineering Applications**" being submitted by Mr. Shivraj Singh Kasana (Regd. No. 951512001) in fulfilment of the requirements for the award of the degree of 'Doctor of Philosophy' in the School of Physics and Materials Science, Thapar Institute of Engineering and Technology (Deemed to be University), Patiala, is an authentic record of the candidate's own work carried out during the period from January 2016 to June 2021 at this institute under my supervision. The matter presented in this dissertation has not been submitted for the award of any other degree in any university.

Dr. O. P. Pandey
Senior Professor,
School of Physics and Materials Science,
Thapar Institute of Engineering and Technology,
Patiala

DECLARATION

I hereby certify that the work which is being presented in this thesis, entitled "**Development of Ultra High Strength Steels for Engineering Applications**", in the fulfilment of the requirements for the award of degree of 'Doctor of Philosophy' in the School of Physics and Materials Science, Thapar Institute of Engineering and Technology (Deemed to be University), Patiala is an authentic record of my own work carried out under the supervision of Dr. O. P. Pandey, Senior Professor, School of Physics and Materials Science, Thapar Institute of Engineering and Technology (Deemed to be University), Patiala.

Shivraj Singh Kasana

This is to certify that the above statement made by the candidate is true to the best of my knowledge

Dr. O. P. Pandey
Senior Professor,
School of Physics and Materials Science,
Thapar Institute of Engineering and Technology,
Patiala

ACKNOWLEDGEMENT

First and foremost, I wish to express my sincere thanks, gratitude and indebtedness to my supervisor, ***Dr. O. P. Pandey*** *(Senior Professor), School of Physics and Materials Science Thapar Institute of Engineering and Technology, Patiala for his valuable guidance, motivation and moral support throughout the entire period of my Ph.D. work. I consider it a great opportunity to do my doctoral programme under his guidance and to learn from his research experience. I gratefully acknowledge him for his valuable advice, helpful criticism, constructive counsel, continuous encouragement and efforts that essentially helped me to accomplish this research work and to get the present work published in various National/International Journals.*

I feel privileged to thank ***Prof. Prakash Gopalan****, Director for encouraging a research-oriented environment in the institute.*

*I am grateful to the Members of the Doctoral Committee (****Dr. Kulvir Singh****,* ***Dr. Puneet Sharma****, and* ***Dr. Tarun Nanda****) for their fruitful suggestions at every stage of my research work.*

I am also grateful to all the faculty members of School of Physics and Materials Science for their direct and indirect support. I also appreciate the cooperation received from staff members of Sophisticated Analytical Instruments Laboratories, TIET Patiala for characterization studies.

I would like to extend the deepest gratitude to my organization management members ***Mr. M. K. Gupta****, Managing Director, and* ***Late Dr. S. K. Goel*** *(Executive Director), Star Wire (India) Ltd, Ballabhgarh Haryana, for the active support and sponsorship for my Ph.D. A very special thanks to* ***Dr. Avnish Kumar****, Manager (R&D) for continuous support and help during experimentation, data interpretation, characterization, and technical discussions. I also thank* ***Mr. Pankaj Saini*** *and* ***Mr. Sudarshan*** *and the entire team of Quality and Material Testing Laboratory for regular support during my work.*

I thank my colleagues ***Mr. Varun Singhal, Ms. Rubi Priya, Mr. Piyush Sharma*** *and other collogues of Functional Material Lab for their assistance and timely support throughout the study.*

*I extend my special thanks to **Dr. Sandeep Sharma** Assistant Professor MMU Mullana, Haryana who reviewed my work at all stages and suggested valuable changes in many instances.*

*I would like to acknowledge our technical and administrative staff of the department **Mr. Indermani Mishra, Mr. Purshotam Singh, Mr. Jant Singh** and **Mr. Lal Ji** for their help at various stages of the work.*

*My most sincere gratitude is extended to my family members, my wife **Savitri Kasana**, sons **Dr. Vivek Kasana** and **Dr. Abhishek Kasana**, daughters in law **Dr. Jyoti** and **Dr. Swati** and grandchildren **Shivanshi, Tanishka, Anshuman** and **Aryan** for their patience, understanding, and encouraging me to follow my dreams.*

*Above all, I thank **Almighty** whose blessings have enabled me to accomplish this research work.*

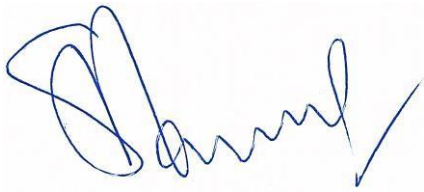

(Shivraj Singh Kasana)

LIST OF PUBLICATIONS

Published Manuscripts:

- Kasana, S. S., & Pandey, O. P. (2019). Effect of electroslag remelting and homogenization on hydrogen flaking in AMS-4340 ultra-high-strength steels. *International Journal of Minerals, Metallurgy, and Materials*, *26*(5), 611-621.

- Kasana, S. S., & Pandey, O. P. (2020). Influence of Chemical Composition and Thermo-Mechanical Processing on the Formation of Delta Ferrite in 10.7 CrMoVNbN Steel. *Transactions of the Indian Institute of Metals*, *73*(10), 2491-2502.

- Kasana, S. S., & Pandey, O. P. (2021). Effect of multipass cold plastic deformation and heat treatment on the mechanical properties of C250 marageing steel for aerospace applications. *Proceedings of the Institution of Mechanical Engineers, Part L: Journal of Materials: Design and Applications*, https://doi.org/10.1177/1464420721989373

- Kasana, S. S., & Pandey, O. P. (2021). Effect of heat treatment on microstructure and mechanical properties of boron containing Ti-Stabilized AISI-321 steel for nuclear power plant application. *Materials Today Communications*, *26*, 101959.

Manuscript under consideration:

- Kasana, S. S., & Pandey, O. P. (2021). Effect of Various Heat Treatments on Microstructure and Mechanical Properties of 300M Ultra High Strength Steel. *Materials Today Communications*, Reff No. MTCOMM-D-21-00718R1 (under revision).

PREFACE

The present work is focused on studies undertaken to improve the mechanical properties of different ultra-high strength steels (UHSS). The subject matter resulting out of the present study has been arranged in **nine chapters** in this Ph.D. thesis. The outline of the chapters is as follows:

- **Chapter 1:** The chapter introduces the basic terms involved in the present research viz. steels, the classifications of steels, etc. This chapter discusses the need and benefit of UHSS steels and also presents the origin of the present research work. The outline of the complete thesis is also covered in this chapter.
- **Chapter 2:** This chapter presents a detailed review of literature on the processing and mechanical properties of UHSS. This includes (i) AMS-4340 steels, (ii) 10.7CrMoVNbN steels, (iii) AISI321 steels, (iv) C250 steels, and (v) 300M steels on which the present work has been done. The chapter also brings forth the summary of the existing literature and also the main gaps in the existing literature in their field of work.
- **Chapter 3:** The chapter presents a brief description of equipment used for testing and characterization of UHSS. This include X-ray diffraction (XRD), Optical microscopy, Scanning electron microscopy (SEM), Energy dispersive spectroscopy (EDS), and different Mechanical tests done for the processed UHSS to fulfill the basic objectives mentioned in this chapter.
- **Chapter 4:** This chapter presents the processing methodology of AMS-4340 steels developed for defense applications viz. gun barrel and ballistic applications. Four different ESR heats E1, E2, E3 and E4 were prepared under different processing conditions. The microstructural investigations revealed that the hydrogen flaking was dominant factor in E1 heat. Because of this the ESR heat E1 was rejected as it could not achieve the desired yield strength. Although, ESR heats E2 and E3 have shown the desired mechanical properties but got rejected during the ultrasonic testing. ESR heat E4 exhibited better mechanical properties among these developed steels. This E4 steel was given longer high-temperature homogenization and two stage anti flacking treatment. The process route used for fabrication of ESR heat E4 showed that this steel is acceptable by the industries.
- **Chapter 5:** This chapter presents the processing methodology of 10.7CrMoVNbN steels for turbine blades, nozzle partition and bucket for supercritical turbine applications. Four different heats viz, Heat 1, Heat 2, Heat 3, and Heat 4 were prepared under different processing conditions. FESEM-EDS analysis confirmed the presence of tempered martensitic matrix, carbides, and δ-ferrite. Field emission scanning electron microscopy and EDS investigations showed that various microstructure constituents are present in the matrix of martensite. It is observed that there is not much variation in hardness, yield strength (YS), ultimate tensile strength (UTS), and % elongation. However, the impact energy of Heat 3 and Heat 4 is much higher than that of Heat 1 and Heat 2. Lower impact in Heat 1 and Heat 2 are due to the presence of higher amount of δ-ferrite. Precipitation of delta ferrite is detrimental to mechanical properties. Further, Cr_{eq} is a very important factor and hence, controlling the chromium equivalent to 12 maxima in this grade of steels has a significant effect on the mechanical properties. The Cr_{eq} ratio of Heat 1 and Heat 2 was higher than 12 (12.99 and 12.47 respectively). Thus, lower impact strength was observed. Further, for Heat 3, Cr_{eq} was 12.05 hence, higher impact strength was observed. Heat 4 presented superior mechanical properties. The Cr_{eq} ratio observed for Heat 4 was lower than 12 (11.59). This indicated that lower Cr_{eq} (lower than 12) improved the mechanical properties of the steel.

- **Chapter 6:** This chapter presents the different processing methodology adopted for AISI321 steels to get better mechanical properties. This particular steel is mainly used in nuclear reactors, heat exchangers and for boiler tubes applications. Two different types of titanium stabilized AISI 321 steels TB1 (without boron; 1 ppm) and TB30 (with boron; 30 ppm) were prepared. Microstructure analysis revealed that TB30 steel exhibits population of borides (Cr_2B/Fe_2B) along with TiN/TiCN precipitates. The number of precipitates is much higher compared to TB1 steel where only TiN and TiCN precipitates exist. For both room temperature and elevated temperature conditions the YS and UTS of TB30 steel in all conditions was higher than the YS of TB1 steel. This could be attributed to the precipitation strengthening of TB30 steel as the TB30 steel revealed a higher precipitate count in comparison to TB1 steel. In addition to this, addition of boron led to the formation of precipitates of Fe_2B, Cr_2B, TIN, and TICN which restricts the dislocation movement and causes an increase in yield strength of TB30 steel.
- **Chapter 7:** This chapter presents the processing methodology of C250 steels for aerospace landing gear applications. Higher magnification microstructure shows the presence of lath martensite, retained austenite and fine distribution of precipitates such as Ni_3Ti and Fe_2Mo. The higher content of precipitates (Ni_3Ti and Fe_2Mo) leads to the improvement in the strength of C250 steels. The martensite laths observed for T0 were coarser in size. The equiaxed laths of martensite are clearly visible in the matrix phase. The YS and UTS of C250 steel in the solution annealed (SA) condition (T0) was minimum and the total elongation and impact strength were maximum. Beyond T14 cold working, a sudden drop in the percentage elongation and impact strength is observed. This could be attributed to the excessive cold working of the steel. The excessive cold work has the tendency to change the grain from crystalline to amorphous, thus beyond T14 cold work, the mechanical properties of the C250 steel resemble to that of a brittle material. Also, beyond T20 the dislocation density of the steel becomes constant thus a marginal change in YS and UTS is observed. Further, cold working leads to the alignment of grains along the cold working direction. From XRD spectra it can be observed that cold working leads to the change in crystal orientation and growth of crystals takes place in the new planes. This growth of crystals in T20 and T21 steel leads to a decrease in percentage elongation of the steel. Best results were observed for T14 cold work steel. The YS, UTS and hardness of T14 C250 steel were 1939.13 MPa, 2123.53 MPa and 56 HRC respectively.
- **Chapter 8:** This chapter presents the processing methodology of 300M steels for automobile and aerospace applications. The microstructure of 300M steel consists of martensite, bainite and retained austenite (RA). Martensite mainly consists of laths parallel to each other while bainite is mainly observed as cross arranged bundles of different sizes. The best combination of mechanical properties was achieved by the IST heat treated 300M steel. IST steel exhibit comparatively better mechanical properties in terms of % elongation, % RA, impact energy with marginal loss in YS and UTS. It attributed good combination of hard martensite, tough bainite and soft retailed austenite microstructure of IST 300M steel. Heat treatment of 300M steel refined the grain size of bainite, martensite and retained austenite. The refinement of microstructure was higher for conventional route (CQT) and modified route (MAT) heat treated 300M steels. The higher refinement in the microstructure increases the grain boundaries in the microstructure. Grain boundaries act as a barrier to the dislocations and increase the resistance to deformation and increase the YS and UTS of steel.
- **Chapter 9:** This chapter summarizes the entire work and discusses the main conclusions drawn from the present study. The main results and findings of the experimental work are included in this chapter. The study revealed that for developing different grade of UHSS different processing route has to be followed to achieve better properties. The UHSS

developed in the present study can be used in specific engineering applications. The mechanical properties achieved by the UHSS in the present study are exceptional and are well within the acceptable range set by the suppliers. Finally, this chapter also presents the major conclusions and recommendations from the present work and the scope for further research in this area.

TABLE OF CONTENTS

CERTIFICATE *i*

DECLARATION *ii*

ACKNOWLEDGEMENT *iii*

LIST OF PUBLICATIONS *v*

ABSTRACT *vi*

TABLE OF CONTENTS *ix*

LIST OF TABLES *xiv*

LIST OF FIGURES *xvi*

CHAPTER 1 INTRODUCTION

OVERVIEW 1

1.1 STEELS 2

1.2 ULTRA-HIGH STRENGTH STEELS 3

1.3 PROPERTIES OF COMMON ULTRA-HIGH STRENGTH STEELS 3

1.3.1 AMS-4340 STEEL 3

1.3.2 10.7CrMoVNbN STEEL 4

1.3.3 AISI-321 STEEL 4

1.3.4 C250 STEEL 5

1.3.5 300M STEELS 6

1.4 STRENGTHENING MECHANISMS OF ULTRA-HIGH STRENGTH STEELS 7

1.4.1 SOLID SOLUTION STRENGTHENING 7

1.4.2 GRAIN REFINEMENT 8

1.4.3 WORK-HARDENING OR STRAIN-HARDENING 8

1.4.4 PRECIPITATION HARDENING 8

1.4.5 TRANSFORMATION STRENGTHENING 8

1.5 APPLICATION OF ULTRA-HIGH STRENGTH STEELS 9

1.6 ORIGIN OF THE STUDY 9

CHAPTER 2 REVIEW OF LITERATURE

OVERVIEW 11

2.1 PROCESS DESIGN 12
2.2 AMS-4340 STEELS 13
2.3 10.7CrMoVNbN STEEL 20
2.4 AISI-321 STEEL 24
2.5 C250 STEEL 31
2.6 300M STEELS 36
2.7 SUMMARY OF LITERATURE 40
2.8 GAPS IN THE LITERATURE 42

CHAPTER 3 DESIGN OF THE STUDY

OVERVIEW 43
3.1 OBJECTIVES 44
3.2 AMS-4340 STEELS 44
3.2.1 BACKGROUND STUDY 44
3.2.2 CHARACTERIZATION AND TESTING 45
3.3 10.7CrMoVNbN STEEL 46
3.3.1 BACKGROUND STUDY 46
3.3.2 CHARACTERIZATION AND TESTING 46
3.4 AISI-321 STEEL 47
3.4.1 BACKGROUND STUDY 47
3.4.2 MICROSTRUCTURAL EXAMINATION 48
3.4.3 MECHANICAL TESTING 48
3.5 C250 STEEL 49
3.5.1 BACKGROUND STUDY 49
3.5.2 CHARACTERIZATION AND TESTING 49
3.6 300M STEELS 50
3.5.1 BACKGROUND STUDY 50
3.5.2 CHARACTERIZATION AND TESTING 50

CHAPTER 4 RESULTS AND DISCUSSION AMS 4340 STEEL

OVERVIEW 53
4.1 AMS-4340 STEELS 54

4.1.1 STARTING MATERIAL 54
4.1.2 PROCESSING ROUTE 54
4.2 CHEMICAL COMPOSITION 59
4.3 MACROSTRUCTURAL EXAMINATION 61
4.4 MICROSTRUCTURE ANALYSIS 62
4.5 TESTING AND EVALUATION 66
4.6 COST ESTIMATION 68

CHAPTER 5 RESULTS AND DISCUSSION 10.7CrMoVNbN STEEL

OVERVIEW 69
5.1 10.7CrMoVNbN STEEL 70
5.1.1 STARTING MATERIAL 70
5.1.2 PROCESSING ROUTE 70
5.2 OPTICAL MICROSTRUCTURES 73
5.3 FESEM-EDS ANALYSIS 75
5.4 MICROHARDNESS ANALYSIS 79
5.5 MECHANICAL PROPERTIES 80

CHAPTER 6 RESULTS AND DISCUSSION AISI-321 STEEL

OVERVIEW 81
6.1 AISI-321 STEEL 82
6.1.1 SELECTION CRITERIA 82
6.1.2 STARTING MATERIAL 82
6.1.3 MANUFACTURING 83
6.1.4 HEAT-TREATMENT 83
6.1.5 EVALUATION OF SENSITIZATION/CORROSION RESISTANT 84
6.2 FESEM-EDS ANALYSIS 84
6.3 MICROSTRUCTURE STUDY OF PROCESSED STEELS 87
6.3.1 AS-ROLLED MICROSTRUCTURE 87
6.3.2 SOLUTION ANNEALED MICROSTRUCTURE 88

6.3.3 MICROSTRUCTURE AFTER STABILIZING TREATMENT 89
6.4 ANALYSIS OF PRECIPITATE COUNTS 89
6.5 MECHANICAL PROPERTIES 91
6.6 CORRELATION BETWEEN MECHANICAL PROPERTIES AND FRACTURE SURFACE 95
6.7 CORRELATION BETWEEN MICROSTRUCTURAL STABILITY AND MECHANICAL PROPERTIES 97
6.8 SENSITIZATION AND CORROSION RESISTANCE 99
6.8.1 SENSITIZATION BEHAVIOR ACCORDING TO ASTM A262 (PRACTICE A) 99
6.8.2 SENSITIZATION BEHAVIOR ACCORDING TO ASTM A262 (PRACTICE E) 100
6.8.3 SENSITIZE BEHAVIOR AFTER LONG SOAKING OF 100 HRS. 101

CHAPTER 7 RESULTS AND DISCUSSION C250 MARAGEING STEEL

OVERVIEW 105
7.1 C250 MARAGEING STEEL 106
7.1.1 STARTING MATERIAL 106
7.1.2 PROCESSING ROUTE 106
7.2 EFFECT OF MULTIPASS COLD DEFORMATION ON THE MICROSTRUCTURE 109
7.3 FESEM MICROSTRUCTURE 113
7.4 DISLOCATION DENSITY 116
7.5 NANOHARDNESS 119
7.6 MECHANICAL PROPERTIES 119
7.7 FRACTOGRAPHY 122
7.8 COST ESTIMATION 125

CHAPTER 8 RESULTS AND DISCUSSION 300M STEEL

OVERVIEW 127
8.1 C250 MARAGEING STEEL 128

8.1.1 STARTING MATERIAL 128
8.1.2 THERMOMECHANICAL PROCESSING 128
8.1.3 HEAT-TREATMENT 129
8.2 MICROSTRUCTURE ANALYSIS 129
8.3 XRD ANALYSIS 132
8.4 MECHANICAL PROPERTIES 139
8.5 FRACTOGRAPHY 140

CHAPTER 9 CONCLUSIONS

OVERVIEW 143
9.1 AMS-4340 STEEL 144
9.2 10.7CrMoVNbN STEEL 144
9.3 AISI-321 STEEL 145
9.4 C250 STEEL 146
9.5 300M STEELS 146
9.6 FUTURE SCOPE 147

REFERENCES 149

LIST OF TABLES

Table No.	Title	Page No.
Table 1.1	Application of different ultra-high strength steels.	9
Table 3.1	Composition and condition of etchants used.	47
Table 4.1	Permissible and designated steel chemistry for AMS-4340 grade steel.	54
Table 4.2	Melting, refining and casting parameters for primary heats.	56
Table 4.3	ESR process parameters.	56
Table 4.4	Slag consumption in respective ESR heats.	57
Table 4.5	Chemical composition of Wacker 2037 ELH slag.	58
Table 4.6	Chemical composition and of the primary heats (wt.%).	60
Table 4.7	Chemical composition of the ESR heats after finish forging and normalizing (wt.%).	60
Table 4.8	Macrostructure examination of ESR heats.	61
Table 4.9	Ultrasonic testing results for different ESR heats.	66
Table 4.10	Non-metallic inclusions (According to ASTM E45 Method A).	66
Table 4.11	Grain size of different ESR heats (According to ASTM E-112 standard).	66
Table 4.12	Desired and achieved mechanical properties for different ESR heats.	67
Table 5.1	Chemical composition and $Cr_{\#\$}$ the ratio of trial heats of 10.7CrMoVNbN steel (wt. %.).	70
Table 5.2	Sample preparation process flow diagram.	72–73
Table 5.3	Volume fraction of austenite, carbides, and δ-ferrite in all Heats measured using the grid intercept method.	75
Table 5.4	Composition analysis of energy spectrum on points as marked in Figure 5.4.	76
Table 5.5	Composition analysis of energy spectrum on points as marked in Figure 5.7.	79
Table 5.6	Microhardness of tempered martensite matrix, carbide, and δ-ferrite in different Heats.	79
Table 5.7	Mechanical properties in hardened and tempered condition.	80
Table 6.1	Chemical composition of secondary melted Ti stabilized AISI 321 steel.	82
Table 6.2	Sample preparation process flow diagram for AISI 321 TB1 and TB30.	83

Table 6.3 Composition analysis of energy spectrum on points as marked in Figure 6.1. 85

Table 6.4 Composition analysis of energy spectrum on points as marked in Figure 6.2. 87

Table 6.5 Volume fraction of precipitates and average austenite grain size of TB1 and TB30 steels in different treatment conditions. 88

Table 6.6 Room temperature mechanical properties of TB1 and TB30 steels. 92

Table 6.7 Elevated temperature tensile properties of TB1 and TB30 steels at 350 ℃ for different conditions. 93

Table 7.1 Chemical composition (wt.%) of C250 steel. 106

Table 7.2 Sample code for all processed condition. 109

Table 7.3 Sample code for cryogenic processing condition. 109

Table 7.4 Composition analysis of energy spectrum on points as marked in Figure 7.5. 115

Table 7.5 Dislocation density of different % cold deformed C250 steel. 118

Table 7.6 Nanohardness values of different % cold deformed C250 steels. 119

Table 7.7 Mechanical properties of C250 grade at different condition. 121

Table 7.8 Mechanical properties of cryogenic treated C250 grade steel at a cold working of 169.44%. 122

Table 7.9 Composition analysis of energy spectrum on points as marked in Figure 7.10. 123

Table 7.10 Composition analysis of energy spectrum on points as marked in Figure 7.11. 125

Table 7.11 Associated cost for the fabrication of fasteners using the conventional route. 126

Table 8.1 Chemical composition (wt. %) primary and remelting SAE 300M steel. 128

Table 8.2 VAR Operating Parameters. 128

Table 8.3 Heat-treatment conditions used for 300M steel. 129

Table 8.4 Williamson-Hall analysis of different heat treated 300M steels. 138

Table 8.5 Dislocation density ($\times 10^{15}$ m^2) of 300M steel using different models. 139

Table 8.6 Mechanical properties of 300M steel after different heat-treatment conditions. 139

LIST OF FIGURES

Figure No.	Title	Page No.
Figure 4.1	Process for the manufacturing of AMS-4340 UHSS.	55
Figure 4.2	Voltage, current and melting rate parameters for ESR heats (a) E1, (b) E2, (c) E3 and (d) E4.	57
Figure 4.3	Heating soaking and high temperature homogenization and forging cycles for ESR ingots E1, E2, E3 and E4.	58
Figure 4.4	Segregation of alloying elements of E1, E2, E3 and E4.	60
Figure 4.5	Macrostructure examination of ESR heats (a) E1 and (b) E4.	62
Figure 4.6	Microstructural characterization of ESR heats normalized at 870°C and tempered at 675°C for (a) E1, (b) E2, (c) E3, and (d) E4.	64
Figure 4.7	Microstructure of ESR heats after final heat-treatment process consisting of hardening at 870°C and tempering at 240°C for (a) E1, (b) E2, (c) E3, and (d) E4.	65
Figure 4.8	Microstructural features of the hydrogen flakes of ESR heat E1.	65
Figure 5.1	CCT diagram of Heat 4.	71
Figure 5.2	Optical microstructures of 10.7CrMoVNbN steel of (a) Heat 1, (b) Heat 2, (c) Heat 3 and (d) Heat 4 at 200X magnification using etchant Kalling No. 1.	73
Figure 5.3	Optical microstructures of 10.7CrMoVNbN steel of (a) Heat 1, (b) Heat 2, (c) Heat 3 and (d) Heat 4 at 200X magnification using sulphuric etchant.	74
Figure 5.4	FESEM microstructure of 10.7CrMoVNbN steel (Heat 1) with delta-ferrite (a) 5000X, (b) 20000X and (c) 20000X magnifications respectively.	76
Figure 5.5	X-ray dot mapping of heat 1 (Figure 5.4b) for V, Cr, Ni, Mn, Fe, Mo, C, Si, N, Ni, and Nb elements.	77
Figure 5.6	Line profiling of Heat 1.	77
Figure 5.7	FESEM microstructure of 10.7CrMoVNbN steel (Heat 4) without delta-ferrite (a) 5000X, (b) 10000X and (c) 20000X magnifications respectively.	78
Figure 5.8	Micro indentations on (a) tempered martensite matrix phase and (b) carbide phase and δ-ferrite phase.	79

Figure 6.1 FESEM microstructure of SA TB1 steel (a) 1000X, (b) 20000X, (c) 20000X and (d) 80000X magnifications respectively. 85

Figure 6.2 FESEM microstructure of SA TB30 steel (a) 1000X, (b) 5000X and (c) 1000X magnifications respectively. 86

Figure 6.3 Optical microstructure of as-rolled (a) TB1 steel and (b) TB30 steel. 87

Figure 6.4 Optical microstructure of solution annealed (a) TB1 steel and (b) TB30 steel. 88

Figure 6.5 Optical microstructure of stabilizes treated (a) TB1 steel and (b) TB30 steel. 89

Figure 6.6 Average values of the precipitates count with respect to precipitates area observed per image field in (a) AR, (b) SA, and (c) ST of TB1 and TB30 steels. 90

Figure 6.7 Optical microstructure of forged (a) TB1 steel and (b) TB30 steel in as-polished condition. 91

Figure 6.8 Engineering stress-strain curves of (a) TB1 steel and (b) TB30 steel at room temperature condition. 92

Figure 6.9 Engineering stress-strain curves of (a) TB1 steel and (b) TB30 steel at elevated temperature of 350 ℃. 93

Figure 6.10 (a) 0.2% yield strength and (b) percentage elongation as a function of temperature for TB1 and TB30 steel under ST condition. 94

Figure 6.11 FESEM analysis of tensile fractrographs of (a) TB1 steel at 2000X, (b) TB1 steel at 8000X, (c) TB30 steel at 2000X, and (d) TB30 steel at 8000X magnification under ST condition at room temperature. 95

Figure 6.12 FESEM analysis of tensile fractrographs of (a) TB1 steel and (b) TB30 steel at 8000X magnification under ST condition at elevated temperature of 350 ℃. 96

Figure 6.13 Microstructure of tensile fractured specimen near to tip of TB1 steel in ST condition at different testing temperature (a) RT, (b) 200 ℃, (c) 350 ℃ and (d) 650 ℃. 97

Figure 6.14 Microstructure of elevated tensile fractured specimen near to tip of TB1 steel in ST condition at different testing temperature (a) RT, (b) 200 ℃, (c) 350 ℃ and (d) 650 ℃. 98

Figure 6.15 Corrosion behavior of (a) TB1-SA, (b) TB1-ST, (c) TB30-SA, and (d) TB30-ST condition at 675^{o}C according to practice A of ASTM A262 standard. 100

Figure 6.16 Corrosion behavior of (a) TB1-SA, (b) TB1-ST, (c) TB30-SA, and (d) TB30-ST condition at 675 ℃ according to practice E of ASTM A262 standard. 101

Figure 6.17 Optical microstructure of sensitized steel at 600 ℃/100 hrs. (a) TB1 steel and (b) TB30 steel. 102

Figure 6.18 Optical microstructure of sensitized steel at 350 ℃/100 hrs. (a) TB1 steel and (b) TB30 steel. 102

Figure 7.1 Methodology used in the present study. 107

Figure 7.2 **(a)** Schematic of the forging cycle and (b) pictorial representation of forging cycle. 108

Figure 7.3 Optical microstructure of (a) T0, (b) T4, (c) T5, (d) T6, (e) T10, (f) T13, (g) T14, (h) T19, (i) T20, (j) T21, and (k) T22 cold rolled steel. 110–111

Figure 7.4 Optical microstructure of (a) T14 (b) T15, (c) T16, (d) T17 and (e) T18 cryogenic heat treated C250 steel etched with Keillings l for 25 min. at 500X magnification. 112–113

Figure 7.5 FESEM microstructure of C250 steel at (a) T0 (b) T4 (c) T14 and (d) T18 conditions at 1000X magnification. 114

Figure 7.6 EDS spectra of point 1, point 2, point 3, point 4 and point 5. 115

Figure 7.7 X-ray dot element maps showing the presence of Fe, Ni, Co, C, Mo, Ti and Al in Figure 7.5 (a). 116

Figure 7.8 (a) XRD of different cold drawn C250 steel and (b) Gaussian fitted data. 118

Figure 7.9 L-D curve of different C250 steels. 120

Figure 7.10 Tensile fractographs of C250 steel at (a) T0 (b) T4, (c) T14 and (d) T18 at 2000X magnification. 123

Figure 7.11 Impact fractographs of C250 steel at (a) T0 (b) T4, (c) T14, (d) T18 at 2000X and (e) T18 at 60000X magnification. 124

Figure 7.12 EDS analysis of point 1 and 2 marked in Figure 7.11. 125

Figure 8.1 Process flow chart for manufacturing of 300M steel. 130

Figure 8.2 Optical microstructure heat treated 300M steel to condition (a) NT (b) CQT (c) IST and (d) MAT at 1000X magnification. 131

Figure 8.3 SEM microstructure 300M steel heat treated to condition (a) NT (b) CQT (c) IST and (d) MAT. 132

Figure 8.4 XRD pattern of different heat-treated samples. 133

Figure 8.5 Gaussian and Lorentzian function of XRD analysis. 134

Figure 8.6 Scherrer equation plots of cos θ versus 1/β for the XRD samples presented in Figure 8.4. 135

Figure 8.7 W-H equation plots of β cos θ versus 4 Sin θ for the XRD samples presented in Figure 8.4. 136

Figure 8.8 W-H equation plots of β cos θ versus 4 Sin θ /E for the XRD samples presented in Figure 8.4. 137

Figure 8.9 W-H equation plots of β cos θ versus 4 Sin θ $(2/E)^{1/2}$ for the XRD samples presented in Figure 8.4. 138

Figure 8.10 Engineering stress-strain curves of different heat treated 300M steel. 140

Figure 8.11 Tensile fractographs of 300M steel with various heat-treated condition (a) NT (b) CQT (c) IST and (d) MAT. 141

Figure 8.12 Impact fractographs of 300M steel with various heat-treated condition (a) NT (b) CQT (c) IST and (d) MAT. 142

CHAPTER 1
INTRODUCTION

OVERVIEW

This chapter presents a general introduction of steels. The low carbon steels, especially the ultra-high strength steels (UHSS) are described in detail. The properties of some common UHSS is described. It also discusses the strengthening mechanisms and applications of different UHSS. Finally, the chapter discusses the origin of the present research work.

1.1 STEELS

Recent years have seen a great development in different type of steels because steels are the basic and desirable materials for variety of engineering applications viz. construction, aerospace, automobile and defence, etc. Classical classification of the steel includes ferritic steels, martensitic steels and austenitic steels. Ferritic steels provide good formability, martensite steels provide good strength whereas austenitic steels provide high temperature stability and corrosion resistance. In the modern era, steels with different strength-ductility combination are necessary. Taking this into account, advanced high strength steels (AHSS) have been processed. AHSS include steels like dual-phase (DP), complex phase (CP) or transformation induced plasticity (TRIP) steels. Due to the great combination of strength and formability, AHSS have shown a great potential for automotive applications [1,2]. The current trend of the industry is weight reduction while maintaining good strength and formability. This led to the development of a new generation of AHSS with extraordinary strength-toughness combination. The development of such steel requires innovation in the design of alloy chemistry and the processing routes. AHSS can be classified into three generations (i) first generation AHSS viz. DP, CP, and TRIP, (ii) second generation AHSS viz. Twin Induced Plasticity (TWIP) and Light-weight with Induced Plasticity (L-IP) steels, and (iii) third generation AHSS viz. advanced DP, advanced CP, and advanced TRIP steels. The first generation AHSS have high strength. However, they have limited deformation and fracture toughness. This restricts the application of these steels in different engineering applications. The second generation AHSS have good strength ductility combinations, but these steels contain high wt.% of alloying elements. This increases the overall cost of the steel and limits their use. Lastly, third generation AHSS steels were developed which provided a good strength-ductility combination and are also economical. In this category the development of complex phase steels have become an interesting area for many engineering applications because of inexpensive alloying elements with considerable reduction in weight without sacrificing mechanical properties [3]. CP steels have a good combination of mechanical properties and ductility because of presence of different phases. In the past decade, the processing of steel has been modified to achieve high strength. This high strength is because processing leads to modification in microstructure which hinders the movement of dislocations. Such steels exhibiting very high strength are called ultra-high strength steels (UHSS). Currently the focus is to develop UHSS for different engineering applications and has become the new area of research.

1.2 ULTRA-HIGH STRENGTH STEELS

The UHSS are a class of steels having very high yield strength and tensile strength. These steels are highly useful because of their high strength with better ductility for different applications. UHSS consists of multi-phase complex microstructure with a ferrite matrix as a primary phase and martensite and/or bainite, with some retained austenite as a secondary phase [4]. These steels are used in the variety of engineering applications and help in reducing the weight of the components. Thinner gauge sheets of UHSS in automobile bodies can reduce the weight of the components which may help to improve the fuel efficiency. Moreover, high toughness can provide the passenger safety. Mechanical properties of UHSS steels depends upon a variety of factors viz. phase composition, their volume fraction, size of precipitates and morphologyof phase constituent [4].

1.3 PROPERTIES OF COMMON ULTRA-HIGH STRENGTH STEELS

UHSS has complex microstructure with a ferrite matrix as a primary phase and martensite and/or bainite, with some retained austenite as a secondary phase. Because of these variations i.e. different phases and their distribution in the overall structure, UHSS show variation in mechanical properties and hence, make them suitable for different properties depending upon their applications. Based upon the requirement few UHSS steels viz. AMS-4340 steel, 10.7CrMoVNbN steel, AISI-321 steel, C250 steel, and 300M steel are discussed as these steels are part of our study in this thesis.

1.3.1 AMS-4340 STEEL

Various UHSS like AMS 4130, 4140 and 4340 are used in the variety of defense applications viz. gun barrel and ballistics. Despite of numerous improvements in steel making processes like electric arc furnace melting, refining, vacuum degassing etc. majority of rejections of steels is accounted to ultrasonic defects and chemical segregation [5]. The component that undergo rejection and are scrapped out is mostly due to defects such as segregation. The UHSS alloyed with Ni, Cr, Mo, V are more prone to hydrogen flacking in comparison to other UHSS steels [6,7]. AMS-4340 steels are normally manufactured through vacuum induction melting (VIM) followed by vacuum arc remelting (VAR). The steels processed by vacuum degassing and re-melting exhibit numerous advantages viz. reduced non-metallic inclusions, reduced gas levels

and superior cast structures as compared to the air-melting.

1.3.2 10.7CrMoVNbN STEEL

10.7CrMoVNbN (K9A62C) is a heat-resisting martensitic stainless steel developed by M/S Toshiba JSW Turbine & Generator Pvt. Ltd. for the manufacturing of turbine blades, nozzle partition and bucket for supercritical turbines [8–10]. This alloy has been tested for high temperature creep properties by Toshiba. The creep rupture strength observed at 650 ^{o}C at 226 N/mm^2 stress, and the rupture time >24 hours. During heat-treatment, the microstructure and mechanical properties are directly influenced by secondary phases, dislocations, and subgrains [11]. However, the presence of delta-ferrite deteriorates the mechanical/welding properties of martensitic heat-resistant steels. Further, the formation of Cr carbides near delta-ferrite decreases the corrosion resistance [12]. For high-temperature applications, the extent of delta-ferrite in heat resisting martensitic stainless steels determines the mechanical properties especially impact energy and weldability [13,14]. Delta-ferrite in weld component fabricated from 9-12 wt.% chromium heat resisting steels promotes the formation of type iv crack on the interface of heat affected zone. This causes the premature creep ruptures failures, especially when parts are in use in service for a long duration at a temperature of more than 600 ^{o}C. In grade P91, type iv cracking is the most dominant mechanism of creep rupture failures [18]. In martensitic steels, delta-ferrite solidifies first which completely/partially transforms to austenite during cooling. The retained δ-ferrite is dissolved by extensive heat-treatment or forging. However, higher temperature heat-treatment greater than 1350 ℃ is necessary to dissolve delta-ferrite in the steel. The presence of delta-ferrite is not economical and leads to undesired grain growth and cracking during cooling. Dissolution rate of delta-ferrite is greatly influenced by deformation. Dissolution rate of delta ferrite is dependent upon dynamic recrystallization and the formation of interior grain boundaries [12,15]. Delta-ferrite concentration can be largely suppressed by the addition of Ni. However, Ni increases the cost of the steel and lowers the martensite start temperature below room temperature.

1.3.3 AISI-321 STEEL

AISI 321 which is commonly used for inlet and outlet tubes of Voda Voda Energo Reactor (VVER) where working temperature is 291^{o}C to 321^{o}C [16]. AISI 321 is preferred material for

third generation VVER reactor compare to nickel-base corrosion resistance alloy such as Alloy 600, Alloy 690 and Alloy800 because it is much cheaper [17].

In Ti stabilized AISI 321 austenitic stainless steel, titanium combines with carbon and nitrogen from rich austenite solid solution to form metal carbides, nitrides and carbonitrides. TiC, TiN, and TiCN are more stable than chromium carbides and do not provide any opportunity for chromium carbide to nucleate along the grain boundary. It helps in avoiding the formation of chromium depletion zone in the proximity of the grain boundaries, thus preventing the intergranular corrosion and intergranular stress corrosion cracking [18–20]. Extensive studies have been carried out on boron addition to austenitic stainless steel. Small amount of boron (10-70 ppm) reduced segregation and and improve the high temperature mechanical properties and oxidation resistance [21–25]. It is due to the fact that the atomic radius of boron is small. The elastic binding energy of boron with defect sites such as dislocations, grain boundaries and vacancy is higher. This results in a strong driving force of the segregation on the defects locations [18]. Addition of boron enhances the heat-resistance properties of austenitic stainless steels. Boron phase precipitation at the grain boundaries and non-equilibrium boron segregation at the grain boundary have collegial effect on the strengthening of 304-B steels [26]. In SS-347 stainless steels, boron addition inhibits the formation of creep cavity and improves the creep rupture strength. Excessive amount of B accelerates the formation of intermetallic compounds which provide adverse effect [27]. Stainless steels with boron greater than 30 ppm when subjected to exposure between 650 and 1050 °C are highly susceptible to the precipitation of orthorhombic borides viz. $(Cr, Fe)_2B$ and $(Cr, Fe, Mo)_3B_2$ [28]. Boron addition (0.2–1.8 %) in steel is done. When the content of B increases, the volume fraction of the eutectic structure (mixture of austenite and $(Fe,Cr)_2B$) increases causing a significant degradation in the mechanical properties [29]. It is also reported that 5 to 7 ppm of boron is found in defect sites and stacking faults in matrix and balance boron precipitates at grain boundaries as $M_{23}(C,B)_6$ of nearly 1–5 nm and gives pinning effect while supressing precipitation of $Cr_{23}C_6$ carbides during sensitization and aging [30].

1.3.4 C250 STEEL

Traditional marageing steels are classified into C200, C250, C300 and C350 grades according to their yield strength levels (ksi) [31–33]. C250 steel is generally used in aerospace applications

[34–36]. Marageing steel contains about 18 wt.% Ni with 8–13 wt.% Co, 3–5 wt.% Mo and small additions of Ti and Al [37,38]. Ni addition to Fe-system generates the necessary thermal hysteresis gap for the transformation of austenite to martensite and vice versa. In the Fe-Ni system, the austenite to martensite transformation is governed by the concentration of Ni [31]. Various authors have reported that the chemistry of marageing steel contains 18% Ni. Addition of nickel and other alloying elements except cobalt lowers the austenite to martensite transformation temperature (M_s and M_f) [39–41]. Further, the addition 8% cobalt raises the M_s and M_f temperature to 230 and 150 ^oC respectively. In the solution annealed state, marageing steel shows excellent formability and greater ability to harden by ageing [42]. The chemistry of marageing steels is chosen in a way that austenite to martensite transformation is independent of the cooling rate. The ageing behaviour of the marageing steels has been studied extensively. At the ageing temperature of 440–650 °C, change in the microstructure was observed [43,44]. The ageing process in the initial phase is represented by recovery of martensitic structure followed by hardening and precipitation of hexagonal Ni_3Ti intermetallic phases. The rapid precipitation of Ni_3Ti phase is because of the fast diffusion of titanium atoms. The intermediate ageing process is represented by the precipitation of Fe_2Mo intermetallic phase, followed by transformation of martensite to austenite [42,45]. Maximum hardening of 18 wt. % of Ni marageing steel was due to the presence of Ni_3Ti and Fe_2Mo intermetallic phases [46,47].

The C250 steel is used for the automobile and aerospace applications where high strength and toughness are of great significance. C250 steel in solution annealed condition is supplied to the automobile and aerospace industry. The steel is then cold worked and deformed to achieve the final components for the automotive and aerospace sector.

1.3.5 300M STEELS

300M steel is a low-alloy UHSS. It is widely used in aircraft and aerospace applications because of their excellent combination of high strength, hardness, fracture toughness and fatigue property [48–50]. 300M steel is basically derived from AISI 4340 steel by alloying of silicon and vanadium [51]. Si and V addition to the steel refined the grain structure. In addition to this, Si and V improved the strength and toughness of steel and also improved the resistance to stress corrosion cracking [52,53]. Si in steel increases the retention capability of high-carbon ductile austenite and inhibits the formation of inter-lath brittle cementite and decreases the toughness and ductility of the steel

[54]. Si forms vanadium carbide that restricts the grain growth of austenite during the austenitizing heat-treatment [55]. The microstructure of quench-tempered 300M steel forging constitutes of martensite, bainite and retained austenite. These phases play a decisive role in final mechanical properties of the steel [49]. The structural modification in the 300M steel due to remelting and phase transformation gives 300M steels a higher yield strength (1615 MPa) and higher tensile strength (1963 MPa) in the quenched and low-temperature tempered conditions [56,57].

1.4 STRENGTHENING MECHANISMS OF ULTRA-HIGH STRENGTH STEELS

The properties of the steels can be altered by changing the desired microstructure. Strengthening and hardening mechanisms are used in different combinations to meet specific properties, such as strength, formability etc. Most common methods used for strengthening of UHSS are solid solution strengthening, grain refinement, work hardening, precipitation hardening, and transformation strengthening [4,58].

1.4.1 SOLID SOLUTION STRENGTHENING

Strength of the material depends upon the dislocation movement in the crystal lattice. The movement of dislocations within the material creates a stress field. When the atoms of other material are introduced in the lattice, local stress field is generated. These stress fields interact with the dislocations and inhibits the motion which increases the strength of the material. In substitutional solid solution, the stress field is spherically symmetric. This indicates that there is no shear stress component. Thus, for substitutional solid solution, solute atoms have no interaction with the shear stress field a characteristic of screw dislocations. However, for the interstitial solid solutions, solute atoms leads to the tetragonal distortion leading to the formation of shear stress field which can interact with edge, screw, and mixed dislocations. All the interactions lead to the formation of bonds between solute atoms and lead to the pinning of the dislocations. Thus, the amount of stress required for the plastic deformation increases and the increase in strength takes place.

1.4.2 GRAIN REFINEMENT

The mechanical properties of UHSS are significantly affected by the grain refinement. The ultrafine grained steels provide superior strength as compared to fine and coarse grained ultra-high strength steels [59].

1.4.3 WORK-HARDENING OR STRAIN-HARDENING

When the material continued to deform plastically beyond the yield point, the shear stress required to continue the plastic deformation increases continuously. Higher degree of stress is required to continue the plastic deformation. The stress required to deform the material in the plastic deformation is called as strainhardening or work hardening. The work hardening of a material is due to the rise in the dislocation density and deformation. The dislocations pile up at the grain boundaries and restricts the further deformation of steel. The higher dislocation density increases the resistance to further plastic deformation by locking of dislocations on slip planes [60].

1.4.4 PRECIPITATION HARDENING

Precipitation/age hardening is a heat-treatment process in which the yield strength of materials is increased. For this process, there must be some partial solid solubility between the solute and solvent atoms. Further, the solid solubility limit should decrease with decrease in temperature. Precipitation hardening is carried out in two steps (i) the material is heated to a single phase region and then quenched to room temperature to form a super saturated solid solution and (ii) ageing is carried out in which the super saturated solid solution is decomposed to form finely dispersed precipitates [60].

1.4.5 TRANSFORMATION STRENGTHENING

The steel processing leads to the phase transformation that enables strengthening by creating specific phase and specific microstructure. For example, higher toughness can be observed in the steel when soft phase ferrite and hard phase martensite or bainite is required. The phase transformation occurs due to the processes like hot rolling, continuous annealing where the steel is cooled from high-temperature austenite phase and transform to harder low-temperature phases. This mechanism is largely utilized for the development of UHSS [61,62].

1.5 APPLICATION OF ULTRA-HIGH STRENGTH STEELS

Different types of UHSS are utilized for variety of applications ranging from automotive, aerospace, thermal, nuclear, and defense applications. The mechanical properties of UHSS are highly influenced by the processing routes used for their manufacturing [63]. Table 1.1 presents a few UHSS steels with various applications.

Table 1.1 Application of different ultra-high strength steels.

UHSS	Application	Author
AMS-4340	Defense applications viz. gun barrel and ballistics	Singh et al. [64], Majumdar and Sadhukhan, [65],
10.7CrMoVN bN Steel	turbine blades, nozzle partition and bucket for supercritical turbines	Toshiba [8–10]
AISI-321	Nuclear reactors, heat exchangers and boiler tubes	Rosenberg and Darr [19], Thorvaldsson and Dunlop [66], Thorvaldsson and Dunlop [67]
C250	Aerospace landing gear applications	Garrison [34], Ding and Liang [35], Ding et al. [36]
300M	Aircraft and aerospace applications	Liu et al. [48], Liu et al. [49], Skubisz and Sinczak [50]

1.6 ORIGIN OF THE STUDY

Despite numerous improvements in steel making processes like electric arc furnace melting, refining, vacuum degassing etc. majority of rejections of steels is accounted for ultrasonic defects and chemical segregation. Pickering [6], observed that the components that undergo rejection and are scrapped out is mostly due to defects such as segregation. The ultra-high strength steels (UHSS) alloyed with Ni, Cr, Mo, V are more prone to hydrogen flacking in comparison to other UHSS steels. Liu et al. [7] have observed that segregation of Ni, Cr, and C occurs from top to bottom and also from center to surface of eletroslag remelting (ESR). This was attributed to the gravity and thermal buoyancy effects in ESR. Singh et al. [64], have observed that hydrogen flacking is a major reason for the rejection of UHSS, especially steels developed for defense applications. Various UHSS like AISI 4130, 4140 and 4340 are used in the variety of defense applications viz. gun barrel and ballistics. Majumdar and Sadhukhan, [65], manufactured Ni-Cr-Mo-V UHSS for gun barrel applications using an alternate route and observed an improvement in mechanical properties. UHSS should be ultra-clean steels with less elemental segregation to achieve isotropic mechanical properties.

For steam turbine applications, the presence of delta-ferrite deteriorates the mechanical/welding properties of martensitic heat-resistant steels. Furthermore, it can disrupt the passivation layer

locally due to Cr depletion in martensite and the development of Cr carbides in delta-ferrite, resulting in corrosion resistance reduction. [12]. For high-temperature applications presence and extent of delta-ferrite in heat resisting martensitic stainless steels determines the mechanical properties especially impact energy and weldability [13,14]. Delta-ferrite in weld component fabricated from 9-12 wt.% chromium heat resisting steels promotes the formation of type iv crack on the interface of heat affected zone. It leads to premature creep rupture failures, especially when parts are in use in service for a long duration at a temperature of more than 600 ^{o}C. In grade P91 type iv cracking is the most dominant mechanism of creep rupture failures [18]. Similarly, for other engineering applications, the failure of material is a critical parameter. For all these specific application the specific category of steel is needed. Thus, the study needs to be carried out to develop different ultra-high strength steels for different engineering applications like nuclear applications, super critical turbines, gun barrels etc.

CHAPTER 2
REVIEW OF LITERATURE

OVERVIEW

This chapter presents an extensive literature review on ultra-high strength steels (UHSS) developed for different engineering applications. The literature review is restricted mainly to five different types of UHSS which have been undertaken in the present research work. The role of alloying elements, chemical compositions, and the heat-treatment procedures adopted for the development of the steels followed by different thermomechanical treatments to enhance the mechanical properties of ultra-high strength is discussed in detail. The review of literature mainly covering the AMS-4340 steels, 10.7CrMoVNbN steels, AISI321 steels, C250 steels, and 300M steels is considered in this review section. Considering the main applications of these steels for different engineering components and their causes for failure while in use has been highlighted in this section. The role of alloying elements to develop the microstructure and corresponding properties has been discussed in this chapter.

2.1 PROCESS DESIGN

Ultra-high strength steels (UHSS) are normally used through vacuum induction melting (VIM) followed by the melting in electro slag re-melting (ESR) or vacuum arc melting (VAR) or both. These steels are mainly used in aircraft components like landing gears, fasteners, jet engine shafts, and other different applications like gun barrels, ballistic resistant armor sheets or plates, high temperature steam turbine parts and coolant tubes in nuclear reactors. Vacuum melting results in very low level of gases in VIM ingot and is especially necessary for melting of alloy steels and super alloys having reactive elements like titanium. Electro slag re-melting (ESR) removes non-metallic inclusions through liquid reducing slag and leads to well defined microstructure due to controlled solidification leading to minimized chemical segregation. But, hydrogen removal does not occur in this process. In VAR process, the dissolved gases like hydrogen, nitrogen, and carbon mono-oxide are removed along with trace elements having high vapor pressures. VAR also results in improvement in oxide cleaning along with directional solidification from bottom to top of VAR ingot. Alloys used for all these applications need to be free from non-metallic inclusions with isotropy in mechanical properties in all directions which is possible through very controlled thermomechanical processing and heat-treatment.

The role of alloy design, steel melting refining and re-melting, thermomechanical processing and heat-treatment adopted to enhance the mechanical properties and microstructural stability has been discussed in this review section. The review articles mainly covering the AMS-4340 steels, 10.7CrMoVNbN steels, AISI321 steels, C250 steels, and 300M steels is considered in this review section. The main applications of these steels and their reasons of failure have also been highlighted in this section. Since, all five categories of steels included in this research review chapter are in industrial use, so the efforts made by different authors to develop these steels and their corresponding properties has been described.

The role of alloy design considering the effect of alloying elements like Carbon [68], Manganese [68], Phosphorus [69,70], Sulphur [71], Silicon [70], Vanadium [72], Chromium [73], Nickel [28], Molybdenum [74], Nitrogen [75], Copper [76], and Cobalt [77] is very important to achieve targeted property which has been used in all these alloy steels.

2.2 AMS-4340 STEELS

AMS-4340 steel is used in a variety of engineering applications viz. Defense applications viz. gun barrel and ballistics. Despite numerous improvements in steel making processes like electric arc furnace melting, refining, vacuum degassing etc. majority of rejections of steels is accounted for ultrasonic defects, hydrogen flaking, and chemical segregation. Hydrogen flaking is major problem in the steel. Considering its application majorly in defence sector, the processing route of this steel requires redesigning to eliminate their existing problem. The work done by different authors is summarized below.

Johnson [78] **in 1874** studied the effect of hydrohen and acids on iron and steels. The authors observed that the hydrogen in the steel got diffused at the atomic level that has led to the increase in the hydrogen embrittlement of steel.

Garr and Troiano [79] **in 1957** studied the hydrogen flaking in heavy alloy steel sections. A 15-ton experimental heat of Cr-Ni-Mo steel with very high hydrogen content was prepared using a electric furnace. Different antiflaking treatments were carried out on the ingot. Antiflaking treatment constituting of isothermal transformation in pearlite range developed flake-free steel forgings. Similar processing cycle in the bainite range was not successful as the complete isothermal transformation was not attained. The authors also observed that the stresse transformation plays a crucial role in flaking of heavy steel sections.

Lai et al. [80] **in 1974** studied the influence of austenitizing temperature on the mechanical properties of as-quenched AMS-4340 steel. The steel was austenized at 870 ℃ and 1200 ℃ respectively. The authors observed that the steel specimen austenitized at 870 ℃ showed martensite twinning whereas no martensite twinning was observed for steel austenized at 1200 ℃. The strain fracture toughness of steel austenized at 1200 ℃ was 80% higher than the steel austenized at 870 ℃. The yield strength of the steel was found to be independent to the austenitizing temperature. The higher austenization temperature enhanced the fracture toughness of the steel specimen.

Choudhury [81] **in 1992** studied the fabrication of superalloys for aerospace applications using

the state of the art vacuum induction melting (VIM)/vacuum arc remelting (VAR) or vacuum induction melting (VIM)/electro slag remelting (ESR) process. The authors reported that VIM process is crucial for the processing of Ni and Co based superalloys as these are susceptible to reactions with nitrogen and oxygen in the atmosphere. The author reported that for very low concentration of hydrogen and exceptional clean steels, vacuum induction melting is necessary and by controlling the environmental factors vacuum arc remelting and electroslag remelting can also be used. The steels processed by vacuum degassing and re-melting exhibit numerous advantages viz. reduced non-metallic inclusions, reduced gas levels and superior cast structures as compared to the air-melting. However, the process itself is very expensive and the overall cost of the finished material is very high.

Fruehan [82] **in 1997** presented a review article on hydrogen flaking and its preventive measures. The author suggested that an anti-flacking treatment (AFT) path to achieve austenite to bainite transformation process by minimizing the hydrogen flaking with minimum elemental segregation and avoiding austenite to martensite transformation during post forging. The authors also studied the factors affecting hydrogen flaking. Microstructure and metallurgical factors, section thickness, steel hardenability, and post forging handling of the steels has a great influence on the hydrogen flaking of the steel. Impurities like nonmetallic inclusions in the steel act as the collection sites for hydrogen thus, increase the hydrogen flaking tendency of the steel. Further, higher concentration of hydrogen is observed along the grain boundaries. Coarser grain size has lower grain boundaries which decreases the tendency of hydrogen flaking. The steels with higher section thickness have a higher susceptibility towards hydrogen flaking. This was the result of decreased efficiency of AFT treatment due to long time requirements. Further, higher hardenability of the steel increases the hydrogen flaking tendency of the steel. After the forging process, improper cooling, excessive rapid cooling, and lack of a proper AFT treatment also leads to an increase in hydrogen flaking of the steels.

Voronenko [83] **in 1997** studied the presence of hydrogen flakes in steels. The author observed that flakes are like thin hair cracks on fracture surfaces. The flakes appear to grow with time which makes them very hazardous defects. Depending on the dimensions, number, and position of flakes in the metal, a significant loss in toughness and ductility of steel is observed. The sudden loss in

properties of steels leads to a catastrophic failure. Further, computation methods suggested by anti-flaking heat-treatment (AFHT) technologies can be used to optimize the diffusion and removal of hydrogen from large forgings. It can also be used to determine the temperature of the melt, hydrogen content during isothermal holding, and hydrogen content in liquid steels. The author recommended the use of AFHT treatment with the final heat-treatment process. This provides elevated toughness to the steels and reduces the flaking in the steels.

Ifergane et al. [84] **in 2001** studied the effect of processing route on the fatigue life of bolts made of AMS-4340 steel for aerospace applications. The authors observed that for improved fatigue life, the threads should be fabricated during cold rolling followed by heat-treatment process. Fatigue life of the bolts was significantly affected by the manufacturing process. Whereas, the mechanical properties of AMS-4340 steel was not significantly affected.

Dimitriu [85] **in 2002** studied the factors affecting flakes and their preventive measures. The authors observed that the flakes are developed due to the tensile strength developed during hot plastic deformation and cooling after the deformation. Thus, for the removal of flakes, hot plasting deformation and cooling should be performed at minimal tesile strength. Further, the flakes can also be reduced by welding.

Mirzaev et al. [86] **in 2006** have done the theoratical modeling to solve the issue of removal of hydrogen by heat-treatment of large forgings. For the isothermal heating of a cylinder in a medium, the authors used various differential equations. Differential equations were utilised to determine the change in hydrogen concentration in forgings based on data on hydrogen concentration at the cylinder axis/or average bulk hydrogen concentration. For forgings with square cross sections, similar equations were constructed for different cross sectional areas. The study revealed that the calculated annealing times of a cylindrical forging increase by three times for a two-fold decrease in hydrogen content in a forging.

Ćwiek [87] **in 2010** studied the preventive methods used against hydrogen degradation of steels. Degradation of hydrogen in steel is a form of faliure thst is complimented by the enviornment. The hydrogen, in combination with residual or applied stress, causes failure, resulting in a decrement in

plasticity, load bearing capacity, and cracking. The author observed five types of hydrogen induced damages like cracking from hydride formation, cracking from precipitation of internal hydrogen hydrogen embrittlement, hydrogen attack, and hydrogen-induced blistering. Next, the author suggested different methods to reduce hydrogen degradation. The most common methods include selection of applicable material, transforming environment to decrease the hydrogen charging, and utilize surface coatings and effective/suitable inhibitors.

Sk et al. [88] **in 2011** studied the hydrogen embrittlement of AMS-4340 steel. The authors observed that the no hydrogen embrittlement was observed for the samples exposed to the hydrogen peroxide vapor of concentration of 1000ppm for 4.8 hours. Increase in concentration of hydrogen peroxide vapor to 1300 ppm and 1600 ppm led to the condensation of the vapor in the chamber and caused brittle fracture of the specimen as confirmed by SEM analysis. Inter-granular fractures along austenitic grain boundaries were visible near the root of the notch in hydrogen embrittled samples.

Tartaglia and Hayrnen [89] **in 2012** studied the fatigue life of austempered and quench-tempered AMS-4340 steels. The authors observed that the fatigue resistance, hardness and yield strength of austempered and quench-tempered AMS-4340 steel was identical. However, the two differed in the elastic and plastic strain regimes. The austempered steel showed high cycle fatigue life than the quench-temper samples. Whereas the quench-tempered steel showed low cycle fatigue life. Although, the fatigue fracture of both steels was similar but, in the overload regions the quench-tempered sections composed of dimple rupture. Whereas, for austempered samples dimple fracture was complimented with quasi-cleavage fracture.

Pickering [6] **in 2013** studied the macro segregation present in the steel ingots. The authors observed that the component that undergo rejection and are scrapped out is mostly due to defects such as segregation. Although, large volume of research is carried out on the steel manufacturing however, the majority of failures are still due to segregation. Due to the increase in the demand of steels in nuclear and pressure vessel applications, chemical homogeneity has become an important parameter for the study. The author observed that the modern day computational models can be

used to predict the segregation and inhomogeneity in steels. These models can be used to reduce the inhomogeneity and macro segregation in the steels.

Sun et al [90] **in 2014** studied the influence of laser clad repair on fatigue nature of AISI4340 steel. The authors observed a decrease in the tensile properties and fatigue life of AISI 4340 as-clad specimen as compared to the substrate material. The decrease in the properties can be attributed to the hard and brittle properties of heat affected zone. Transformation of clad layer to secondary hardening grade steel improved fatigue and tensile properties as compared to the quench and temper grade AISI 4340 steel. Post heat-treatment improved the tensile properties and fatigue life of the specimen.

Vrbek et al. [91] **in 2015** studied the changes in hydrogen content during steelmaking. The authors observed an increase in hydrogen concentration during steelmaking. The value reaches maximum during casting in tundish. The hydrogen concentration was observed to be lower for ACF steelmaking technology (aluminium and calcium free technology) in comparison to KL (aluminium technology) steelmaking technology. Further, the authors also described the changes in the solubility of hydrogen at various stages of steel manufacturing and also suggested different methods to measure hydrogen content in liquid and solid state.

Arh et al. [92] **in 2016** studied the different electroslag remelting (ESR)process. The authors observed that ESR process is crucial process as it provides a good control on solidification, microstructure, and chemical homogeneity of the steel. ESR also enables lower inhomogeneity and provides better mechanical properties. ESR process is suitable to develop high-alloyed steels with a controlled chemical composition. The steels processed using ESR heats can be used in aerospace, thermal power plants, nuclear power plants, chemical engineering, military equipment, and special tools etc.

Liu et al. [7] **in 2016** studied the structural evolution in steel ingot manufactured using electroslag remelting (ESR) technique. The authors observed that the segregation of Ni, Cr, and C occurs from the top to bottom and from center to surface of ESR. This was attributed to the gravity and thermal buoyancy effects of the steel during ESR processing. The lower solid solubility of carbides in α phase led to the increase in the precipitation of carbides. The authors also reported that a suitable

heat-treatment process can be used to dissolve the excessive carbides and lower the dendrite segregation.

Majumdar and Sadhukhan, [65] **in 2016** studied the properties of Ni-Cr-Mo-V steel for gun barrel applications. UHSS for gun barrel applications using an alternative electroslag remelting (ESR) route was developed. The authors observed that Ni-Cr-Mo-V steel offered a significant improvement in the tensile strength, impact strength and fracture toughness for alternative processing route followed by heat-treatment. The mechanical properties were found to be comparable with the gun barrel specifications. The improved properties of Ni-Cr-Mo-V steel were able to withstand the high explosive loads of the gun barrels. UHSS should be ultra-clean steels with less elemental segregation to achieve isotropic mechanical properties. For this application, manufacturing of UHSS is carried out in vacuum using vacuum induction melting process followed by vacuum arc remelting.

Ali et al. [93] **in 2017** studied the electroslag refining of CrNiMoWMnV ultra-high strength steel. The authors observed that during refining, the synthetic slag provided a superior yield of alloying elements with the exception of Si. The higher loss of Si was attributed to high oxidation of Si to SiO_2. Further, SiO_2 reacts with calcium oxide in the slag and forms stable calcium silicate which lowers the activity of silicon dioxide. The authors observed that ESR process is crucial secondary refining processes, this is due to the relative low production cost, low capital investment and ability to produce high quality steel. Further, to manufacture UHSS, the chemical composition of the slag and the activity of the elements in the molten metal should also be considered.

Singh et al. [64] **in 2017** observed that hydrogen flacking is a major reason for the rejection of UHSS, especially steels developed for defense applications. Various UHSS like AISI 4130, 4140 and 4340 are used in the variety of defense applications viz. gun barrel and ballistics.

Konopel et al. [94] **in 2018** developed a way to measure the concentration of hydrogen in the solid steel. The authors observed that the vacuum techniques used to measure the hydrogen concentration provides reliable results as compared to the method of heating and melting in a carrier gas.

Steneholom et al. [95] **in 2018** studied the influence of various control parameters on the manufacturing of the steel. The authors observed that the control on deslagging and deoxidation processes was crucial to achieve a clean steel. If the deslagging process is not carried out in a suitable manner, the steel will have lower aluminium concentration and hence, an increase in the oxygen content can be observed. Next the authors observed that vacuum degassing is important to manufacture clean steel i.e. it should be free from oxygen, sulphur and other impurities.

AlSumait et al. [96] **in 2019** studied the fatigue life of 4340M steel. The authors observed that the shot peening with the coverage of 200 % showed best results with applied stress of 1378 MPa. For 200 % coverage, the optimum fatigue life was observed. For 300 % coverage, higher fatigue life was observed for the applied load of 1448 MPa. However, for 4340M steel with 55 HRC hardness decreased the fatigue life significantly as compared to 200% coverage.

Ghazali et al. [97] **in 2020** studied the plasticity and fracture of AISI 4340 steels at different loading conditions. The authors observed that for smooth bar specimens, a reduction of 23 % and 30 % in fracture strain was observed for 32 HRC and 39 HRC specimens over the 16 HRC specimens respectively. Further, for the sharp notch samples, the fracture strain of 32 HRC and 39 HRC specimens was 21.6 % and 39.2 % lower to the 16 HRC specimen respectively. For large flat grooved samples, the reduction of 22.3 % and 54.7 % in fracture strain was observed for 32 HRC and 39 HRC specimens. Further for small flat grooved specimen, the fracture strain of 32 HRC and 39 HRC specimens was 31% and 58.1% lower to the 16 HRC specimen respectively.

Laliberté-Riverin et al. [98] **in 2020** studied the hydrogen embrittlement of AISI 4340 high strength steel. The authors observed that the incremental loading test was not able to detect the embrittlement in compact tension samples C(T) or sustained-load test (SLT) samples. Thermal desorption spectroscopy (TDS) showed a sharp peak around 300 °C. This was attributed to the hydrogen located in the coating and interface between the coating and the steel. The authors believed that the hydrogen is released with the evaporation of coating at the temperature of 300 °C. The TDS peak intensity was significantly greater than the interfacial region.

Pavinzadesh et al [99] **in 2021** studied the effect of edge reduction of induction hardened spur gear made of AISI 4340 steel. The authors observed that for highest machine power maximum case depth with minimum edge effect at root and tip is achieved for spur gear. The research provides a thorough investigation of case depth in the presence of magnetic flux concentrators under a variety of process parameters, as well as a solid guideline for edge effect during the induction hardening process.

From the above literature it can be observed that many authors have worked on the development of AMS-4340 steels. However, hydrogen flaking and hydrogen embrittlement were the main causes of failure of the steels. To overcome this issue, authors proposed the use of VIM and VAR process for fabrication of the steels. The authors reported that the advanced steel processing techniques like VIM, VAR, and ESR offered a significant improvement in the tensile strength, impact strength and fracture toughness of the steels. Further, a few authors have also suggested the use of anti-flaking heat-treatment as an alternative way to reduce hydrogen embrittlement of the AMS-4340 steels. VIM process is crucial for the processing of Ni and Co based superalloys as these are susceptible to reactions with nitrogen and oxygen in the atmosphere.

2.3 10.7CrMoVNbN STEELS

10.7CrMoVNbN (K9A62C) is a heat-resisting martensitic stainless steel used for the application of turbine blades, nozzle partition and bucket for supercritical turbines. The presence of delta-ferrite deteriorates the mechanical/welding properties of martensitic heat-resistant steels. Further, the formation of Cr carbides near delta-ferrite decreases the corrosion resistance. Further, chromium depletion in martensite and the precipitation of delta-ferrite, leads to the reduction in corrosion resistance of the steel. Based upon the aforesaid discussion, the literature pertaining to the 10.7CrMoVNbN steels is presented below.

Hättestrand and Andrén [100] **in 2001** studied the effect of strain on precipitation reactions during creep of 9 % chromium steel. The authors observed that the coarsening of nitrides is independent of strain. Next, the laves phase precipitates are higher in the creep related samples as compared to the isothermally aged samples. Further, the volume fraction of nitride precipitates remained constant during creep testing.

Masuyama [101] **in 2001** studied the history of the heat-resistant steels in power plants. The authors reported that for environmental and energy conservation concerns, the temperature of steam in the steam power plants has been raised to 600 ℃. Japan and Europe have adopted the steam temperature of 630 ℃ in their thermal power plants. The next aim of steam power plants is to increase steam temperature to 650 ℃. Thus, a new heat resistant steel for boiler and turbine applications are being developed. Among the variety of steels being developed for super critical steam cycles, major focus is given to the steels with 9–12% Cr. Ferrite steels with 9–12% Cr provide superior properties as compared to conventional austenitic stainless steels. The ferrite steels with 9–12% Cr have creep rupture strength of 140 MPa at 600 ℃ for 100 000 hours.

Ennis and Czyrska-Filemonowicz [102] **in 2003** studied the recent developments in the creep resistant steels for power plant applications. The authors reported that the 9% Cr steels are of great interest in the power plant applications. The martensitic transformation in Cr steels produces high dislocation density which in turn increases the hardness of the steels. The dislocation density of the steel decreases with the increase in the operating temperature. This can be attributed to the recovery effects of steel at high temperature. The authors also observed that at temperatures >600 ℃, the oxidation resistance of 9% Cr steel is not high enough for use in thin-walled components. For the aforesaid applications, steels with 11% Cr steels has shown a great potential.

Carrouge et al. [14] **in 2004** studied the effect of delta-ferrite on impact strength of martensitic stainless steel. The impact test indicated that 14% delta-ferrite in martensitic matrix of 60 mm steel increased the ductile-to-brittle transformation temperature by 50 ℃ as compared to the complete martensitic 80 mm steel. Further, the decrease in the amount of delta-ferrite from 14 to 2% improved the ductile-to-brittle transition temperature to a level comparable the tempered parent steel. Testing of the simulated heat affected zone showed that toughness of the material was independent of the presence of the delta-ferrite. The ductile-to-brittle transformation temperature of the specimen was comparable to the parent steel and was observed to be lower than the heat-treated specimens having 14% delta-ferrite.

Kaybyshev et al. [103] **in 2010** studied the martensitic steels (Fe–9Cr alloy) for boiler pipes and steam pipelines. The maximum temperature achieved by the boiler tubes of steam power plants is generally 620 ℃. The martensitic steels can withstand creep. The working life of Fe–9Cr steels is calculated till the time up to which the nano carbonitrides are dispersed in the steel.

Wang et al. [13] **in 2010** studied the influence of delta-ferrite on the impact strength of 13Cr-4Ni steel. The authors reported that the presence of delta-ferrite in the steel reduces the impact strength and increases the ductile to brittle transformation temperature of the steel. The presence of delta-ferrite decreased crack initiation/propagation. But it does not affect the impact energy of the material.

Takasawa and Miki [104] **in 2011** developed the blade rotors for high pressure steam power plant applications. First rotor with high chromium steel was used in 1971. JSW has developed a Ni-Fe base superalloy (FENIX-700) for turbine rotor applications. The steel is capable to withstand a temperature of 700 ℃. Similar to the high Cr ferritic steels, the superalloys developed in the present study increase the efficiency of fossil power plants and reduce the greenhouse gas emissions.

Martorano et al. [105] **in 2012** predicted the content of delta-ferrite in stainless steel castings. The authors reported that the method developed by using different combinations of chromium/nickel equivalents and the iso-ferrite lines from Schaeffler diagram provide superior prediction with lowest relative errors. The authors also observed that the rise in the cooling rate from 0.78 to 2.7 K/s decreased the fraction of delta-ferrite. On the other hand, statistical hypothesis tests showed that it is effective in only 50% of the samples which contain ferrite in the microstructure.

Prat et al. [106] **in 2013** studied the role of laves phase on creep strength of heat-resistant 9 % chromium steels. Kinetic modeling was performed using DICTRA software. The predictions clearly indicate that laves phase precipitates form clusters and have irregular shape. This phase is found in close proximity to the $M_{23}C_6$ carbides, along martensite lath boundaries. The simulation results show that the kinetics of growth of Laves phase was faster in the first 1000 hours of creep and reached at equilibrium at about 10,000 h. It was also observed that the growth kinetics of laves

phase was slower to the $M_{23}C_6$ carbides. The final equilibrium is reached at 13,000 h. The authors concluded that the low carbon content with 9% chromium steel provides the best creep resistance. **Abe** [107] **in 2015** studied the development of high temperature resistant material for steam power plant applications. The authors reported that substantial progress has been made in the development of high temperature resistant Ni-base alloys and 9–12 % Cr martensitic steels. The steels are capable of working till 700 ℃. Martensitic 9–12 % Cr steels can be a substitute for the expensive Ni-base alloys on thick boiler sections and turbine components. The steels provide a superior creep-rupture strength, good weldability, minimal loss in strength of welded joints, and lower creep-fatigue properties.

Nair and Kumanan [108] **in 2015** studied different materials for supercritical power plant components. The authors concluded that only nickel-based alloys are suitable for applications above 760 ℃. The authors also reported numerous studies being carried out on the manufacturing of nickel-based alloys using different manufacturing processes. Welding of nickel-based alloys is also a challenge as nickel has low weldability and form weak weldments. Welding and forming are of prime importance in the boiler fabrication whereas machining plays a role in the fabrication of valves, turbine blades, vanes and other accessories.

Tao et al. [11] **in 2016** studied the effect of quench and temper process on the mechanical properties of X12CrMoWVNbN10-1-1 steel. The authors observed that the austenitized sample consisted of typical lath type martensite with small quantity of retained austenite and negligible delta-ferrite. After tempering at 570 ℃, no retained austenite was observed. However, the tempering led to the formation of chromium rich precipitates viz. M_7C_3, Cr-rich $M_{23}C_6$, Cr-rich M_2N and niobium rich precipitates like MN. The tempering leads to the formation of sub grains which decreases the dislocation density. The authors also observed that the maximum hardness and impact strength obtained after heat-treatment was 283 HV and 33.6 J respectively.

Liu et al. [109] **in 2017** studied the effect of forging process for the removal of delta-ferrites in 10Cr12Ni3Mo2VN steel. Delta-ferrite in electroslag remelted ingots of steel can be eliminated by heating the steel at a high temperature. The delta-ferrite dissolution rate is dependent upon the heating rate. Hence, the time required for complete dissolution of delta-ferrites is high. The authors

reported the deformation as an alternate method to dissolve delta-ferrite. Deformation process increases the dynamic recrystallization and leads to the formation of interior grain boundaries which significantly increases the dissolution rate of delta-ferrites. The authors designed a multidirectional forging process which completely eliminated the delta-ferrite and achieved a fine and uniform matrix microstructure.

Niessen et al. [12] **in 2017** have done the kinetics modeling of delta-ferrite formation in martensitic stainless steel. DICTRA model was used for the kinetic modeling. The kinetic model predicted that micro-segregation due to solidification will homogenize within 2–3 seconds of cooling. Further the retained delta-ferrite is a result of incomplete austenitic transformation. The model also predicted well the concentration of delta-ferrite with the partitioning of Cr and Ni. Further, the authors predicted that the slower cooling leads to a decrease in the delta-ferrite. The results were found to be comparable with the experimental results.

Singh and Nath [110] **in 2021** studied the effect of cyclic treatment of the dissolution of delta-ferrite. The authors reported that during the cyclic heat-treatment at 950 ^{o}C, the carbides dissolved at the interface of delta-ferrite and martensite. The dissolution of delta-ferrite began with the diffusion of alloying elements and the conversion of delta-ferrite to austenite. Small concentration of delta-ferrite in the microstructure had no significant effect on the microhardness or bulk hardness of the steel. But the concentration of delta-ferrite has a great influence on the mechanical properties of the steel. For the delta-ferrite content of 6.3 % the yield strength, tensile strength, and hardness increased by 69.5 %, 35.5 %, and 50 % respectively.

2.4 AISI321 STEELS

AISI 321 steels are used in the applications of nuclear reactors, heat exchangers and boiler tubes. Chromium carbide in the stainless steels nucleate along the grain boundary and lead to the formation of chromium depletion zone in the proximity of the grain boundaries and forms intergranular corrosion and intergranular stress corrosion cracking. The failure of austenitic stainless steels can be reduced by the addition of titanium to the steels. Titanium combines with carbon and nitrogen rich austenite phase to form metal carbides, nitrides and carbonitrides. TiC, TiN, and TiCN are more stable than chromium carbides. However, these carbides lose their

effectiveness at elevated temperatures. TiC, TiN, and TiCN carbides gets dissolved in the steel when exposured to the temperatures between 650–1050°C. To overcome this issue, boron is added to the steel. The addition of boron has a great influence on the precipitation behaviour at grain boundaries and helps to improve the high temperature mechanical properties and oxidation resistance. Based upon the aforesaid discussion, the literature pertaining to the AISI 321 steels has been presented below.

Thorvaldsson and Dunlop [67] **in 1980** studied the precipitation behavior of Ti-stabilized austenitic stainless steel. The authors observed that MC precipitated at the dislocations and stacking faults whereas, $M_{23}C_6$ got precipitated at the intergranular boundaries. After the ageing of 5000 hours, MC precipitates started to migrate to intergranular sites. The MC precipitates on stacking faults had higher stability in comparison to MC precipitates on the dislocations.

Karlsson et al. [111] **in 1982** studied the grain boundary segregation in boron added austenitic stainless steel. The authors monitored the grain boundaries of boron added steels using atom probe microscopy. During cooling (From solution annealing), boron in the steel tends to segregate at the grain boundaries. Atom probe microscopy revealed minimal Cr depletion near the boundary.

Thorvaldsson and Dunlop [66] **in 1982** studied the precipitation behavior of austenitic stainless steel. The authors observed that both stabilizing elements viz. Nb and Ti were present in the MX precipitates. A significant proportion of chromium was dissolved in the MX precipitates. This effect was superior for the nitrides than for the carbides. This increased the solubility of nitrides and leads to the coarsening of the grain during high-temperature aging. The authors also observed that with longer ageing time the TiC precipitates partially transformed to M23C6. Thus, Nb was considered to be a better stabilizing agent in comparison to Ti.

Herman et al. [112] **in 1992** studied the precipitation kinetics of microalloyed hot-rolled high strength low alloy (HSLA steels. The authors observed that the precipitation rate depends on the transformation temperature and is independent of the cooling rate. Higher cooling rate decreases the incoherent fraction and increases the coherent precipitation during the precipitation hardening.

Yao [113] **in 1999** studied the grain boundary hardening of 304 austenitic stainless steel. The authors observed that the grain boundary hardening decreased below 900 ℃. Changes in grain boundary hardening are linked to the dissolution of $M_{23}X_6$ carbides and the precipitation of M_2B borides. At the ageing temperature of 900 ℃, the non-equilibrium segregation of boron improved the grain boundary hardening of steel.

Min et al. [114] **in 2002** studied the effects of TiC and $Cr_{23}C_6$ carbides on fatigue and creep properties of AISI321 stainless steel. Creep and fatigue tests were carried out using a total strain range-controlled creep-fatigue tests at 600 ℃. The creep life of aged alloys containing TiC carbide was superior to alloys having $Cr_{23}C_6$ carbides. This was attributed to the higher cavitation resistance offered by TiC as compared to $Cr_{23}C_6$. The authors observed that the strong interfacial affinity between TiC and matrix decreases the formation and growth of cavities in TiC containing alloys.

Min et al. [115] **in 2004** studied the effect of the carbides on grain boundary cavitation resistance of AISI321 stainless steel. The creep/fatigue life of fine and coarse MC/MN aged alloys was superior to $M_{23}C_6$ aged alloy. The difference in the creep/fatigue life can be attributed to stronger cavitation resistance of MC/MN carbides as compared to the $M_{23}C_6$ carbides. Further, the rate of formation and growth of grain boundary cavities is lower for MC/MN carbides as compared to the $M_{23}C_6$ carbides. The authors concluded that for grain boundary cavitation in austenitic stainless steels and the type of carbides is more dominant factor as compared to the density of carbides.

Laha et al. [116] **in 2005** studied the effect of titanium, boron, and cerium on creep properties of austenitic stainless steel. The authors observed that the creep strength of Ti stabilized austenitic stainless steel was higher. The large quantities of fine precipitates of TiC/TiN improved the creep strength of the steel. TiC/TiN precipitates are highly stable and reduces the coarsening of the grains and increases the rupture strength of the steel.

Laha et al. [27] **in 2005** studied the influence of boron segregation on creep and cavitation in SS-347 austenitic stainless steel. The Authors observed that the addition B and Ce improved the ductility and creep rupture strength of SS-347 stainless steel. In the absence of sulphur

contamination, boron segregation on the cavity surface reduced creep cavity growth. This improved the creep and cavitation resistance of the steel. The segregation of boron on the cavity surface can be attributed to the removal of Sulphur by the addition of Ce.

Lima et al. [117] **in 2005** studied the sensitization study on AISI 304L, 316L, 321 and 347 austenitic stainless steel. The authors observed that all the steels did not show the sensitization at 380 ℃. At the operating temperature of 500 ℃, sensitization was observed for both low carbon stainless steels and AISI 321 stainless steel. Whereas, for AISI347 steel, sensitization was observed at 550 ℃. The authors also observed that the stabilized steels showed a higher resistant to sensitization. Niobium was observed to be an efficient stabilizing agent than titanium.

Pardo et al. [20] **in 2007** studied the effect of Ti, C and N on intergranular corrosion of AISI316 and AISI321 stainless steels. The authors observed that the addition of titanium to the steel improves the intergranular corrosion resistance. Titanium leads to the formation of titanium carbide that decreases the formation on chromium-rich carbides. Further, TiC formation decreases the carbon concentration below 0.03 wt.% and improves the sensitization resistance. The addition of Mo to AISI 316Ti steel decreases the precipitation of chromium-rich carbides and increases the stability of TiC. Mo acts as a substitute for chromium and inhibits the formation of chromium carbides and also intermetallic compounds which further protect the matrix from chromium depletion.

Moura et al. [18] **in 2008** studied the effect of stabilization heat-treatment on hardness and intergranular corrosion resistance of AISI321 stainless steel. The authors reported that the steel can be used for elevated temperature applications due to its higher creep and intergranular corrosion resistance. However, for services in the sensitization temperature range (450–850 ℃), the steel should be heat treated to a higher temperature where the precipitation of TiC takes place. The authors also observed that the highest temperature for stabilization should be 950 ℃. Samples stabilized at 975–1000 ℃ and aged at 600 ℃ for 100 h showed good combination of properties.

Farahat and Bitar [118] **in 2010** studied the influence of niobium, titanium and cold deformation on mechanical properties of austenitic stainless steels. The authors observed that the YS, UTS, and

% elongation of steel without niobium and titanium additions was 280 MPa, 615 MPa, and 65% respectively. On the addition of 0.4 wt.% Nb and Ti, the YS, UTS, and % elongation was observed to be 400 MPa 650 MPa, and 48% respectively. Further, increase in the concentration of Nb and Ti to 1.5 wt.% had no influence on the mechanical properties.

Nikulin et al. [119] **in 2010** studied the high temperature characteristic of 18Cr-9Ni-W-Nb-V-N stainless steel. The authors observed that the steel exhibited irregular flow at temperatures ranging from 530–680 ℃. The high temperature yield strength (YS) and ultimate tensile strength (UTS) increased significantly. The YS and UTS remained unchanged from 350–740 ℃.

Han et al. [120] **in 2012** studied the influence of hot rolling temperature on grain size and precipitation hardening of martensitic steels.. The authors observed that hot rolling in titanium microalloyed low-carbon martensitic steel leads to the precipitation of TiC. Moreover, the concentration of TiC precipitates hot rolled at 950 ℃ was finer and higher than that the steel rolled at 1100 ℃. The grain refinement and precipitation of hot rolled steel at 950 ℃ was superiour to the steel hot rolled at 1100 ℃. The effective grain refinement achieved for steel hot rolled at 950 ℃ was 1.4 μm. The steel rolled at 950 ℃ showed superiour strength, dislocation strengthening and precipitation strengthening than steel rolled at 1100 ℃.

Han et al. [121] **in 2012** studied the influence of titanium addition and quenching on the mechanical properties of low carbon martensitic steel. The authors observed that the reheating and quenching in the temperature range of 900–1000 ℃ led to a significant grain refinement. This was attributed to the high concentration of nano sized precipitates of TiC. In addition to this, the large concentration of TiC precipites improved the elastic modulus. The authors concluded that reheating and quenching process is suitable for improved grain refinement and improved mechanical properties.

Green et al. [122] **in 2015** studied the formation of ferrite in AISI321 steel. The authors observed that the ferrite in AISI321 steel dissolved at 800 ℃ and formed on cooling of steel beyond 200 ℃. At room temperature, significant ferrite content was observed in AISI321 steel. Whereas, the DeLong diagrams predicted an austenite-martensite microstructure. DeLong diagram displayed

that nitrogen concentration has a great influence on the austenite stability. Further, thermal aging of AISI321 steel led to the austenite-to-ferrite transformation. The authors observed that the austenite-to-ferrite transformation is accompanied by an increase in volume. This comes into relevance in the components fabricated with tight dimensional tolerances.

Liu et al. [123] **in 2015** studied the properties of high boron alloyed stainless steel. The authors observed that the boride in as-cast microstructure is in the form of long strips of $(Fe,Cr)_2B$ phase with petal shaped TiB_2 phase. Further, the formation of TiB_2 phase decreased the concentration of $(Fe,Cr)_2B$ phase. Both type of borides disintigrated after hot rolling and uniformly distributrd throughout the matrix. It was observed that the TiB_2 phase was uniformly distributed throughout the matrix. The mechanical properties of boron alloyed stainless steel containing Ti was superiour.

Bai et al. [24] **in 2018** studied the influence of boron on the precipitation of S31254 steel. The authors observed that as compared to the boron-added alloy, higher quantity of sigma phase precipitated at the grain boundaries. The addition of 40 ppm boron to the S31254 steel decreased the sigma phase precipitation in the austenitic matrix. Further, the precipitation time was observed to be maximum at 950 ℃.

Ghazani and Eghbali [124] **in 2018** studied the influence of hot deformation on the microstructure of AISI321 austenitic stainless steel. The deformation process was carried out at temperature range and strain rates of 800–1200 ℃ and 0.001–1 s^{-1} respectively. The authors observed that the dynamic recovery was the main restoration process for the temperature range of 800–950 ℃. Whereas, for the temperature range of 1000–1200 ℃ dynamic recrystallization was the prevailing softening mechanism. Both dynamic recovery and recrystallization was confirmed using transmission electron microscopy. The authors observed that the increase in the deformation temperature increased the fraction of high angle boundaries and also a decrease in the fraction of low angle boundaries was observed. Further, the deformation process at the temperature of 800 ℃ and 850 ℃ leads to the precipitation of $M_{23}C_6$ at the austenite grain boundaries. This increases the activation energy required for deformation.

Hafez et al. [21] **in 2018** studied the boron-titanium austenitic stainless steel alloys for power reactors. Solution hardening and precipitation strengthening effects were improved by adding B and Ti to the steel. These elements are carbide or nitride formers. The addition of B to steel increased the rate of formation of intermetallic compounds while lowering the ductility of the steel. The high work hardening rate of Ti-containing austenite stainless steels was linked to their mechanical characteristics. Borated stainless-steel samples outperformed other austenitic stainless steels in terms of corrosion resistance. Boron-titanium stainless steels provided a superior combination of mechanical properties. This makes them a suitable steel for nuclear reactor applications.

Jambor et al. [125] **in 2018** studied the effect of sensitizing of the AlSI316Ti austenitic stainless steel on fatigue properties. The authors observed that the heat-treatment 600°C/100h led to the sensitization of AISI316Ti. Fatigue test results of ultra-high cycle showed a decrease in the fatigue strength with increase in the number of cycles. Sensitization had an inverse relation with the fatigue properties of AISI316Ti steel in the ultra-high cycle region. The effect was prominent for lower loading amplitudes and higher volume of loading cycles. The fatigue strength of steel in the ultra-high cycle region was found to be 20% lower than the initial state. While, for higher loading amplitudes and lower loading cycles fatigue strength difference is nearly zero.

Sharma et al. [30] **in 2019** studied the influence of boron in heat treated steels. The authors observed that the boron addition to the steel can be made through the deoxidation and degassification of the liquid steel followed by the addition of boron. Further, boron protectors like Ti/Al are also added to prevent the formation of BN and B_2O_3. Boron addition is generally kept below 80 ppm to prevent the hot shortness. In addition to this, authors also observed that high reheating/heat treating temperatures led to the phenominon of boron fade. In the absence of boron protectors, Ti/Al BN formation takes place. Boron leads to the formation of $M_{23}(B,C)_6$ and boro-cementites of C, B, Cr, Mo, and microalloying elements such as Nb, V. The authors concluded that for superiour hardenability and toughness boron contents should be between 10–20 ppm.

Salhi et al. [126] **in 2019** studied the corrosion and tribocorrosion behaviours of AISI321, AISI431 and FDMA borided and non-borided steels. The authors observed that the boride layer showed superiour mechanical properties as compared to the base steel substrates.

Won et al. [29] **in 2019** studied the influence of annealing on mechanical properties of stainless steels. The authors observed that the content of $(Fe,Cr)_2B$ increased with the increase in the concentration of boron. After annealing at 1180 ℃, the morphology of $(Fe,Cr)_2B$ transformed from plate-like shape to spherical shape. Further, the brittle fracture of the boride was dominant before the heat-treatment. However, the transition in failure mode from brittle to ductile was noted after heat-treatment. The authors also observed that the addition of 1.78 wt.% boron, led to the complete homogenization of Cr and Ni in the austenite matrix. Further, homogenization after annealing at 1180 ℃ for 192 h led to a simultaneous improvement in the strength and ductility of the austenitic stainless steel.

James et al. [127] **in 2020** studied the weld solidification cracking of 304L stainless steel water tank. The authors observed that the primary reason for the cracking was the excessive residual restraint stresses resulting from the weld-fit-up and welding practice.

Li et al. [128] **in 2021** studied the mechanical properties of AISI321 steel after aluminizing and annealing treatment. The authors noted that aluminizing process lowered strength and ductility of stainless steel. On the other hand, aluminized steel had a lower strength and a higher ductility after annealing. This is related to grain growth and the creation of annealing twins. For the aluminized steel, the fracture model found is cleavage fracture. After annealing, however, there was mixed intergranular and transgranular fracture.

2.5 C250 STEELS

C250 steel is generally used in aerospace applications. Maraging steel contains around 18 wt% Ni with high levels of 8–13 wt% Co, 3–5 wt% Mo and small additions of Ti and Al. Ni addition to Fe-system generates the necessary thermal hysteresis gap for the transformation of austenite to martensite and vice versa. In the Fe-Ni system, the austenite to martensite transformation is governed by the concentration of Ni. The main challenge with the C250 steel is the cost. Addition

of high nickel and chromium in the steels increased the overall cost of the steel. A vast literature is available on reducing the cost of the C250 steels. One of the effective way to decrease the overall cost of C250 steel is the cold rolling of the steels. Based upon the aforesaid discussion, the literature pertaining to C250 steels is presented below.

Garrison [34] **in 1990** studied the ultra-high strength steels for aerospace applications. The authors reported that the ultra-high strength steels are used in a variety of engineering applications. New alloys with superior mechanical properties are adopted for aerospace applications. Ultra-high strength steels with yield strengths >1725 MPa provide superior fracture toughness along with better corrosion resistance and are used as advanced material for engineering applications. The better properties in the steels can be achieved by minimizing the inclusions in the steels.

Vasudevan et al. [129] **in1990** studied the precipitation strengthening of 18 wt.% nickel maraging steels. The authors observed that the refinement of cobalt free high titanium T250 steel was achieved due to the refinement and distribution of Ni_3Ti precipitates. The precipitates resist the coarsening effect which increases the strength of the steel. On the other hand, for the steels with high chromium and low titanium, strengthening was initially achieved due to the presence of Ni_3Ti and Fe_2Mo precipitates for longer times. The authors also observed that the resistance to austenite reversion is dependent upon the relative nickel content in the martensite matrix.

Sha et al. [46] **in 1993** studied the precipitation reactions in maraging steels. The effect of alloying elements Ti, Al, Mo, Si, Mn, Ni, Cr, and Co are discussed. Co lowers the matrix solubility of Mo. Ti and Mo provide hardening to the maraging steel. However, Ti is much more active precipitation agent than Mo. Mo leads to the formation of Fe_7Mo6/x phase instead of Laves phase. The austenite reversion behaviour is affected by the amount of Ni precipitates and the presence of Cr in the steels. Other phases, such as the gamma and zeta phases, play vital role in age hardening in some of the maraging alloys.

Vishwanathan et al. [45] **in 1993** studied the precipitation hardening of 350 grade maraging steel. The authors observed that for early stages of ageing, the strengthening is achieved by the heterogeneous precipitation of intermetallic compounds of Ni_3(Ti, Mo) and Fe_2Mo. It was

observed that superior mechanical propertied viz. YS (2195 MPa), UTS (2227 MPa), and % elongation (5.3 %) was achieved for specimen aged at 510 ℃ for 3 hours.

Sinha et al. [41] **in 1998** studied the influence of ageing on mechanical properties of cobalt free 18Ni maraging steel. The authors observed that the tensile properties and plane strain fracture toughness of M250 were comparable to T250 steel. The Ni_3Ti precipitate present in the steel provides an excellent resistance to coarsening and improve the yield and tensile strengths which in turn increase the toughness of steel.

Tewari et al. [42] **in 2000** studied the precipitation in 18 wt.% nickel maraging steel. The author observed that for ageing temperature below 500 ℃, the evolution of particles takes place due to the collapse of the unstable BCC lattice. For ageing temperature greater than 500 ℃, precipitation of A_3B type of phases is observed.

Lee et al. [39] **in 2003** studied the influence of heat-treatment on microstructures of C250 maraging steel. The authors observed that the microhardness of solution treated C250 maraging steel can be increased by 16.2% after flow forming. To improve the hardness and strength of steel direct ageing process is needed. The tensile strength of formed C250 maraging steel is independent of the work hardening. For superior mechanical properties direct solutionizing route was preferred.

Guo et al. [130] **in 2004** studied the phase transformation kinetics of 18Ni C250 maraging steel. The authors observed that during ageing, austenite transformation and precipitation process was governed by controlling the lattice diffusion of substitutional atoms. Further, during ageing, the process of precipitation was at the equilibrium before peak hardness was achieved. This indicated that hardening effect may be due to the coarsening of the precipitates.

Guo and Sha [131] **in 2005** studied the precipitate fraction in Al-Si-Cu alloys. The authors observed that the precipitations of Al2Cu and Si both affect the lattice of the matrix. During ageing, the change in lattice parameters was measured using XRD process. The formation Al_2Cu phase was observed for the ageing process.

Arabi et al. [132] **in 2006** studied the influence of Ti content on the mechanical properties of C300 steel. The authors observed that the increase in Ti from 0.7– 2 wt. % in the melt increased the vol. % of inclusions. Further, the addition of Ti increased the hardness and formation of fine structure of martensite. Strength and toughness of steel increased upto 0.7 % Ti addition. Beyond this i.e. Ti >0.7 wt.% the toughness of steel gradually reduced. For Ti content >1.5 wt.%, the fracture mode changed from ductile to brittle nature.

Jha et al. [40] **in 2010** studied the high fracture toughness of maraging steel. The authors observed that for superior mechanical properties, the control on thermomechanical treatment and microstructure during forging is required for high fracture strength.

Mukhopadhyay et al. [133] **in 2010** studied the tensile deformation of M250 maraging steel. The authors observed a decrease in strength and increase in % elongation till ageing of 10 hours. This was attributed to the precipitation of Ni_3Ti phase. The increase in strength was observed till ageing of 40 hours. This was due to the formation of precipitates of Fe_2Mo along with the precipitates of Ni_3Ti phases. The increase in the ductility of steel for 10–40 hours ageing was attributed to the dissolution of needle like Ni_3Ti precipitates and formation of spherical Fe_2Mo precipitates. The authors also observed that ageing beyond 40 hours decreased the strength and increased the ductility. This was due to the transformation of martensite to austenite and precipitate coarsening.

Marcisz and Stepien [44] **in 2014** studied the short time ageing of M350 maraging steel. The authors observed that hardness value in the range of 450–525 HV was achieved for samples aged at 480–500 ℃ for 15–60 seconds without deformation. Hardness of 600 HV was achieved for steels aged at 600 ℃ for 15 seconds. Deformation after the ageing process increased the hardness and dislocation density of the steel. The hardness value of 600–630 HV was achieved for samples aged at 480–550 ℃ for 30 seconds. The hardness of the specimen increased from 370 HV to 590–630 HV for ageing at 460–490 ℃ for 30 minutes.

Ding et al. [35] **in 2015** studied the effect of grinding on the phase transformation and residual stress of maraging C250 steel. The authors observed that the phase transformation induced by

grinding cannot reduce the residual stress on the surface layer. For improved surface quality with minimal residual stresses the grinding wheel revolution should be kept between 3.09–3.57 rpm.

Galindo-Nava and Rivera-Díaz-del-Castillo [134] **in 2015** studied the microstructure and strength of lath martensite. The authors observed that the yield stress and microstructure were successfully predicted. The model was further used to describe the yield stress of maraging steel and dual-phase steel. The prediction model was validated against experimental data. The predicted results were found to be in close comparison to initial microstructure and tempering conditions.

Marcisz et al. [43] **in 2017** studied the mechanical properties of 18Ni 350 grade maraging steels. Short time ageing was carried out at 550 ℃ for 600 seconds. The authors observed that the superior mechanical properties can be achieved by short time ageing process. Superior mechanical properties viz. hardness (48–56 HRC), UTS (2000–2250 MPa), YS (1930–2170 MPa), % elongation (7–8 %) and impact strength of 20 J/cm^2 were obtained.

Tian et al. [135] **in 2017** studied the new maraging stainless steel and evaluated the toughness and corrosion resistance of the steel. The authors developed high strength (1920 MPa), high toughness (80 MPa·m$^{1/2}$) maraging steel with good corrosion resistance. The authors observed that Ni_3Ti precipitates and Mo-rich phases were responsible for the strengthening of maraging steel. During ageing process, the precipitation of Ni and Ti was faster in comparison to Mo.

Chakravarthi et al. [32] **in 2018** studied the hot workability of M300 maraging steel. The authors observed that the optimum temperature and strain rate parameters from the power dissipation map, strain rate sensitivity map and instability map 1125–1200 ℃ and 0.001–0.1 s^{-1} respectively. Dynamic recrystallisation was the dominant softening mechanism at high temperature and intermediate strain rate domain.

Saatamoienen et al. [136] **in 2018** studied the effect of tempering and rolling temperature on mechanical properties of direct-quenched steel. The rolling temperature had a significant effect on austenite grain structure. The YS in the longitudinal direction increased during tempering. This was attributed to the presence of strong temper resistant alloying elements viz. Mo, V and Cr. The

authors observed that the finish rolling temperature had no significant effect on the dislocation density of the direct quenched martensite. Tempering led to a decrease on the dislocation strengthening of the steel.

Sun et al. [33] **in 2018** studied the creep resistance of the novel UHSS maraging steel. The authors observed that the mechanical properties of maraging steel were dependent upon the heat-treatment process. With proper heat-treatment process an optimum combination of mechanical properties viz. YS (>1800 MPa), UTS (~2000 MPa), % elongation (~8 %) can be attained at room temperature. Further, a superior creep rupture life of >2000 h was achieved under the stress and temperature conditions of 700 MPa and 500 ℃ respectively. The authors also observed that the austenisation and ageing temperatures were the influential parameters that govern the resultant mechanical properties of the maraging steel.

Ding et al. [36] **in 2020** studied the effect of cubic boron nitride wheel topography on phase transformation of C250 maraging steel. The authors observed that the effect of grinding wheel morphology on phase transformation is more sensitive during micro-grinding. To reduce the thermal damage during grinding, the feed rate of the workpiece should be high for small cutting depth and also the excessive speed of grinding wheel should be avoided.

Shamsdini et al. [137] **in 2021** studied the texture orientation in tensile loaded maraging steels. The steel showed a martensitic structure with some retained austenite. In the as-built situation, the additive manufacturing technique increases mechanical strength and ductility, with a greater improvement in the horizontal direction. Furthermore, heat treatment increases the mechanical strength of wrought, horizontal, and vertical additive material into the same range. The ductility, on the other hand, was higher in the horizontally aged samples.

2.6 300M STEELS

300M steel is a commercial low-alloy ultrahigh-strength steel widely used in aircraft and aerospace applications because of their excellent combination of high strength, hardness, yield ratio, fracture toughness and fatigue property. 300M steel is basically derived from AISI 4340 steel by the addition of alloying elements like Si and a small amount of Si. The inclusion of Si and Si refines

grains while also increasing strength, toughness, and stress corrosion cracking resistance. The retention of ductile high-carbon austenite is done by high Si content, which prevents the generation of brittle inter-lath cementite layers carrying reduced ductility and toughness. The main cause of failure of the steel is the processing methodology. Several authors have proposed different processing routes for the manufacturing of 300M steels. The authors have used multiple annealing cycles for the processing of steels but this increases the cost of the steels. Thus, based upon the aforesaid discussion, the literature pertaining to the 300M steels is presented below.

Khan and Badeshia [138] **in 1990** studied the transformation of bainite in 300M steel. The authors observed that the microstructure of 300M steel is strongly affected by substitutional solute concentration. Bainite transformation was observed to be higher for homogenized samples than that of the as-received samples. The results predicted the bainite transformation by the model used was observed to be similar to the experimental results of bainite transformation in heterogeneous 300M steel.

Tomita and Okawa [139] **in 1995** studied the effect of heat-treatment on mechanical properties of 300M steel. The authors observed that the microstructure of modified heat treated 300M steel consists of martensite, carbide free upper bainite, and retained austenite. Superiour fracture toughness was observed when steel has 50 vol.% bainite along with tempered martensite and retained austenite for 320 ℃ tempering. Steel heated at 320 ℃ showed improved tensile strength, % elongation and impact energy. For steel heated to 350 ℃, decrease in impact strength and tensile strength is observed. This was due to the increase in the % elongation of the steel. Further increase in heat treated temperature to 400 ℃ increases the % elongation and impact strength, but had no effect on the strength of the steel. The improvement in the mechanical properties of the steel after heat-treatment can be attributed to the formation of stable austenite and accicular lower bainite along with martensite.

Tomita [140] **in 2000** studied the fracture toughness of UHSS, medium carbon and low alloy steels for aerospace applications. The ultra-high strength steels, medium carbon (0.25–0.50 wt.%) steels and low alloy steels containig Cr, Mo. Ni, Si, and V have been used in the aerospace applications. Such steels can easily attain the YS of ~1400 MPa but lack in fracture toughness.

The authors suggestes that the fracture toughness of afforesasid steels can be improved by controlling the microstructure. This can be achieved by thermal and thermo-mechanical treatment and/or control and modification of sulphur inclusions or by designing a new alloy chemistry.

Luo et al. [141] **in 2010** studied the influence of tempering on mechanical properties of bainitic steel. The authors observed that the non quenched non tempered steel consists of granular bainite comprising of bainitic-ferrite laths, retained austenite and martensite. The volume fraction of retained austenite decreased with increase in the tempering temperature. Best mechanical properties were achieved for non quenched steel tempered at 350 ℃. The non quenched steel tempered at 450 ℃ shows brittle nature. This could be attributed to the formation of carbides.

He et al. [142] **in 2012** studied the properties of quenched 300M steel. The authors observed that the microstructure of electron beam welded joints of 300M steel consisted of tempered martensite. The strength of the welded joint was observed to be lower to the base metal. With proper heat-treatment the tensile strength of the joint reached to 1900 MPa which was about 97 % of the base metal strength.

Luo et al. [143] **in 2012** studied the deformation behavior of 300M ultra-high strength steel. The authors observed that dynamic recovery was an effective softening mechanism for deformation at temperature of 900 ℃. Dynamic recrystallization was observed for the strain rate of 25 s^{-1}. For deformation at 1100 ℃, the dynamic recrystallization process is complete. For the strain rate of 0.7 s^{-1} and temperature of 900–1140 ℃, unstable nature of deformation takes place. The deformation temperatures between 1100–1140 ℃ and strain rate of 0.1–0.16 s^{-1} was found to be the optimum deformation condition of 300M steel.

Zhao et al. [144] **in 2013** studied the influence of quench-temper-partition on mechanical properties of 300M steel. The authors observed that the quench-temper-partition processed steels had a higher fraction of austenite as compared to the quench-temper process. After quench-temper-partition, a significant increase in ductility and toughness was noted whereas, no major improvement in the strength was observed. The quench-temper steels consisted of thin film like retained austenite along with wide martensite strips. While, the quench-temper-partition steels

resulted in large volume of thick austenite accompanied by narrow strips of martensite. The authors concluded that the quench-temper-partition of 300M steels showed better ductility and toughness.

Liu et al. [145] **in 2016** studied the influence of temperature on mechanical properties of 300M steel. The authors observed that the microstructure of quenched-tempered 300M steel consisted of tempered martensite, bainite and a small fraction of retained austenite. With increase in the tempering temperature the eta carbide precipitates changed to cementite. The increase in the tempering temperature decreased the hardness whereas the UTS and YS increased initially and then decreased. Maximum UTS and YS achieved after tempering at 290 ℃ was 1966 MPa and 1661 MPa respectively.

Liu and Li [57] **in 2018** studied the martensite transformation in 300M steel. The authors observed that the water quenching of pre-deformed 300M steel resulted in mixed microstructure consisting of lath martensite, twinned martensite and retained austenite. Greater proportion of lath martensite are generated in the deformation-quenched 300M steel with lower strain rate.

Skubisz et al. [146] **in 2018** studied the properties of direct quenched 300M steel. The authors observed that the direct quenched 300M steel forged at 1000 ℃ provided mechanical properties similar to quench tempered heat treated 300M steel. The YS, UTS, impact strength (room temperature), and hardness observed for direct quench 300M steel was 2200 MPa, 2000 MPa, 48 J/cm^2 and 54 HV respectively.

Liu et al. [147] **in 2019** studied the effect of microstructure on the impact properties of 300M steel. The authors observed that the microstructure of the 300M ultra-high strength steel composed of martensite and bainite. Heat-treatment refines the microstructure. It consists of uniformly distributed martensite and lower bainite. The impact toughness of 300M steel was 9 J/cm^2, which improved to 25 J/cm^2 after heat-treatment. The fracture mode observed for 300M steel was quasi-cleavage fracture which changed to ductile fracture mode in heat treated 300M steels.

Liu et al. [148] **in 2020** studied the effect of isothermal temperature on the transformation of bainite and the resulting mechanical properties of 300M steel. The authors observed that the

microstructure of isothermal heat treated 300M steel consisted of upper bainite with small amount of martensite. The proportion of upper bainite decreased with decrease in isothermal temperature. However, the content of lower bainite and martensite increased gradually. The hardness of the 300M steel decreased with increase in temperature till 400 ℃. A marginal decrease in the YS and UTS was observed for decrease in isothermal temperature from 440 ℃ to 320 ℃. While, a sharp increase in YS and UTS was observed for isothermal temperature of 280 ℃.

Liu et al. [149] **in 2020** studied the ductility of 300M steel through isothermal bainitic transformation. The authors observed that the microstructure of 300M steel comprised of martensite, bainite and retained austenite. The hardness of 464 HV was observed after holding time of 20 min. The hardness of the steel decreased with the rise in the holding time. The hardness of the steel dropped to 428 HV afer the holding time of 80 min. Further, the increase in the holding time leads to a gradual increase in the tensile strength and ductility of the steel from 1348–1332 MPa and 33% respectively. This can be attributed to the precipitation of eta-carbides in the lower bainite. This hinders the dislocation movement which improves the strength and ductility.

Dang et al. [150] in 2021 studied the surface integrity of 300M steels. The results indicated that 10-pass ultrasonic surface rolling process (USRP) treatment can generate a highly smooth surface with Ra of 7 nm. The surface layer created nanocrystalline phase. The sample surface was subjected to a significant compressive residual stress of around 950 MPa and a depth of around 800 m. Grain refinement, work hardening, and compressive residual stress all worked together to improve surface hardness roughly 30.9%. It's worth noting that the USRP-induced benefits in surface integrity and wear resistance of 300M steel tend to be saturated as the number of processing passes increases.

2.7 SUMMARY OF LITERATURE

Authors have worked on the variety of ultra-high strength steels for different engineering applications. A vast literature is available on the improvement of mechanical properties of various steels. The summary of literature is presented below:

- Although, large volume of research has been carried out on the AMS-4340 steel manufacturing however, the majority of failures are still due to segregation, hydrogen

embrittlement, and hydrogen flaking. The segregation of Ni, Cr, and C occurs from top to bottom and also from center to surface of ESR. The authors observed that Ni-Cr-Mo-V steel offered a significant improvement in the tensile strength, impact strength and fracture toughness by adopting alternative processing route followed by heat-treatment. VIM process is crucial for the processing of Ni and Co based superalloys as these are susceptible to reactions with nitrogen and oxygen in the atmosphere.

- For super critical steam cycles, major focus is given to the steels with 9–12% Cr. Ferrite steels with 9–12% Cr provide superior properties as compared to conventional austenitic stainless steels. Nickel based alloys are suitable for applications above 760 ℃. Martensitic steels (Fe–9Cr alloy) can be used for boiler pipes and steam pipelines of power plants at steam temperatures of 620 ℃. Substantial progress has been made in the development of high temperature resistant Ni-base alloys and 9–12 % Cr martensitic steels. The steels are capable of working till the 700 ℃. Martensitic 9–12 % Cr steels can be a substitute for the expensive Ni-base alloys on thick boiler sections and turbine components.
- AISI321 steel is used in nuclear applications. Ferrite in steels gets dissolved at 800 ℃. When cooling beyond 200 ℃ it again appears. The large quantities of fine precipitates of TiC/TiN improved the creep strength of the steel. Creep/fatigue life can be attributed to stronger cavitation resistance of MC/MN carbides as compared to the $M_{23}C_6$ carbides. Titanium leads to the formation of titanium carbide that decreases the formation of chromium-rich carbides. The formation of TiB_2 phase decreased the concentration of $(Fe,Cr)_2B$ phase. Both type of borides disintigrated after hot rolling and get uniformly distributrd throughout the matrix.
- The authors observed that the refinement of cobalt free high titanium T250 steel was achieved due to the refinement and distribution of Ni_3Ti precipitates. The strengthening is achieved by the heterogeneous precipitation of intermetallic compounds of Ni_3(Ti, Mo) and Fe_2Mo. The alloying elements discussed are Ti, Al, Mo, Si, Mn, Ni, Cr, and Co. Co lowers the matrix solubility of Mo. Ti and Mo provide hardening to the maraging steel. However, Ti is much more active precipitation agent than Mo. YS increased during tempering. This was attributed to the presence of strong tempering resistant alloying elements viz. Mo, V and Cr.
- 300M ultra-high strength steel is composed of martensite and bainite. Microstructure of quenched-tempered 300M steel comprised of tempered martensite, bainite and a small fraction of retained austenite. The ultra-high strength steels, medium carbon (0.25–0.50 wt.%) steels

and low alloy steels containig Cr, Mo. Ni, Si, and V have been used in the aerospace applications.

2.8 GAPS IN THE LITERATURE

- Ultra-high strength steels like AMS-4340 are normally manufactured through vacuum induction melting (VIM) followed by vacuum arc remelting (VAR). However, the process is quite expensive. Thus, an alternate method needs to be developed for the for the fabrication of AMS-4340 UHSS.
- The main reason for the failure of the turbine blades was the formation of δ-ferrite. For the aforesaid application, 10.7CrMoVNbN steel with minimum delta-ferrite content (maximum δ-ferrite 2 %) is required. Thus, limited studies have been reported on the control of δ-ferrite in 10.7CrMoVNbN steel using chemical composition, thermo-mechanical processing and heat-treatment.
- AISI 321 is preferred material for third generation VVER reactor compared to nickel-base corrosion resistance alloy such as INCONEL alloy 600, 690 and 800 because it is much cheaper. AISI 321 can be alloyed with Ti to improve the mechanical propertied. However, limited study related to the addition of boron AISI321 steel have been done. Addition of boron helps in the formation of precipitates of borides which provide superior mechanical properties.
- The C250 steel is used for the automobile and aerospace applications where high strength and toughness are of great significance. C250 steel in solution annealed condition is supplied to the automobile and aerospace industry. However, limited work has been done on the extent of cold working till which the material can be used without a significant loss in mechanical properties. This will provide an opportunity to the automotive and aerospace industries to directly procure the cold rolled C250 steel according to the dimensions desired for the required applications.
- A systematic study on heat-treatment processes is highly desired to improve the mechanical properties with minimum cost of 300M steels. Limited studies are reported on the effect of conventional heat-treatment, effect of modified heat-treatment and effect of isothermal heat-treatment on desired microstructure and mechanical properties.

CHAPTER 3
DESIGN OF THE STUDY

OVERVIEW

On the basis of the literature gap, the objectives setup for the present work to develop different class of ultra-high strength steels (UHSS) are described in the beginning of this chapter. The details of the testing and characterization of five different UHSS viz. AMS-4340 steel, 10.7CrMoVNbN steel, AISI-321 steel, C250 steel, and 300M steels selected in the present investigation has been described. The chapter include different characterization techniques used in the present study. The characterization techniques include X-ray diffraction (XRD), Optical microscopy, Scanning electron microscopy (SEM), Energy dispersive spectroscopy (EDS), Rockwell hardness testing, Vickers hardness testing and Mechanical testing along with their operating parameters.

3.1 OBJECTIVES

Extensive literature is available on the processing of UHSS. However, despite of numerous improvements in steel making processes like electric arc furnace melting, refining, vacuum degassing etc. majority of rejections of steels is accounted for ultrasonic defects and chemical segregations. Thus, the focus of the present work was to study the fabrication process of different UHSS using state of the art smelting and refining processes. The research work included studying the effect of different heating rates, isothermal holding temperatures, holding periods, cold drawing, and cooling rates on the mechanical properties of different UHSS steels. The aim of the present work was *"to fabricate different ultra-high strength steels for improved engineering applications"*.

The key issues taken up during the research work are:

- To develop ultra-high strength steels (UHSS) viz. AMS-4340, C250, 10.7CrMoVNbN, AISI321, and 300M steels with improved toughness for different engineering applications.
- Optimum use of strengthening mechanisms in manufacturing and heat-treatments to achieve best combination of strength, hardness and fracture toughness in proposed UHSS.
- To study the effect of alloy design, thermo-mechanical processing and heat-treatment on microstructure and mechanical properties of UHSS.
- To evaluate and characterize microstructure and mechanical properties of proposed UHSS.
- To perform fractrography analysis on different UHSS steels and determine the structure property relationship.

In the present study five different type of UHSS have been processed and developed. The details of their background and characterization techniques is presented below.

3.2 AMS-4340 STEELS

3.2.1 BACKGROUND STUDY

This steel is a medium carbon steel. It contains mostly of nickel, chromium, molybdenum, Si as alloying elements. This is ultra-high strength aircraft quality steel with high hardenability. The steel finds its applications in manufacturing highly stressed aircraft components like landing gears

and many more other applications such as gun barrels, glider bomb shells, laser guided glider bomb shells. This steel was developed for Rafael and Israel Military Industries (presently Elbit Systems Israel) for glider bomb shells and gun barrels and other similar applications. Applications of this steel require following essential quality parameters like:

- Ultra-cleanliness in terms of nonmetallic inclusions.
- High hardenability to achieve J19 MM=53 HRc and J32mm=50 HRc minimum hardness.
- Highest degree of isotropy in mechanical properties in longitudinal and transeverse directions to take care of multidirectional service stresses.
- Free from any delayed cracking due to presence of hydrogen flakes caused by dissolved internal hydrogen.
- Extremely high strength along with good ductility and toughness.
- Good impact toughness at low temperature (-40℃) as components face low temperature and impact loading conditions during service.

The preferred route for making this steel is vacuum induction melting (VIM)+ vacuum arc remelting (VAR) which makes it very costly. To take care of high cost proposed route of air melting in electric arc furnace +ladle refining+ vacuum degassing was used in place of vacuum induction melting and subsequently electroslag remelting was used in place of VAR.

The details of processing of these steels including different heat-treatment procedures adopted to achieve the desired microstructure has been given in the results and discussion section (Chapter 4). The basic characterization and mechanical testing done for the developed steel is described below.

3.2.2 CHARACTERIZATION AND TESTING

In order to check the hydrogen flaking in this steel, 50 mm wide slice was cut from this circular sample and polished on 120, 240, 400, 600 grit size polishing paper followed by 20–25 min hot acid etching by boiling in commercial hydrochloric acid to reveal the hydrogen flakes according to ASTM A604 standard [151]. Macrographs are taken on a portion of 50×80 mm area. To observe various structural features of ESR heats, microstructural characterization was carried out on optical microscope (Zeiss-Axio Observer D1M, Carlzeiss, Germany). Further, mechanical properties are evaluated on universal testing machine (DX-600, Instron USA) according to ASTM A370 standard [152] and ASTME23 standard. Impact testing (IT-30, FIE, India) is performed at sub-zero

temperature (-40°C) according to ASTM A370 standard [152]. Segrigation of different alloying elements is observed through spectroscropy technique (Spectro Lab M9, Germany). For segrigation analysis, a transewerse slice of steel of 340 mm dia and 25 mm thickness is cut. From this slice, a transverse rectangular slice of 175×30 mm is cut from the centrel portion.

3.3 10.7CrMoVNbN STEELS

3.3.1 BACKGROUND STUDY

10.7CrMoVNbN steel is used in the application of turbine blades, nozzles and buckets for steam generator SG 650 by M/S Toshiba JSW Power Ltd. Chennai. The steel got rejected during testing. The main causes of failure of 10.7CrMoVNbN steel was (i) rejection of finish machine blades during final magnetic particle inspection (MPI) and (ii) poor service life and failure due to presence of delta-ferrite. The failures lead to huge financial losses pertaining to the material wastage and loss in power generation. The problems were analyzed by carrying out the MPI analysis and characterization of the failed turbine blade. This encouraged the need to undertake the present study. The problem was addressed by undertaking the following steps.

- Designing the chemical composition with varying chromium equivalent.
- The MPI indications led to observed that the failure/rejection of finish machined blades occurred for the segregation corresponding to the centerline of ESR ingot. An approach of upsetting and multi-directional forging was employed to distribute the centerline segregation leading to the decrease in the percentage of delta-ferrite.

This resulted in reducing the cost of turbine blades with no rejection at final finish machined stage. The details of the procedure adopted for the processing of the steel is described in results and discussion section (Chapter 5) to have the coherency of the presented work. Different characterization and testing done for this steel is given below.

3.3.2 CHARACTERIZATION AND TESTING

Samples after heat-treatment of all the heats were cut for metallography investigation. These samples were ground and polished according to the standard metallographic practice. The samples were etched using two different etchants listed in Table 3.1. The samples were analyzed under an optical microscope (Model: DMi8A, Leica) using bright field mode. Delta-ferrite content is

determined according to AMS 235A on the samples which were selectively etched to reveal only δ-ferrite [153]. In order to observe the influence of δ-ferrite on mechanical properties, hardness, tensile tests [154] and impact tests [155] were carried out in hardened (1090 ^{o}C/2hrs→ oil quenched) and tempered (670 ^{o}C/4hrs→ air-cooled) condition according to standard specification (PN KS01923-p, Toshiba) [15]. Hardness testing was done at Brinell hardness tester make FIE model RASN-B using a 3000kgf load with a 10 mm tungsten ball [156].

Table 3.1 Composition and condition of etchants used.

Name	Composition	Etching Procedure	Specificity
Kalling's-1 [157]	5g $CuCl_2$ + 100 ml HCl + 100 ml Methanol	Immersion of sample	Reveals martensite only
Sulphuric etchant [14]	20 ml H_2SO_4 + 0.01 g NH_4CNS + 80 ml H_2O	Immersion of samples and electrolytic etching at 4 V for 20 s	Reveals δ-ferrite but not martensite

Standard cylindrical tensile specimens were prepared according to ASTM E8M-08 [158] specifications and tested at room temperature using a tensile testing machine [Model: 600DX, Make: Instron]. Charpy V-notch impact specimens of dimension 10×10×55 mm. were prepared according to ASTM E23-07 [159] specification and tested at room temperature on impact testing machine [Model: IT-30, Make: FIE]. Hardness measurements on the matrix and secondary phases (carbides and δ-ferrite) were also done on the Vickers micro-hardness tester [Model: HMV, Make: Shimadzu] using 25 gram load with a dwell time of 15 seconds. Average of five readings along with standard deviation is reported for all mechanical testings. For morphology and compositional analysis, samples were analyzed under field emission scanning electron microscope (FESEM) equipped with an energy dispersive X-ray spectrometer (EDS).

3.4 AISI321 STEELS

3.4.1 BACKGROUND STUDY

AISI321 steel is used in the inlet outlet tubes of nuclear reactors by Nuclear Power Corporation Ltd., Mumbai India. In order to improve the service life of the components, boron was added to the AISI321 steel. Further by improving microstructure stability of the steels at elevated temperatures with improved service life of the steel can be obtained. Materials used in high steam temperature generators (STG) and nuclear reactors are iron-nickel and nickel base superalloys like

Inco800 and Inco625 which are very costly. Thus, AISI321 can provide a cheap alternate for these materials with better properties.

Here also the details of the heats and their subsequent processing has been given in the results and discussion section (chapter 6) for simplicity. The other characterization and testing done for this steel is described below.

3.4.2 MICROSTRUCTURAL EXAMINATION

All specimens were prepared according to the standard metallographic practice. Next, the specimens were electrolytically etched with 10 % oxalic acid. The samples were then analyzed under an optical microscope (Model: DMi8A, Leica) using bright field mode. Precipitates volume fraction was analysed at 100X magnification with the help of image analyser software (Leica Application Suite Version 4.11.0). An average of 20 image fields are reported for each condition. The grain size was measured according to ASTM E112-15 standard [160]. Sensitization behaviour was also observed by optical microscope according to ASTM A262 standard [161]. For morphology and chemical analysis samples were analyzed under field emission scanning electron microscope (FESEM, Model: Nova Nano FE-SEM 450, FEI) equipped with an energy dispersive X-ray spectrometer (EDS).

3.4.3 MECHANICAL TESTING

Cylindrical tensile specimens (6.25 mm gauge diameter with 25 mm gauge length) were prepared according to ASTM E8M-08 standard (for room temperature) [158] and ASTM E-21 standard (at elevated temperatures) [162] for tensile tests. Thereafter, tensile testing was performed on a tensile testing machine (Model: 600DX, Instron) at room temperature and elevated temperature (100 ℃, 200 ℃, 350 ℃, 500 ℃, 650 ℃, 800 ℃ and 950 ℃) conditions. Hardness measurement was carried out on the Brinell hardness tester (Model: RASN-B, FIE) using 187.5 Kgf load, 1.5 mm ball diameter and 15 seconds dwell time. The hardness and mechanical testing results presented in the study were taken as the average of three specimens at a given testing condition.

3.5 C250 STEELS

3.5.1 BACKGROUND STUDY

C250 steel was developed for Indian Space Research Organization (Vikram Sarbhai space center Thiruvantpuram, India) for their use in various applications like rocket motor casing and other components needing very high strength along with high fracture toughness. The present study was undertaken to see the effect of cold working on solution treated material to decrease the cost of C250 steels and to find the limit of cold work without adding any intermediate solution anneal treatment in between two cold work passes.

The details of the procedures adopted for heat-treatment is given in results and discussion section (Chapter 7) to have better understanding. However, the characterization and testing done for this steel is given in the following paragraph.

3.5.2 CHARACTERIZATION AND TESTING

All specimens were prepared according to standard metallographic practice. The specimens were etched with Keilings 1 reagent. The samples were observed under an optical microscope (Model: DMi8A, Leica) using bright field mode. For morphology and chemical analysis, samples were analyzed under field emission scanning electron microscope (FESEM, Model: Nova Nano FE-SEM 450, FEI) equipped with an energy dispersive X-ray spectrometer (EDS). Hardness measurements were carried out on the Brinell hardness tester (Model: RASN-B, FIE) using a 187.5 Kgf load and 1.5 mm ball diameter with a dwell time of 15 seconds. X-ray diffractometer (XRD, Philips X'Pert with Cu Kα radiation) was utilized to analyze the constituent phases, crystallite size and strain rate. X-ray measurements were carried out in step scan mode with interval size of 0.02, time per step of 3 s and angular interval 40^{o}–90^{o}. Nanohardness of different phases was also measured using Vickers nanohardness testing (TI 950 Tribo Indenter, Hysitron, Incorporation, Minneapolis, US) at 10mN load and dwell time of 5 seconds. Further, tensile testing was carried out using a tensile testing machine (Model: 600DX, Instron). Cylindrical tensile specimens were prepared according to ASTM E8M-08 [158] specification.

3.6 300M STEELS

3.6.1 BACKGROUND STUDY

300M steel was developed for Elbit systems Israel (Formerly Israel Military Industries) for the use in aerospace and defence applications like manufacturing of landing gears of aircrafts, glider bomb body shells with GPS and or laser guided controls. Glide bombs capacity varies from 125 kg to 1000kg. The essential requirement of 300M steel are the ultraclean steels having minimum level of harmful nonmetallic inclusions of sulplide, alumina, silicate, globular oxides, and other inclusions like carbides and carbonitrides according to ASTM E45-method A. Since, components made from this material encounter very low temperature of about -40℃, good impact toughness at this temperature is required along with very high strength.

The details of the manufacturing and heat-treatment cycles adopted to fulfil the above requirements has been presented in the results and discussion section (Chapter 8). Other characterization and testing investigations done for this steel is described below.

3.6.2 CHARACTERIZATION AND TESTING

Samples for characterization were drawn from different heat-treated ingots. Microstructural examinations of all heat-treatment conditions were performed using optical microscope (Model: Observer D1M, Carl Zeiss). The selected samples were also analyzed under field emission scanning electron microscope (FESEM, Model: Nova Nano FE-SEM 450, FEI) equipped with an energy dispersive X-ray spectrometer (EDS). Metallographic samples were prepared according to standard metallographic practice and etched with picral (5g pictric acid+10 ml HCl+100 ml methanol). X-ray diffractometer (XRD, Philips X'Pert with Cu Kα radiation) was utilized to analyze the constituent phases, crystallite size and internal strain. X-ray measurements were carried out in step scan mode with interval size of 0.02, time per step of 3 s and angular interval 40^{o}–90^{o}. Mechanical properties viz. hardness, tensile strength and Charpy V-notch impact tests were also done. For tensile testing, cylindrical tensile specimens of 5 mm diameter and 25 mm gauge length were prepared according to ASTM E8M-08 standard [158]. Tensile testing was carried out using a tensile testing machine (Model: LFMZ-50KN, Walter+ Baiag) at room temperature. Hardness measurements was performed on Rockwell hardness tester (Model: RASN-B, FIE) with diamond indenter at the load of 150 Kgf and dwell time of 15 seconds. Charpy V-

notch impact specimens of dimension 10×10×55 mm were prepared according to ASTM E23 [159] specification and tested at room temperature. The results presented in the study are the average of three samples at the given condition. SEM-EDS was also used to analyze the fracture surface after mechanical tests.

CHAPTER 4
RESULTS AND DISCUSSION
AMS 4340 STEEL

OVERVIEW

AMS-4340 steels have been developed for defense applications where hydrogen flaking was the main problem. The steel is used for multiple applications by M/S Rafael, France and Israel Military Industries (presently Elbit Systems Israel). They reported the failure due to hydrogen flaking in their steels. In this work, experiments done by designing different heat-treatment cycles for this steel is reported. The details of the structural variation in each heat-treatment cycle is reported in reference to the hydrogen flaking. After analyzing all the heat-treatment processing parameters, a suitable heat-treatment cycle was designed to eliminate the hydrogen flaking. All the developed steels have been subjected to mechanical testing to make the finally developed steel acceptable for its end application. The role of microstructure and its influence on mechanical properties has also been discussed. Finally, cost estimation study of the developed alternate process has been done and compared with the existing practice.

4.1 AMS-4340 STEELS

4.1.1 STARTING MATERIAL

In the present investigation, AMS-4340 grade steel was manufactured for defense applications especially for use in gun barrels of a renowned defense industries. Table 4.1 presents the designated and permissible chemical composition for AMS-4340 steel.

Table 4.1 Permissible and designated steel chemistry for AMS-4340 grade steel.

Element	C	Si	Mn	P	S	Cr	Mo	Ni	Cu	Al	V
Permissible limit (wt%)	0.38-0.43	0.15-0.35	0.65-0.90	0.010 Max	0.010 Max	0.70-0.90	0.20-0.30	1.65-2.00	0.35 Max	-	-
Designed limit (wt%)	0.40	0.25	0.86	0.007	lowest	0.86	0.27	1.89	lowest	0.02	0.05-0.10

4.1.2 PROCESSING ROUTE

Figure 4.1 presents the detailed flow chart representing the processes used for the manufacturing of AMS-4340 UHSS. The entire process is designed to achieve a standard chemistry and required properties for AMS-4340 grade steel. The steel is melted in an electric arc furnace (EAF) followed by refining in ladle refining furnace (LF) and vacuum degassing (VD).

The steel is cast into cylindrical electrodes, which are further subjected to electro slag remelting (ESR) in an inert argon atmosphere. After ESR the steel is annealed, hot press forged, and normalized. Further, the samples are prepared for quality and testing evaluation. Three different heats (D1, D2, and D3) are prepared using the processing route as shown in Figure 4.1. D1, D2, and D3 represents the primary processing including electric arc furnace (EF), ladle refining furnace (LF), vacuum degassing (VD) and casting into cylindrical electrodes. Table 4.2 presents the detailed processing parameters for the manufacturing of primary heats D1, D2, and D3. Further, the primary heats are subjected to ESR process. The primary heat D1 is converted to ESR heat E1, D2 is converted to ESR heat E2 and E3, while, D3 is converted to ESR heat E4. Primary heats D1and D3 each consisted of one cylindrical electrode of diameter 720 mm. Whereas, primary heat D2 consists of two cylindrical electrodes of 480 mm diameter. Thus, after ESR primary heat D2 is converted to two ESR heats i.e. E2 and E3. Figure 4.2 and Table 4.3 presents the various ESR process parameters for ESR heats E1, E2, E3, and E4. Further, the inert gas intake flow for ESR process was kept constant at 10 liter/min.

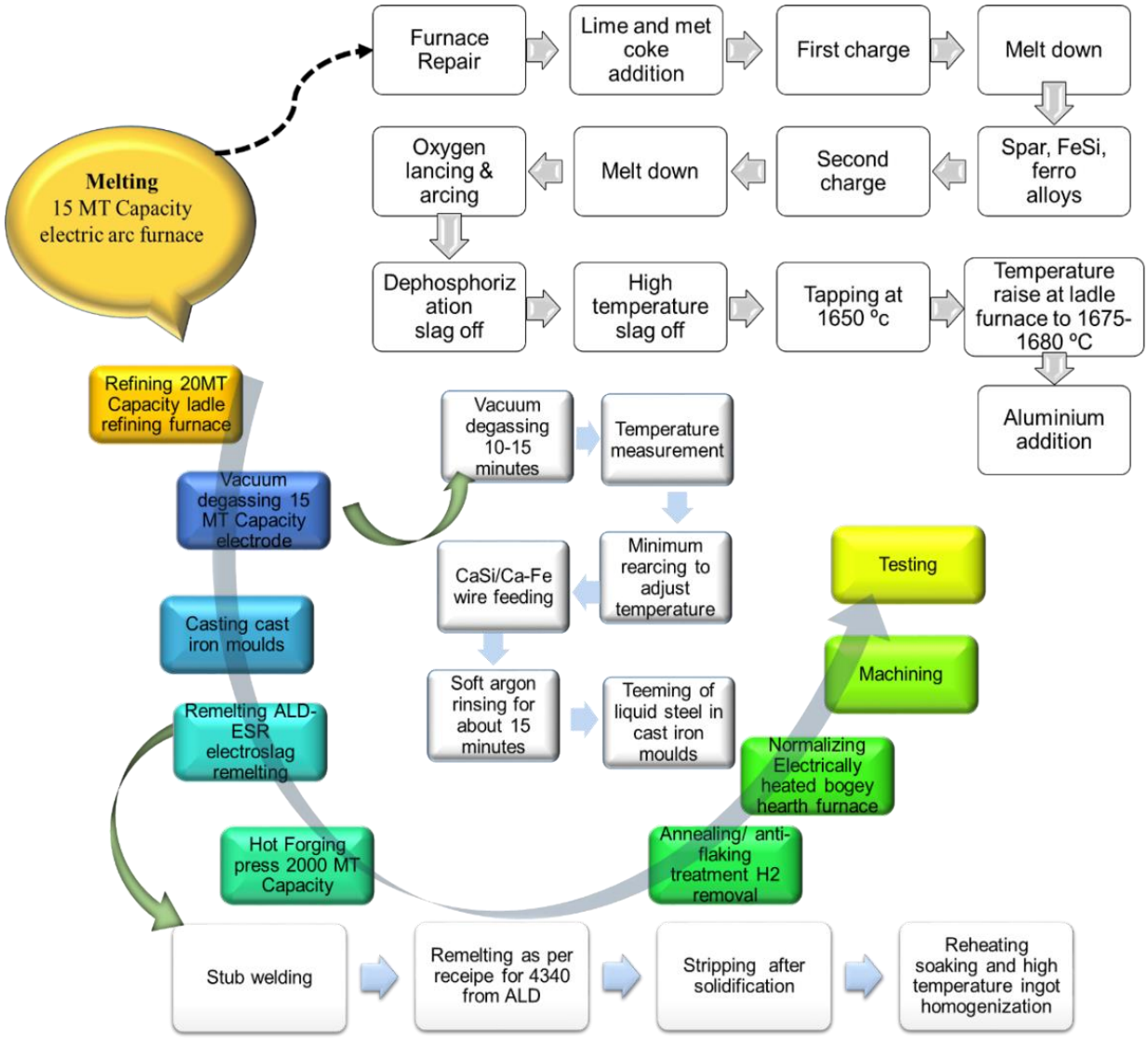

Figure 4.1 Process for the manufacturing of AMS-4340 UHSS.

Table 4.2 Melting, refining and casting parameters for primary heats.

S. No.	Process parameter	Heat no.		
		D1	**D2**	**D3**
1	Charge wt.	14520 kg	13170 kg	14510 kg
2	Charge mix	Mild Steel scrap-8870kg + DMR249 steel scrap-2150kg + Alloy steel with 3% Ni-3500 + lime-180kg. Total metallic charge-14520kg	Mild Steel scrap-8270kg + DB6 tool steel scrap-2100kg + Alloy steel with 3% Ni-2350 + skull 4340-450kg + lime-180kg + M/coke-300kg. Total metallic charge-13170kg.	Mild Steel scrap-4750kg + 21Cr steel scrap-2020kg + Alloy steel with 3% Ni-7230kg + Alloy steel with 3% Ni Mo(0.40%)-510kg + lime-200kg.+ M/coke-300kg. Total metallic charge-14510kg
3	Tapping temp.	1643℃	1642℃	1655℃
4	Mould temp.	72℃	76℃	82℃
5	VD before temp.	1675℃	1635℃	1645℃
6	H_2 before VD ppm	5.1	4.7	3.7
7	VD hold time at low pressure in min	10	12	15
8	Vacuum level (milli bar)	1	0.9	0.7
9	H_2 after VD ppm	1.7	1.7	1
10	Temp. After VD	1517℃	1552℃	1538℃
11	Re-arcing time to achieve the ladle	30 Min	15 Min	10 Min
12	Casi wire feeding (34gm ca per meter)	Nil	Nil	60 meter
13	Al level before Ca feeding	0.03%	0.04%	0.04%
14	Teeming time	28.10 Min	17.05 Min	20.50 Min
15	Feeding time	5.30 Min	4.27 Min	4.20 Min
16	Ar flow in shroud	72 LPM	68 LPM	64 LPM
17	Cylindrical electrode	DIA. 720-01PCS	DIA.-480-02PCS	DIA. 720-01PCS
18	Cast wt.	13400 kg	12200 kg	13500 kg

Table 4.3 ESR process parameters.

Primary Heat no.	ESR heat no.	Dia. (mm)	Melt rate					
			Start phase ($kg.min^{-1}$)		**Melt Phase ($kg.min^{-1}$)**		**Hot topping ($kg.min^{-1}$)**	
			Min.	Max.	Min.	Max	Min.	Max.
D1	E1	900	0	15.49	13.5	14.95	8.61	14.31
D2	E2	600		10.54	9.69	10.68	4.55	10.23
	E3			10.11	9.7	11.23	4.02	10.16
D3	E4	900		16.47	12.7	14.25	4.37	13.56

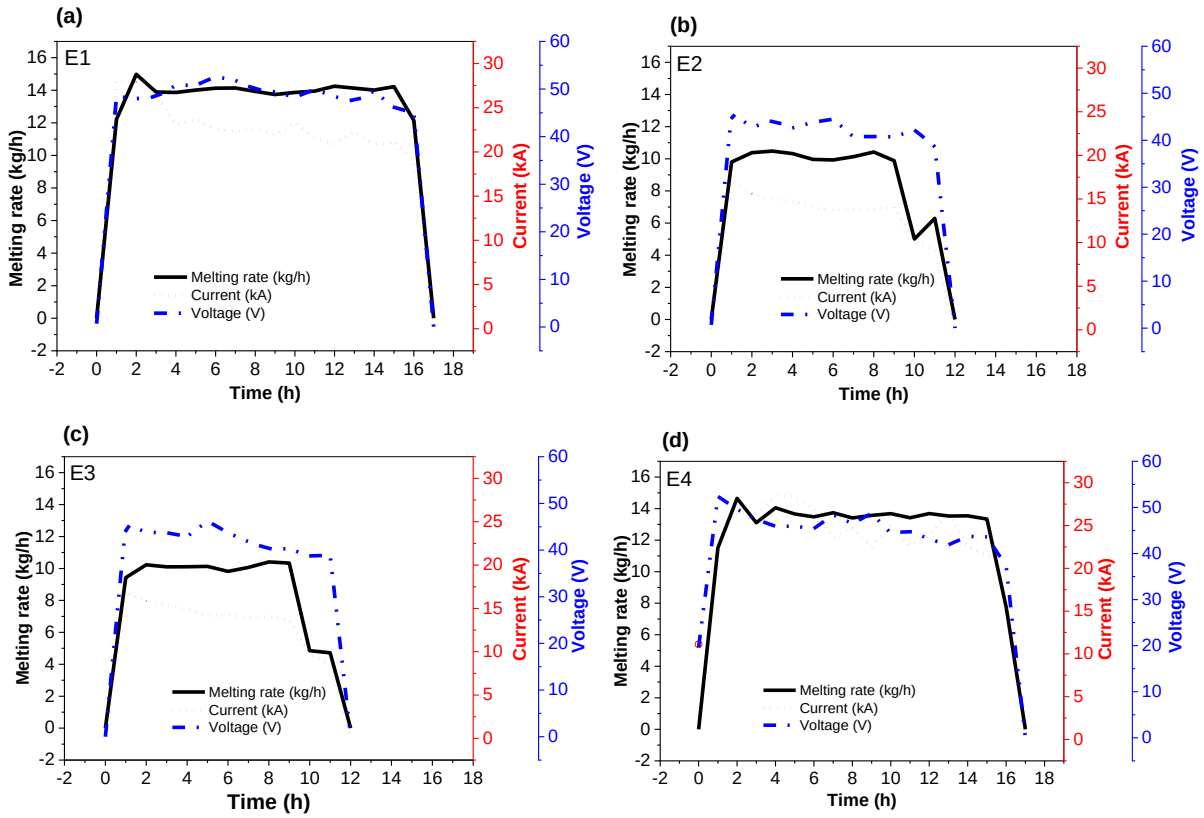

Figure 4.2 Voltage, current and melting rate parameters for ESR heats (a) E1, (b) E2, (c) E3 and (d) E4.

Table 4.4 presents the slag consumption for different ESR heats E1, E2, E3, and E4. Slag helps in capturing the non-metallic inclusions during ESR process. In the present work Wacker 2037 ELH slag is used which is an extra low hydrogen slag. Table 4.5 presents the chemical composition of Wacker 2037 ELH slag. Wacker 2037 ELH slag was used according to the recommendation of ESR furnace supplier. A new sealed drum of slag 2037 ELH was opened in every melting. The unused left-over slag in the drum if not consumed was further protected from atmosphere by keeping the same under a positive pressure of argon, where dry argon gas of ultra-high purity was employed.

Table 4.4 Slag consumption in respective ESR heats.

	E1	**E2 and E3**	**E4**
Total (kg)	250	110	250
Initial (kg)	30	20	30
Using slag feeder (kg)	220	90	220
Used slag (kg)	125	55	Not used

Table 4.5 Chemical composition of Wacker 2037 ELH slag.

	CaF_2	CaO	Al_2O_3
Weight percentage wt.%	60%	20%	20%

After remelting, the ESR ingots E1, E2 and E3 are subjected to heating, soaking/homogenization and forging followed by antiflaking treatment. Whereas, for ESR ingot E4 two antiflaking treatments one in semistage and other after finish forging is applied. After the antiflacking treatment the samples were air cooled to room temperature. Figure 4.3 presents the time-temperature heat-treatment curves for heating soaking and high temperature homogenization and forging cycles for ESR ingots E1, E2, E3 and E4. For ESR ingot E1 homogenization is carried out at 1220℃ for 14 h, for ESR ingots E2 and E3 homogenization is carried out at 1220℃ for 12 h. For the ESR ingot E4 homogenization is carried out at 1220℃ for 30 h before hot forging. The ESR ingots E1, E2, and E3 are hot forged from the initial dia of 900 mm, 600 mm, and 600 mm respectively to a dia of 340 mm. Whereas, ESR ingot E4 is semi forged from a 900 mm dia to 500 mm dia. After forging, anti-flaking treatment is given at 680℃ to the ESR ingots E1, E2, E3, and E4 followed by air cooling. Further the semi-finished ESR ingot E4 is again heated and homogenized at 1220℃ for 6–8 h, finish forged (from the dia. of 500 mm to 340 mm dia), and subsequently given second anti flacking treatment at 680℃ for 130 h, followed by air cooling [79,80,86,163]. ESR Heat E1 is forged from 900 mm dia ingot by drawing one upsetting drawing to 340 mm dia resulting in overall reduction ratio more than 10.5:1. ESR heat E2 and E3 are forged from 600 mm dia by drawing-upsetting-drawing-upsetting-drawing to 340 mm dia to achieve overall reduction of more than 10.6:1. Similarly ESR heat E4 is forged from 900 mm dia by drawing- upsetting-drawing-upsetting drawing to achieve overall reduction ratio more than 11.8:1. The forged bars are normalized, tempered, and machined to the desired specifications. Further, for macrostructure investigation and to distinguish the hydrogen flakes a transverse slice of 320 mm dia and 30 mm thickness was cut.

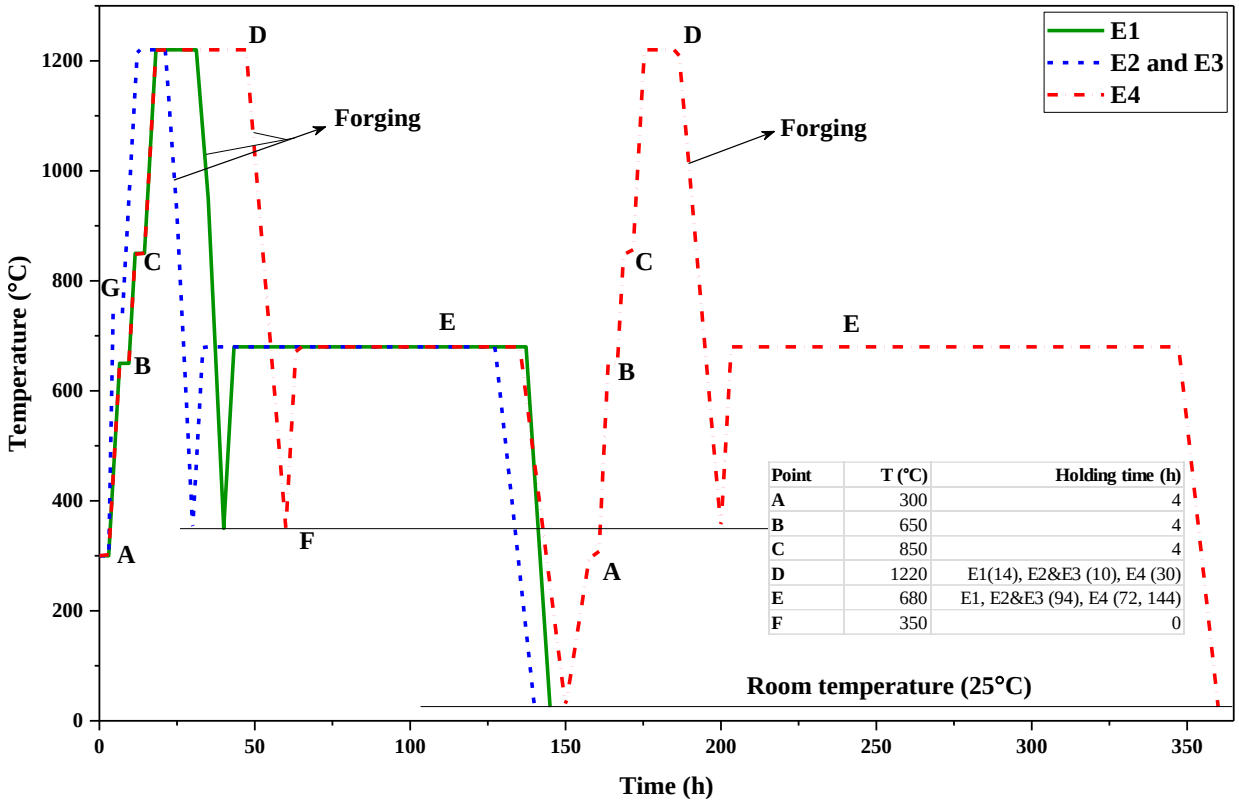

Figure 4.3 Heating soaking and high temperature homogenization and forging cycles for ESR ingots E1, E2, E3 and E4.

4.2 CHEMICAL COMPOSITION

Table 4.6 presents the chemical composition of the primary heats D1, D2, and D3. Table 4.7 presents the chemical composition of the ESR heats E1, E2, E3, and E4 after finish forging and normalizing. ESR is being performed in the inert argon atmosphere. This leads to a decrease in the levels of macro and micro segregation. The advancement in the ESR furnace technology has given freedom to control the operating parameters more accurately. The process parameters of the ingots manufactured via. ESR route are critically and accurately controlled. This leads to the development of very sound solidified structure with good homogeneity and without any internal defects [92,164,165].

Further, good chemical homogeneity in ingot, high temperature homogenization prior to hot forging process (thermo-mechanical treatment) results in isotropy in the forgings after ESR. The mechanical properties achieved after thermo-mechanical processing and heat-treatment results in almost similar mechanical properties in both longitudinal and transverse directions upon forging after ESR [92,166,167].

Table 4.6 Chemical composition and of the primary heats (wt.%).

H. No	C	Si	Mn	P	S	Cr	Mo	Ni	V	W	N	H
D1	0.395	0.255	0.86	0.007	0.002	0.88	0.26	1.87	0.005	0.001	0.007	0.00017
D2	0.400	0.26	0.85	0.008	0.002	0.84	0.28	1.865	0.01	0.02	0.005	0.00018
D3	0.395	0.25	0.775	0.008	0.001	0.83	0.275	1.92	0.004	0.008	.0026	0.0001

Table 4.7 Chemical composition of the ESR heats after finish forging and normalizing (wt.%).

H. No.	C	Si	Mn	P	S	Cr	Mo	Ni	V	W	N	H
E1	0.410	0.250	0.84	0.007	0.002	0.85	0.252	1.83	0.06	0.001	0.0078	0.00019
E3	0.410	0.25	0.87	0.007	0.002	0.82	0.27	1.825	0.07	0.018	0.0057	0.0002
E3	0.410	0.25	0.87	0.007	0.002	0.82	0.27	1.823	0.07	0.02	0.0057	0.0002
E4	0.415	0.248	0.83	0.007	0.001	0.80	0.263	1.82	0.08	0.004	0.0031	0.00013

Figure 4.4 presents the variation in compostion of major alloying elements along the diameter starting from surface.

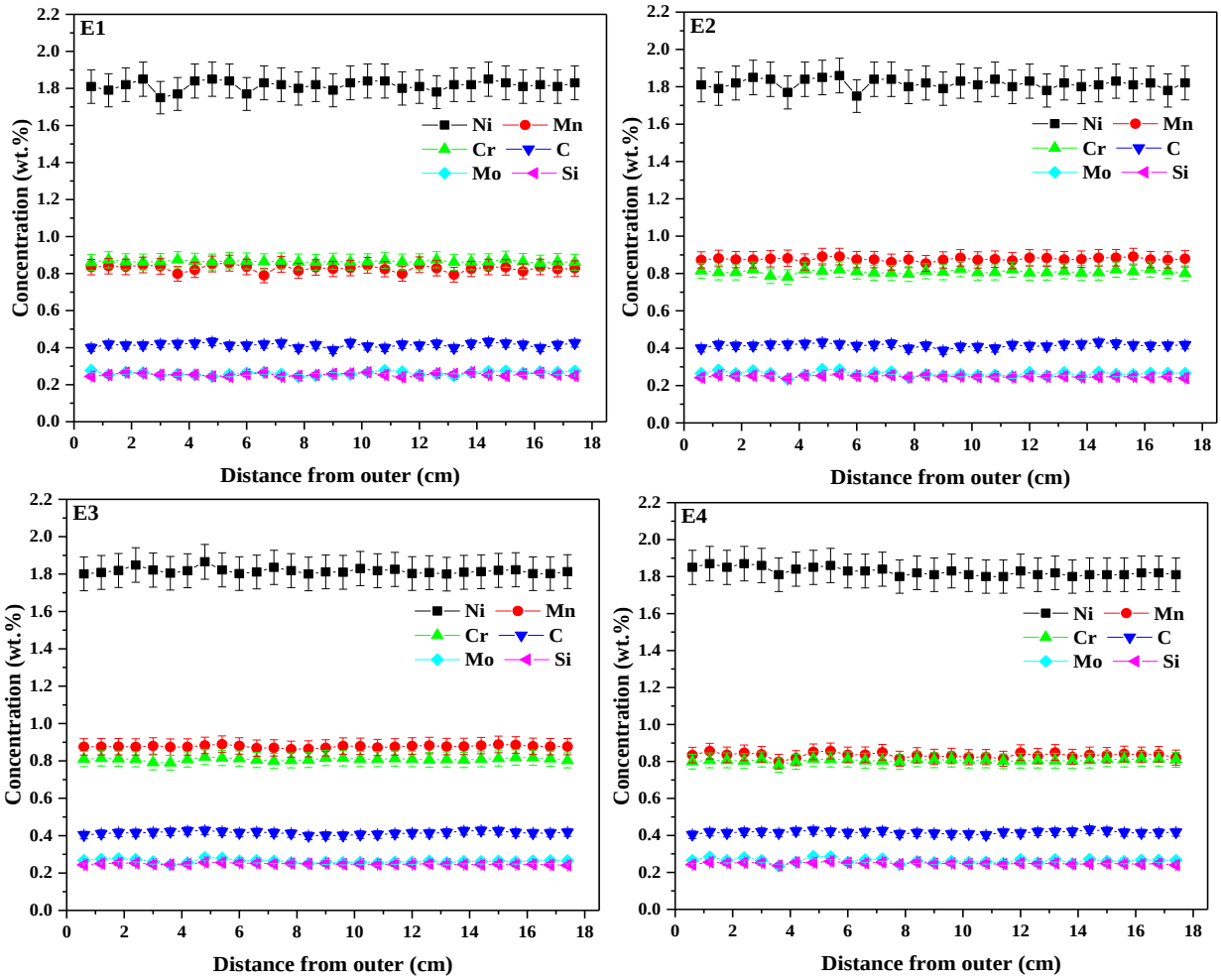

Figure 4.4 Segregation of alloying elements of E1, E2, E3 and E4.

As observed from Figure 4.4 ESR heat E4 shows minimum segregation in comparison to E1, E2, and E3 heats. This is because of additional high temperature homogenization and two stage anti flacking treatment. Although, two homogenization and antiflaking cycles could have been highly effective for microscopic segregation, but unsatisfactory spectro analysis results were observed for ESR heats E1, E2 and E3. To improve the macro elemental segregation, ESR heat E4 was subjected to longer homogenization time as compared to ESR heats E1, E2, and E3. ESR heat E4 (with longest homogenization cycle and two antiflaking treatments) showed least elemental segregation and maximum diffusion of hydrogen on the macro scale.

4.3 MACROSTRUCTURAL EXAMINATION

Table 4.8 presents different macro features observed in the samples. Figure 4.5a presents the macrostructure of hydrogen flakes as observed on 50 mm×80 mm sample for one of the ESR heats E1. Similar hydrogen flakes were also observed in ESR heats E2 and E3. However, ESR heat E4 was free from hydrogen flakes (Figure 4.5b).

The dissolved hydrogen in the steels has a tendency to get absorbed on sites like segregation regions and non-metallic inclusions [82]. For E1, E2 and E3 the soaking and homogenization at 1220 ℃ at nearly 20–30 min/inch was probably insufficient to minimize segregation. This may lead to the development of possible sites for hydrogen accumulation. Thus, increase in the threshold of hydrogen is observed. This critical amount of hydrogen manifests as flaking [82]. Whereas, for E4 an additional homogenization of about 20 min/inch has led to the distribution of segregation, leading to a decrease in the accumulation of hydrogen below the hydrogen flaking threshold value. Further, reduction in hydrogen flacking was observed with the two-stage anti flaking treatment provided for E4 (i.e. one in semi forged stage and one after final forging).

Table 4.8 Macrostructure examination of ESR heats.

Condition	**E1**	**E2**	**E3**	**E4**
Flute crack	Absent	Absent	Absent	Absent
Sponginess	Absent	Absent	Absent	Absent
Flakes	Present	Present	Present	Absent
Dendrites	Present	Present	Present	Present

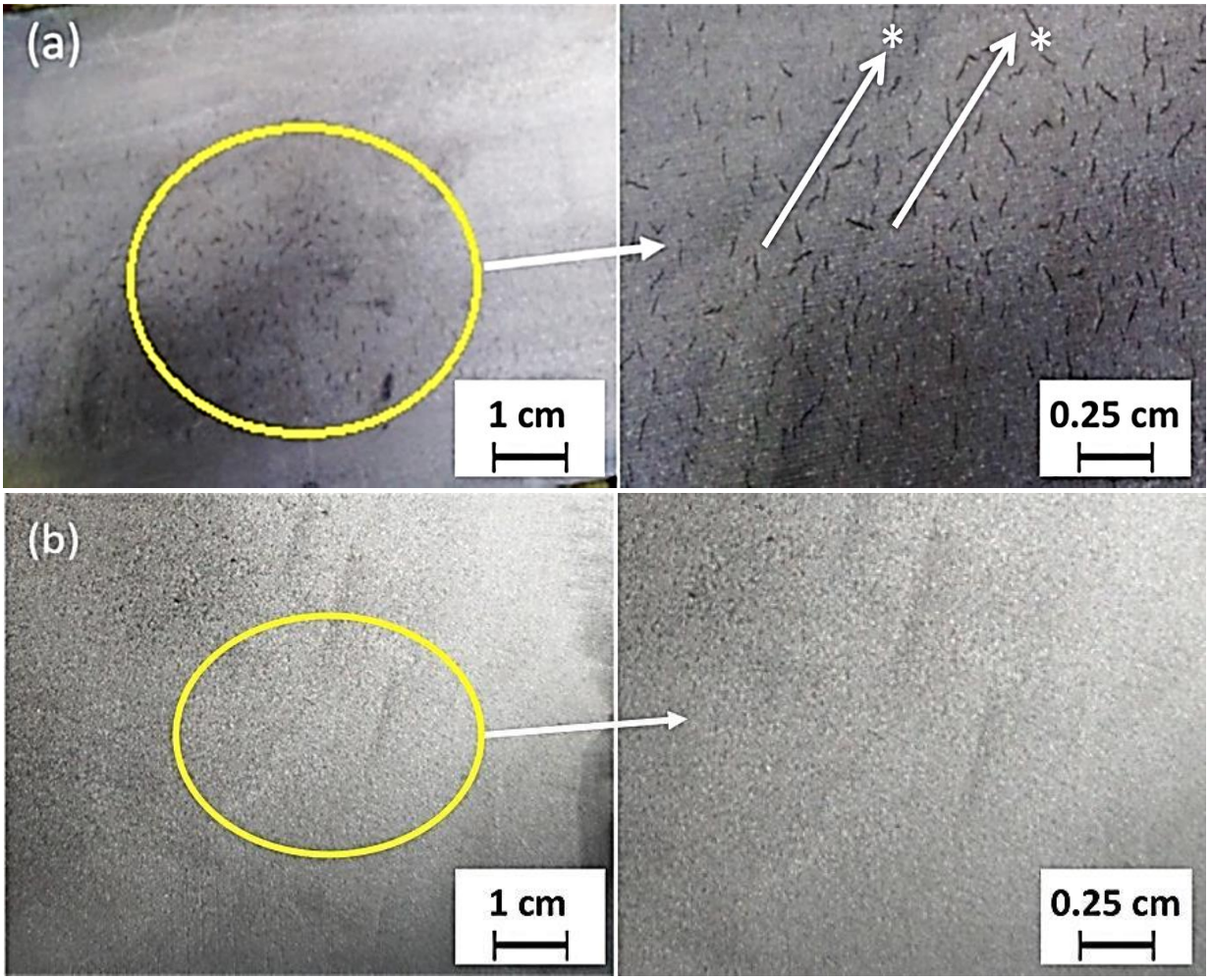

Figure 4.5 Macrostructure examination of ESR heats (a) E1 and (b) E4. Note: * indicates aligned hydrogen inclusions leading to crack initiations

4.4 MICROSTRUCTURE ANALYSIS

Figure 4.6 presents the microstructural features of ESR heats normalized at 870 ℃ and tempered at 675 ℃. Figure 4.6a presents the structure of E1 steel. The structure is a coarse tempered martensitic/ bainitic type. There are some fine carbides also. Because of this the yield point reduces (discussed later). Figure 4.6b presents the microstructure of E2 steel exhibiting similar structure to that of ESR heat E1. However, some randomly oriented carbides are also seen. This may enhance the yield point and also the ultimate tensile strength. In Figure 4.6c the features observed in E1 and E2 are absent. The structure corresponding to E3 steel shows homogenous distribution of all the phases present in the steel. These structures are more refined and may lead to better ductility and higher strength. The colonial growth of phases as observed in E1 and E2 are absent. The

structure may exhibit isotropic properties. However, some growth of the tempered microstructure is seen. The microstructure observed for E4 steel is more refined. The phases are distributed uniformly and most importantly the aligned growth of different phases is absent. When compared to E1 and E2 steels the features are more refined. However, the phases observed for the E4 steel are similar to that of the E3 steel. But a more refined structure is observed. This may be due to the additional homogenization and antiflaking treatment given to the ESR heat E4 (Figure 4.6d). The structural properties are in tune to the mechanical properties exhibited by these steels (Table 4.12). Figure 4.7 presents the structural features of ESR heats E1, E2, E3, and E4 after hardening (870 ℃) and tempering (240 ℃) treatment. The structural features here also are in tune to that observed in Figure 4.6. Higher hardening temperature has led to coarser structure for steel E1. It is also possible that the strain induced in the steel got relaxed during hardening treatment that has led to the development of colonial patches at some places as can be seen in Figure 4.7a. Such structural features observed shows some type of segregation of alloying elements also, which got redistributed during the hardening and tempering treatment. Hydrogen may get trapped at these sites. Figure 4.7b presents the microstructure of E2 steel. The structure is more refined and homogenized in comparison to E1 steel. However, at some places coarser structure compared to the other area can be seen where mixed structure comprising of martensite and bainite is observed. Figure 4.7c presents the structure of E3 steel. The microstructural features of E2 and E3 steel are similar. The only difference observed is that there is no colonial growth. However, the carbide phase at certain places is aligned. Figure 4.7d presents the microstructure of E4 steel. When compared to the microstructure of E1, E2, and E3, the structure of E4 is more refined and uniform. The growth of all the present phases is uniform and isotropic in nature.

While analyzing the structural features presented in Figure 4.6 and Figure 4.7, it is observed that the heat-treatment cycles followed for the steel E4 has led to the development of refined and uniform structure. This type of structures has led to the distribution of hydrogen flakes throughout the structure. Such distribution of hydrogen flakes may not lead to stress concentration zone and avoid failure of steel.

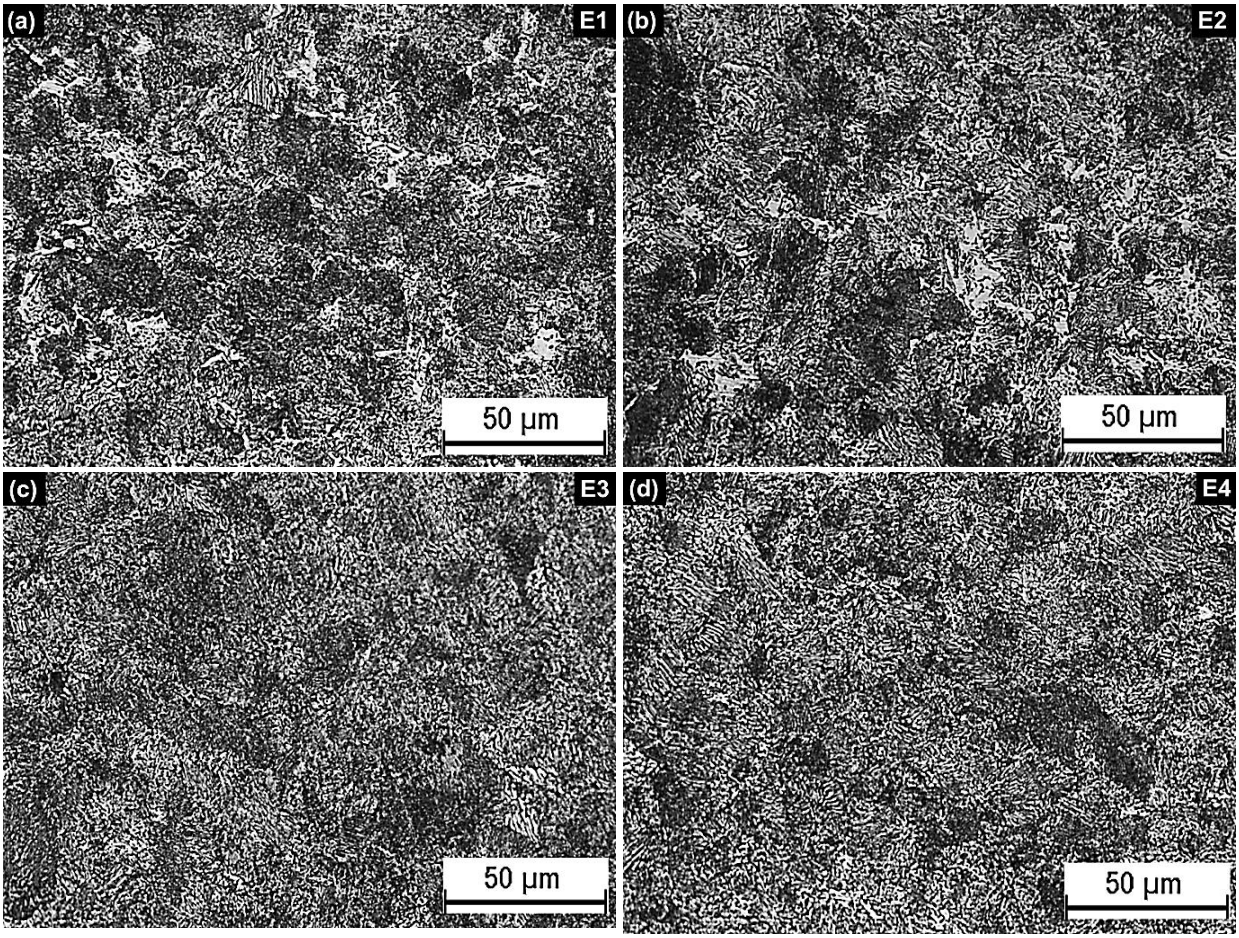

Figure 4.6 Microstructural characterization of ESR heats normalized at 870°C and tempered at 675°C for (a) E1, (b) E2, (c) E3, and (d) E4.

Figure 4.8 depicts the microstructural features of a crack originated from hydrogen flakes in ESR heat E1. As shown in Figure 4.5a (marked by an arrow) the cracks originate from the hydrogen flakes, joins together and propagates further in due course of time. The variation in crack thickness from one point to other point is a clear indication of the origin of crack from these flakes. These cracks further move towards other cracks as can be seen from Figure 4.8. Origin of such growth can also be seen in other places of the structure. Such features may lead to the decrease in strength and ductility of material. It may also lead to the catastrophic failure of steels.

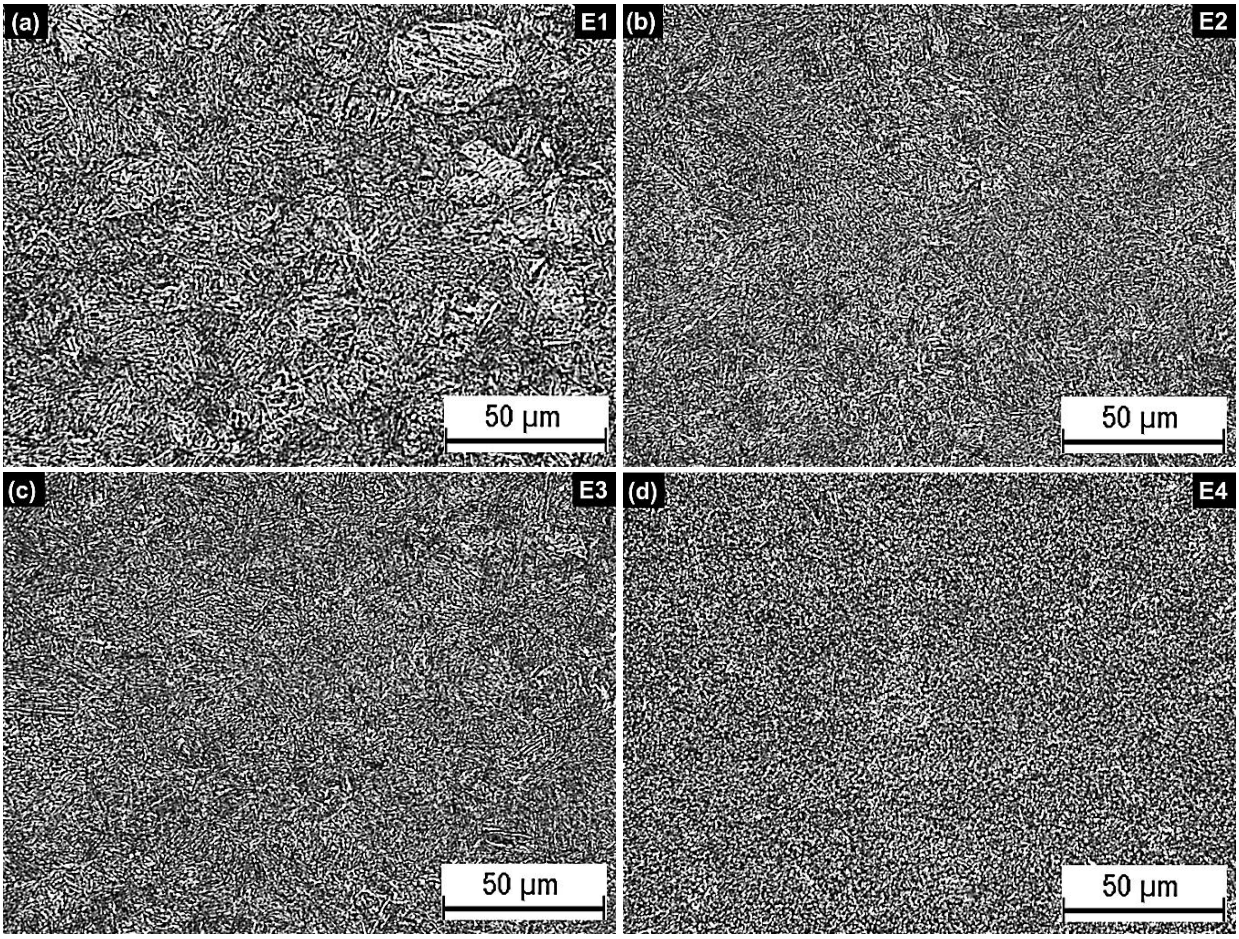

Figure 4.7 Microstructure of ESR heats after final heat-treatment process consisting of hardening at 870 ℃ and tempering at 240 ℃ for (a) E1, (b) E2, (c) E3, and (d) E4.

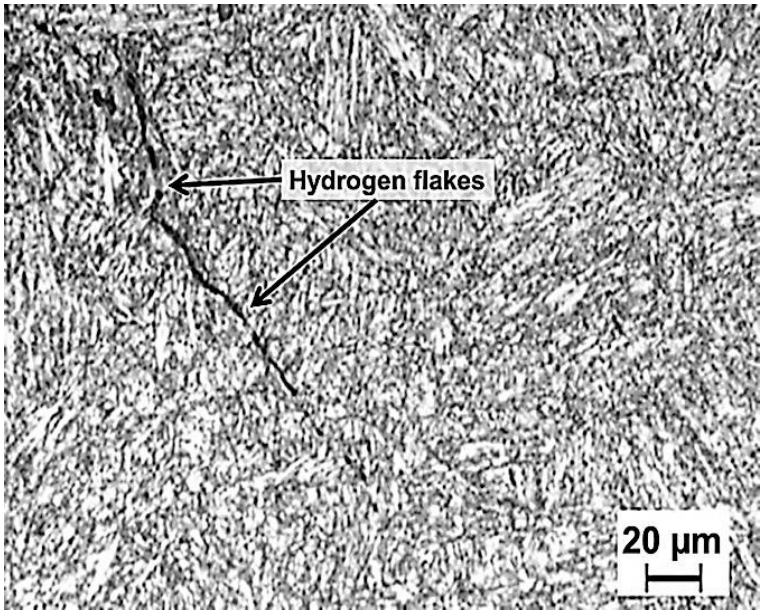

Figure 4.8 Microstructural features of the hydrogen flakes of ESR heat E1.

4.5 TESTING AND EVALUATION

Ultrasonic testing is performed to observe the internal defects of the ESR heats. It is observed that due to the presence of hydrogen flakes in E1, E2, and E3 the rate of rejection for ultrasonic defects is very high. For ESR heat E1, maximum rejection of 80% and for the ESR heat E4 no rejection is observed. Table 4.9 presents the ultrasonic test results as has been checked according to Rafael Specification No. 5036 R4 & AMS 2370 with 1.2 mm FBH reference by USN-60 (Kraut Kramer) using probe B-4S-(57746) of diameter 24mm, horizontal range 0–350 mm covering 360° where coolant used is Mobil oil.

Table 4.9 Ultrasonic testing results for different ESR heats.

Heat No.	Total forged Length (mm)	Ok Length (mm)	Rejected Length (mm)	% Rejection
E1	14500	2200	11800	~80%
E2	6500	1950	4550	~70%
E3	6500	2070	4430	~68%
E4	14300	14300	0	0%

Table 4.10 presents the non-metallic inclusions present in different ESR heats. Since, the ESR process used in the manufacturing of E1, E2, E3, and E4 is identical, hence a negligible change in the non-metallic inclusions is observed.

Table 4.10 Non-metallic inclusions (According to ASTM E45 Method A) [168].

Heat no.	Type A		Type B		Type C		Type D	
	Thin	Thick	Thin	Thick	Thin	Thick	Thin	Thick
E1	0	0	1.5	0.5	0	0	1.0	0.5
E2	0	0	1.0	0.5	0	0	1.0	0.5
E3	0	0	1.0	0.5	0	0	1.0	0.5
E4	0	0	0.5	0.5	0	0	0.5	0

A finer grain size is observed for ESR heat E4 in comparison to ESR heats E1, E2, and E3 (Table 4.11). The refinement of the grain size leads to the improvement in the mechanical properties of ESR heat E4.

Table 4.11 Grain size of different ESR heats (According to ASTM E-112 standard) [160].

S. No	ESR heat	Grain size
1	E1	5.0 ASTM
2	E2	5.0-5.5 ASTM
3	E3	5.0-5.5 ASTM
4	E4	6.5-7.0 ASTM

Table 4.12 present the target mechanical properties and the mechanical properties achieved for ESR heats E1, E2, E3, and E4. ESR heat E1 is rejected as it could not achieve the desired yield strength. Although, ESR heats E2 and E3 have shown the desired mechanical properties but got rejected during the ultrasonic testing. ESR heats E2 and E3 achieved the desired mechanical properties due to the smaller diameter ingots. ESR heat E4 achieved the best combination of mechanical properties due to the longer high-temperature homogenization and two stage anti flacking treatment. The process route used for processing of ESR heat E4 showed the best properties (ultrasonic and mechanical) and has been accepted.

Table 4.12 Desired and achieved mechanical properties for different ESR heats.

S. No.	Heat No.		YS (MPa) (0.2% PS)	UTS (MPa)	Elongation (%)	Reduction area (%)	Impact strength at -40℃ (Joule)
1.	Requirement Longitudinal		1496 Min.	1793 Min.	10 Min.	30 Min.	25
	Requirement Transverse		1496 Min.	1793 Min.	5 Min.	25 Min.	25
2.	**E1**	Long.	1482.4	1795.8	9.6	28.5	26, 24, 26
		Trans.	1467.3	1781.4	8.2	26.0	20, 24, 22
3.	**E2**	Long.	1522.9	1832.6	10.8	33.6	28, 26, 27
		Trans.	1499.7	1805.8	9.5	30.0	25, 26, 26
4.	**E3**	Long.	1531.8	1847.5	10.5	32.8	27, 26, 26
		Trans.	1506.0	1812.9	10.0	31.0	26, 25, 25
5.	**E4**	Long.	1590.7	1946.7	11.4	39.4	42, 40, 42
		Trans.	1573.4	1905.8	11.8	36.4	38, 39, 38

In this study we reported different processing routes to manufacture ESR heats E1, E2, E3, and E4. Hence, three different processing routes were used to manufacture AMS-4340 UHSS. Further, for ESR heat E1, E2, and E3 a single antiflacking and homogenization cycle is used, whereas for ESR heat E4 two homogenization and antiflacking cycles are used. Homogenization of ESR heat E1 is carried out for 14 h, and for ESR heat E2 and E3 homogenization is carried out for 12 h. It is observed that the homogrnization time-period given to ESR heats E1, E2, and E3 is not sufficient to remove elemental segregation. Therefore, ESR heat E4 is given longer homogenization time (30 h) before the start of forging. ESR heats E1, E2, and E3 are forged to the final required diameter in a single forging cycle and for ESR heat E4 two forging cycles are used. Two forging cycle routs followed in case of E4 has led to the better distribution of alloying elements and decrease in elemental segregation. Further, ESR heats E1, E2, and E3 were given a single antiflacking treatment with the holding time of 5.3 h per inch of diameter. Hydrogen flakes are clearly visible

for these heats. Moreover, ESR heat E4 is given an additional antiflacking treatment with the holding time of 9.5 h per inch. No hydrogen flakes and minimum elemental segregation (within acceptable limits) is observed for heat E4. Therefore, the processing route used to manufacture ESR heat E4 is an optimum processing path to develop AMS-4340 UHSS within the acceptable limits.

4.6 COST ESTIMATION

The present study investigates an alternate route to develop defect free AMS-4340 steel for defense applications. So, the costing parameters of the normally existing VIM+VAR and the currently developed process both are compared. A cost review was done for UHSS manufactured through VIM+VAR and air-melt+ESR route. Cost of production through VIM was 1.5 times to that of the conventional air melting. Next, during remelting in ESR and VAR operational cost of VAR is about 20% lesser than ESR as VAR does not use any prefused slag as ESR which is very costly. On the other hand, in VAR process both electrode and VAR ingot need removal of surface impurities and non-metallic inclusion by machining all over the diameter resulting in 6-8% loss in overall yield of the UHSS steel [81,169].

The electrode in ESR can be used in as cast condition whereas, the electrodes for VAR must be surface processed (e.g. grinded, machined) for best cleanliness and less oxides on the surface layer. In both ESR and VAR high end quality in regard to the chemical homogeneity and cleanliness is achieved. However, in VAR the final ingot achieved is 20% smaller than the starting ingot and electrode [170]. The energy consumption for homogenization cycle of 25-ton material to reach soaking/homogenizing temperature of 1220 ℃ is 69 (standard cubic meter/ ton) SCM/ton while during soaking the gas consumption is 17 SCM/ton. Whereas, for antiflaking treatment power consumption during heating to antiflaking temperature of 680℃ was observed to be 164 KWH and during soaking 32 KWH for 25-ton material. Thus, additional cost in longer homogenization and two AFT cycles is much lower than cost associated with VIM+VAR process.

CHAPTER 5
RESULTS AND DISCUSSION
10.7CrMoVNbN STEEL

OVERVIEW

10.7CrMoVNbN (K9A62C) is a heat-resisting martensitic stainless steel developed by M/S Toshiba JSW Turbine & Generator Pvt. Ltd. for the manufacturing of turbine blades, nozzle partition and bucket for supercritical turbines. The presence of delta-ferrite has a harmful effect on the mechanical and welding properties for martensitic heat-resistant steel. In the present study, an alternate route has been developed to control the failure of steel by the inclusion of delta-ferrite. In the present work the failure of delta-ferrite is controlled by controlling the chromium equivalent in the steel. The chapter presents the microstructural characterization of the processed steels. Next the chapter also discusses the FESEM-EDS analysis of the processed steels. Finally, the role of microstructure and its influence on mechanical properties has also been discussed.

5.1 10.7CrMoVNbN STEELS

5.1.1 STARTING MATERIAL

Four heats of 10.7 CrMoVNbN steel were cast at M/S Star Wire (India) Ltd., Ballabgarh (Haryana) after designing the chemical composition having the addition of different amount of austenite and ferrite stabilizers to investigate the influence of chemistry on the formation of delta-ferrite in this heat-resisting martensitic stainless steel. Ferrite and austenite stabilizers were designed in such a manner that Cr_{eq} can vary for all Heats. Cr_{eq} was calculated using the formula given in the De-Long diagram as shown on Equation 5.1 [15].

$$\mathbf{Cr_{eq}} = \%Cr + \%Mo + 1.5Si + 0.5Nb \quad (5.1)$$

The De-long diagram was used only as a basic guideline since it is only an empirical model and thus the accuracy of phase estimation after solidification is not expected to be high as it does not consider the effect of centerline segregation in the solidified ingot. Moreover, it does not describe the kinetics of formation and retention of δ-ferrite at higher temperatures at which it forms and solidifies first which transforms to austenite at a later stage.

First two heats (Heat 1 and Heat 2) were designed by keeping slightly higher (Cr_{eq}) values and another two heats (Heat 3 and Heat 4) were cast keeping slightly lower Cr_{eq} values. **Chemical composition range was taken from M/s Toshiba specification, where much liberty was not available to increase Ni_{eq}** [101]. Chemical compositions and Cr_{eq} of all four respective trial heats is given in Table 5.1. Figure 5.1 presents the CCT diagram of Heat 4 of 10.7CrMoVNbN steel.

Table 5.1 Chemical composition and Cr_{eq} the ratio of trial heats of 10.7CrMoVNbN steel (wt. %.).

Heat No.	C	Si	Mn	Cr	Mo	Ni	Al	Nb	V	W	Co	N	Cr_{eq}
Heat 1	0.16	0.42	0.73	11.19	0.96	0.54	0.011	0.43	0.19	0.018	0.030	0.04	**12.99**
Heat 2	0.16	0.37	0.65	10.83	0.89	0.52	0.008	0.4	0.17	0.011	0.032	0.06	**12.47**
Heat 3	0.18	0.31	0.66	10.45	0.92	0.42	0.021	0.44	0.18	0.003	0.020	0.05	**12.05**
Heat 4	0.19	0.25	0.73	10.21	0.82	0.36	0.007	0.38	0.21	0.029	0.027	0.055	**11.59**

5.1.2 PROCESSING ROUTE

Primary melted heats were subjected to electro slag re-melting in a state of art electro slag re-melting (ESR) furnace with inert gas protection supplied by ALD Germany. 600 mm diameter

cross-section and 2700 mm length ESR ingots were given high-temperature homogenization at 1200 ℃ @ 30 minutes/25 mm.

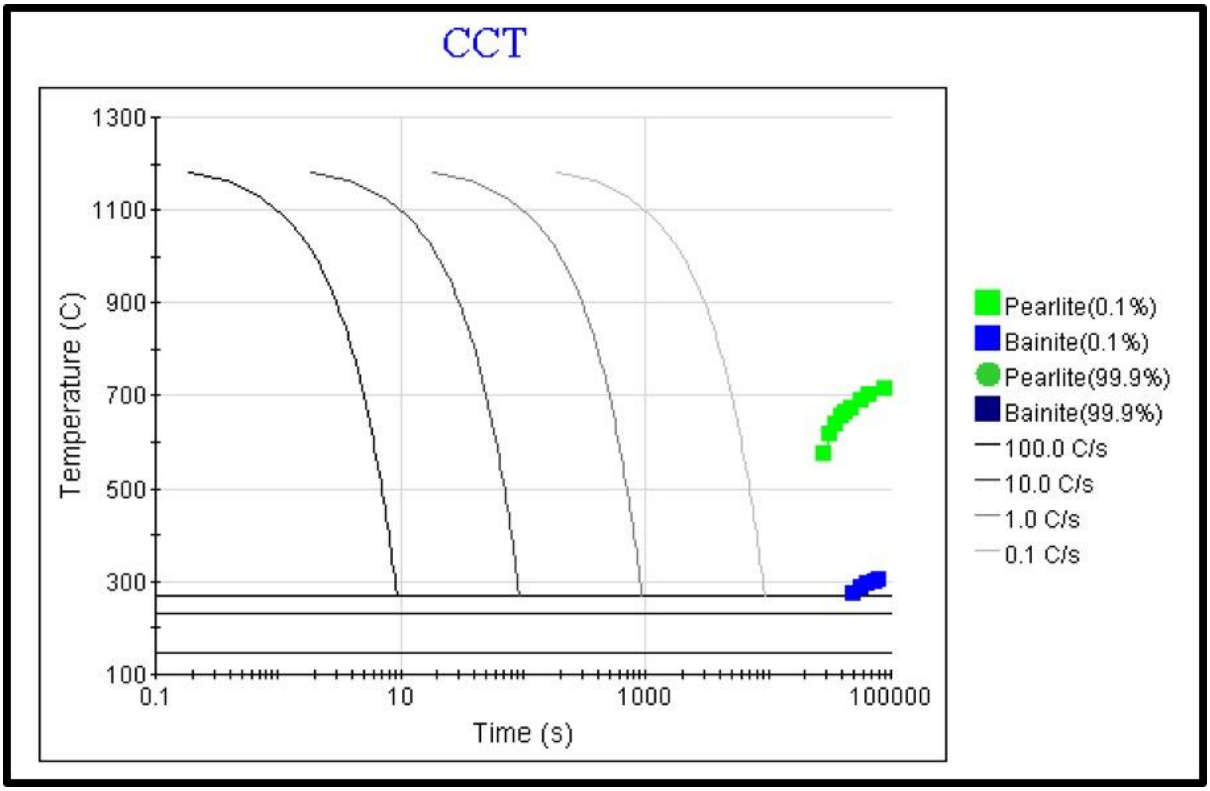

Figure 5.1 CCT diagram of Heat 4.

Thereafter, forging to semis was done after high-temperature homogenization before starting of forging. Forging consisted of three upsetting-drawing sequences and then forging to semi size of 170 mm round corner square to ensure multi-directional flow to break the cast structure and distribute the centreline segregation from the point of view of eliminating the formation of δ-ferrite formation. Thereafter, forged 170 mm square semis were hot rolled to the desired section of 94x62 mm and length of 4000 to 5000 mm as shown in Table 5.2. Thereafter hardening and tempering heat-treatment were done according to Toshiba specification [101]. Required samples for this investigation were collected from the finished machined turbine blades pertaining to heat 1, 2, 3 and 4. Out of these samples only heats 1 and 2 were showing linear indication during MPI [171–173] test after the finished machining operation of turbine blades for use in steam turbine generator (STG660) of 660 MW.

Table 5.2 Sample preparation process flow diagram.

S.no	Activity	Description
1	Primary electrode dia 480 mm casting after primary melting	
2	ESR of 480 mm dia electrode into 600 mm dia ESR ingot, 2700 mm long weight about 6000kg	
3	Top, bottom end discarding and surface grinding	Standard discard length 60 mm. from the top side and 90 mm. from the bottom side
4	Heating to 1200°C and homogenizing for 12.5 hrs @ 30 minutes /25 mm, followed by forging to semis in following steps	On 2000-ton hydraulic forging press. Make ERIE, USA
4a	Upsetting to from 2700 mm to 1350 mmx850 mm dia	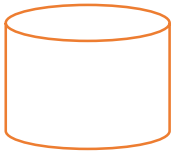
4b	Drawing after turning 90° to 600 mm. dia. X 2700 mm. L	
4c	Upsetting ii as in 4a	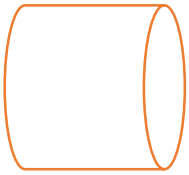
4d	Drawing as in 4b	
4e	Upsetting iii as in 4a and 4c	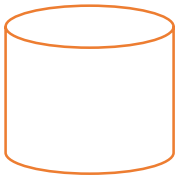
4f	Drawing as in 4b and 4d to 600 mm. dia x2700 mm. l	
4g	Reheating to 1180°C and forging to 170 mm. square	In the gas-fired reheating furnace, duly calibrated
4h	Post forging annealing at 680°C/12 hrs	In electrically heated boggie hearth furnace duly calibrated
4i	Surface grinding and rolling stock cutting for final rolling 94 mm. X 62 mm.	

4j	Annealing of bars at 680°C/6 hrs.	In electrically heated boggie hearth furnace calibration according to API 6a standard
4k	Hardening at 1090°C/4hrs followed by oil quenching in oil (servo quench 1) and keeping in oil for 2 hrs.	In electrically heated boggie hearth furnace duly calibrated according to API 6a standard
4l	Tempering at 670°C/6hrs followed by air cooling	In electrically heated boggie hearth furnace with circulating fan, duly calibrated
4m	Evaluation of mechanical properties and microstructure on LOM and FE-SEM	In well-equipped mechanical test lab and metallography on LOM and FE-SEM

5.2 OPTICAL MICROSTRUCTURES

The optical microstructure of 10.7Cr steel of heats 1 to heat 4 etched with Kalling's-1 etchant is shown in Figure 5.2. Kalling's-1 etchant clearly shows the presence of tempered martensite. The tempered martensite matrix for Heat 4 was more refined when compared to Heat1.

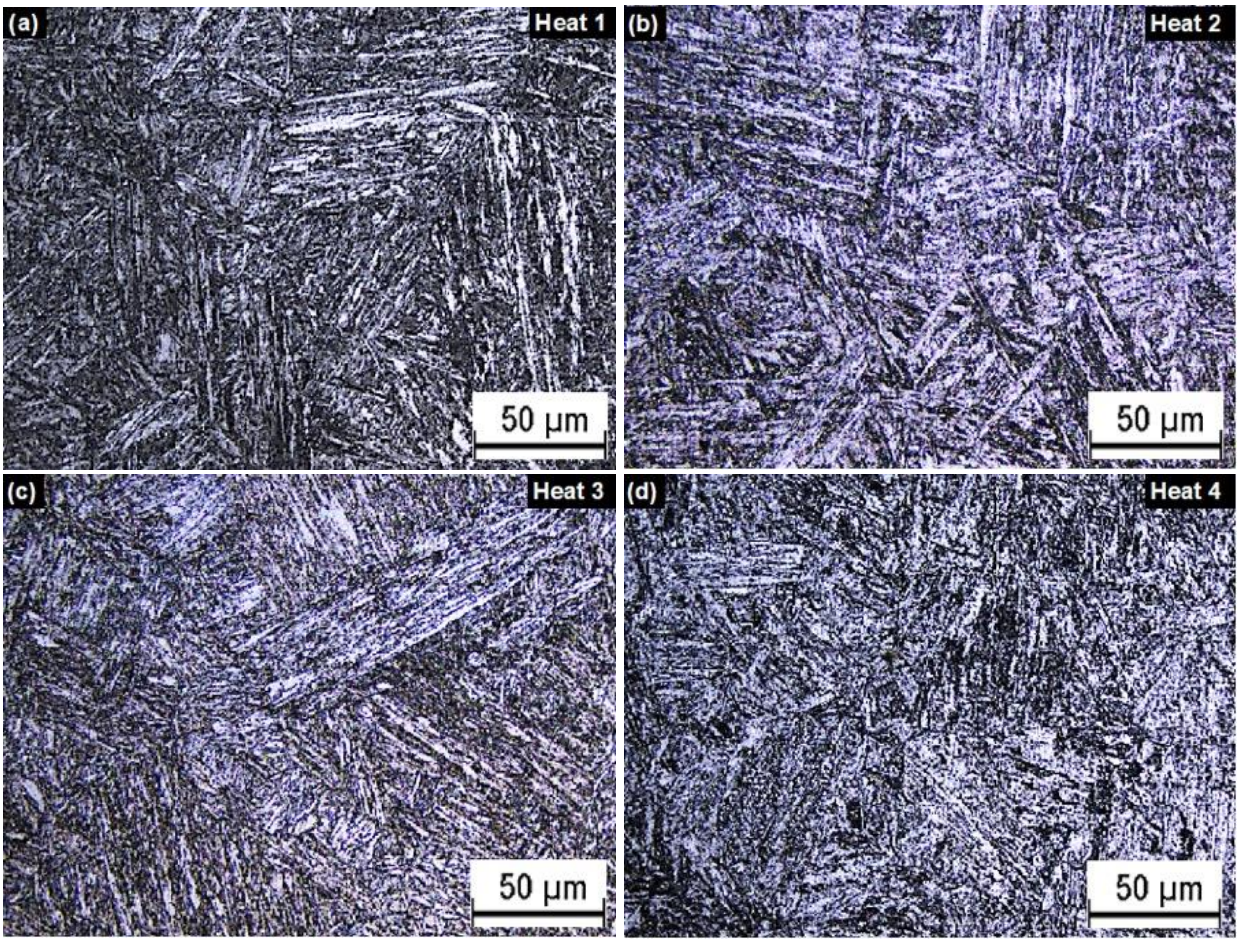

Figure 5.2 Optical microstructures of 10.7CrMoVNbN steel of (a) Heat 1, (b) Heat 2, (c) Heat 3 and (d) Heat 4 at 200X magnification using etchant Kalling No. 1.

Figure 5.3 demonstrates the microstructure after etching with a sulphuric acid etchant to selectively reveal δ-ferrite. It can be seen that heat 1 exhibits a higher amount of δ-ferrite compared to other heats. The lowest amount of δ-ferrite is observed in heat 4. It could be due to the lower Cr_{eq} compared to heat 1 to 3, which restricted the formation of δ-ferrite. In addition, multiple multi-directional forging also eliminates the δ-ferrite up to greater extent in all heats. The volume fraction of martensite (matrix), carbides, and δ-ferrite is presented in Table 5.3. The volume fraction of the δ-ferrite which was checked by using the grid intercept method according to AMS2315A on samples selectively etched to reveal only δ-ferrite, decreases from heat 1 to heat 4 as shown in Table 5.3. It can be seen that the presence of δ-ferrite content has come down drastically to as low as 0.3% and no linear stringers are observed in the structures while both heats 1 and heat 2 show long stringers of delta-ferrite.

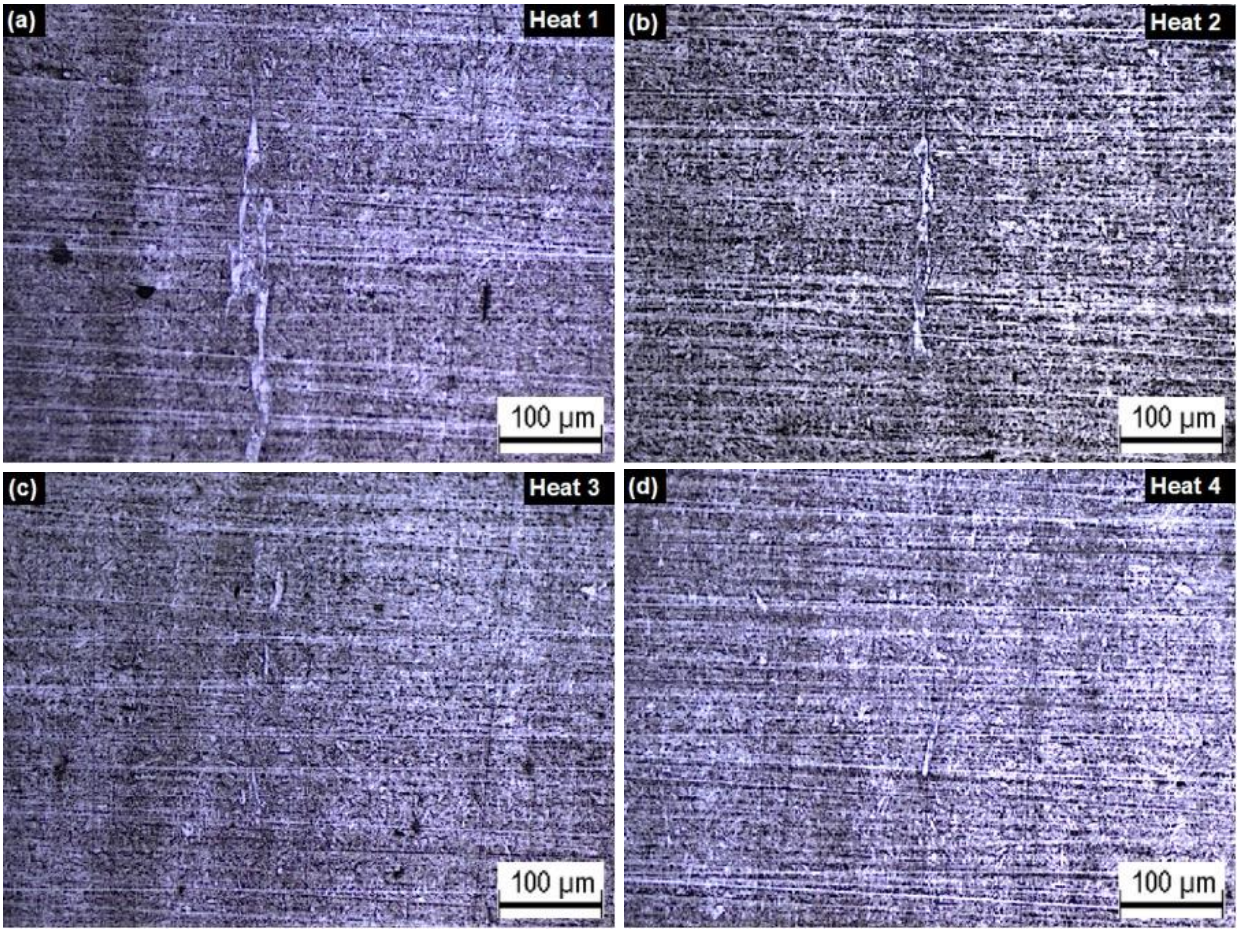

Figure 5.3 Optical microstructures of 10.7CrMoVNbN steel of (a) Heat 1, (b) Heat 2, (c) Heat 3 and (d) Heat 4 at 200X magnification using sulphuric etchant.

Table 5.3 Volume fraction of austenite, carbides, and δ-ferrite in all Heats measured using the grid intercept method.

Heat No.	*Volume fraction of Martensite (%)*	*Volume fraction of Carbides (%)*	*Volume fraction of δ-ferrite (%)*
Heat 1	93.6±0.04	3.2±0.03	3.2±0.04
Heat 2	94.95±0.05	2.9±0.04	2.15±0.02
Heat 3	96.8±0.04	2.5±0.02	0.7±0.02
Heat 4	96.9±0.06	2.8±0.02	0.3±0.03

5.3 FESEM-EDS ANALYSIS

The purpose of FESEM-EDS analysis was to confirm the presence of tempered martensite matrix, carbides, and δ-ferrite. Field emission scanning electron microscopy and EDS investigations show various microstructure constituents in the matrix of martensite. Morphology of martensite, carbide, and δ-ferrite of heat-1 is shown in Figure 5.4. Figure 5.5 presents the X-ray dot mapping of selected elements that show the presence of carbides and δ-ferrite. The concentration of carbides forming elements (Nb, Mo) is found richer, where carbide is present.

Table 5.4 shows the composition analysis of tempered martensite matrix, carbides, delta-ferrite-martensite interface, and delta-ferrite on points 1, 2, 3, and 4 marked in Figure 5.4 (a-c). It is observed that there is an enrichment of Mo and Nb at the interface of the martensite-delta-ferrite interface which is in agreement with earlier research wherein phase transformation of a similar alloy is studied for chromium contents of 6 to 16% [105]. However, chromium content in delta-ferrite is found lower than the martensite matrix and delta-ferrite-martensite interface which could be due to different heat-treatment in this investigation and earlier research [105].

Figure 5.6 presents the line profiling of Heat 1 specimen. It can be observed that along the interface, a decrease in Fe concentration was observed. Further, an increase in the Cr concentration is seen. Whereas, the concentration of Mo remains nearly constant. Delta-ferrite draws Cr from the matrix which leads to a rise in the concentration of Cr and reduces the concentration of Fe along δ-ferrite-tempered martensite interface.

Figure 5.7 shows the FESEM microstructure of Heat 4. It can be seen that δ-ferrite is not present in the structure due to its designed chemistry as well as multiple forging. Only carbides are observed in the microstructure. Table 5.5 provides the elements (wt. %) analyzed through EDS for points marked 1, 2, and 3. In 10.7CrMoVNbN steel, precipitates are largely of two different sizes. The larger sized precipitates in the size range of 5–10 μm correspond to NbMoC carbides. While the smaller sized precipitates up to the size range of 2 μm max. corresponds to NbC precipitates.

The first type of precipitate is distributed mainly along the lath boundaries and the prior grain boundaries to prevent their migration and to suppress recrystallization. The latter precipitate is dispersed within the matrix to hinder the dislocation movement.

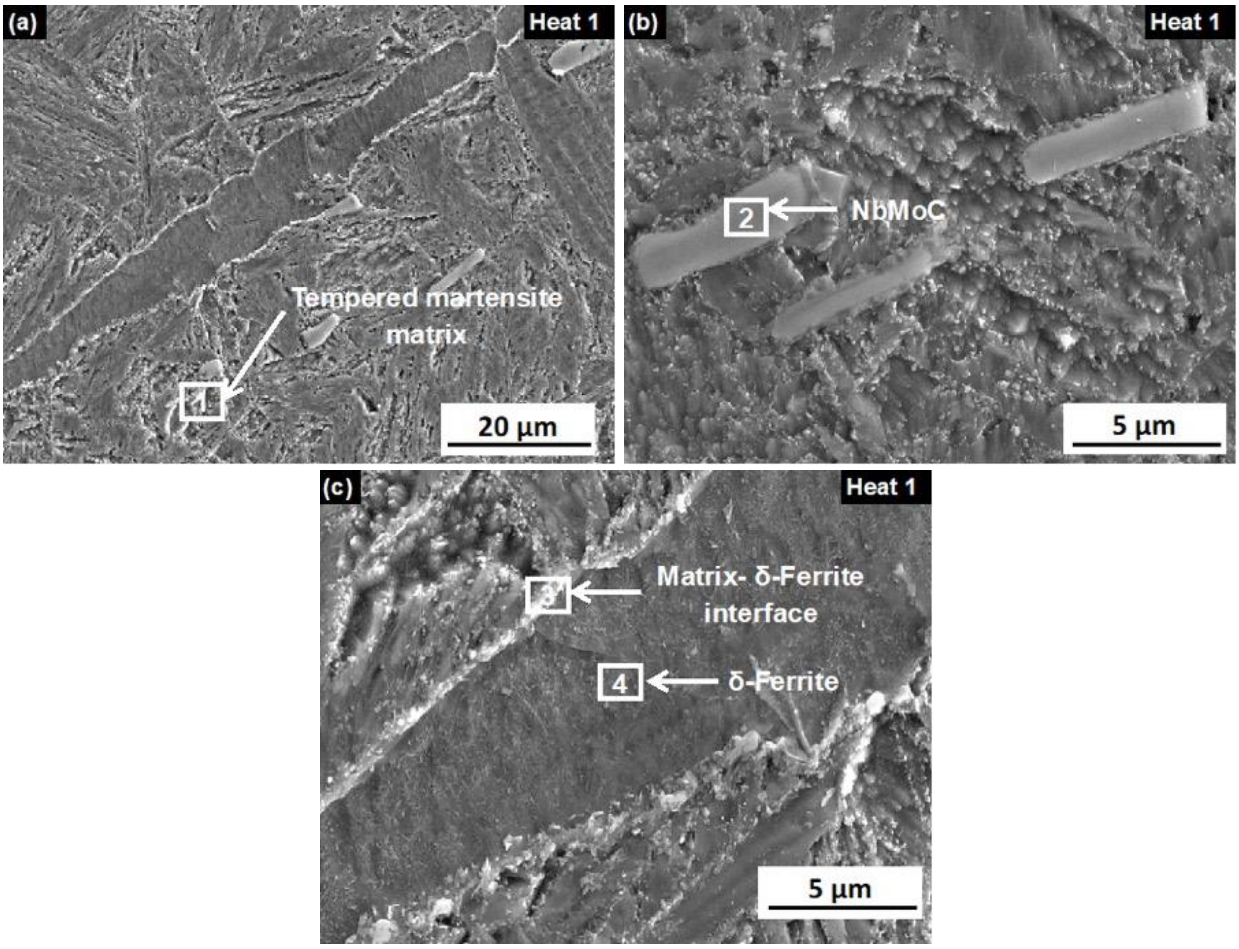

Figure 5.4 FESEM microstructure of 10.7CrMoVNbN steel (Heat 1) with delta-ferrite (a) 5000X, (b) 20000X and (c) 20000X magnifications respectively.

Table 5.4 Composition analysis of energy spectrum on points as marked in Figure 5.4.

Point (Phase)	***Chemical composition (wt. %)***									
	Fe	***Cr***	***Ni***	***C***	***Mn***	***Mo***	***Nb***	***Si***	***V***	***N***
1 (Martensite matrix)	79.58	12.53	00.28	4.77	1.50	0.36	0.23	0.19	0.30	0.25
2 (NbMoC)	63.08	2.88	0.47	12.57	0.43	1.39	63.08	0.09	0.59	3.67
3 (Matrix δ-ferrite interface)	66.55	14.00	0.31	12.93	1.39	2.79	1.22	0.34	0.26	0.21
4 (δ-ferrite)	67.75	9.71	0.60	16.40	0.89	2.44	0.09	0.42	0.30	1.40

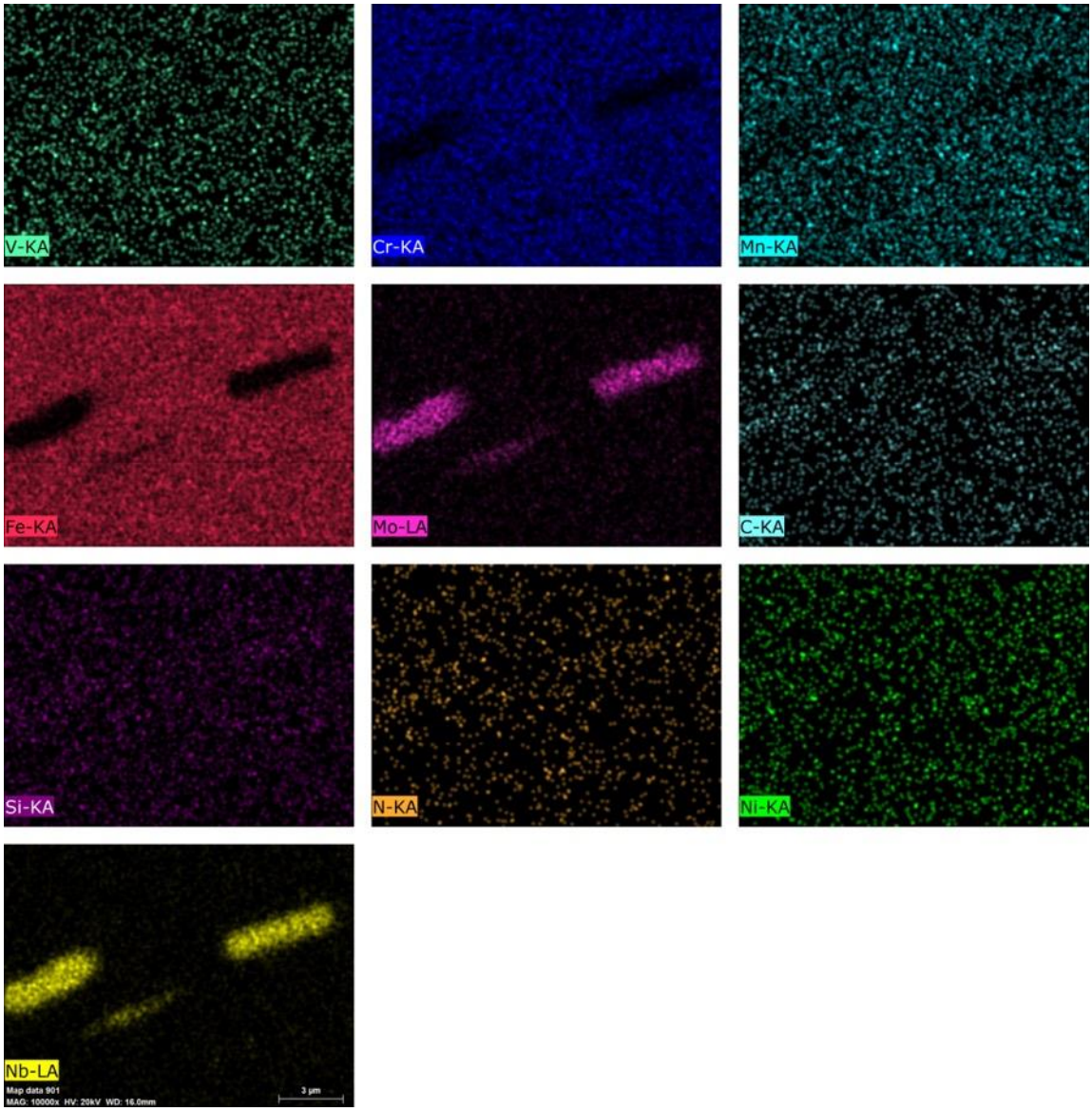

Figure 5.5 X-ray dot mapping of heat 1 (Figure 5.4b) for V, Cr, Ni, Mn, Fe, Mo, C, Si, N, Ni, and Nb elements.

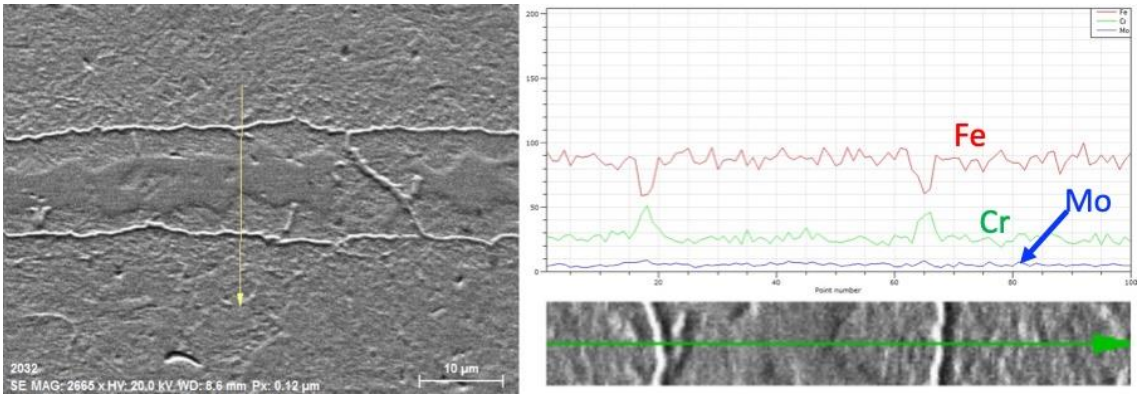

Figure 5.6 Line profiling of Heat 1.

The size and distribution of primary NbMoC is very important to determine the mechanical properties of 10.7CrMoVNbN steel. However, since δ-ferrite was the main reason for the rejection of finished machined turbine blades occurred in magnetic particle inspection which prompted to talk more on ferrite. According to Toshiba specifications, the material failure was largely due to δ-ferrite. According to the supplier specifications, the maximum permissible limit of δ-ferrite in steel was 2% max. The chemical composition of heats was tested by optical emission spectrometer (OES) and the contents of δ-ferrite were checked by grid intercept methods given in AMS2315A. It was observed that calculated and actual values of δ-ferrite were comparable as given in Table 5.3.

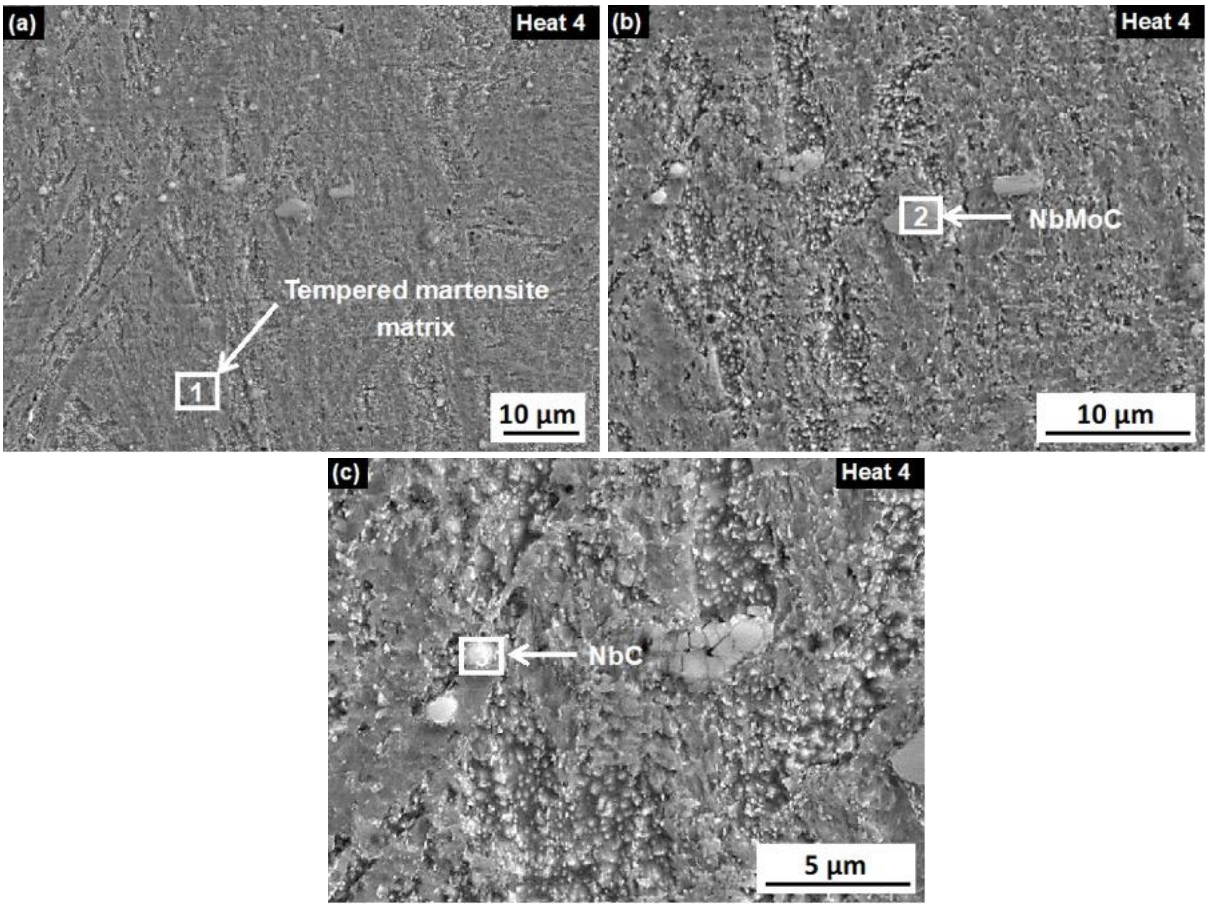

Figure 5.7 FESEM microstructure of 10.7CrMoVNbN steel (Heat 4) without delta-ferrite (a) 5000X, (b) 10000X and (c) 20000X magnifications respectively.

Table 5.5 Composition analysis of energy spectrum on points as marked in Figure 5.7.

Point (Phase)	*Chemical composition (wt. %)*									
	Fe	***Cr***	***Ni***	***C***	***Mn***	***Mo***	***Nb***	***Si***	***V***	***N***
1 (Martensite Matrix)	73.65	10.23	0.26	12.20	1.39	1.15	0.09	0.26	0.11	-
2 (NbMoC)	17.27	2.93	0.63	20.71	0.76	1.14	53.04	0.10	0.86	2.56
3 (NbC)	16.02	3.35	0.26	19.95	0.45	0.81	55.10	0.15	0.99	2.92

5.4 MICROHARDNESS ANALYSIS

Microhardness analysis confirmed the presence of various phases in different heats 1, 2, 3, and 4. Microhardness was performed at a load of 25 gm with the dwell time of 15 seconds. Three distinct phase regions were observed. Delta-ferrite is a very soft phase having a hardness of 278-285 HV. The tempered martensite matrix phase had a hardness of 314-320 HV whereas the hardness of carbides was in the range of 679–691 HV. Table 5.6 presents the microhardness of different phases present in Heat 1, Heat 2, Heat 3, and Heat 4. Figure 5.8 presents the micro indentations taken on various phases.

Table 5.6 Microhardness of tempered martensite matrix, carbide, and δ-ferrite in different Heats.

	Tempered martensite matrix	**Carbide**	**δ-ferrite**
Heat 1	314±5	684±6	285±6
Heat 2	316±7	691±8	278±7
Heat 3	320±9	679±5	-
Heat 4	318±7	681±4	-

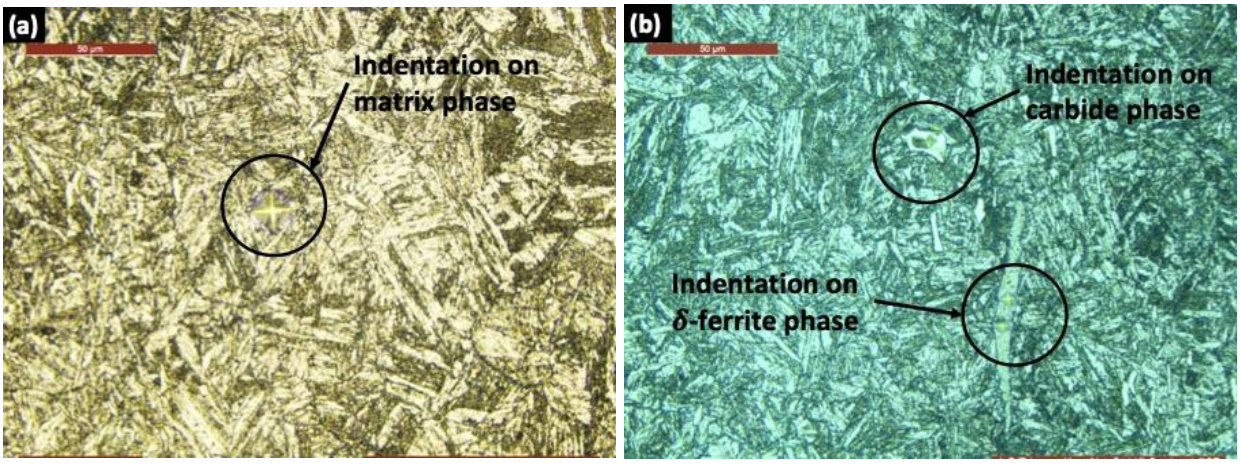

Figure 5.8 Micro indentations on (a) tempered martensite matrix phase and (b) carbide phase and δ-ferrite phase.

5.5 MECHANICAL PROPERTIES

The mechanical properties of all four heats are summarized in Table 5.7. It is observed that there is not much variation in hardness; yield strength (YS), ultimate tensile strength (UTS), and % elongation. However, the impact energy of Heat 3 and Heat 4 is much higher than that of Heat 1 and Heat 2. Lower impact in Heat 1 and hear 2 are due to a higher amount of δ-ferrite.

Table 5.7 Mechanical properties in hardened and tempered condition.

	Hardness (BHN)	**0.02%YS (MPa)**	**UTS (MPa)**	**% Elong.**	**% RA**	**Impact Energy (J)**
Specified value	321 max.	695 min.	970 min.	15 min.	50 min.	11 min.
Heat 1	321±6	906±9	1056±12	17±2	53±3	17±1
Heat 2	321±7	877±8	1028±15	18±2	54±5	19±2
Heat 3	311±8	856±6	1033±13	18±1	55±6	26±3
Heat 4	321±5	879±7	1052±16	19±3	56±4	28±2

Precipitation of delta-ferrite is detrimental to mechanical properties. The second reason is that difference in microstructure and strength between delta-ferrite and martensite matrix would cause stress concentration during deformation. Stress concentration is always favorable to crack formation and crack propagation. Therefore, delta-ferrite promotes the formation and propagation of cracks. Although delta-ferrite has more chromium content nearly 14.7% at its interface with martensite as compared to martensite base matrix, its contribution in deterioration of impact toughness cannot be overruled [174]. Further, Cr_{eq} is a very important factor, so, controlling chromium equivalent to 12 maxima, in this grade of steels has a great influence on the mechanical properties. The Cr_{eq} ratio of each steel is shown in Table 5.1. It can be observed that the Cr_{eq} ratio of Heat 1 and Heat 2 was higher than 12 (12.99 and 12.47 respectively). Thus, lower impact strength was observed. Further, for Heat 3 Cr_{eq} was 12.05 hence, higher impact strength was observed. Heat 4 presented superior mechanical properties. The Cr_{eq} ratio observed for Heat 4 was lower than 12 (11.59). This indicated that lower Cr_{eq} (lower than 12) improved the mechanical properties of the steel.

CHAPTER 6
RESULTS AND DISCUSSION
AISI-321 STEEL

OVERVIEW

AISI 321 steel is commonly used for inlet and outlet tubes of Voda Voda Energo atomic Reactor (VVER). The steel usually works in the temperature range of 291^{o}C to 321^{o}C. AISI 321 steels are generally stabilized with titanium. Titanium leads to the formation TiC, TiN, and TiCN. These have high stability as compared to chromium carbides. To further enhance high temperature resistance, boron is added to the AISI321 steel. Boron leads to the formation of metal borides which have a high temperature stability. In the present study, a processing route has been described to develop titanium and boron stabilized AISI 321 steels. This chapter presents the details of FESEM and optical microstructure of AISI-321 steel. Next, the chapter discusses the mechanical properties of AISI-321 steels at room temperature and elevated temperatures. The chapter also discusses the fractrography analysis of steel after tensile testing and impact testing. Finally, the sensitization study was also carried out on the AISI-321 steel.

6.1 AISI321 STEELS

6.1.1 SELECTION CRITERIA

It is learnt from the literature that AISI 321 should possess the excellent properties to meet the Voda Voda Energo atomic Reactor (VVER) requirement. Hence, optimum amount of Ti and B were selected followed by solution annealing and stabilization treatment at suitable temperature. To observe the effect of residual Ti on microstructure and mechanical properties, Ti was kept slightly higher than minimum theoretical requirement (% Ti= [5 × (C + N)). B was chosen 30 PPM which helps in strengthening the grain boundaries in order to raise creep rupture strength. After that material was subjected to tensile test at room temperature and elevated temperature (100 ℃, 200 ℃, 350 ℃, 500 ℃, 650 ℃, 800 ℃ and 950 ℃; soaking time of 30 minutes) conditions. The inlet and outlet water tubes of a VVER reactor work in temperature range of 291–321℃, thus 350 ℃ is the design temperature. Short-time tensile properties are most important selection criterion up to 482 ℃ working temperature where austenitic stainless steel behaves in elastic manner. Therefore, yield point determined by short-time tensile test becomes a major factor than creep [119]. Since, the operating temperature range of water tube in VVER reactors is 291–321℃ which is less than 0.5Tm (Tm melting temperature of the steel in Kelvin) so creep testing was not included in this study [175]. Titanium stabilized AISI 321 was also sensitized at 350 ℃ and 675 ℃ and for 100 hours to observe the long duration structure-properties-performance correlation.

6.1.2 STARTING MATERIAL

Two different types of titanium stabilized austenitic steel (AISI 321) were prepared at M/S Star Wire (India) Ltd. Ballabgarh, Haryana. AISI 321 steels without boron (1 ppm) and with boron (30 ppm) are designated as TB1 and TB30 respectively. Steel compositions were designed for no delta-ferrite after solidification by balancing Ni_{eq} and Cr_{eq} and Ti (wt. %) was selected as [5 × (C + N)] % minimum. Materials were prepared by following air melting route (electric arc furnace (EAF) → argon oxygen decarburization (AOD) → vacuum degassing (VD) → ladle refining furnace (LRF) → electrode casting) followed by electro slag remelting (ESR) to achieve an ingot of 600 mm dia. Table 6.1 presents the chemical composition of primary ingots TB1 and TB30 AISI 321 steels.

Table 6.1 Chemical composition of secondary melted Ti stabilized AISI 321 steel.

Steel	C	Si	Mn	P	S	Cr	Mo	Ni	Ti	B	N	Fe
TB1	0.079	0.700	1.720	0.021	0.002	17.59	0.248	10.75	0.45	0.0001	0.010	Bal.
TB30	0.078	0.695	1.714	0.021	0.002	17.57	0.247	10.78	0.46	0.0030	0.011	Bal.

6.1.3 MANUFACTURING

ESR ingot corresponding to TB1 and TB30 heats were forged to 100 mm round cornered square (RCS) billets. After surface grinding, the billets were charged in pusher type reheating furnace for rolling where soaking and homogenization was done for two hours at 1220 ℃. Temperature of the reheated billets was checked by infra-red temperature gun before entering to first rolling pass. Temperature was observed in the range of 1180–1190 ℃. Rolling mill configuration was 18-inch three high cross-country mill two stands (4 passes) + 12-inch three high cross-country mill four stands (8 passes) +12-inch three high continuous mill with four stands (4 passes). Total sixteen passes were used to roll the billet in 17 mm diameter and finishing temperature was attained in the range of 940–960 ℃. Table 6.2 presents the methodology used for the sample preparation in the present study.

Table 6.2 Sample preparation process flow diagram for AISI 321 TB1 and TB30.

S. No.	Activity description
1	Primary electrode dia. 480 mm casting after primary melting
2	ESR of 480 mm dia. electrode into 600 mm dia. ESR ingot, 2700 mm long weight about 6000kg
3	Top, bottom end discarding and surface grinding
4	Heating to 1200^0C and homogenizing for 12.5 hrs. @ 30 minutes /25 mm, followed by forging to semis in following steps
4a	Upsetting from 2700 mm to 1350 mmx850 mm dia.
4b	Drawing after turning 90^0 to 600 mm dia. x2700 mm length
4c	Reheating to 1180^0C and forging to 170 mm square
4d	Rolling to 17 mm dia. in a three high continuous rolling mill
4e	Solution annealing at 1050 ℃/30 minutes followed by water quenching and collecting samples of TB1 and TB30 in multiple of 4-meter-long bars

6.1.4 HEAT-TREATMENT

In order to observe the influence of heat-treatment on microstructure and mechanical properties of rolled product, 17 mm rolled bars were also prone to solution annealing at 1050 ℃ for 30 minutes followed by water quenching. Soaking time is given according to AMS 2759/4C standard [176]. Thereafter, stabilization treatment (860 ℃/4 hrs. → Air Cooling) was also given to TB1 and TB30 steels. To observe the influence of different microstructures on the mechanical properties of TB1

and TB30 steels, samples of three different conditions were taken. In the present study the TB1 and TB30 steels under as-rolled, solution annealed, and solution annealed+ stabilization treated samples are termed as AR, SA, and ST respectively.

6.1.5 EVALUATION OF SENSITIZATION/CORROSION RESISTANT

Corrosion resistance of TB1 and TB30 is evaluated in SA and ST condition according to ASTM A262 standard [161]. Samples of SA and ST condition were sensitized at 675 ℃ for 1 hr following practice A and practice E. In practice A, samples were prepared according to standard metallographic practice and then electrolytically etched in 10 % oxalic acid solution to compare step, dual and ditch type structure according to ASTM A262 standard. Thereafter, in another set of experiments, finely polished TB1 and TB30 steel samples of SA and ST conditions were sensitized at 675 ℃ for 1 hr. and evaluated by following the procedure called practice E. In this case first the samples were boiled in copper-coppersulphate+16 % sulfuric acid solution for 15 hrs. followed by bending the samples at 180°. Samples of TB1 and TB30 in SA and ST conditions were also sensitized at 675 ℃ and 350 ℃ for long soaking time of 100 hrs. followed by air cooling to observe the corrosion for long time exposure at sensitizing temperatures.

6.2 FESEM-EDS ANALYSIS

Figure 6.1 and Figure 6.2 presents the FESEM images of TB1 and TB30 steels under solution annealed condition respectively. Optical micrographs showed the presence of precipitates of different shape and sizes. However, based upon the optical microscopy it is not possible to identify different precipitates. Thus, to quantify various precipitates in TB1 and TB30 steels, FESEM and EDS analysis was performed. Figure 6.1 presents the FESEM-EDS analysis of TB1 steel under solution annealed condition. As shown in Figure 6.1a uniform distribution of precipitates was observed for TB1 steel. Figure 6.1(b–d) presents the high magnification FESEM images showing enlarged images of carbides. The carbides have been marked with 1-6. EDS analysis was carried out on the respective points marked as 1-6. EDS analysis demonstrated that TB1 steel contained titanium nitride (TiN) and carbide $M_{23}C_6$ (where M=Cr and Fe) and titanium carbonitride (TiCN). The chemical composition of the phases in the microstructure are given in Table 6.3. Round corner square shape precipitate was observed as TiN having the higher N/Ti ratio. TiCN precipitate was

also observed in the structure having almost equal N/Ti and C/Ti ratios. Some amount of $M_{23}C_6$ carbide is also found at the grain boundary.

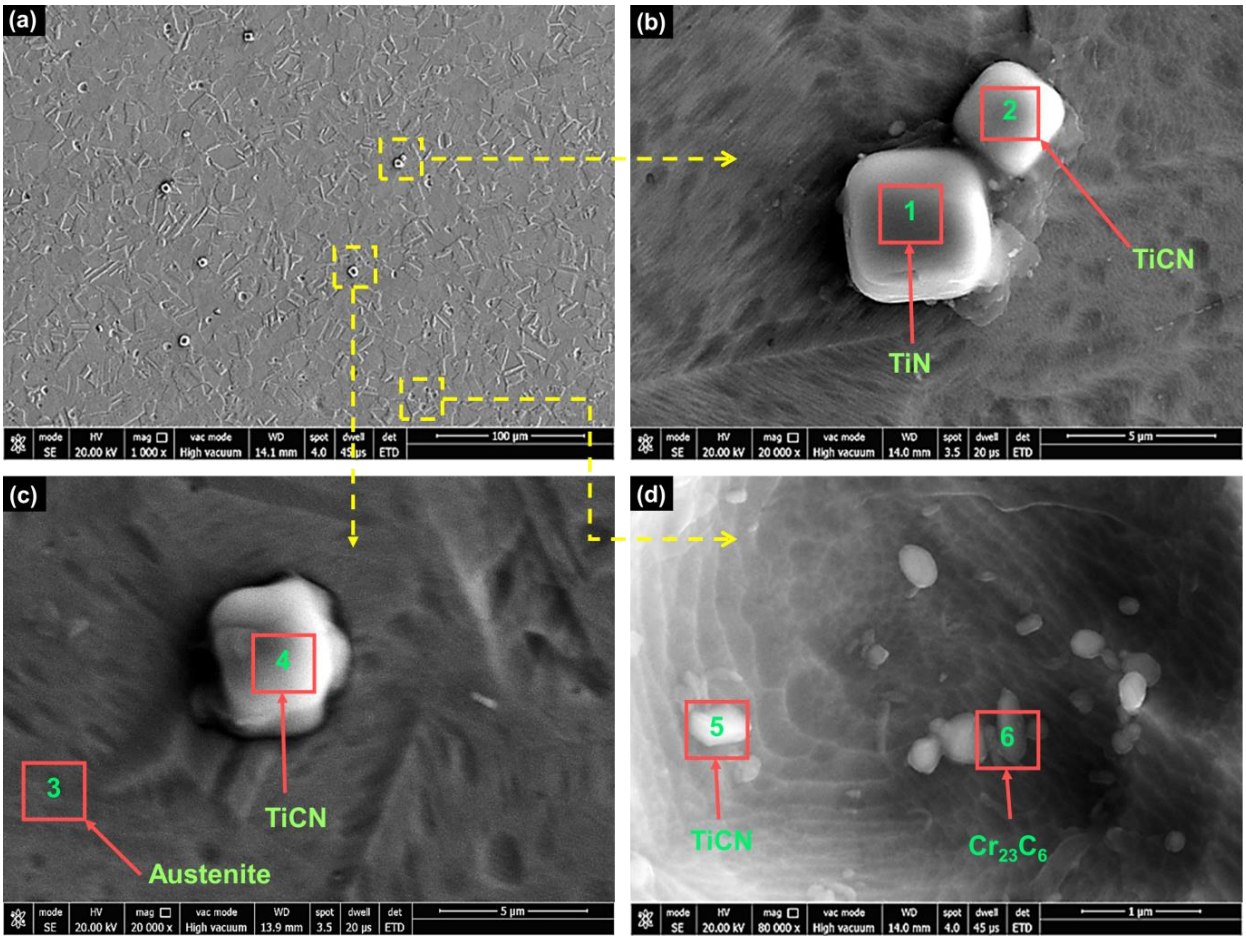

Figure 6.1 FESEM microstructure of SA TB1 steel (a) 1000X, (b) 20000X, (c) 20000X and (d) 80000X magnifications respectively.

Table 6.3 Composition analysis of energy spectrum on points as marked in Figure 6.1.

Phase	Chemical composition (wt. %)									
	Fe	**Cr**	**Ni**	**C**	**Mn**	**Mo**	**Ti**	**Si**	**V**	**N**
Austenite	63.14	18.82	9.25	4.01	2.44	1.31	0.34	0.32	0.26	0.10
TiCN	2.12	1.21	0.34	14.59	0.14	1.10	65.56	0.08	0.52	14.33
TiN	1.86	0.94	0.30	3.30	0.20	0.73	71.56	0.08	0.25	20.77
$Cr_{23}C_6$	14.14	57.84	9.38	14.25	2.05	0.72	0.68	0.34	0.06	0.53

Figure 6.2 shows the FESEM micrographs of TB30 steel under solution annealed condition. The austenite grain size observed for TB30 steel is finer than TB1 steel (Figure 6.1a and Figure 6.2a). Larger number of precipitates were observed for TB30 steels as compared to TB1 steel. The

precipitates for TB30 steels are generally located at the grain boundaries. Figure 6.2b-c presents the magnified FESEM images showing various precipitates. Different precipitates are marked as 1,2, and 3. EDS analysis was carried out on these particles. Chemical composition of the phases in the microstructure is given in Table 6.4. TiN, TiCN precipitates along with large number of borides Fe_2B and Cr_2B precipitates was observed. In this structure borides Fe_2B and Cr_2B precipitates are also seen along with TiN and TiCN. It is due to the addition of boron. The formation of Fe_2B and Cr_2B borides has led to increase in yield strength stability of service components at an operating temperature of 350 ^oC (discussed later).

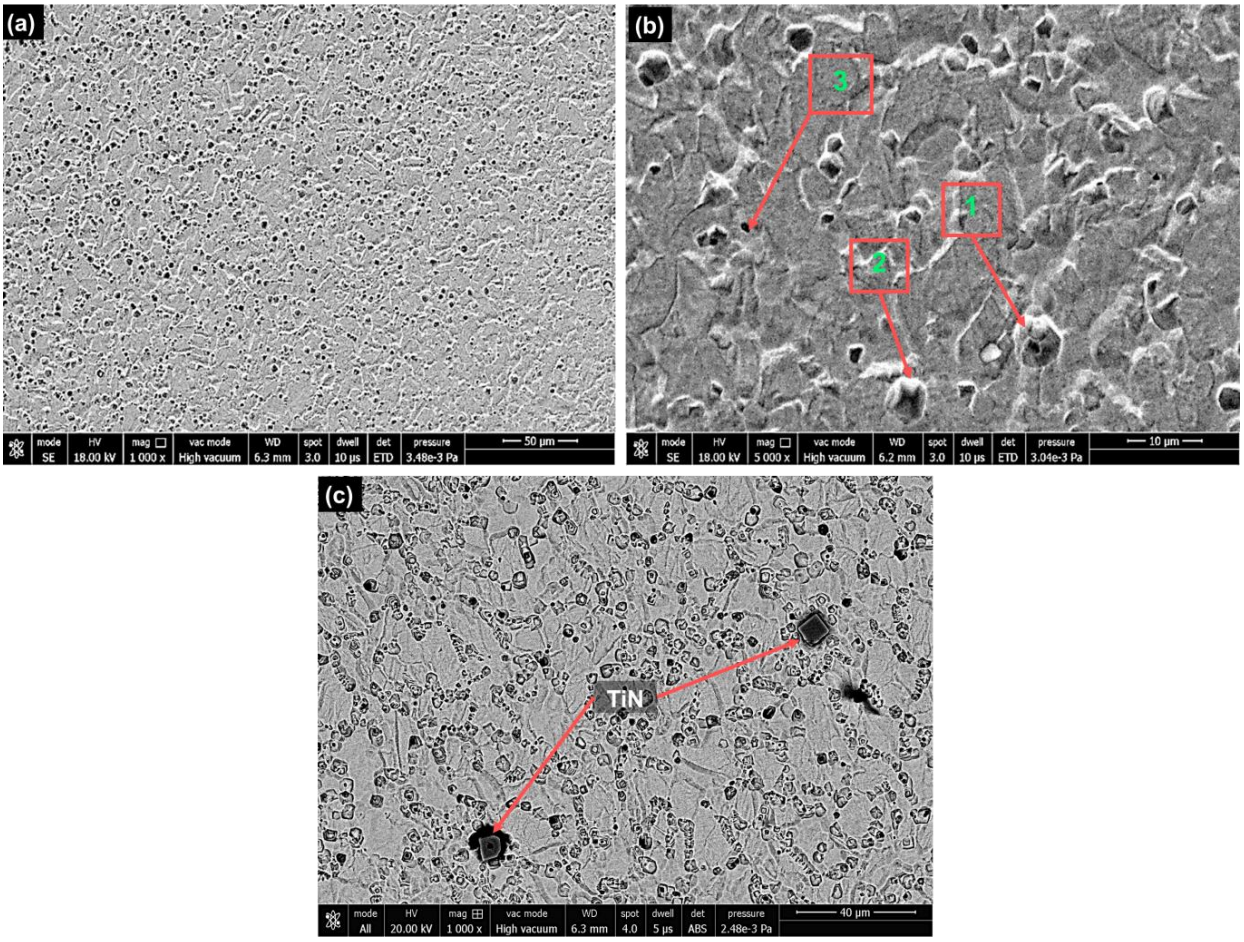

Figure 6.2 FESEM microstructure of SA TB30 steel (a) 1000X, (b) 5000X and (c) 1000X magnifications respectively.

It can be clearly seen from the FESEM microstructures (Figure 6.1 and Figure 6.2) that TB30 steel exhibits population of borides (Cr_2B/Fe_2B) along with TiN/TiCN precipitates. The number of precipitates is much higher compared to TB1 steel where only TiN and TiCN precipitates exist.

These findings are in tune with the earlier report by Hafez et. al. [15] done on titanium-boride modified SS-316 steel.

Table 6.4 Composition analysis of energy spectrum on points as marked in Figure 6.2.

Point (Phase)	Chemical composition (wt. %)										
	Fe	**Cr**	**Ni**	**C**	**Mn**	**Mo**	**Ti**	**Si**	**V**	**N**	**B**
1 (Fe_2B/Cr_2B)	37.00	10.17	4.98	13.13	1.44	1.48	**10.66**	0.28	0.31	**2.24**	**18.30**
2 (Fe_2B/Cr_2B)	37.62	9.85	5.23	**22.25**	1.65	0.23	**1.17**	0.44	0.17	**1.43**	**17.05**
3 (Fe_2B/Cr_2B)	53.98	14.43	6.20	1.84	2.93	0.56	1.26	0.39	0.45	0.23	17.73

6.3 MICROSTRUCTURE STUDY OF PROCESSED STEELS

6.3.1 AS-ROLLED MICROSTRUCTURE

As-rolled microstructures of TB1 and TB30 steels are shown in Figure 6.3. It can be seen that both steels comprise of very fine austenite grains along with precipitates of carbides, nitrides and carbonatites. It could be due to the thermomechanical processing with higher reduction ratio, which provides the driving force for recrystallization of grains.

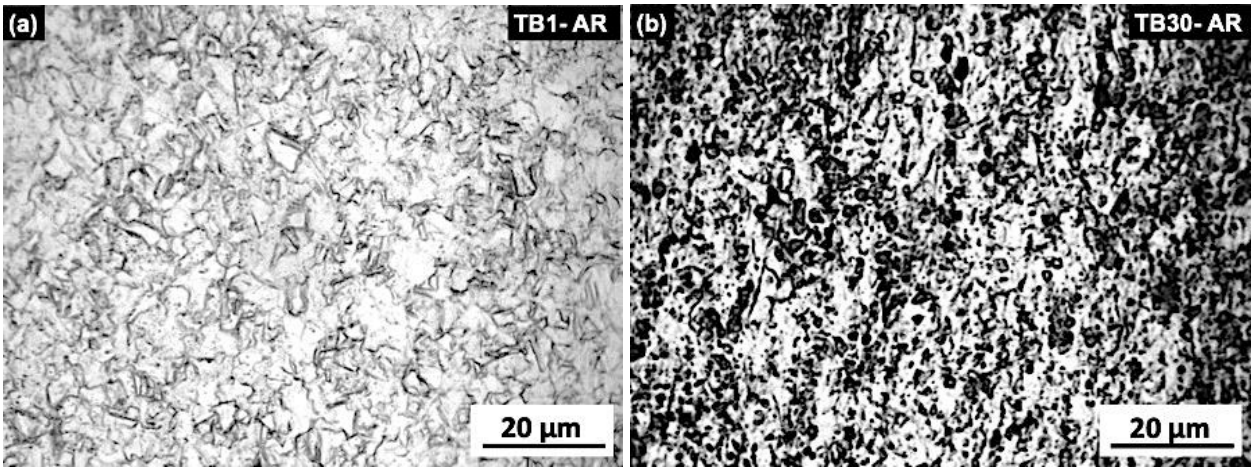

Figure 6.3 Optical microstructure of as-rolled (a) TB1 steel and (b) TB30 steel.

Table 6.5 summarizes the volume fractions of precipitates and average size of austenite in TB1 and TB30 steels. It can be observed that the amount of precipitates are slightly higher in TB30 compared to TB1 steel. Carbon and nitrogen as interstitial elements in TB1 and TB30 steels promote the formation of titanium precipitates such as nitrides, carbides and carbonatites. Chromium carbide ($Cr_{23}C_6$) may also precipitate at grain boundary during cooling of rolled bars

in TB1 steel. In addition, the boron present in TB30 steel may also precipitate as M_2B (M = Fe, Cr). Such type of boride is also observed in SS316 with 40 PPM of boron [177].

Table 6.5 Volume fraction of precipitates and average austenite grain size of TB1 and TB30 steels in different treatment conditions.

Steel	Volume fraction of precipitates (%)			Austenite grain size (ASTM No.)		
	AR	***SA***	***ST***	***AR***	***SA***	***ST***
TB1	11.35	14.21	19.42	13	12	10
TB30	13.48	15.05	23.63	13	13	13.5

6.3.2 SOLUTION ANNEALED MICROSTRUCTURE

Figure 6.4 shows the microstructure after solution treatment. Here grains are more pronounced as compared to rolled steels indicating that chromium carbide is dissolved. Average grain size also increased through the coarsening process, thereby decreasing the density/population of the precipitates and increasing the average distance between the precipitates.

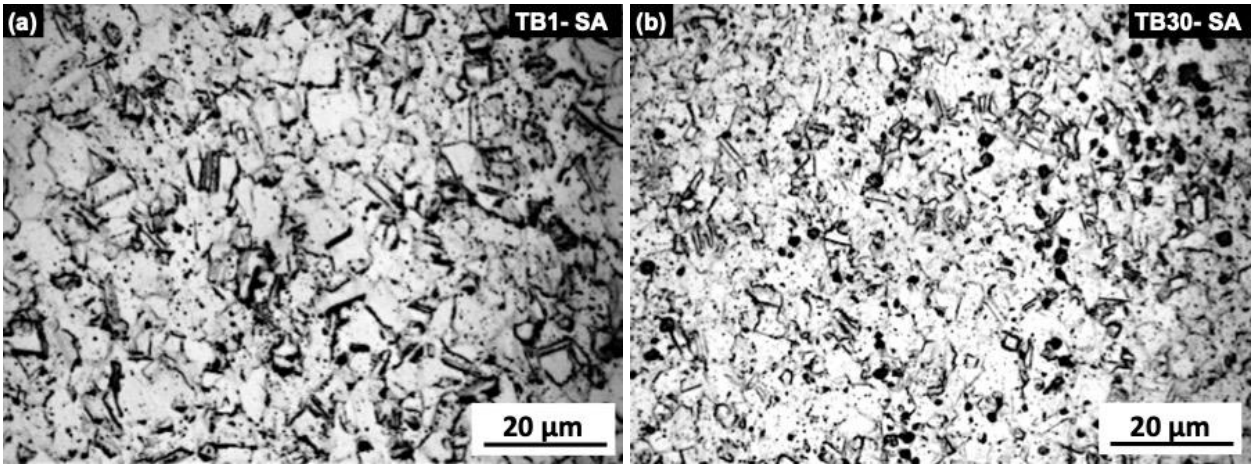

Figure 6.4 Optical microstructure of solution annealed (a) TB1 steel and (b) TB30 steel.

It was observed that the volume fraction of the precipitates decreases as compared to the as-rolled structure due to its part dissolution into the matrix after gaining the required energy. Slightly coarse grains in comparison to as-rolled steels are observed, which indicate that grain growth has occurred at this temperature. However, grains in TB30 steel are finer than that of TB1 steel. It is already reported that considerable enrichment of boron exists at the grain boundary after cooling from the solution temperature of 1050^0C at a cooling rate of 60 ℃/s [22,178–180].

6.3.3 MICROSTRUCTURE AFTER STABILIZING TREATMENT

Figure 6.5 demonstrates the microstructure after solution treatment followed by stabilizing treatment.

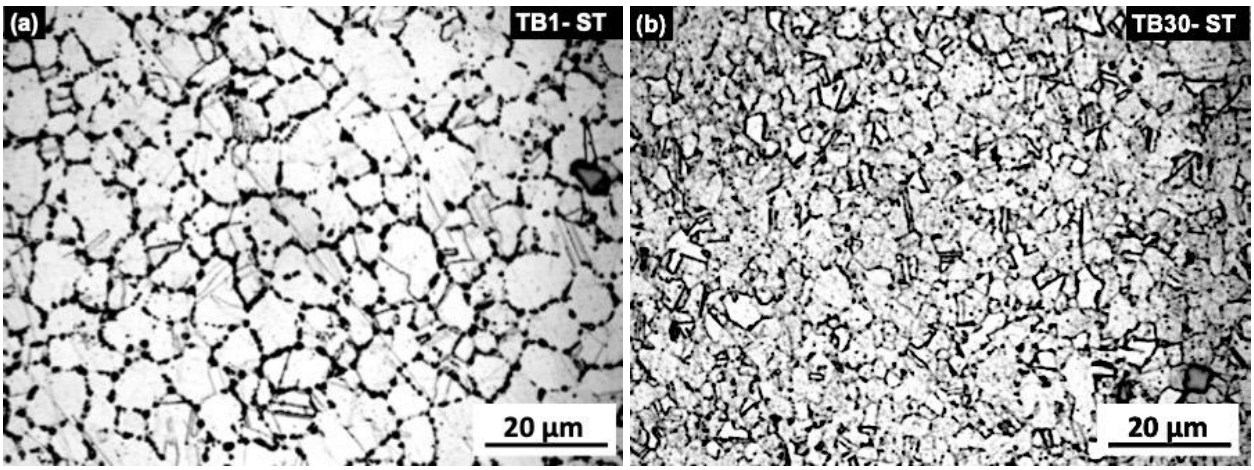

Figure 6.5 Optical microstructure of stabilizes treated (a) TB1 steel and (b) TB30 steel.

It is observed that stabilizing treatment bound the carbon by forming titanium carbides. It can be confirmed from the volume fraction of precipitates which is increased after stabilizing treatment compared to solution annealed condition. It is interesting to note that grain growth is restricted due to the pinning effect of precipitates. Higher amount of precipitates in TB30 steel results in fine grain size than TB1 steel due to pinning effect.

6.4 ANALYSIS OF PRECIPITATE COUNTS

Figure 6.6 presents the quantitative analysis of average count and size of precipitates for forged, rolled, and solution annealed conditions. A substantial difference in the precipitate count was observed for both TB1 and TB30 steels under all the given conditions. The count of smaller precipitates i.e. size in the range of 1-10 μm^2 is much higher in all conditions. It is due to the low finishing temperature during the forging and rolling, which promotes the precipitation of secondary phases [112]. It is also observed that precipitate count of 10-20 μm^2 decreased from AR to SA to ST condition. Presence of precipitates influence the mechanical properties of the steels as they hinder the dislocation movement [120,121]. From Figure 6.6b and Figure 6.6c, it can be seen that, TB30 steel has a substantial higher number of precipitates count in comparison to TB1 steel. TB1 steel exhibits the TiN and TiCN precipitates. In addition to this, in TB30 steel the boron

addition also leads to the formation of Fe_2B and Cr_2B precipitates [177,181]. Thus, TB30 steel has a higher count of precipitates when compared to the TB1 steel.

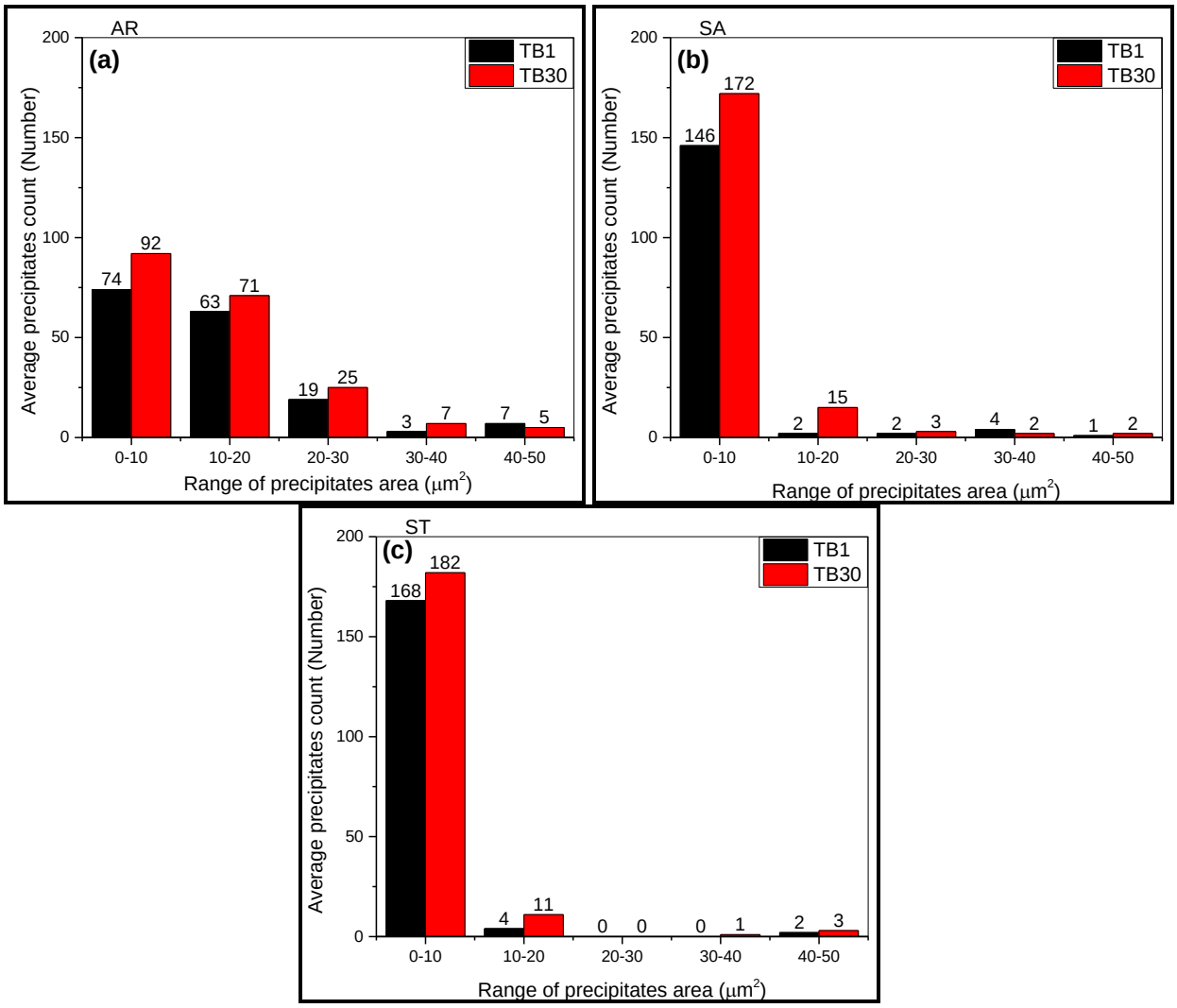

Figure 6.6 Average values of the precipitates count with respect to precipitates area observed per image field in (a) AR, (b) SA, and (c) ST of TB1 and TB30 steels.

Further, the optical micrographs of TB1 and TB30 steel in unetched condition are also presented in Figure 6.7. The concentration of precipitates is slightly higher in TB30 steel when compared to TB1 steel. Carbon and nitrogen as interstitial elements in TB1 and TB30 steels promote the formation of titanium nitride (TiN) and titanium carbonitride (TiCN) precipitates. Addition of titanium to the steels prevents the formation of $Cr_{23}C_6$ precipitates. This prevents the depletion of chromium from the matrix of AISI 321 steels. Precipitates of boron are insoluble in steels at all temperatures [21]. Thus, a fine distribution of Fe_2B and Cr_2B precipitates in TB30 steel may lead

to an increase in the service life of inlet and outlet tubes of VVER type nuclear reactor [123]. Addition of boron to the steel has also led to the fine and uniform distribution of precipitates as shown in Figure 6.7b.

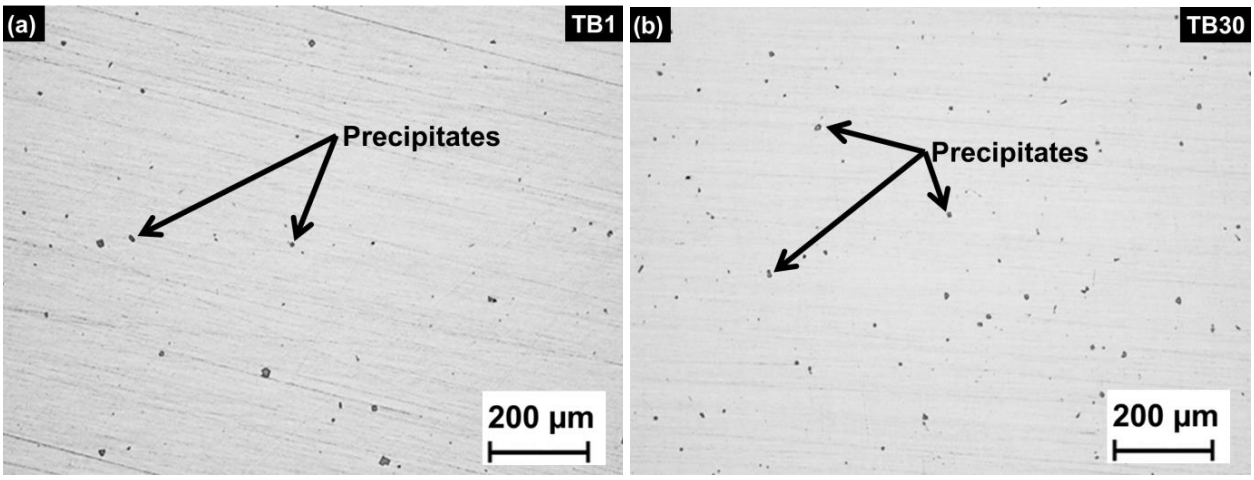

Figure 6.7 Optical microstructure of forged (a) TB1 steel and (b) TB30 steel in as-polished condition.

6.5 MECHANICAL PROPERTIES

In the present investigation mechanical testing was performed on TB1 and TB30 steel in forged, rolled, and solution annealed condition on 17 mm sized rods. Figure 6.8 presents the engineering stress-strain curves for TB1 and TB30 steel under AR, SA, and ST conditions at room temperature. Table 6.6 presents the mechanical properties of TB1 and TB30 steels in AR, SA, and ST conditions at room temperature. Addition of boron to the steel increased the yield strength (YS) and ultimate tensile strength (UTS) of the steels. YS of TB30 steel in AR, SA, and ST conditions improved by 19%, 20%, and 12% over TB1 steel respectively. Whereas, the improvement in UTS observed for AR, SA and ST conditions was 5%, 8%, and 7% over TB1 steel respectively. For TB30 steel, a marginal decrease in percentage elongation, retained austenite (RA) percentage, and hardness was observed over TB1 steel.

The VVER type nuclear reactor components work at 350^{o}C which require high yield strength at elevated temperature. AISI 321 steel is solution annealed to enhance the corrosion resistance and yield strength during performance. Thus, mechanical testing of AISI 321 steels at the elevated temperature of 350 ^{o}C is essential. Figure 6.9 presents the engineering stress-strain diagram of TB1 and TB30 steel at AR, SA, and ST condition at elevated temperature of 350 ^{o}C.

Table 6.6 Room temperature mechanical properties of TB1 and TB30 steels.

Steel	Condition	Hardness (BHN)	0.2%Y.S. (MPa)	U.T.S. (MPa)	Y.S/U.T.S Ratio	% Elong.	% RA
TB1	AR	160±6	286±9	630±15	0.45	56	76
	SA	290±8	229±11	579±12	0.40	61	78
	ST	250±7	222±8	576±16	0.39	60	79
TB30	AR	150±7	341±5	662±13	0.52	48	73
	SA	265±4	275±6	625±12	0.44	52	75
	ST	220±8	248±7	616±12	0.40	53	74

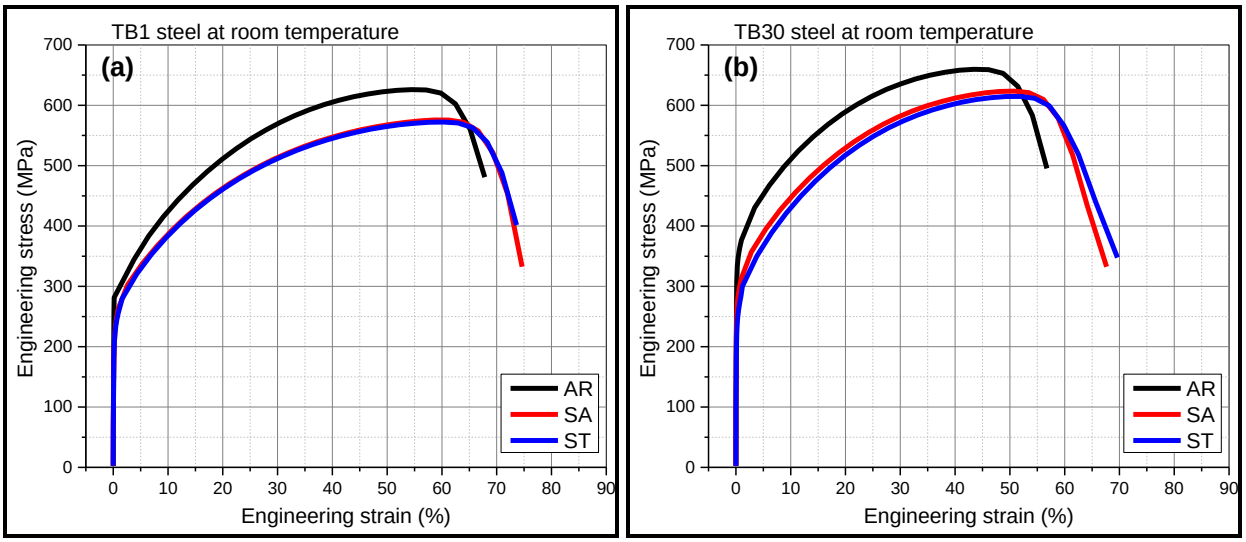

Figure 6.8 Engineering stress-strain curves of (a) TB1 steel and (b) TB30 steel at room temperature condition.

Table 6.7 presents the mechanical properties of TB1 and TB30 steels in AR, SA and ST conditions at elevated temperature of 350 ^{o}C. Addition of boron to the steel has led to the improvement in yield strength of steels. YS of TB30 steel in AR, SA, and ST conditions improved by 17%, 8%, and 21% over TB1 steel respectively. Whereas, the improvement in UTS observed for AR, SA and ST conditions was 4%, 4%, and 6% over TB1 steel respectively. Percentage elongation of TB30 steel was lower than TB1 steel in all conditions. For both room temperature and elevated temperature conditions the YS and UTS of TB30 steel in all conditions was higher than the YS of TB1 steel. This could be attributed to the precipitation strengthening of TB30 steel as the TB30 steel revealed a higher precipitate count in comparison to TB1 steel. In addition to this, addition of boron led to the formation of precipitates of Fe_2B, Cr_2B, TIN, and TICN which restricts the dislocation movement and causes an increase in yield strength of TB30 steel.

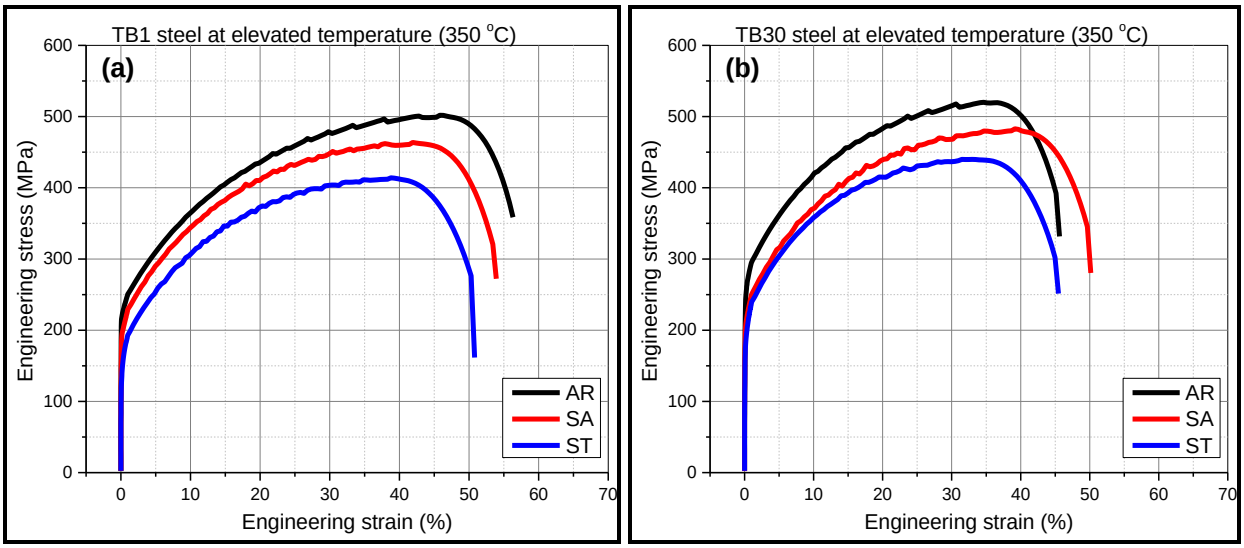

Figure 6.9 Engineering stress-strain curves of (a) TB1 steel and (b) TB30 steel at elevated temperature of 350 ℃.

Table 6.7 Elevated temperature tensile properties of TB1 and TB30 steels at 350 ℃ for different conditions.

Steel	Condition	0.2%Y.S. (MPa)	U.T.S. (MPa)	Y.S/U.T.S Ratio	% Elongation	% RA
TB1	**AR**	225±9	501±14	0.45	46	70
	SA	201±13	466±12	0.43	45	73
	ST	163±6	416±8	0.39	41	75
TB30	**AR**	262±12	521±11	0.50	41	71
	SA	216±11	484±14	0.45	42	69
	ST	198±7	441±11	0.45	40	68

YS to UTS ratio for both TB1 and TB30 steels was calculated for all conditions at room temperature and elevated temperature. At room temperature, YS to UTS ratio of TB30 steels at elevated temperature under rolled and solution annealed condition was similar to those observed for room temperature at same conditions (Table 6.6 and Table 6.7). Lower YS to UTS ratio signifies higher work hardening rate of the steel. YS to UTS ratio of the steels remained nearly constant indicating better yield strength stability at elevated temperatures. Also, with lower YS to UTS ratio higher factor of safety can be observed. This indicated an increase in the service life of component and also lowers the probability for failure of the components at elevated temperatures. For nuclear reactor applications high strength at elevated temperatures is required. Addition of boron to Ti stabilized AISI-321 steel which is already being used in the nuclear power plants, has provided higher strength at room temperature as well as at elevated temperature [123,182]. Lower YS to UTS ratio improves the work hardening rate and yield strength stability of the steel. The

main reason behind this difference is the existence of different interfaces within the steel structure. In TB30 steel boron being an additional element gets precipitated mostly along the grain boundaries, and creates relatively higher hindrance for recrystallization and dislocation movement. Further, for AR, SA, and ST TB30 steel the strength parameters are much higher than TB1 steel. This is because for these conditions the specimens were air cooled so the recrystallication has occurred. This has promoted the process of recrystallization and has fine distribution of precipitates. Since, the number count of these precipitates in SA and ST condition is high so obstacle for dislocation motion is higher. Because of these reasons, the strength parameter for TB30 steel at higher temperature is more compared to TB1 steel. Thus, SA and ST TB30 steel is more suitable material to replace the inlet and outlet water tubes of VVER type nuclear reactor.

Elevated tensile testing at room temperature (RT), 100 ℃, 200 ℃, 350 ℃, 500 ℃, 650 ℃, 800 ℃ and 950 ℃ were also carried out. Figure 6.10 presents the yield strength and % elongation of TB1 and TB30 steel at ST condition as a function of temperature. For solution annealed and stabilized treated TB1 and TB30 steel, it can be seen that TB30 steel shows high yield strength at all testing temperature as compared to TB1 steel, which could be attributed to fine austenite grain along with large number of precipitates along the grain boundaries and also within the grain (Figure 6.10a). For nuclear reactor applications high strength at elevated temperatures is required. Next, for % elongation, there is not much variation is observed for TB1 and TB30 steel up to 650 ℃. Thereafter TB30 steel showed high % elongation than TB1 steel up to 950 ℃ (Figure 6.10b).

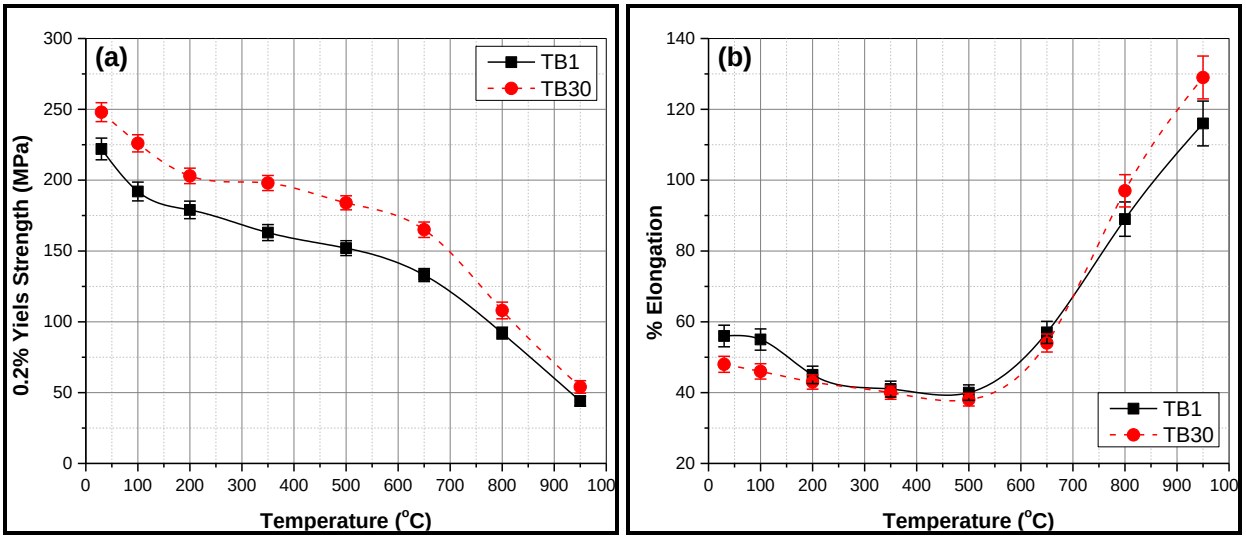

Figure 6.10 (a) 0.2% yield strength and (b) percentage elongation as a function of temperature for TB1 and TB30 steel under ST condition.

6.6 CORRELATION BETWEEN MECHANICAL PROPERTIES AND FRACTURE SURFACE

Figure 6.11 presents the SEM analysis for tensile fractrographs of TB1 and TB30 steel in ST condition at room temperature. The fractrographs at room temperature depicts the dimple like structure indicating the ductile failure of TB1 and TB30 steel. The dimple size is governed by number of factors viz. precipitate size, shape and distribution an also on the microvoids that are nucleated in the steel. When void nucleation sites are few and widely spaced, the microvoids grow to a larger size before coalescence giving rise to the appearance of a fracture surface containing large dimples. The size of dimples observed for TB1 steel was larger than that of the TB30 steel (Figure 6.11a and Figure 6.11b).

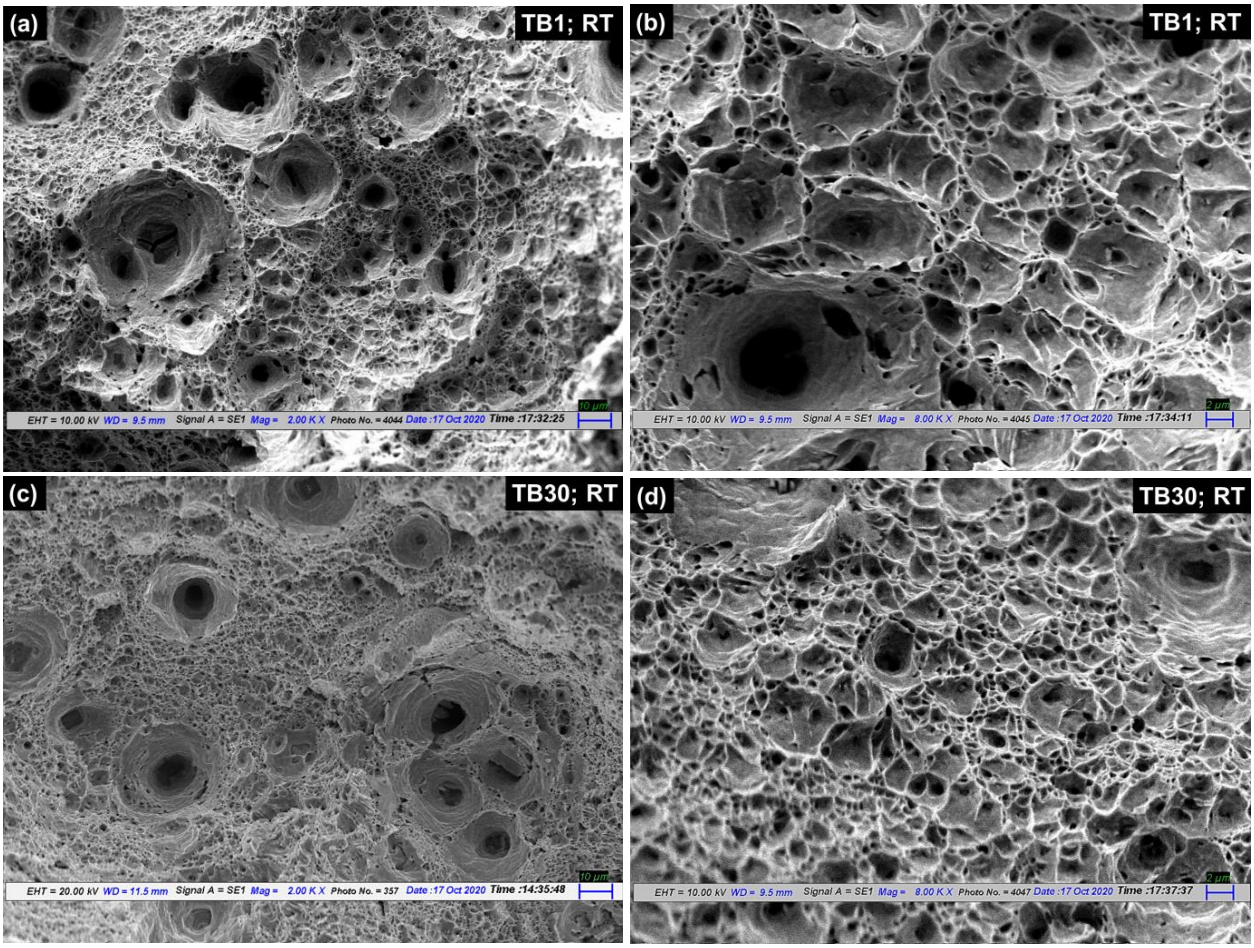

Figure 6.11 FESEM analysis of tensile fractrographs of (a) TB1 steel at 2000X, (b) TB1 steel at 8000X, (c) TB30 steel at 2000X, and (d) TB30 steel at 8000X magnification under ST condition at room temperature.

The larger size dimples of TB1 steel indicate higher ductility of TB1 steels. Small and shallow dimples are formed when a large number of precipitates/voids are activated and adjacent microvoids join before they grow into a large size. The shape of the dimple is primarily governed by the internal stress in the material and also on the formation of the microvoids. The small dimples observed for TB30 steel could be the resultant of the localized deformation between the precipitates and the void nucleation sites while the size of the final dimple is dependent upon the inter precipitate distance in the matrix of TB30 steel (Figure 6.11c and Figure 6.11d). For TB30 steel sample higher number of precipitates was observed (Figure 6.6). Thus, the growth of voids is restricted to small size. The deformation along the particle occurs due to the particle shearing. This gives rise to the localized deformation near the precipitates and as a result small and shallow dimples are observed along the fracture surface.

Figure 6.12 presents the FESEM fractographic analysis of tensile specimen of TB1 and TB30 steel under ST condition at elevated temperature of 350 ℃. The fracture is mainly of ductile nature with the formation of microvoids and spread transgranular by coalescence. Large size dimples are observed for TB1 steel as compared to TB30 steel (Figure 6.12). For TB30 steel, finer and shallow dimples are observed (Figure 6.12b). The fracture results observed in the study compliment the fracture characteristics of TB1 and TB30 AISI 321 steels.

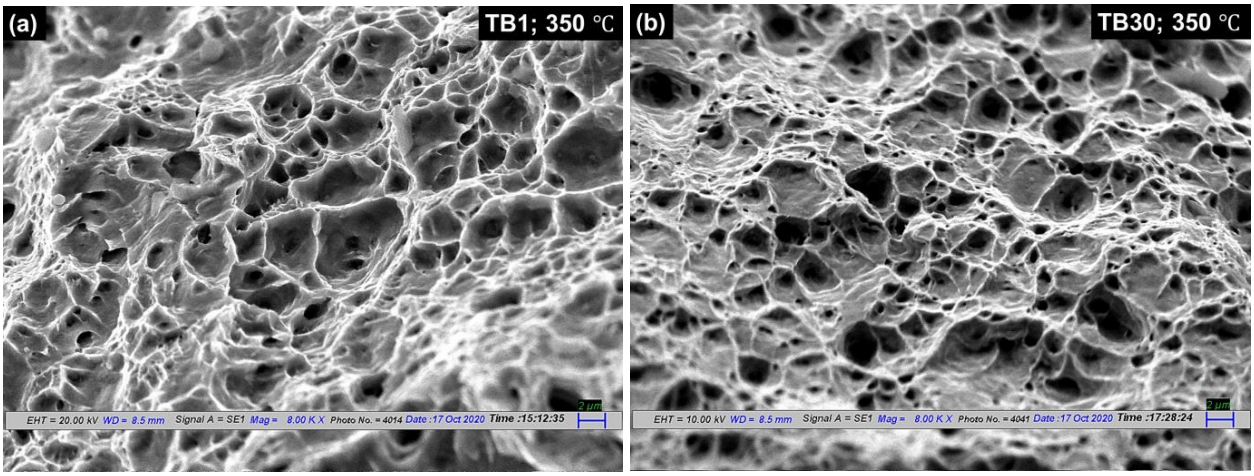

Figure 6.12 FESEM analysis of tensile fractrographs of (a) TB1 steel and (b) TB30 steel at 8000X magnification under ST condition at elevated temperature of 350 ℃.

The bigger dimples show the higher ductility of the steel. Higher ductility of TB1 steel leads to a slightly lower YS and UTS of the steel. As the dimple size reduces, the ductility of the steel reduces

and the increase in the YS and UTS is observed. The FESEM fractrographs at room temperature and elevated temperature compliment the mechanical properties presented in Table 6.6 and Table 6.7.

6.7 CORRELATION BETWEEN MICROSTRUCTURAL STABILITY AND MECHANICAL PROPERTIES

Microstructure of tensile fractured specimen near to tip of TB1 and TB30 steel in ST condition at different testing temperature RT, 200^{o}C, 350^{o}C, and 650^{o}C are shown in Figure 6.13 and Figure 6.14 respectively.

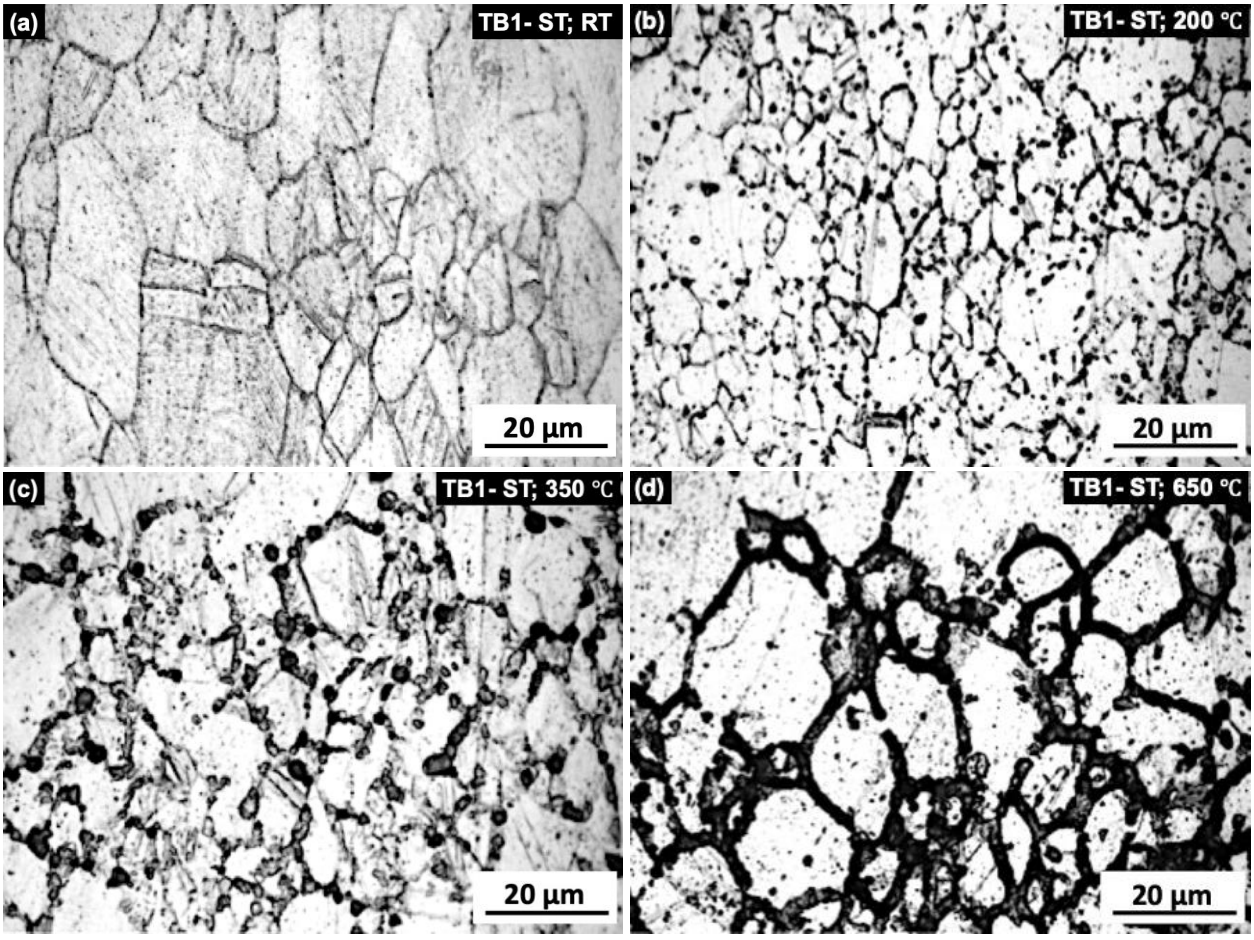

Figure 6.13 Microstructure of tensile fractured specimen near to tip of TB1 steel in ST condition at different testing temperature (a) RT, (b) 200 ℃, (c) 350 ℃ and (d) 650 ℃.

The grain size of TB1 steels was coarser than TB30 steels. As appeared from the micrographs, the sensitization increased with the increase in testing temperature. As observed from the

microstructure (Figure 6.13) carbides are majorly located within the grains of AISI321 steel. With the increase in temperature the carbides migrate towards the grain boundaries. The concentration of carbides along the grain boundaries increased with increase in temperature as shown in Figure 6.13(a-d). The carbides accumulate at the grain boundaries and leads to the increase in the sensitization resulting in the formation of ditch type structure according to ASTM A262 standard [161]. Carbides are brittle and leads to the failure of steels along the grain boundary. Thus, a decrease in tensile strength is observed with increase in testing temperature.

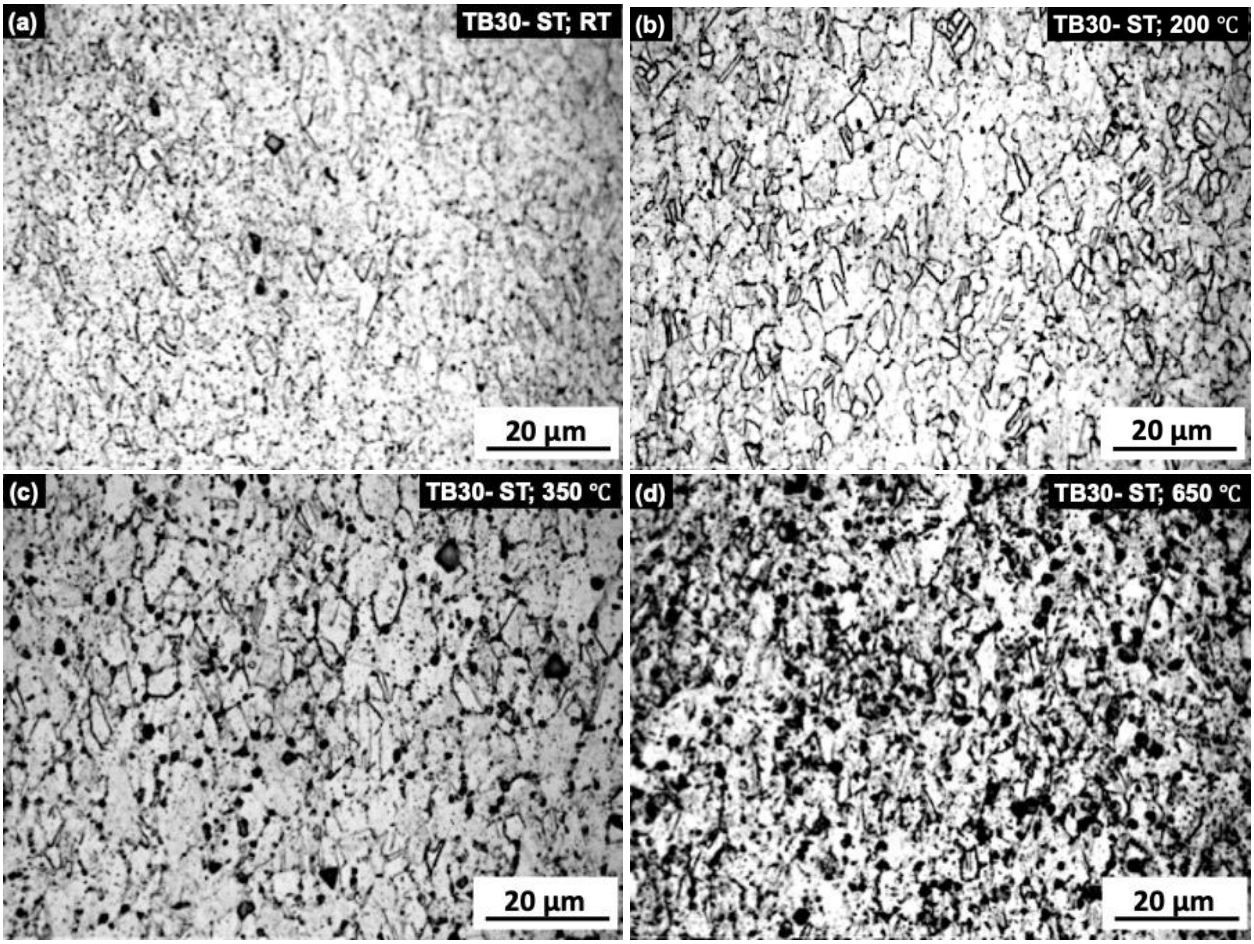

Figure 6.14 Microstructure of elevated tensile fractured specimen near to tip of TB1 steel in ST condition at different testing temperature (a) RT, (b) 200 ℃, (c) 350 ℃ and (d) 650 ℃.

The grain size of TB30 steels was finer in comparison to TB1 steels. For TB30 steels higher precipitate count was observed which restricts the deformation process (Figure 6.14). This leads to increase in YS and UTS of TB30 steels as compared to TB1 steel. Further, the sensitization in TB30 steels was lower in comparison to TB1 steels. This could be attributed to the formation of

stable carbides as compared to TB1 steels. These findings are in good agreement with the literature [117].

6.8 SENSITIZATION AND CORROSION RESISTANCE

Sensitization refers to precipitation of chromium carbides along the grain boundaries and depletion of chromium content near to it when austenitic steel is heated and cooled in between 450-850 ℃. In this condition material becomes venerable to intergranular corrosion and at high temperature it undergoes intergranular stress corrosion cracking in the presence of aqueous environment. The degree of sensitization is mainly governed by chemical composition of steel, cold work, grain size, and developed microstructure during heating and cooling cycle. Corrosion resistance study is based on the sensitization of AISI 321 steels. Intergranular corrosion resistance of TB1 and TB30 steel is evaluated in SA and ST condition according to ASTM A262 standard [161]. According to the ASTM A262 standard the microstructures obtained were classified into three types: "step" structure with no ditches at grain boundaries; "dual" structure, with some ditches at grain boundaries; and, "ditch" structure, with one or more grains completely surrounded by ditches [161].

Mainly two type of sensitisation tests viz. practice A and practice E were performed on the TB1 and TB30 steels under SA and ST conditions. For practice A samples were sensitized at 675 ℃ for 1 hr. whereas for practice E specimen were sensitized at 675 ℃ for 1 h. followed by boiling of samples in copper-coppersulphate+16% sulfuric acid solution for 15 hrs. and then bending the samples at 180°.

6.8.1 SENSITIZATION BEHAVIOR ACCORDING TO ASTM A262 (PRACTICE A)

Figure 6.15 presents the micrographs of samples after sensitisation test according to practice A method. TB30 steels show no sign of sensitisation as compared to TB1 steel. Figure 6.15a, Figure 6.15c, and Figure 6.15d show step structure whereas, Figure 6.15b shows dual structure with some ditches. Higher sensitisation leads to the formation of higher number of carbides on the grain boundaries. This makes the grain boundaries susceptible to the intergranular corrosion. Thus, higher sensitisation leads to a lower corrosion resistance of the steels. AISI-321 TB30 steel under ST condition shows minimum sensitization thus, these steels have higher corrosion resistance and are preferred for inlet and outlet water tubes of VVER type nuclear reactors. Practice A is generally

used in co-relation with other practice tests mentioned in ASTM A262 standard. Thus, for the study to complement practice A practice E was also performed.

6.8.2 SENSITIZATION BEHAVIOR ACCORDING TO ASTM A262 (PRACTICE E)

Figure 6.16 presents the micrographs of samples after sensitisation test according to practice E method. Samples were sensitized at 675 ℃ for 1 hr. followed by boiling in copper-coppersulphate + 16% sulphuric acid solution for 15 hrs. and then bent at 180°. TB1 steel under SA condition developed cracks indicating the formation of ditch type microstructure leading to sensitization and intergranular corrosion (Figure 6.16a). TB30 steel under SA condition revealed a finer microstructure (Figure 6.16b). No sensitization was observed for TB30 steel under SA condition. Further, for TB1 steel under ST condition shows partly orange-peel structure with intergranular fissures indicating the dual type microstructure with some ditches (Figure 6.16c).

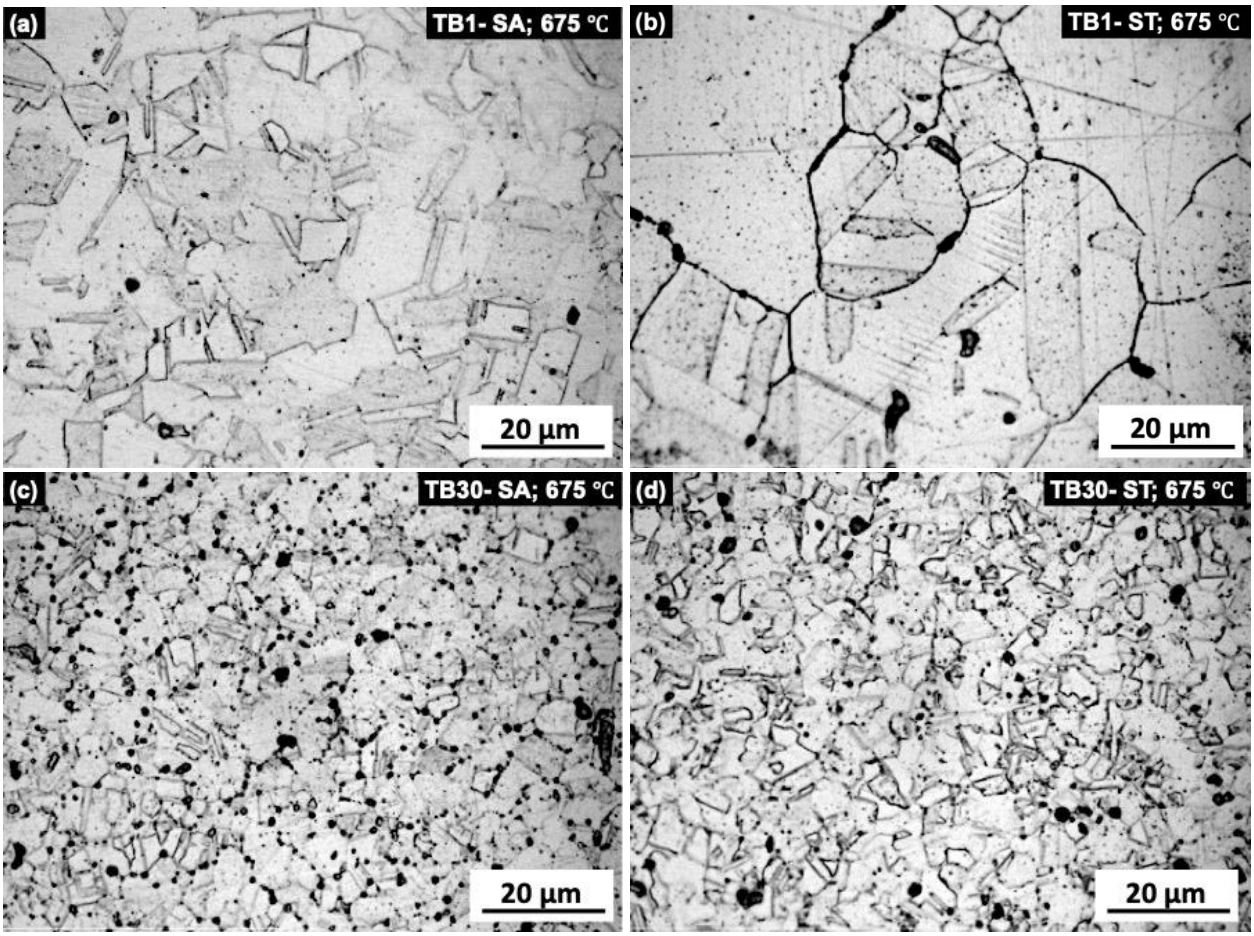

Figure 6.15 Corrosion behavior of (a) TB1-SA, (b) TB1-ST, (c) TB30-SA, and (d) TB30-ST condition at 675ºC according to practice A of ASTM A262 standard.

Lastly, TB30 steel under ST condition indicated a very fine orange-peel type structure. This indicated that minimal sensitization and maximum corrosion resistance was observed for TB30-ST steel. Thus, TB30 steels under SA and ST condition passed the testing criteria set by the supplier for AISI 321 steels. This steel generally works between the temperature range of 291–321℃. Under these conditions TB30-SA and TB30-ST steels provide best results for the material to be used in the inlet and outlet tubes of VVER type nuclear reactor.

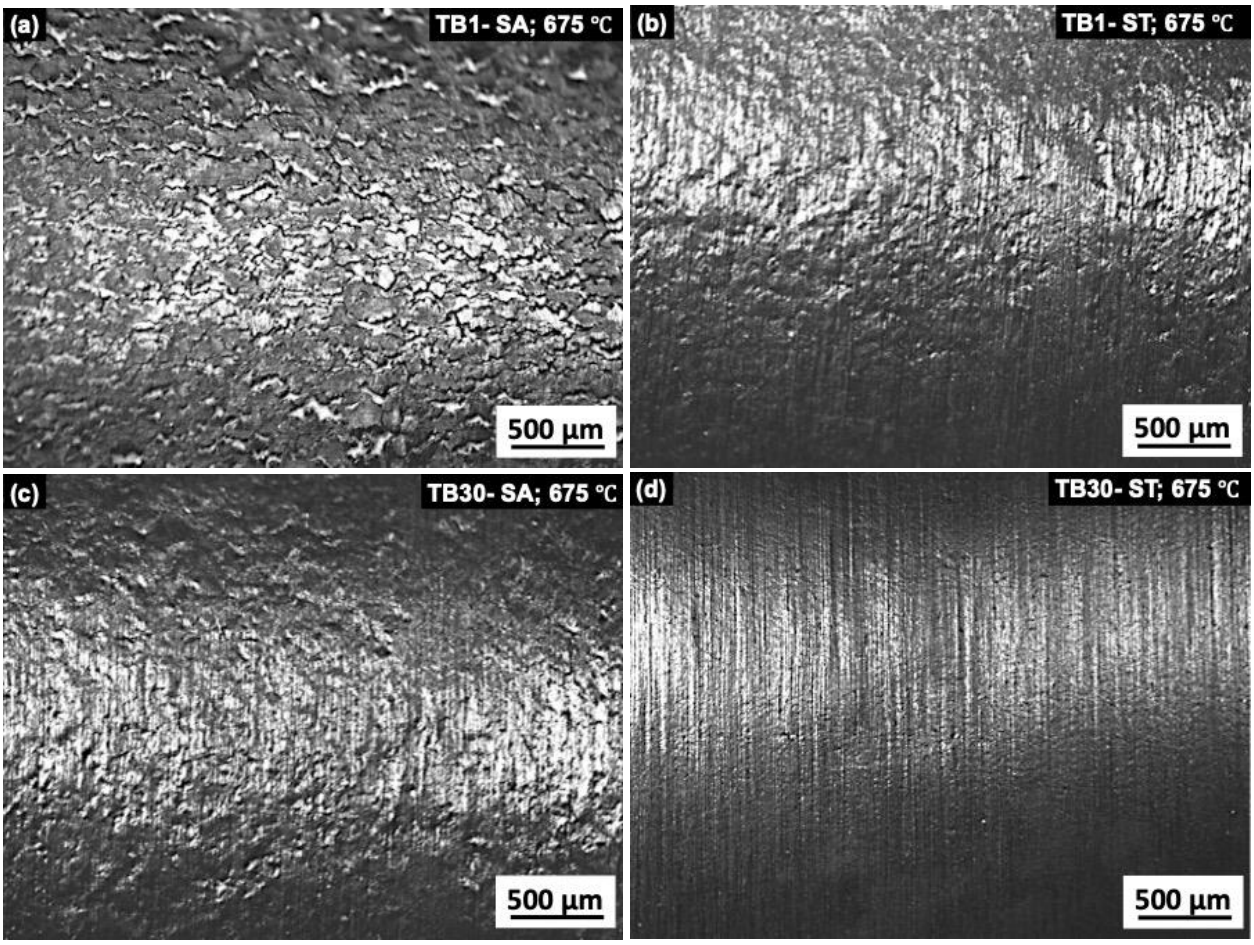

Figure 6.16 Corrosion behavior of (a) TB1-SA, (b) TB1-ST, (c) TB30-SA, and (d) TB30-ST condition at 675 ℃ according to practice E of ASTM A262 standard.

6.8.3 SENSITIZE BEHAVIOR AFTER LONG SOAKING OF 100 HRS.

Sensitization behavior of steels was also checked for long durations of soaking time. Samples were boiled at 675 ℃/100 hrs. and 350 ℃/100 hrs. respectively. Figure 6.17 presents the microstructure after solution treatment followed by sensitization treatment at 675 ℃/100 hrs. It is observed that long duration holding at 675 ℃ leads to the formation of grain boundary carbides. Grain boundary

is most favorable place to form $Cr_{23}C_6$ carbide. It is well known that carbides precipitate preferentially at site of high strain energy (e.g. dislocation tangles and vacancy). If boron has effectively removed the sites of high strain energy at the grain boundary, carbides would not be able to precipitate so easily as is normally observed in other steels. However, it is reported that if boron is protected from nitrogen using titanium, then boron tends to forms complex $Cr_{23}(B, C)_6$ particles on TiN. $Cr_{23}(B,C)_6$ carbide generally form in the temperature range of 600–950 ℃ for long duration of holding [177].

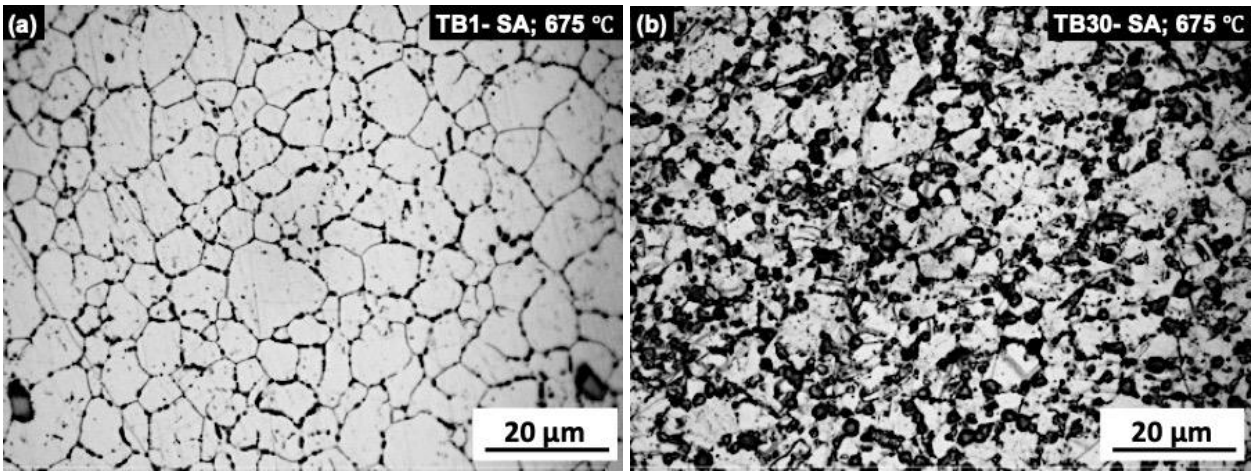

Figure 6.17 Optical microstructure of sensitized steel at 600 ℃/100 hrs. (a) TB1 steel and (b) TB30 steel.

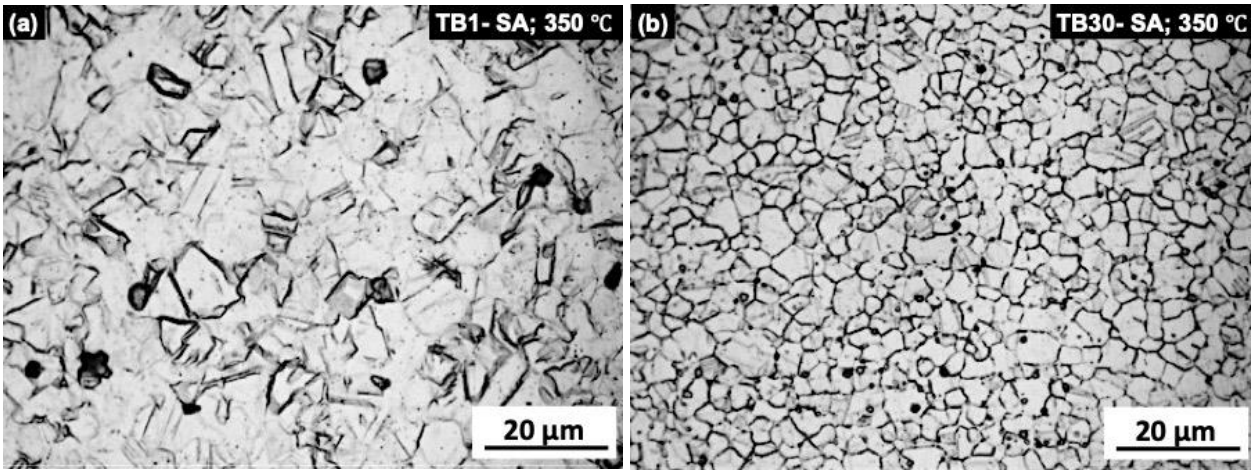

Figure 6.18 Optical microstructure of sensitized steel at 350 ℃/100 hrs. (a) TB1 steel and (b) TB30 steel.

Microstructure of steels at 350 ℃ sensitization for 100 hrs. is shown in Figure 6.18. It is observed that tendency of grain boundary carbide formation is less compared to sensitization at 675 ℃. It is due to the fact that sensitization at low temperature required very long duration of holding. TB30 steel under SA and ST condition are less prone to sensitization and provide superior mechanical properties and improved corrosion resistance.

CHAPTER 7
RESULTS AND DISCUSSION
C250 MARAGEING STEEL

OVERVIEW

C250 steel is a maragring steel and is generally used in aerospace applications. Marageing steel contains around 18 wt% Ni with high levels of 8–13 wt% Co, 3–5 wt% Mo and small additions of Ti and Al are used for different section thickness for aerospace applications. The addition of alloying elements to the steel increases its cost. To reduce the section thickness, different percentage of cold working is carried out on the steels. This, chapter presents the details of optical microstructure and FESEM of different cold worked C250 marageing steel. The EDS analysis of the steels was also performed. In addition to this, dislocation density of the steels was also calculated from the XRD analysis. The chapter also discusses the nanohardness and the mechanical properties of C250 marageing steel. Finally, the cost estimation of the C250 steel was also performed.

7.1 C250 STEELS

7.1.1 STARTING MATERIAL

Vacuum induction melted (VIM) and vacuum arc remelted (VAR) processed C250 ingots of 500 mm diameter and 2500 mm in length were purchased from M/S Aubert & Duval, France. Table 7.1 presents the chemical composition of as-received C250 steel.

Table 7.1 Chemical composition (wt.%) of C250 steel.

Element wt.%	Standard requirements (AMS 6512C and AMS 6520C)	Value certified by Aubert &Dual	Actual values checked
Carbon	0.000–0.03	0.00100	0.00095
Silicon	0.000–0.10	0.047	0.043
Mangenese	0.000–0.10	0.020	0.018
Sulphur	0.000–0.012	0.00031	0.00025
Phosphorus	0.000–0.015	0.0031	0.0032
Nickel	17.00–19.00	18.40	18.42
Molybdenum	4.00–5.20	4.71	4.74
Aluminium	0.04–0.15	0.128	0.129
Cobalt	7.50–8.50	8.00	8.02
Copper	0.02–0.04	0.044	0.040
Titanium	0.30–0.50	0.436	0.440
Iron	balance	balance	balance
Zirconium	0.000–0.020	0.0055	0.0052
Boron	0–0.0030	0.0003	0.0002
Chromium	0–0.10	0.06	0.055
Nitrogen	<0.0030	0.0019	0.0017
Oxygen	<0.0030	0.0013	0.0014
Hydrogen	<0.0002	0.00012	0.00014

7.1.2 PROCESSING ROUTE

Figure 7.1 presents the methodology used in the present study. The as-received ingots of C250 steel were subjected to hot forging process in a 2000 MT hydraulic forging press. Figure 7.2 presents the schematic and pictorial representation of the forging cycle used in the present study. Forging was carried out using drawing, upsetting, and drawing sequence to intermediate size (semi-forged state) and allowed to air cool to room temperature.

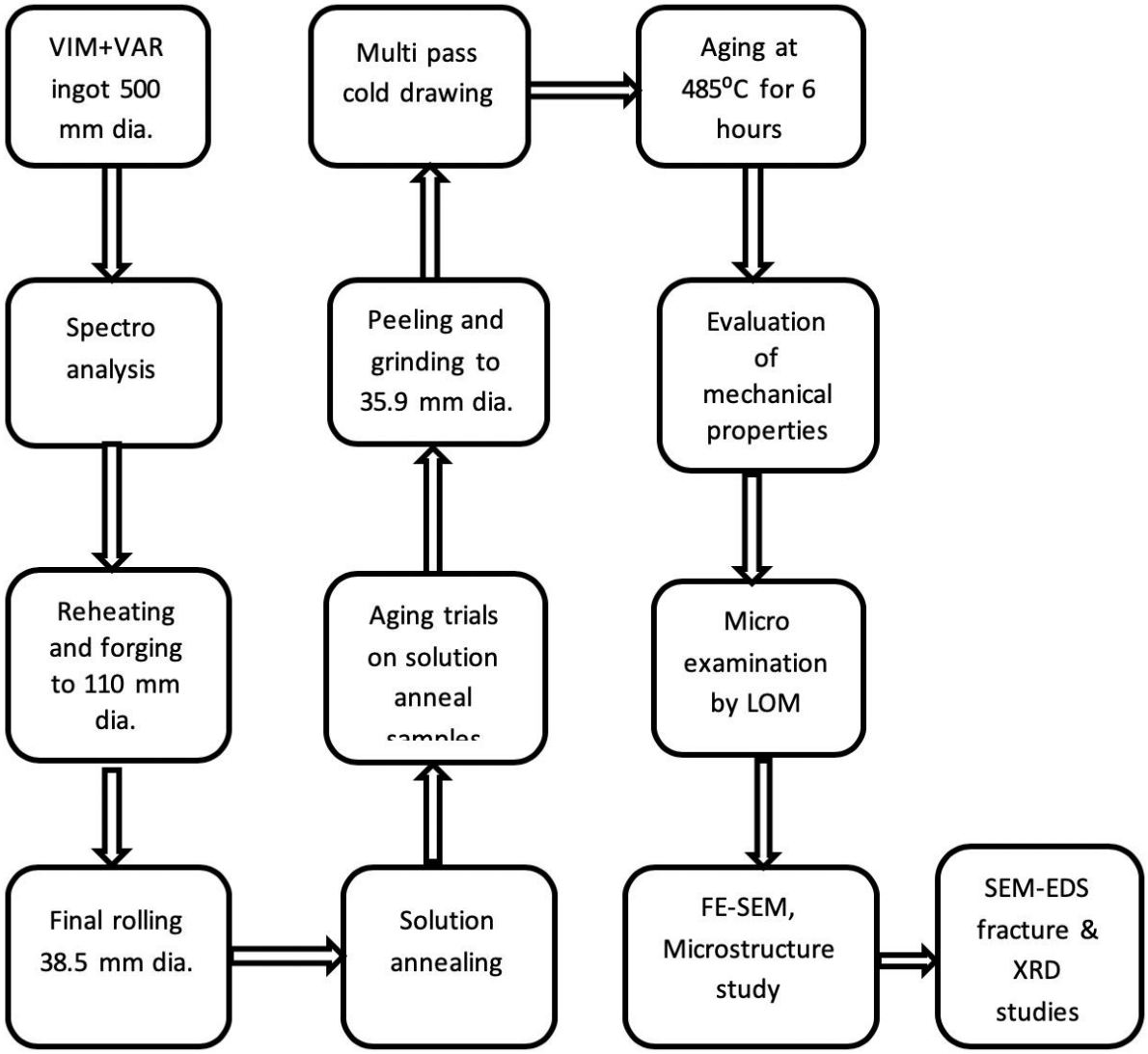

Figure 7.1 Methodology used in the present study.

The ends of the semi-forged specimen were cut to achieve a square face for upsetting operation during subsequent forging. During the forging process, the 500 mm diameter of the ingot was forged in multiple steps of upsetting-drawing into billets of 110 mm diameter. Final forging pass was completed in the range of 850–900 ^{o}C followed by air cooling. The forged billets of 110 mm diameter were subjected to a continuous rolling mill to attain cylindrical bars of 38.5 mm diameter. Thereafter, the rolled bars (38.5 mm diameter) were also subjected to triple solution annealing SA (950^{o}C/45min→ WQ (water quenched) → 950^{o}C/45 min WQ→820 ^{o}C/60 min→ AC (air cooled)). CCT diagram of C250 steel revealed that the complete martensite transformation of C250 steel

would take place even for the Air-Cooling route. Solution annealed samples were then subjected to cold drawing process to observe its effect on microstructure and mechanical properties. Prior to cold drawing, 38.5 mm diameter bars were peeled to 35.9 mm diameter to remove scales and ovality. Finally, the cold working was carried out as given in Table 7.2.

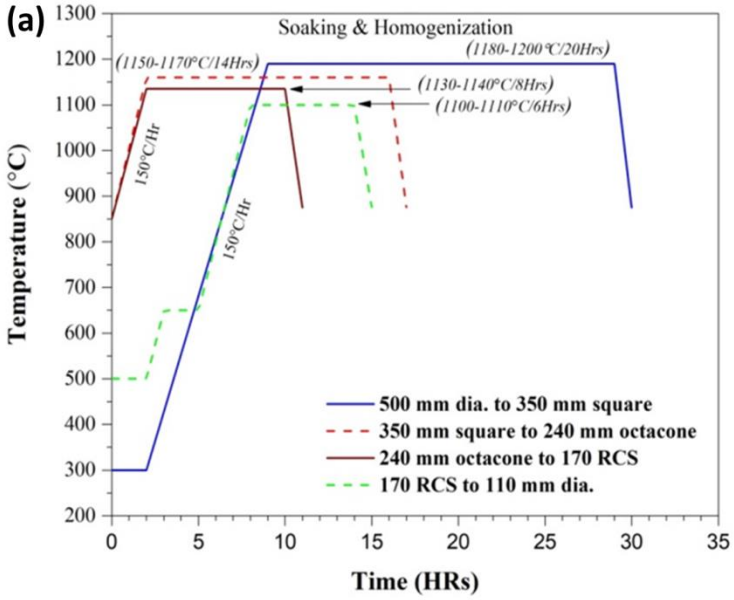

(b) Forging Cycle	Schematic Representation
500 mm dia. to 350 mm square	
350 mm square to 240 mm octagon	
240 mm octagon to 170 mm round cornered steel (RCS)	
170 mm RCS to 110 mm dia.	

Figure 7.2 (a) Schematic of the forging cycle and (b) pictorial representation of forging cycle.

Table 7.2 Sample code for all processed condition.

Sample code	Processing conditions	Diameter of bar (mm)	% Cold work (cumulative)
T0	SA(950^0C/45mts→WQ→950^0C/45mts→WQ→820^0C/60mts→AC)	38.5	0
T4	SA+Ageing* (485^0C/6 hrs→AC)	35.9	0
T5	SA+ cold work pass 1+Ageing*	33.05	15.26
T6	SA+cold work pass 2+Ageing	30.05	32.58
T7	SA+cold work pass3+Ageing	27.05	51.65
T10	SA+cold work pass4+Ageing	24.05	73.67
T11	SA+cold work pass5+Ageing	20.05	104.21
T12	SA+cold work pass 6+Ageing	18.00	123.36
T13	SA+cold work pass 7+Ageing	16.00	144.34
T14	SA+cold work pass 8+Ageing	13.75	169.44
T19	SA+cold work pass 9+Ageing	11.70	197.04
T20	SA+cold work pass 10 +Ageing	9.95	224.73
T21	SA+cold work pass 11+Ageing	8.00	260.10
T22	SA+cold work pass 12+Ageing	6.25	299.07

SA: Solution annealed
RT: room temperature
WQ: water quench
AC: air cooled
* Ageing condition (485^0C/6 hrs→AC) for each condition.

Further, T14 cold drawn samples (drawn to 169.44% cold work) were also processed under cryogenic conditions in dry ice at -82 ^{o}C followed by natural ageing (0, 48, 96, and 144 hours) at room temperature and artificial ageing at 485 ^{o}C/6 hrs→AC. The aim of processing of the steel under the cryogenic conditions is to go beyond the M_f temperature (martensite finish temperature). Table 7.3 presents the designations, cryogenic conditions, and cumulative cold working (%).

Table 7.3 Sample code for cryogenic processing condition.

Sample code	Processing conditions	Diameter of bar (mm)	% Cold work (cumulative)
T15	SA+cold work pass 8+6 hrs at -82^0C +Ageing	13.75	169.44
T16	SA+cold work pass 8+6hrs at-82^0C+48 hrs at RT+Ageing	13.75	169.44
T17	SA+cold work pass 8+6 hrs at -82^0C+96 hrs at RT+ageing	13.75	169.44
T18	SA+cold work pass 8+6 hrs at -82^0C+144 hrs at RT+Ageing	13.75	169.44

7.2 EFFECT OF MULTIPASS COLD DEFORMATION ON THE MICROSTRUCTURE

Figure 7.3 presents the optical micrographs of T0, T4, T5, T6, T10, T13, T14, T19, T20, T21, and T22 samples. For T0 and T4 samples lath like martensite is observed (Figure 7.3a and 7.3b). Lath type martensite is a vital phase for high-strength applications of the steel. During solution

annealing, the transformation of austenite to martensite causes high shear strain in the matrix. Thus, to minimize the strain energy fine lath martensite are formed. Fine lath martensite has a high dislocation density. This increases the strength of the steel containing lath type martensite [134].

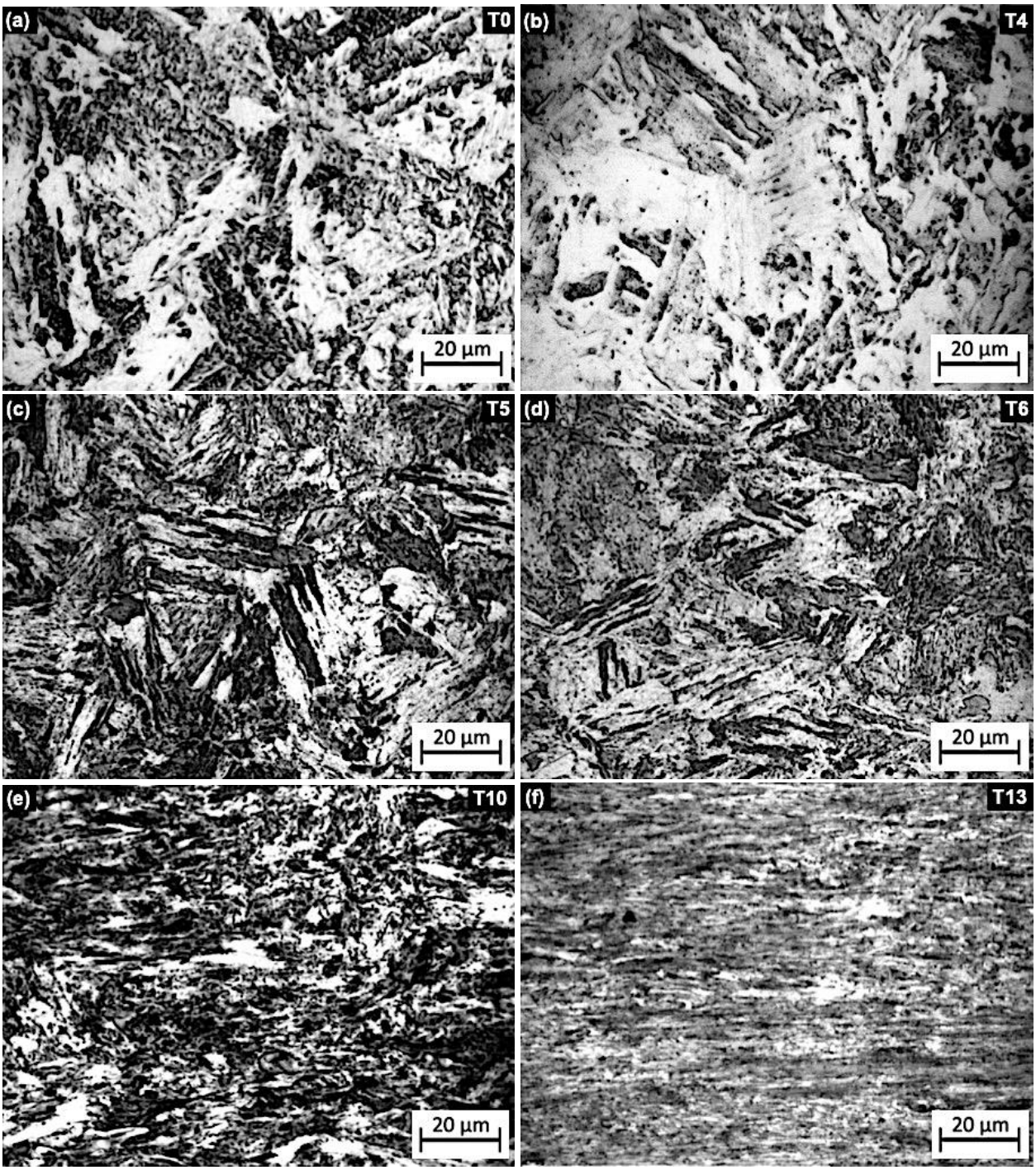

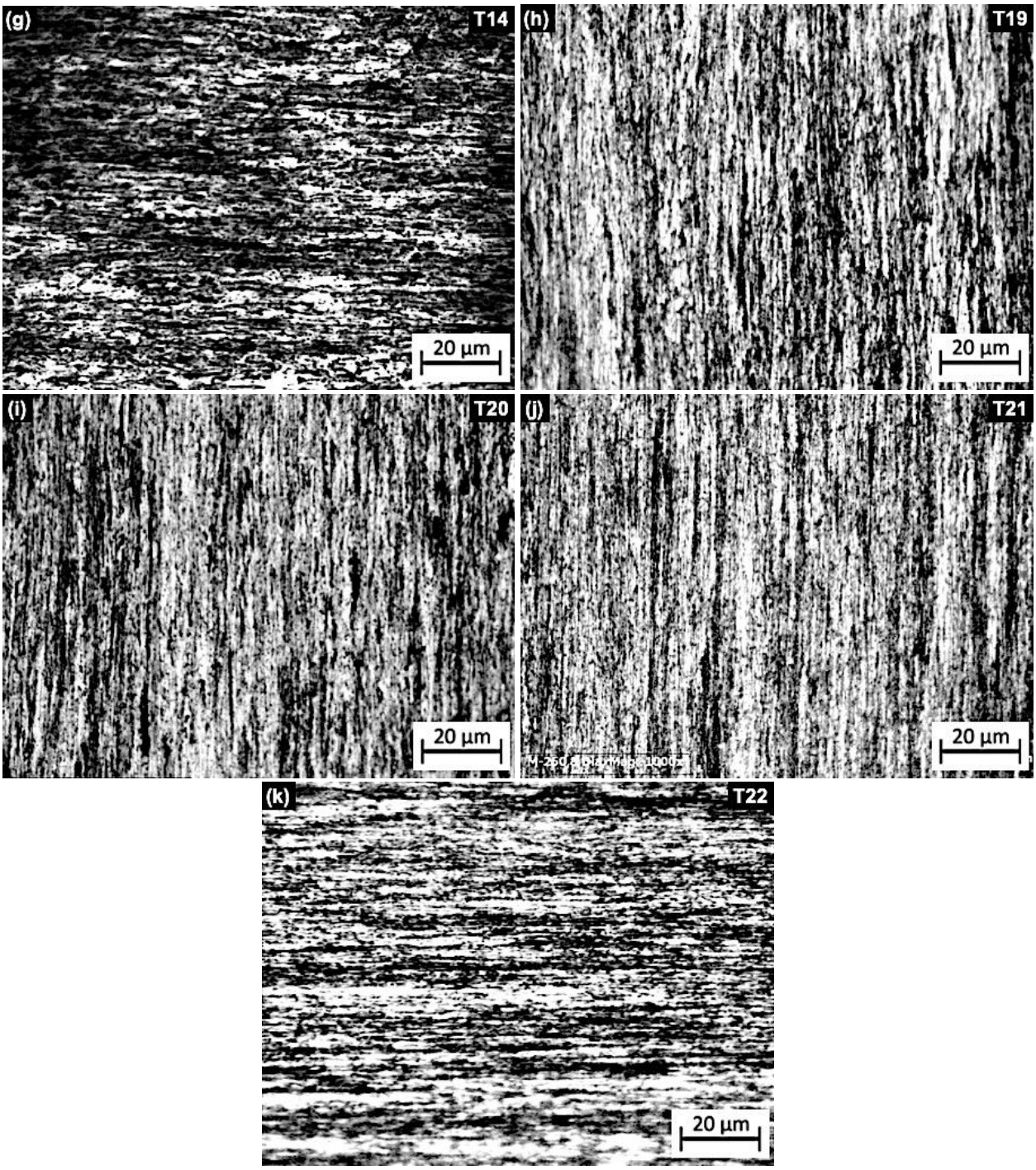

Figure 7.3 Optical microstructure of (a) T0, (b) T4, (c) T5, (d) T6, (e) T10, (f) T13, (g) T14, (h) T19, (i) T20, (j) T21, and (k) T22 cold rolled steel.

Further, cold working from 15.29% to 299.07% increases the grain refinement of the maraging steel. Elongated and oriented grains in the direction of cold working were observed. This feature is more pronounced with an increase in cold working as shown in Figure 7.3(c–k). The lath

martensite exhibited high hardness and resists the deformation along the cold deformation direction. Thus, with the increase in cold work, the lath type microstructure breaks into finer laths as is evident from Figure 7.3(c–k). The feature becomes more dominant with the increase in cold working. The grain size also got refined from T4 to T14. Beyond T14 the grains become highly elongated in the direction of cold working (Figure 7.3(h–k)).

Further, after T14 cold deformation, the samples were cryogenic treated according to the conditions mentioned in Table 3.12. Figure 7.4a–e presents the effect of cryogenic treatment (6 hours at –82 °C) on 169.44% cold deformed steels kept at room temperature for different times followed by ageing. Very fine martensite laths in the direction of cold deformation were observed. The cryogenic treatment converts the retained austenite to martensite. Thus, a further refinement in the lath type martensite is observed as shown in Figure 7.4(a–e).

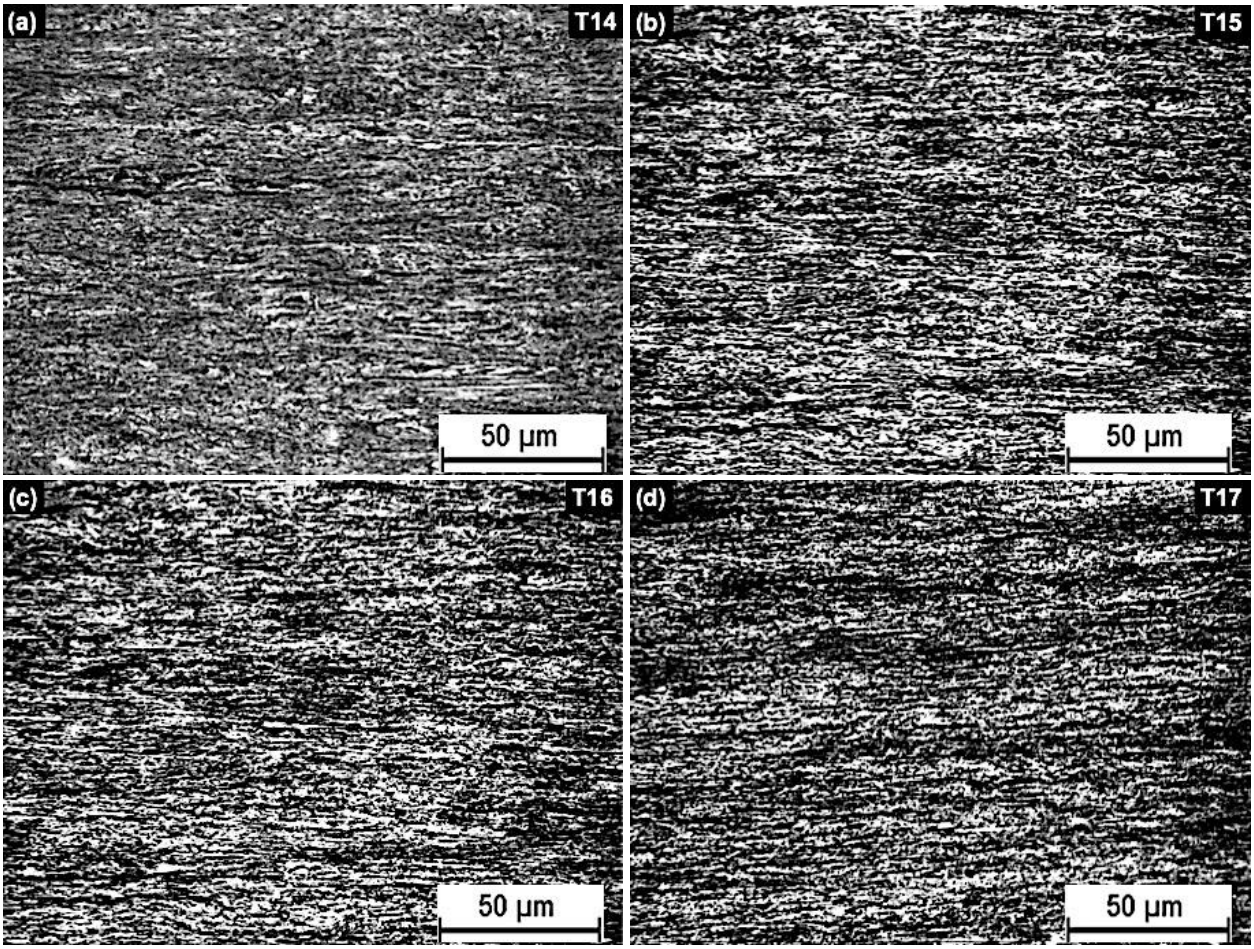

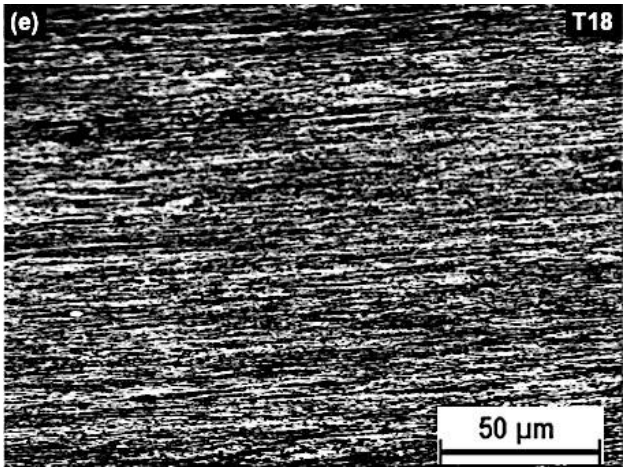

Figure 7.4 Optical microstructure of (a) T14 (b) T15, (c) T16, (d) T17 and (e) T18 cryogenic heat treated C250 steel etched with Keillings l for 25 min. at 500X magnification.

7.3 FESEM MICROSTRUCTURE

FESEM microstructure of C250 steel for T0, T4, T14 and T18 conditions is shown in Figure 7.5. Higher magnification microstructure shows the presence of lath martensite, retained austenite and fine distribution of precipitates such as Ni_3Ti and Fe_2Mo. The higher content of precipitates (Ni_3Ti and Fe_2Mo) leads to the improvement in the strength of C250 steels [47]. The martensite laths observed for T0 were coarser in size.

The equiaxed laths of martensite are clearly visible in the matrix phase. The martensite laths have a random morphology throughout the microstructure (Figure 7.5a). The solution annealing of C250 steel revealed minimal deformation of martensite laths with fine precipitation of phases like Ni_3Ti and Fe_2Mo (Figure 7.5b). Cold working leads to the deformation of martensite laths. Martensite laths appear to be deformed in the direction of cold work. The microstructure of T14 cold rolled steel is finer in comparison to T0 and T4 steel (Figure 7.5c). With an increase in cold working, the martensite laths are broken and refined in the direction of the drawing. Cold drawing increases the hardness of the steel and restricts the deformation process. For high cold working, the microstructure of C250 steel gets distorted and an extended grain shape is observed (Figure 7.5c and 5d).

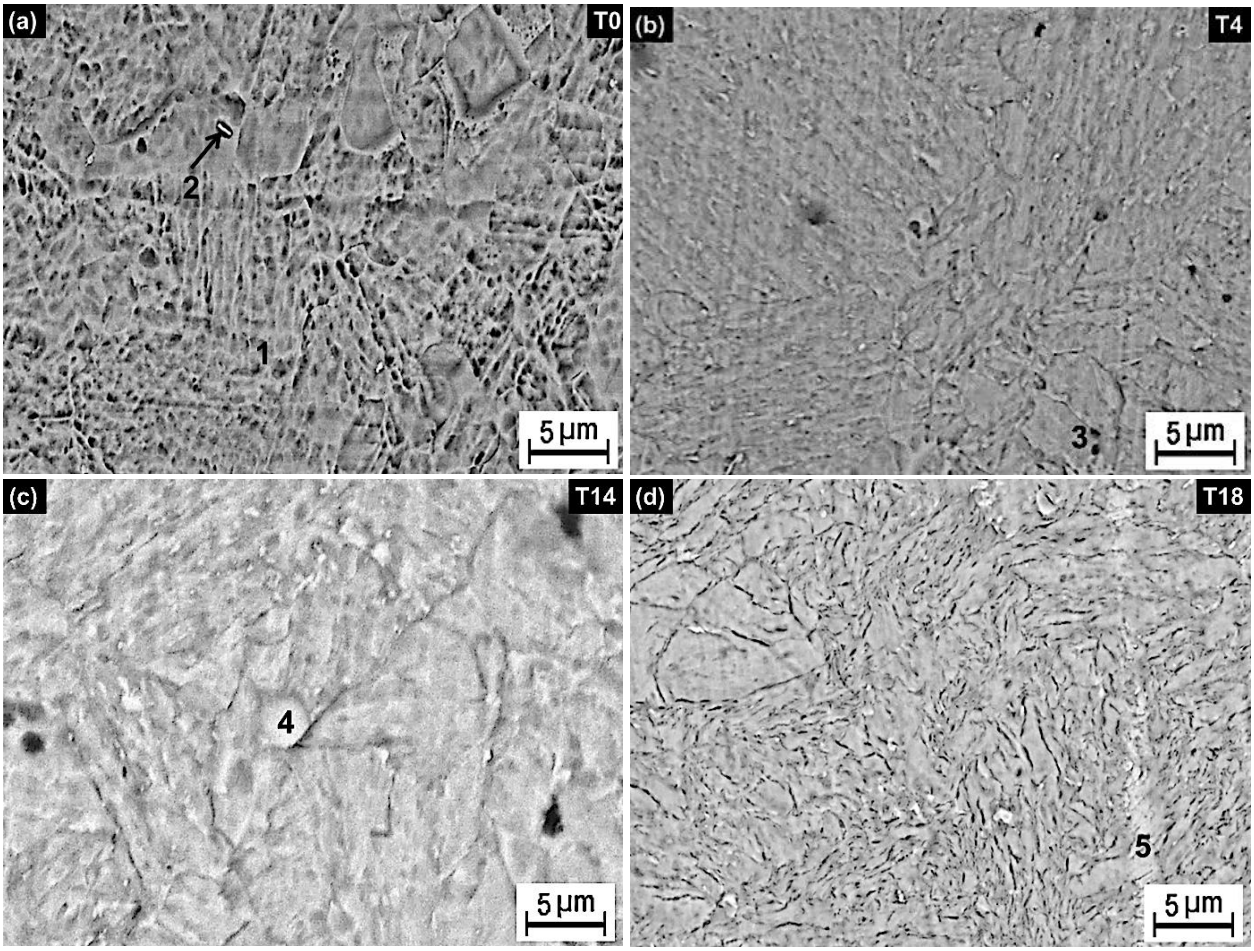

Figure 7.5 FESEM microstructure of C250 steel at (a) T0 (b) T4 (c) T14 and (d) T18 conditions at 1000X magnification.

EDS spectra of points marked in Figure 7.5 is presented in Figure 7.6. Table 7.4 also represents the chemical composition of each point. EDS analysis shows the presence of different elements thus indicating the formation of different precipitates viz. Ni_3Ti and Fe_2Mo. The fine and uniform distribution of these precipitates leads to the improvement in the strength of C250 marageing steel [47]. Although carbon in C250 steel is nearly 0.00095 wt.% however, the carbon composition in EDS is approximately 5%. This is due to the carbon tape used for the mounting of the samples.

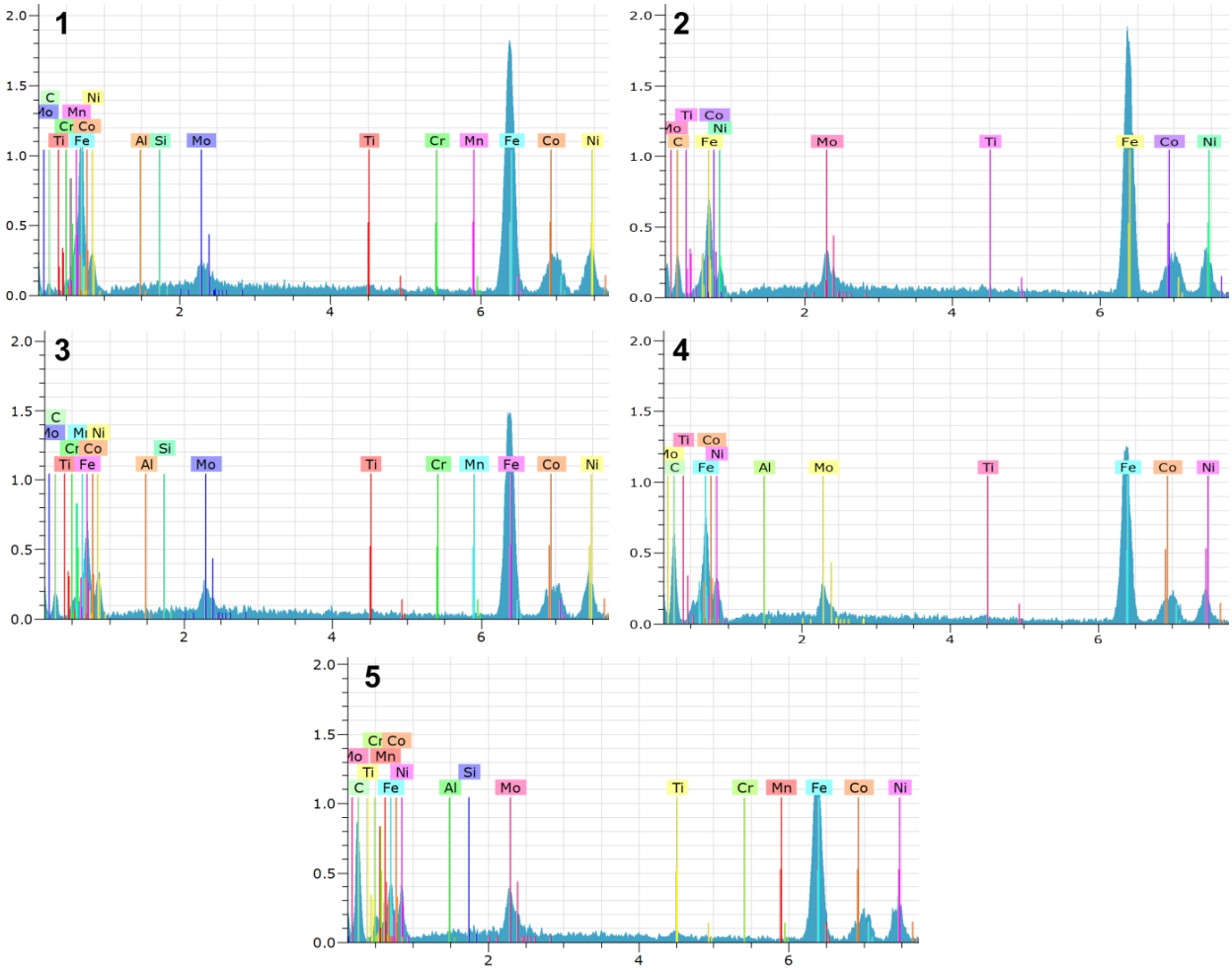

Figure 7.6 EDS spectra of point 1, point 2, point 3, point 4 and point 5.

Table 7.4 Composition analysis of energy spectrum on points as marked in Figure 7.5.

Points (Phases)	Chemical composition (wt. %)									
	Fe	**Ni**	**Co**	**C**	**Mo**	**Ti**	**Cr**	**Mn**	**Al**	**Si**
1 (Matrix)	63.18	15.47	10.14	5.09	4.63	0.47	0.36	0.34	0.18	0.12
2	64.47	15.53	8.54	5.80	5.14	0.51	-	-	-	-
3	63.72	15.64	8.78	4.82	5.31	0.34	0.39	0.44	0.34	0.23
4	63.74	15.94	10.05	5.29	4.51	0.35	-	-	0.12	-
5	62.44	13.44	10.17	4.77	7.05	1.05	0.22	0.37	0.23	0.25

Figure 7.7 shows the X-ray dot elemental map of alloying element present in C250 steel under solution annealed condition (T0). Homogeneous distribution of all the elements can be observed from X-ray dot mapping of the steel.

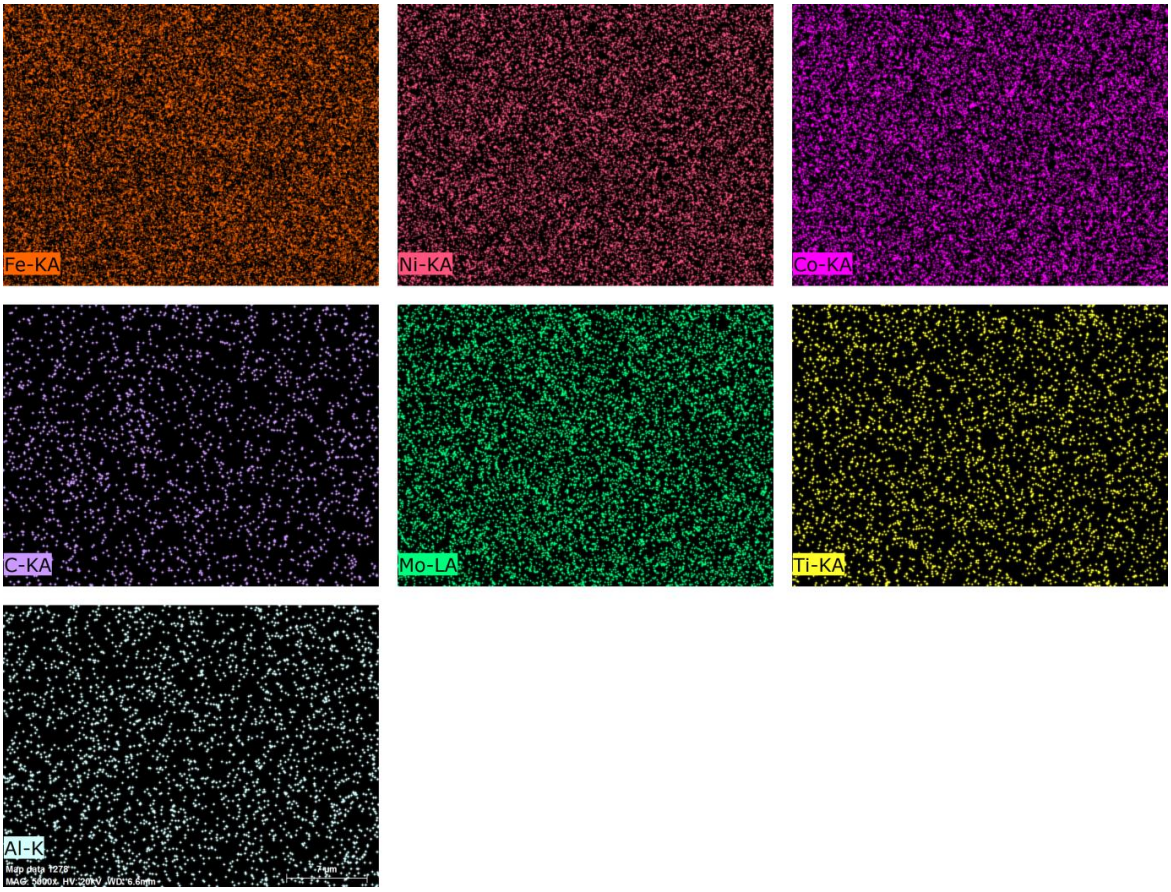

Figure 7.7 X-ray dot element maps showing the presence of Fe, Ni, Co, C, Mo, Ti and Al in Figure 7.5 (a).

7.4 DISLOCATION DENSITY

Figure 7.8a presents the XRD spectra of C250 steel under T0, T4, T5, T14, T20, and T21 condition. In the XRD patterns, three peaks corresponding to planes (110), (200), and (211) of iron-nickel ($Fe_{10.8}Ni$) (ICDD 03-065-7753) suggesting the cubic structure (space group lm-3m) can be seen. The peaks in the spectrum of the C250 steel correspond to the body-centered-cubic (bcc) matrix. Beyond T5 peak shifting in the XRD pattern is observed. This shifting was attributed to the deformation of a material under the effect of cold working. Next, to determine the dislocation density, crystallite size is required. Crystallite size is calculated using the Williamson-Hall (W-H) analysis. Bragg angle (2θ) and corresponding full width half maxima (FWHM) β_{hkl} is determined by curve fitting in origin using Gaussian and Lorentzian function (Figure 7.8b). The peak is assumed to be symmetric along the Bragg angle (2θ).

Crystallite size is determined using the Scherrer equation which is a volume weight quantity and is dependent upon β_{hkl}. Scherrer equation is presented in Equation 7.1 [183]. In this, the peak

broadening is attributed to the crystallite size. Further, Stokes and Wilson proposed the broadening of peaks due to strain formulation [183].

$$D = \frac{k.\lambda}{\beta_{hkl}.\cos\theta_{hkl}} \quad (7.1)$$

Where

D: Crystallite size (nm)

K: shape factor

θ_{hkl}: Bragg angle

β_{hkl}: FWHM

λ: X-ray wavelength 0.15406 nm

Mathematical formula for peak broadening due to strain (ε) called as induced strain is given by Equation 7.2.

$$\beta_{hkl} = 4\varepsilon.\tan\theta_{hkl} \quad (7.2)$$

Dislocation densities were calculated using the Williamson-Hall method Equation 7.3 [136].

$$\rho = \sqrt{\rho_p \rho_s} \quad (7.3)$$

Where,

ρ: dislocation density

ρ_p: dislocation density calculated from particle i.e. crystallite size

ρ_s: dislocation density calculated from strain broadening

The calculated values of ρ_p and ρ_s is done by Equation 7.4 and Equation 7.5 [184].

$$\rho_p = \frac{3n}{D^2} \quad (7.4)$$

$$\rho_s = \frac{k\varepsilon^2}{Fb^2} \quad (7.5)$$

Where,

n: dislocations per block face, assumed as 1

k: factor k is assumed as 14.4 for body-centered cubic metals

F: interaction factor assumed to be 1

b: burger vector taken as 0.2485 nm

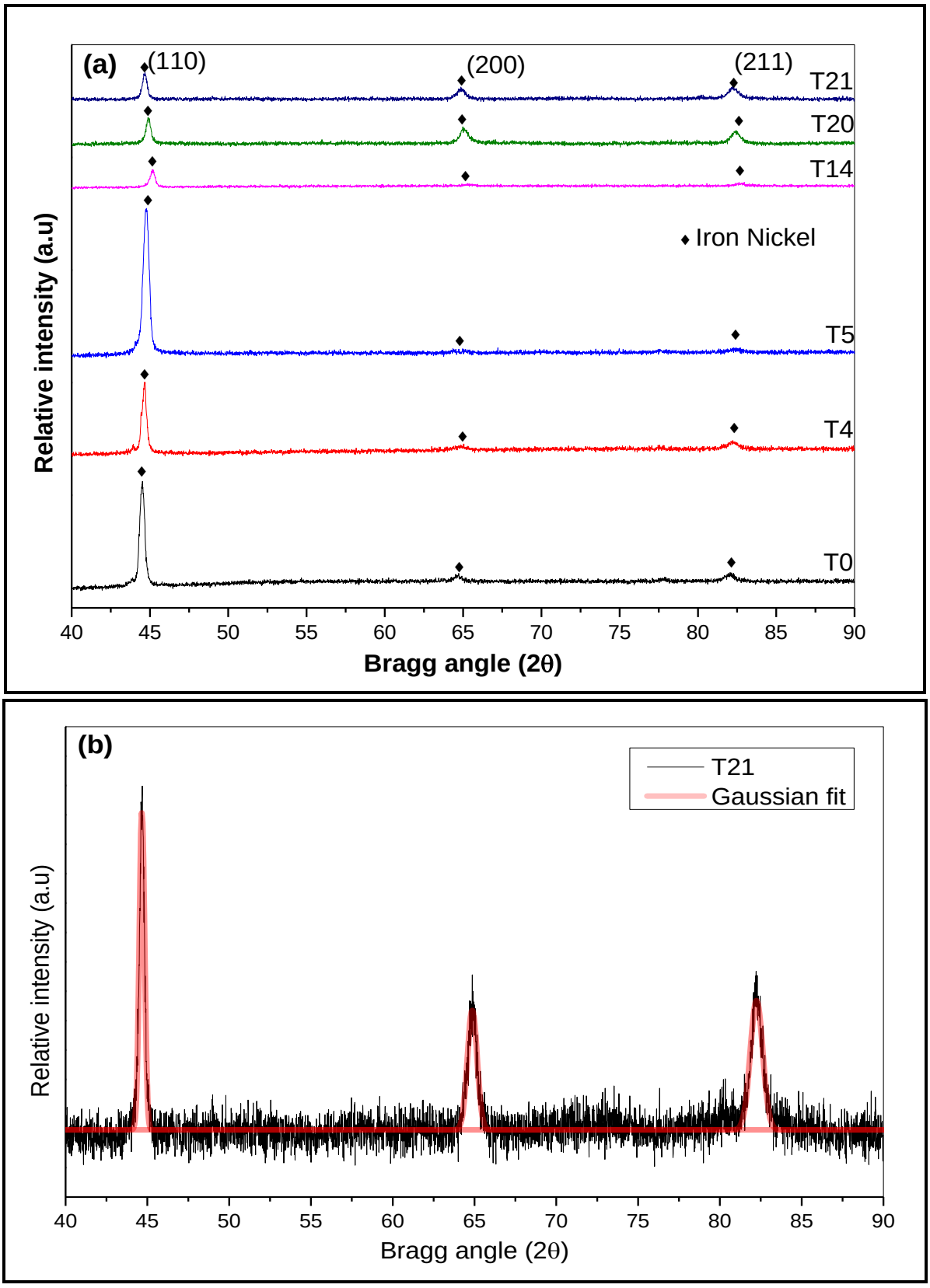

Figure 7.8 (a) XRD of different cold drawn C250 steel and (b) Gaussian fitted data.

Table 7.5 presents the calculated dislocation density for different cold rolled C250 steels. Increase in cold rolling increased the dislocation density of the steels. The increase in the dislocation density of the steel leads to an increase in the hardness and mechanical properties of the steel. The dislocation density of C250 steel increased with the increase in cold working till T20 beyond which the decrease in the dislocation density is observed.

Table 7.5 Dislocation density of different % cold deformed C250 steel.

Composition	D (nm)	$\boldsymbol{\varepsilon \times 10^{-3}}$	$\boldsymbol{\rho_p}$ × 10^{15} (m^{-2})	$\boldsymbol{\rho_s}$ × 10^{15} (m^{-2})	$\boldsymbol{\rho}$ × 10^{15} (m^{-2})
T0	18.49	4.21	8.77	4.11	6.01
T4	17.17	4.68	10.17	5.11	7.21
T5	16.27	4.75	11.33	5.26	7.72
T14	18.06	4.25	9.19	4.21	6.22
T20	17.41	4.39	9.89	4.51	6.68
T21	17.82	4.41	9.45	4.55	6.55

7.5 NANOHARDNESS

Table 7.6 presents the nanohardness of different % cold deformed C250 steel. The nanohardness of the steel increased with the increase in cold working. Complete lath type martensite was observed in the microstructure. The hardness of the lath type martensite increased with the increase in cold working as can be observed from Table 7.6. Best nanohardness was observed for T14 C250 steel. Beyond this, for T15–T22, the nanohardness value remained constant. Figure 7.9 presents the load-displacement curves for T0, T4, T5, and T14 samples. For the load of 10 mN, the displacement of T14 steel was lower as compared to the other steel samples.

Table 7.6 Nanohardness values of different % cold deformed C250 steels.

Formulation	**Nanohardness (GPa)**
T0	5.89±0.48
T4	6.23±0.47
T5	6.93±0.63
T14	9.25±0.85

7.6 MECHANICAL PROPERTIES

The variations of 0.2% yield strength (YS), ultimate tensile strength (UTS), and hardness etc. of C250 steel in all conditions are summarized in Table 7.7. The YS and UTS of C250 steel in the SA condition (T0) was minimum and the total elongation and impact strength were maximum. The

low YS and UTS of C250 steel under T0 condition could be attributed to the absence of strengthening precipitates in the matrix at solution annealed condition (Figure 7.5a).

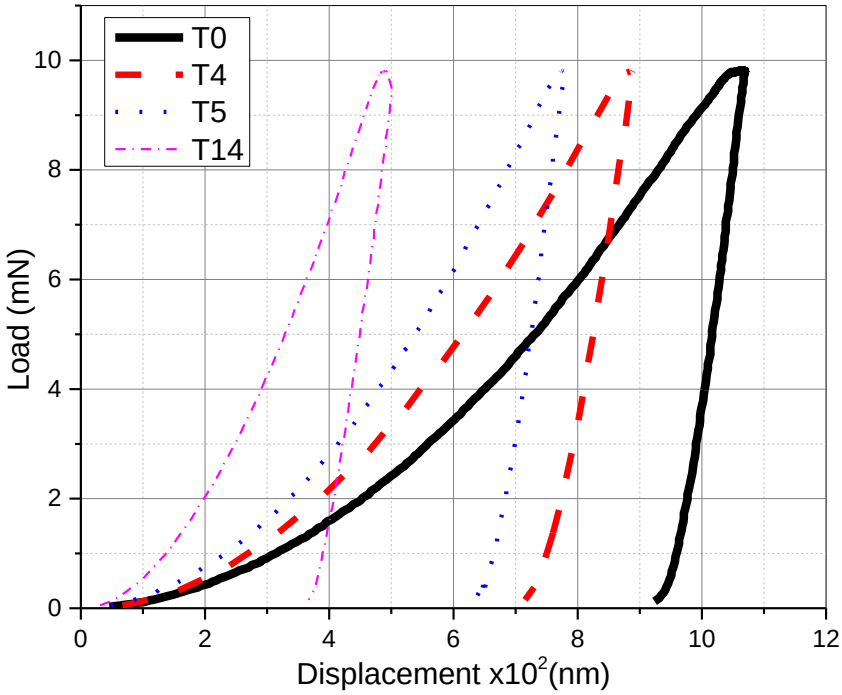

Figure 7.9 L-D curve of different C250 steels.

The YS and UTS of C250 steel increased with ageing treatment (T4). This increase in YS and UTS is attributed to the increase in the concentration of the precipitates (Ni_3Ti and Fe_2Mo) during the ageing process (Figure 7.5b). The increase in YS and UTS is also followed by a marginal decrease in the impact strength and percentage elongation. The precipitation of Fe_2Mo and Ni_3Ti intermetallic phase has led to an increase in the hardness of the C250. These intermetallic compounds provide a hindrance to dislocation movement and with increased deformation, their content also increases. Hence, with increased deformation process an increase in YS and UTS of the steel is observed. Next, with an increase in the cold deformation, the hardness of the steels increased. The martensite laths start aligning in the direction of the cold working. Also, the cold working leads to the work hardening of the C250 steels. The dislocations in the steel start moving towards the grain boundaries and increase the work hardening rate of the steels which in turn increases the YS and UTS of the steel. Further, a decrease in the percentage elongation and impact strength is observed. Beyond T14 cold working, a sudden drop in the percentage elongation and impact strength is observed. This could be attributed to the excessive cold working of the steel.

The excessive cold work has the tendency to change the grain from crystalline to amorphous, thus beyond T14 cold work, the mechanical properties of the C250 steel resemble to that of a brittle material (Table 7.7).

Table 7.7 Mechanical properties of C250 grade at different condition.

Sample code	Hardness (HRC)	UTS (MPa)	0.2%YS (MPa)	Elongation (%)	Reduction in area (%)	V-notch Impact (J)
T0	32	1197.34	998.64	36.8	75.8	212
T4	38	1857.11	1817.7	32.4	56.8	208
T5	41	1900.82	1852.54	11.4	57.1	34
T6	44	1937.32	1897.9	10.8	57.9	30
T7	49	1971.32	1943.01	11.2	61.1	30
T10	51	2011.65	2005.00	12.8	60.1	28
T11	53	2069.61	2061.99	11.0	59.2	22
T12	52	2137.55	2091.45	10.8	57	22
T13	53	2123.53	1939.13	10.4	58.8	20
T14	56	2193.57	2158.4	10.8	48.2	20
T19	54	2371.10	2364.4	4.0	28.5	18
T20	55	2378.5	2358.7	3.6	28.1	14
T21	55	2250.5	2219.4	2.8	5.6	6.25
T22	55	2167.3	2161.3	2.0	3.49	2.0

Also, beyond T20 the dislocation density of the steel becomes constant thus a marginal change in YS and UTS is observed. Further, cold working leads to the alignment of grains along the cold working direction. From XRD spectra it can be observed that cold working leads to the change in crystal orientation and growth of crystals takes place in the new planes. This growth of crystals in T20 and T21 steel leads to a decrease in percentage elongation of the steel. Best results were observed for T14 cold work steel. The YS, UTS and hardness of T14 C250 steel were 1939.13 MPa, 2123.53 MPa and 56 HRC respectively.

Table 7.8 presents the mechanical properties of cryogenic treated cold worked samples. The cryogenic treatment of the C250 steel led to the complete transformation of retained austenite to martensite. Martensite is a harder phase and resists deformation hence, a marginal increase in YS, UTS, and hardness is observed for cryogenic treated samples. The mechanical properties also improved with the increase in the resting time at room temperature before ageing. The best results were observed for T18 (SA+cold work pass 8+6 hrs at -82^0C+144 hrs at RT+Ageing) samples with a marginal loss in ductility and impact strength.

Table 7.8 Mechanical properties of cryogenic treated C250 grade steel at a cold working of 169.44%.

Sample code	Hardness (HRC)	UTS (MPa)	0.2%YS (MPa)	Elongation (%)	Reduction in area (%)	V-notch Impact (J)
T15	54	2192.96	2167.11	10.8	54.3	24
T16	55	2180.64	2140.47	10.4	55	22
T17	57	2175.03	2127.57	11.2	57	24
T18	57	2207.28	2195.15	9.6	57.1	22

7.7 FRACTOGRAPHY

Fracture surface analysis of solution annealed, aged, and cold deformed C250 steels are carried out with the help of SEM. Figure 7.10 presents the SEM micrographs of the fractured surfaces after the tensile test for solution annealed, aged, and cold worked steels. The fractographs of the specimen at different conditions indicate ductile dimple type fracture as shown in Figure 7.10(a–d). For solution annealed condition (T0 condition), large size and deep dimples are observed (Figure 7.10a). The dimple size is governed by number and distribution of microvoids that are nucleated in the steel. When void nucleation sites are few and widely spaced, the microvoids grow to a larger size before coalescence giving rise to the appearance of a fracture surface containing large dimples. For aged steel sample (T4 condition), the dimples observed are smaller and shallow compared to the T0 condition. The number of small and shallow dimples increased with an increase in cold working (Figure 7.10c and 7.11d). Small and shallow dimples are formed when a large number of voids are activated and adjacent microvoids join before they grow into a large size. The shape of the dimple is primarily governed by the internal stress in the material and also on the formation of the microvoids. The small dimples observed for aged C250 steel could be the resultant of the localized deformation between the precipitates and the void nucleation sites while the size of the final dimple is dependent upon the inter precipitate distance in the matrix of C250 steel. For the aged steel sample higher number of precipitates was observed (Figure 7.5b).

Thus, the growth of voids is restricted to a small size. The deformation along the particle occurs due to the particle shearing. This gives rise to the localized deformation near the precipitates and as a result, small and shallow dimples are observed along the fracture surface. The shallowest dimples were observed for T18 condition steel (Figure 7.10d). The formation of very fine dimples in the cold rolled condition in C250 steel is attributed to the fracture of very fine intercrystalline precipitates. The shallow dimples in the aged specimens were the result of joining the microvoids

by shear along the slip bands. Table 7.9 present the chemical composition of selected points over Figure 7.10.

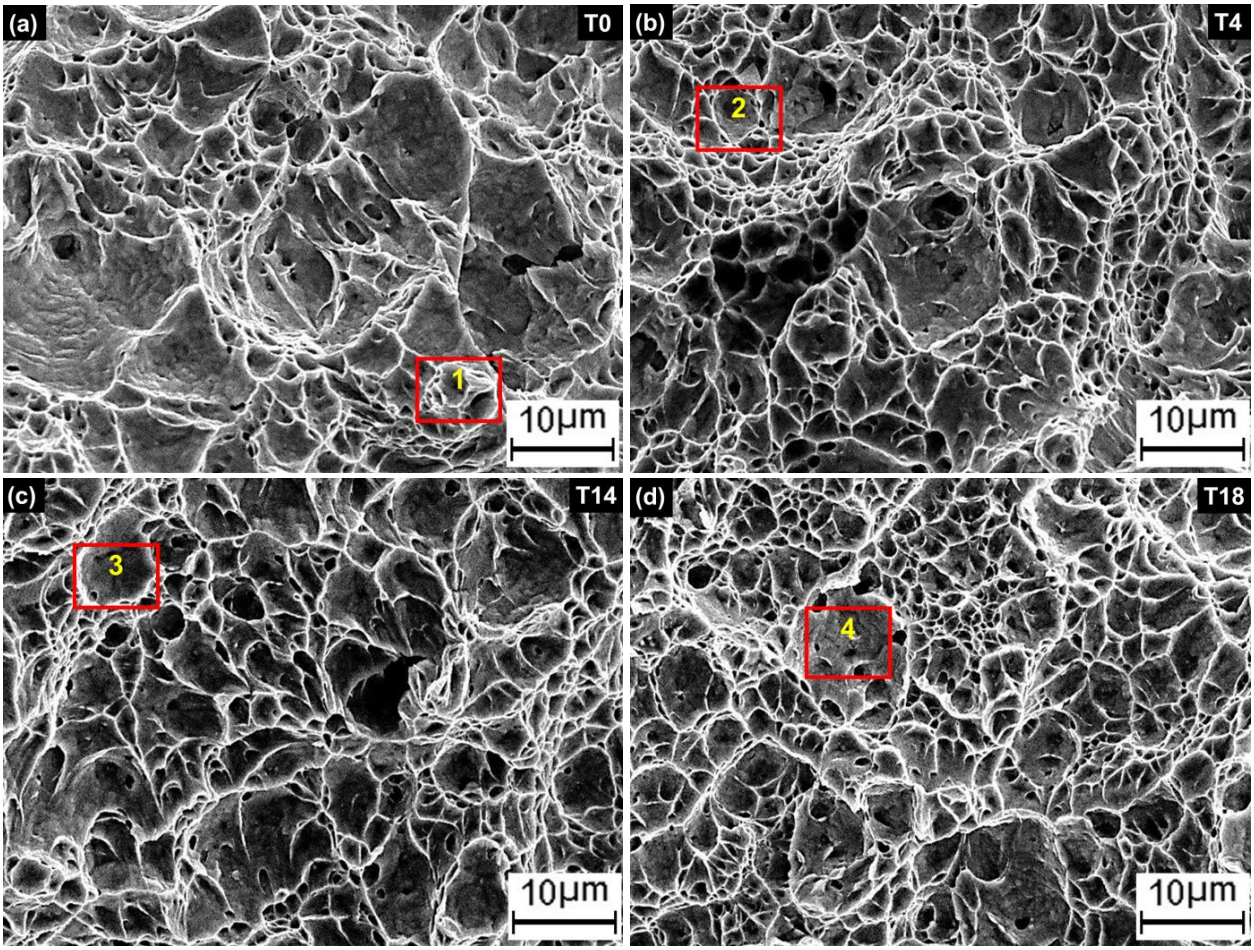

Figure 7.10 Tensile fractographs of C250 steel at (a) T0 (b) T4, (c) T14 and (d) T18 at 2000X magnification.

Table 7.9 Composition analysis of energy spectrum on points as marked in Figure 7.10.

Points	Chemical composition (wt. %)					
	Fe	**Ni**	**Co**	**Mo**	**Ti**	**Al**
1	65.97	18.12	8.34	6.60	0.56	0.42
2	67.01	17.65	8.60	5.84	0.63	0.28
3	79.48	9.54	10.16	0.64	0.17	0.00
4	71.03	15.32	8.69	4.36	0.30	0.32

Figure 7.11 presents the fracture surface of Charpy test samples indicating fracture mode for T0, T4, T14 and T18 conditions. The fracture is mainly of ductile nature with the formation of microvoids and spread transgranular by coalescence. Large size dimples are observed for T0 solution annealed condition (Figure 7.11a).

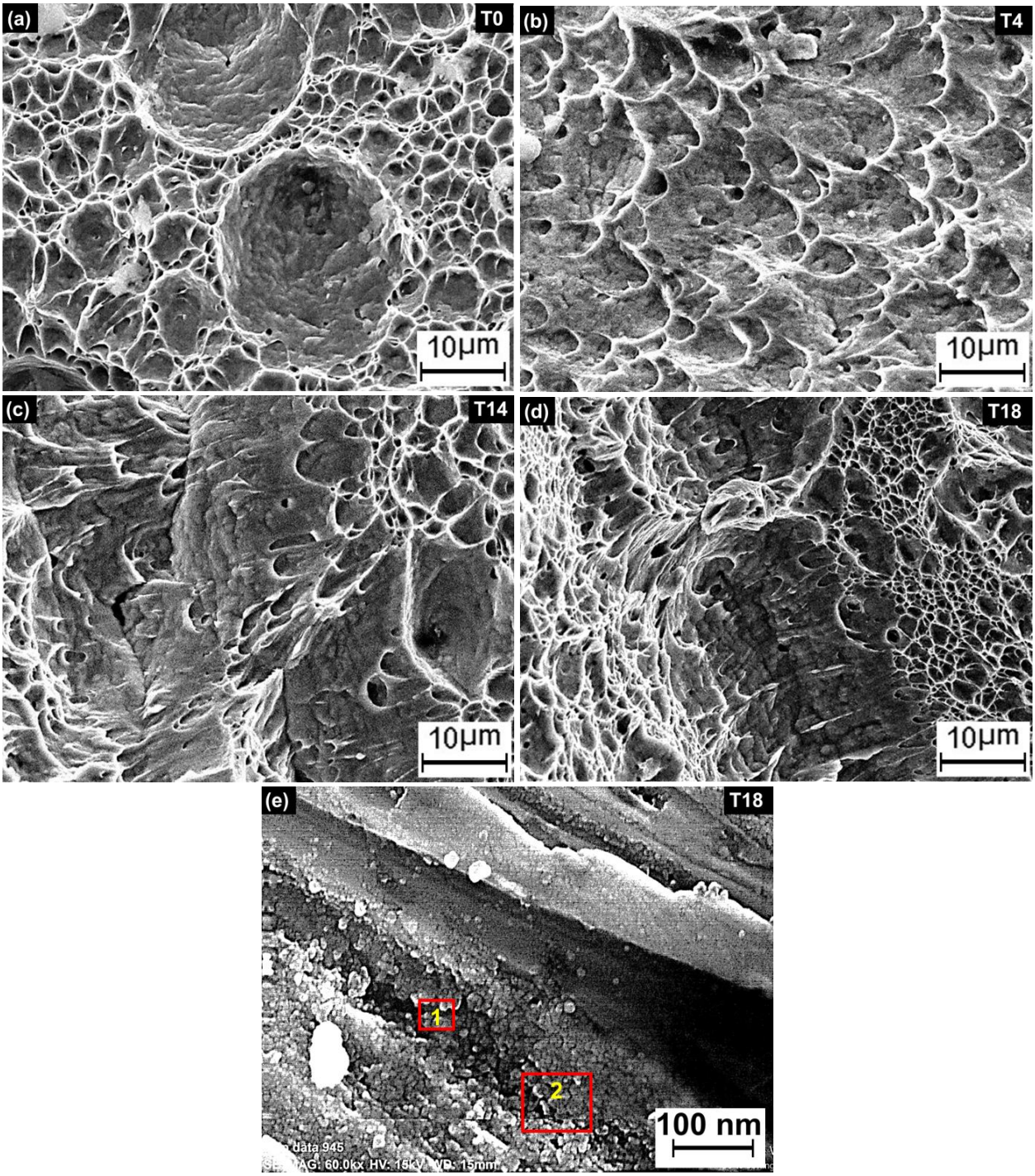

Figure 7.11 Impact fractographs of C250 steel at (a) T0 (b) T4, (c) T14, (d) T18 at 2000X and (e) T18 at 60000X magnification.

For aged samples (T4 condition), finer and shallow dimples are observed (Figure 7.11b). Further, for cold worked C250 steels the dimple size is very fine and narrow. The fracture results observed in the study compliment the fracture characteristics of precipitation hardened alloys. In these steels, the microvoids nucleate at the precipitates due to (a) stress-strain incompatibility between the

precipitates and the matrix, (b) localized deformation of soft matrix adjacent to the grain boundary precipitates, and (c) shearing of precipitates by dislocations leading to the formation of inhomogeneous planar slip bands within the grains. These slip bands can rupture at grain boundaries and, successively, apply large stress concentrations to supplement the grain boundary fracture.

Figure 7.12 presents the EDS analysis of points 1 and 2 marked in Figure 7.11. Table 7.10 present the chemical composition of selected points over Figure 7.11. The peaks of Fe, Ni, Co, Mo, and Ti etc. are observed.

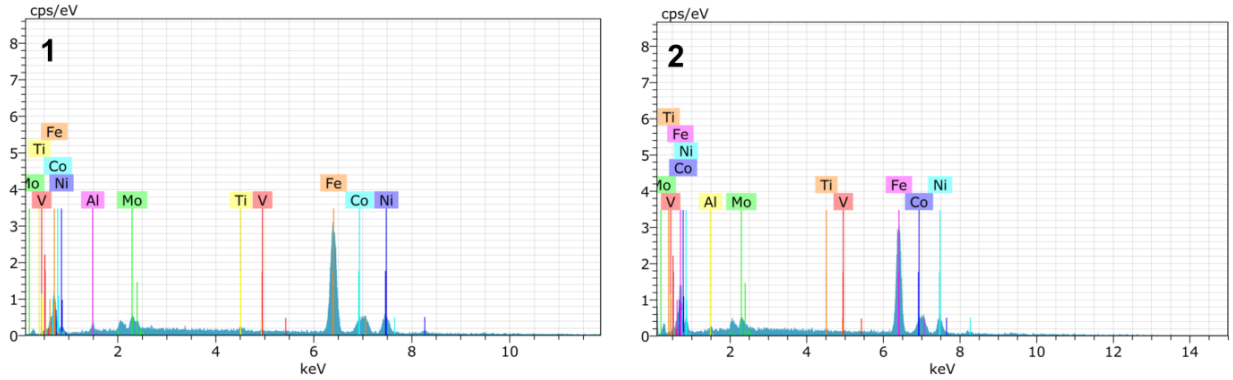

Figure 7.12 EDS analysis of point 1 and 2 marked in Figure 7.11.

Table 7.10 Composition analysis of energy spectrum on points as marked in Figure 7.11.

Points	Chemical composition (wt. %)					
	Fe	Ni	Co	Mo	Ti	Al
1	67.69	18.15	10.25	2.65	1.02	0.24
2	68.98	17.57	9.97	2.60	0.42	0.46

SEM fractographs of tensile and impact samples show some elongation of dimples in the cold working direction. The size of the dimples reduced indicating, the transition of fracture nature from ductile regime to the brittle regime. At higher cold work the intergranular tearing is observed which results in loss of ductility and impact toughness of solution annealed samples.

7.8 COST ESTIMATION

Cold working decreases the overall production cost of the components for automobile and aerospace applications. For fasteners of different sizes, two routes viz. conventional route and cold

working route are followed. Table 7.11 presents the steps followed and associated cost for the fabrication of fasteners using conventional route after hot rolling from a diameter of d1 mm.

Table 7.11 Associated cost for the fabrication of fasteners using the conventional route.

Steps for fastener fabrication	**Associated cost INR/1000 kg**
Hot rolling	5500
Solution annealing	4000
Peeling (two peeling cuts of 1mm each on diameter)	5500
Centerless grinding	4000
Cold heading	3000
Straightening	1500
Ageing	3000
Total cost from hot rolling to ageing	**26500**

If the fasteners of different diameter are to be prepared, the peeling cost of each diameter will increase. If the fasteners with base diameters decreasing by 1 mm are to be made into 10 different diameter fasteners then, the cost of 10 sizes will be incurred. From an initial hot rolled size of 38 mm diameter the fasteners of diameter 36, 35 …….12 mm, are made then the peeling cost will be there for all the sizes. For alternate route due to the cold working, different diameter bars are available for peeling and centreless grinding. Thus, a significant saving in the hot rolling, solution annealing, peeling and centreless grinding cost is observed. The total cost of making fasteners using alternate route is reduced to INR 19000 /1000 kg providing a saving of INR 7500/ 1000 kg.

CHAPTER 8
RESULTS AND DISCUSSION
300M STEEL

OVERVIEW

300M steel is a low-alloy ultrahigh-strength steel. It is widely used in aircraft and aerospace applications. 300M steel is derived from AISI 4340 steel. 300M steel consists of small additions of silicon and a small amount of vanadium which improve the grain refinement and also improves the strength, toughness, and resistance to stress corrosion cracking. 300M steels generally consists of yield strength (1615 MPa) and higher tensile strength (1963 MPa) however, a great loss in ductility is observed. This lowers the toughness of the steel. Therefore, in the present study an alternate route is developed to achieve a good strength-ductility combination which improves the toughness of the steel. This chapter presents the details of optical microstructure and SEM of 300M steel. XRD analysis was used to calculate the dislocation density and internal stress of the steel. The chapter also discusses the mechanical properties of 300M steel. Finally, the fractrography analysis of the fractured samples was also carried out.

8.1 300M STEELS

8.1.1 STARTING MATERIAL

300M steel was prepared at M/S Star Wire (India) Ltd. Ballabgarh, Haryana. The steel was prepared by the air melting route consisting of electric arc furnace (EAF)→ladle refining furnace (LRF)→vacuum degassing (VD)→electrode casting (580 mm diameter). Next, the primary melted heats were subjected to vacuum arc melting in state of art vacuum arc remelting (VAR) furnace supplied by ALD Germany. After remelting VAR specimen of 650 mm diameter and 2700 mm length were prepared. Table 8.1 presents the chemical composition of the primary melted heat and VAR remelted 300M steel. VAR processing parameters is shown in Table 8.2.

Table 8.1 Chemical composition (wt. %) primary and remelting SAE 300M steel.

Melting	C	Si	Mn	P	S	Cr	Mo	Ni	V	Cu	H	O	Fe
Primary	0.42	1.70	0.73	0.008	0.002	0.84	0.43	1.87	0.079	0.052	1.6ppm	20ppm	Bal.
Remelting	0.42	1.72	0.65	0.008	0.002	0.86	0.44	1.85	0.082	0.050	0.4ppm	6ppm	Bal.

Table 8.2 VAR Operating Parameters.

Parameters	Values
Mold Length (mm)	3300
Ingot Length (mm)	2690
Ingot Diameter (mm)	650
Electrode Diameter (mm)	580
Melt Rate (Kg/h)	450
DC Current (kA)	13
Applied Voltage (V)	24
Gap Length (mm)	15

8.1.2 THERMOMECHANICAL PROCESSING

Thereafter, VAR ingots of 650 mm diameter and 2700 mm length were homogenized at high temperature of 1160 °C at the rate of 30 minutes/inch. After homogenization, the heats were forged (double upsetting-drawing sequences) to the final forging size of 150 mm diameter. To ensure multi-directional properties, the cast structure was disrupted and the centreline segregation was reduced.

8.1.3 HEAT-TREATMENT

The as-forged bar was further normalized at 927 °C/1 hour→ air cooled and tempered at 650 °C/4 hours→ air cooled in batch-type heating furnace. Square samples of 30×30 mm in longitudinal and transverse directions were cut from normalized bar for conventional and modified heat-treatment. The designation of different heat-treatment conditions is given in Table 8.3. Figure 8.1 presents the process flow chart showing the process of fabrication of 300M steel.

Table 8.3 Heat-treatment conditions used for 300M steel.

Heat-treatment	Designation	Heat-treatment
Normalized Tempered	NT	Normalized(927°C/1Hr→AC)+Tempering(650°C/4Hr→AC)
Conventional Route	CQT	Hardening(870°C/1Hr→OQ)+ Double Tempering (302°C/2Hr→AC)
Isothermal Route	IST	Austenitizing (870°C/1Hr)→Isothermal transfer (300°C/30 min)→OQ + Tempering (180°C/2Hr→AC)
Modified Route	MAT	Hardening(870°C/1Hr→OQ) + Ambient Temperature Ageing for 8 days + Tempering (120°C/12Hr→AC)

Note: *AC-Air Cool, OQ- Oil quench*

8.2 MICROSTRUCTURE ANALYSIS

Figure 8.2a–d presents the optical micrographs of 300M steel after different heat-treatment. The microstructure of 300M steel consists of martensite, bainite and retained austenite (RA). Martensite mainly consists of laths parallel to each other while bainite is mainly observed as cross arranged bundles of different sizes. The bainite packet cross the martensite packet and divides it into finer units. Microstructure of NT condition showed higher retained austenite than IST, CQT and MAT conditions. Microstructure of CQT condition exhibited fine tempered martensite laths/plates compared to IST, MAT and NT conditions. It could be due to the direct quenching to oil followed by double tempering above martensite start temperature i.e. 290°C. Further, isothermal holding at 300°C increased the volume fraction of lower bainite which is tough in nature.

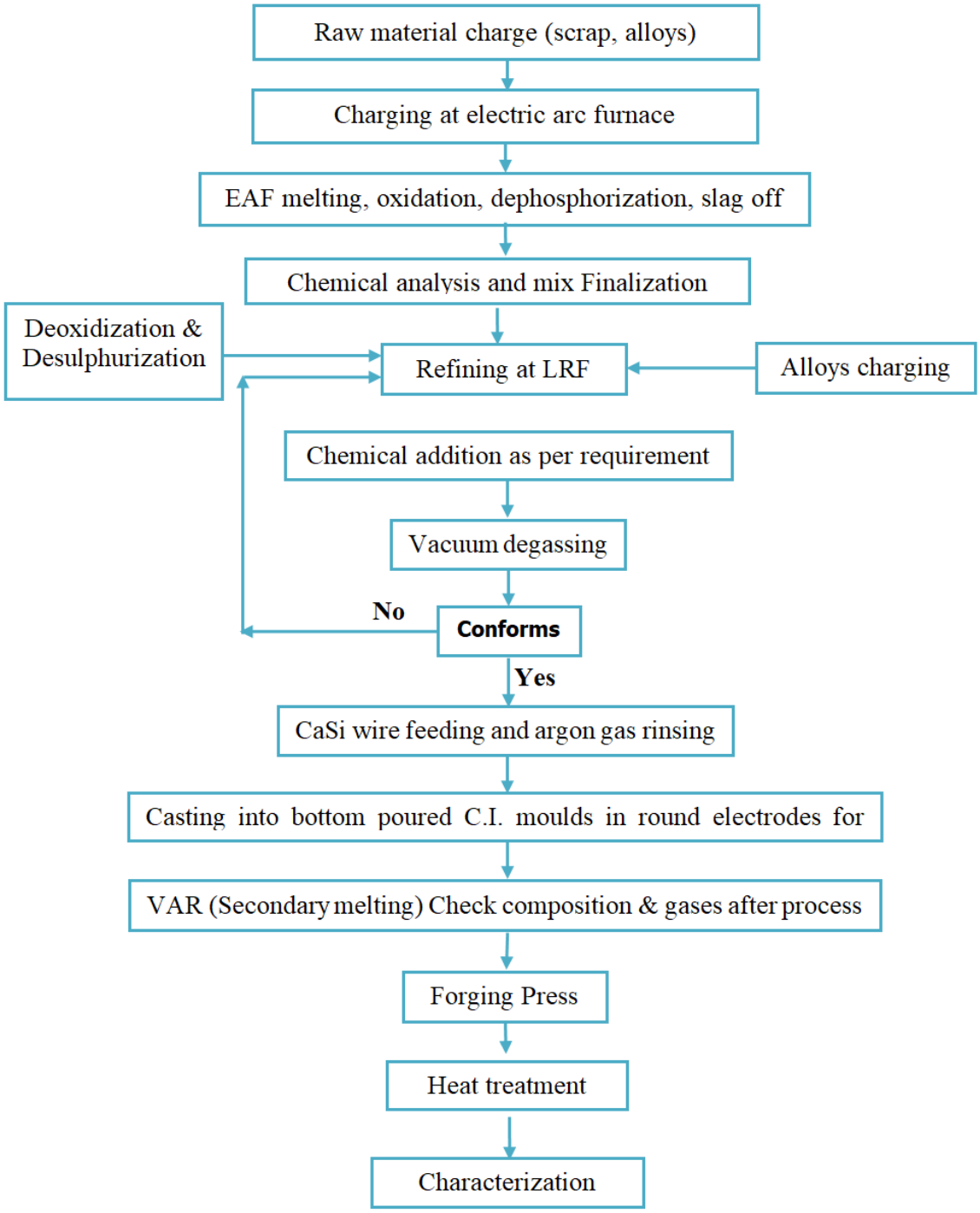

Figure 8.1 Process flow chart for manufacturing of 300M steel.

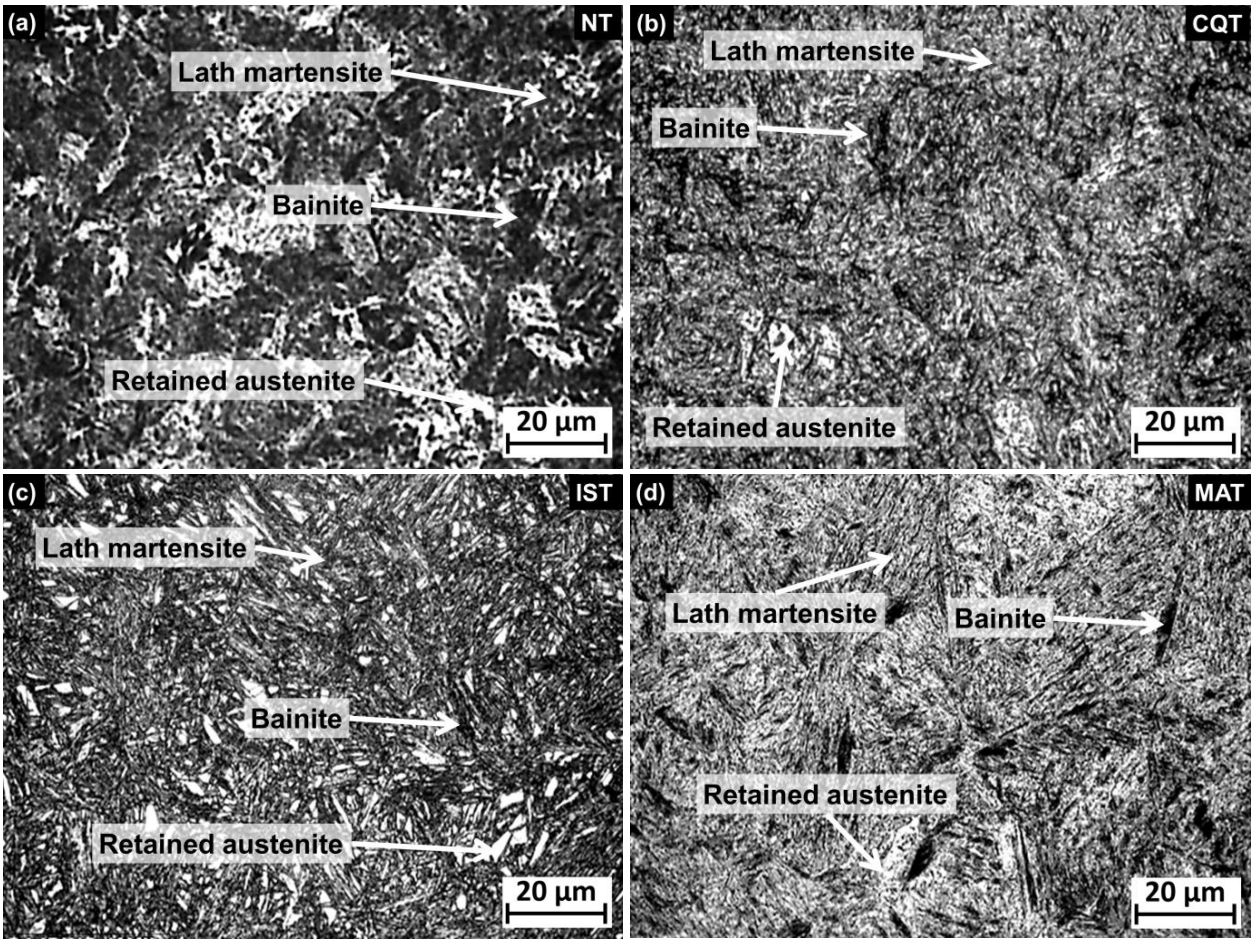

Figure 8.2 Optical microstructure heat treated 300M steel to condition (a) NT (b) CQT (c) IST and (d) MAT at 1000X magnification.

SEM microstructure of 300M steel, heat treated at different conditions is shown in Figure 8.3. It is observed that martensite consists of a large number of parallel laths. In case of IST, morphology of lower bainite presents the laths of cross arrangement. Time Temperature Transformation (TTT) diagrams of the 300 M steel shows the martensite start transition temperature (Ms) is about 277 ℃ and start and end points of bainitic transformation temperature is 466 ℃ and 270 ℃ [185]. It is also reported that austenite to bainite transformation start when holding time is over 100 second and completely transform after holding time excesses to 10000 second. The isothermal heat-treatment temperature (300℃) lies in bainitic transformation temperature range and some austenite transformed to bainite. The other austenite will transform to martensite when the temperature is below the Ms point during the subsequent quenching process. Simultaneously, small amount of austenite remained. Therefore, the microstructure of IST 300M steel is the mixture of martensite, bainite and retained austenite.

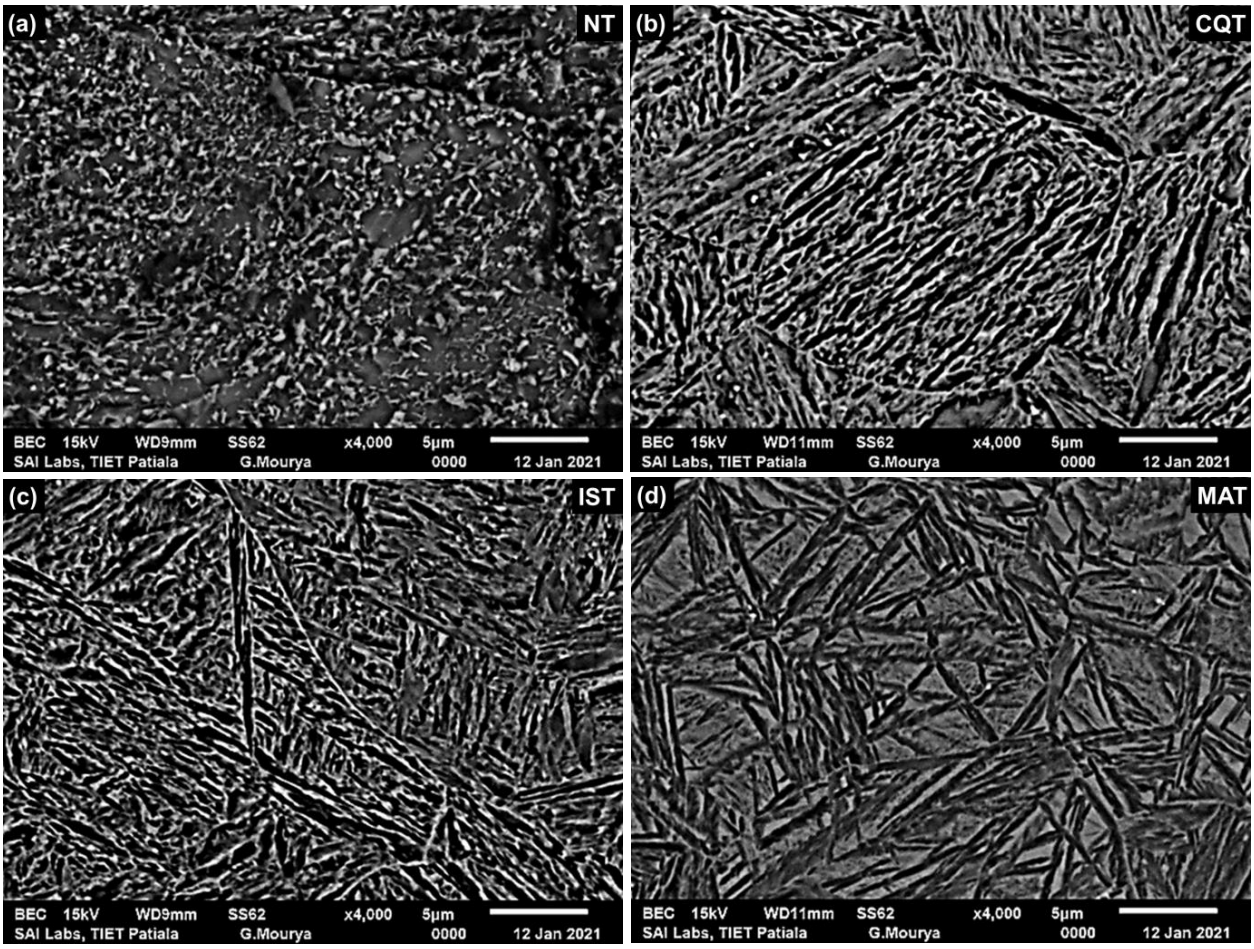

Figure 8.3 SEM microstructure 300M steel heat treated to condition (a) NT (b) CQT (c) IST and (d) MAT.

8.3 XRD ANALYSIS

X-ray diffraction spectra corresponding to NT, CQT, IST and MAT condition is shown in Figure 8.4. In the XRD patterns, peaks corresponding to planes (101), (110), (200), and (211) of iron-carbon ($C_{0.055}Fe_{1.945}$) (ICDD 00-044-1290) suggesting the Tetragonal crystal structure (space group 14/mmm) can be seen. The peaks in the spectrum of 300M steel correspond to the body centered tetragonal (BCT) matrix. The intensity of martensite peaks was higher for MAT heat treated 300M steel sample. It indicates that MAT 300M steel possess the thick plate/lath of martensite compared to other conditions.

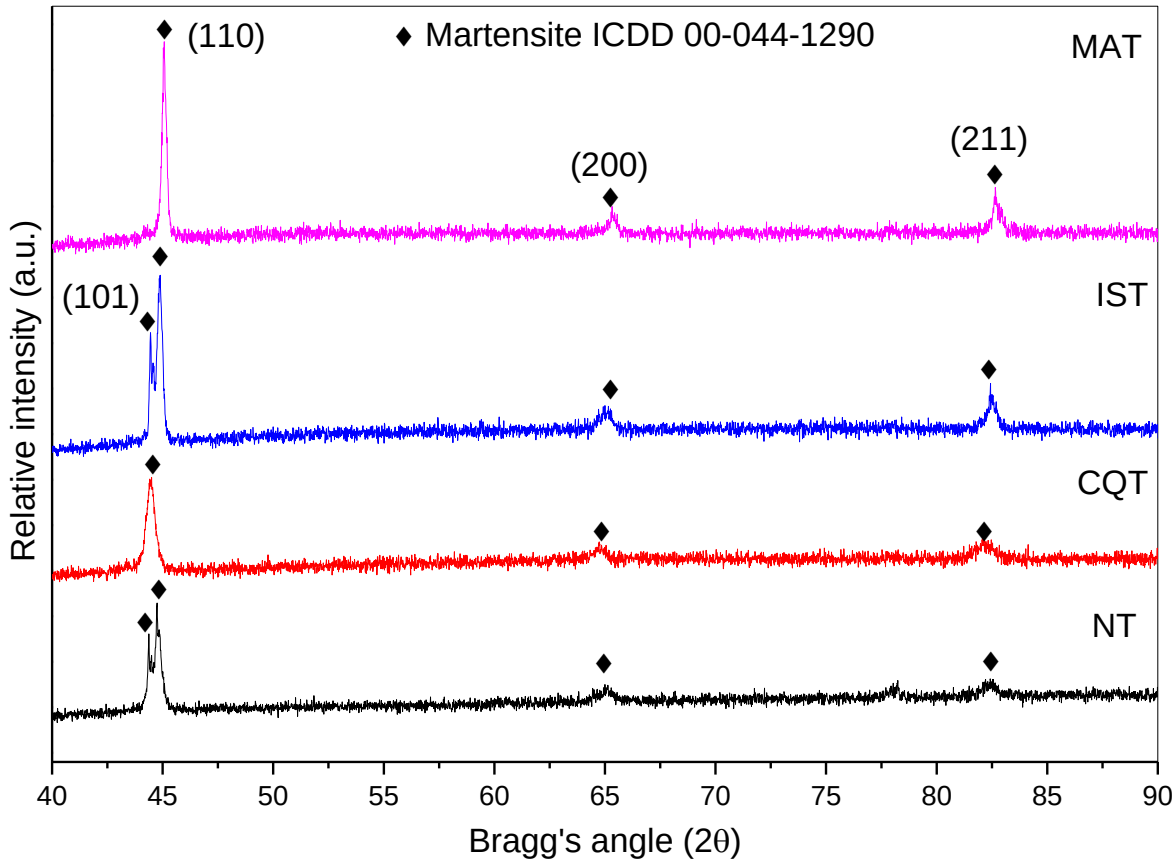

Figure 8.4 XRD pattern of different heat-treated samples.

Next, to determine the dislocation density, crystallite size is required. Crystallite size is calculated using the Williamson-Hall (W-H) analysis. Bragg angle (2θ) and corresponding full width half maxima (FWHM) β_{hkl} is determined by curve fitting in origin using Gaussian and Lorentzian function (Figure 8.5).

The peak is assumed to be symmetric along the Bragg angle (2θ). Crystallite size is determined using the Scherrer equation which is a volume weight quantity and is dependent upon β_{hkl}. Scherrer equation is presented in Equation 8.1 [183]. In this, the peak broadening is attributed to the crystallite size. Further, Stokes and Wilson proposed the broadening of peaks due to strain formulation [183].

$$D = \frac{k.\lambda}{\beta_{hkl}.\cos\theta_{hkl}} \tag{8.1}$$

Where

D: Crystallite size (nm)

K: shape factor

θ_{hkl}: Bragg angle

β_{hkl}: FWHM

λ: X-ray wavelength 0.15406 nm

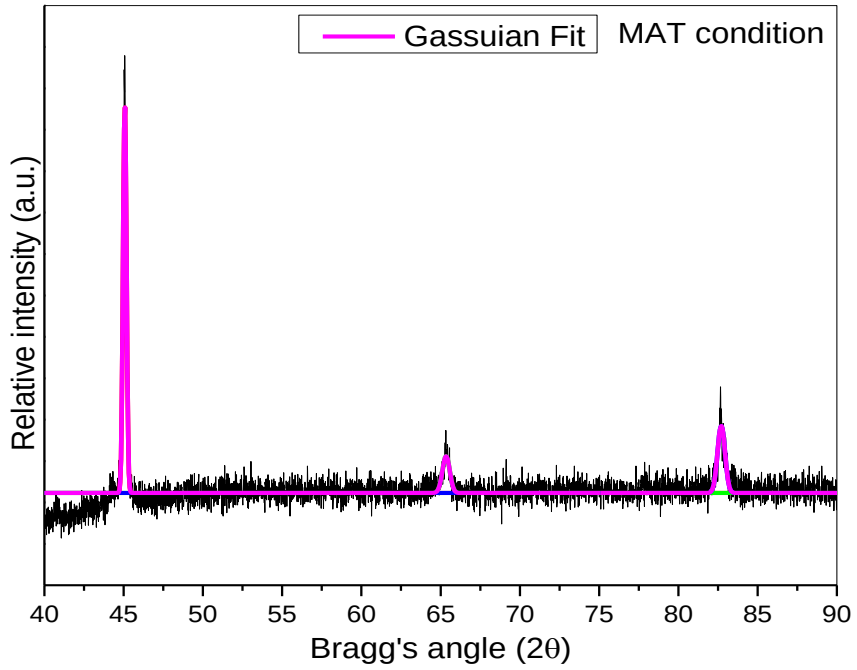

Figure 8.5 Gaussian and Lorentzian function of XRD analysis.

Figure 8.6 presents the plot of cos θ versus 1/β of Scherrer equation. The slope of the above graphs indicates $K\lambda/D$ from which the crystallite size can be calculated. The calculated crystallite size is presented in Figure 8.4.

Mathematical formula for peak broadening due to strain (ε) called as induced strain is given by Equation 8.2.

$$\beta_{hkl} = 4\varepsilon.\tan\theta_{hkl} \quad (8.2)$$

β_{hkl} is the combination of Equation 8.1 and Equation 8.2 and W-H plot is used to separate the individual effects.

$$\beta_{hkl}.\cos\theta_{hkl} = \frac{k\lambda}{D} + 4\varepsilon.\sin\theta_{hkl} \quad (8.3)$$

Equation 8.3 presents the uniform strain model (USM) of W-H analysis with an assumption that strain distribution is isotropic throughout the crystal.

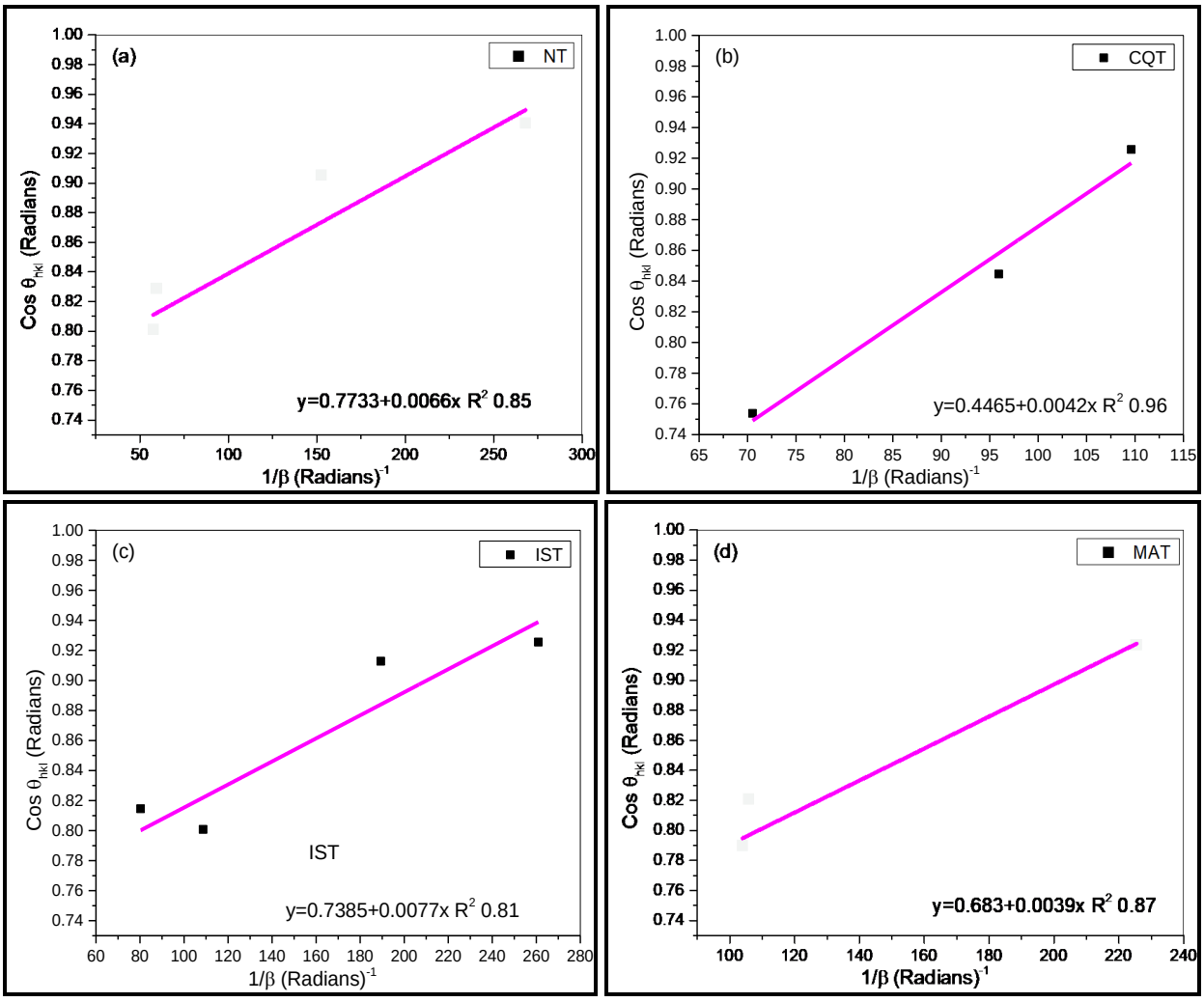

Figure 8.6 Scherrer equation plots of cos θ versus 1/β for the XRD samples presented in Figure 8.4.

Figure 8.7 presents the plots of $\beta_{hkl}.\cos\theta_{hkl}$ and $4\sin\theta_{hkl}$ for USM model. The magnitude of strain and size can be estimated from the slope and intercept of graph plotted between '$\beta_{hkl}.\cos\theta_{hkl}$' and '$4\sin\theta_{hkl}$' respectively. Figure 8.8 presents the graph between 4 Sin θ/E_{hkl} as X-axis and β cos θ along Y-axis. UDM model is related to an isotropic (perfect) crystal system in all (hkl) planes. The slope (4 Sin θ) and intercept ($K\lambda/D$) of fitted line represents the strain and crystal size, respectively.

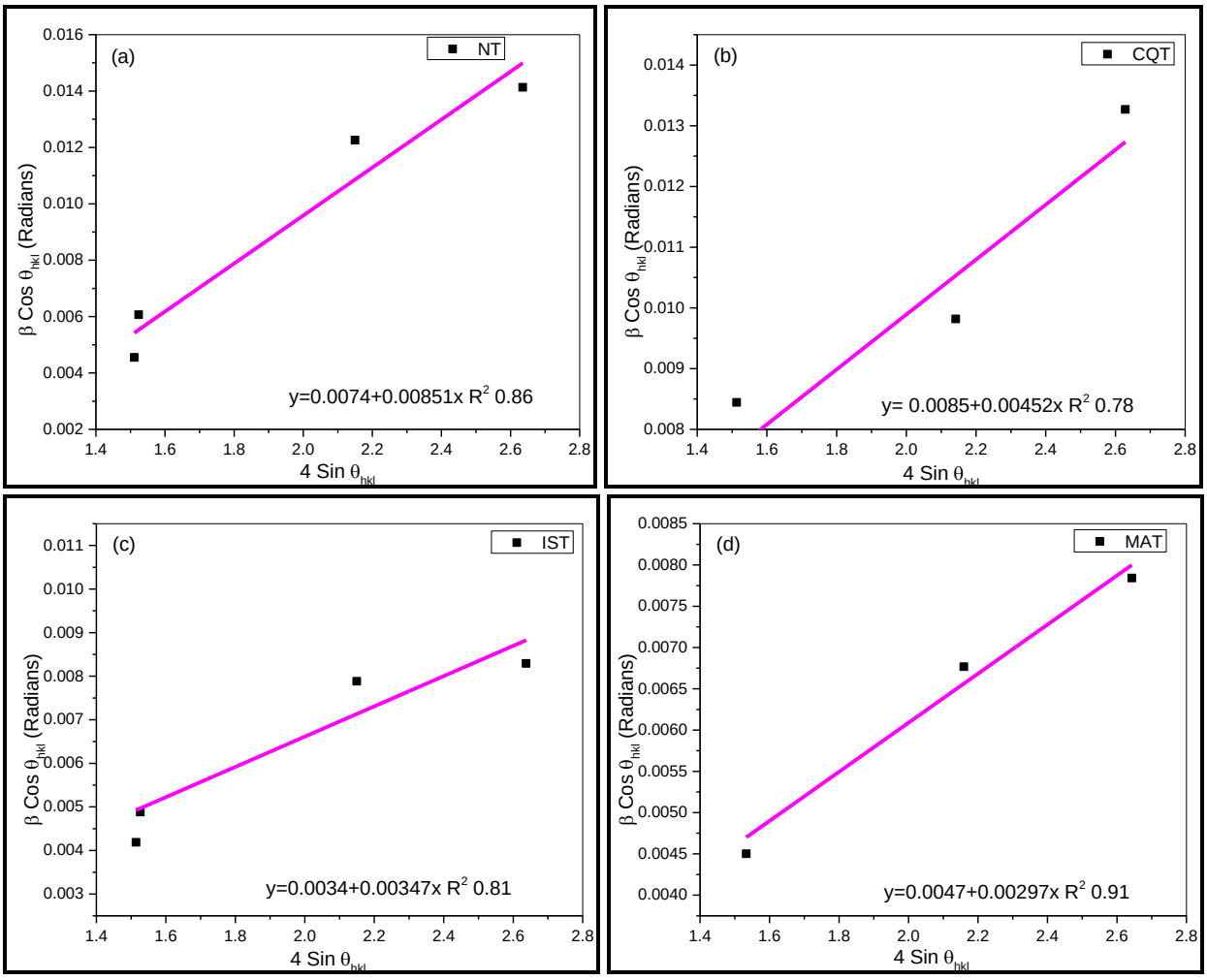

Figure 8.7 W-H equation plots of β cos θ versus 4 Sin θ for the XRD samples presented in Figure 8.4.

Since many of the cases strain homogeneity does not hold therefore, stress homogeneity and strain energy homogeneity are considered [183]. W-H analysis suggests USDM (Equation 8.4), and USEDM (Equation 8.5) models.

$$\beta_{hkl}.\cos\theta_{hkl} = \frac{k\lambda}{D} + \frac{4\sigma \sin\theta_{hkl}}{E_{hkl}} \tag{8.4}$$

$$\beta_{hkl}.\cos\theta_{hkl} = \frac{k\lambda}{D} + 4\sin\theta_{hkl}\left(\frac{2\upsilon}{E_{hkl}}\right)^{0.5} \tag{8.5}$$

For tetragonal crystal system Young's modulus along the normal direction of lattice plane (hkl) is given by Equation 8.6 [186].

$$\frac{1}{E_{hkl}} = \frac{s_{11}(h^4+k^4)+(2s_{12}+s_{66})h^2k^2+(2s_{13}+s_{44})(h^2+k^2)L^2+s_{33}L^4}{(h^2+k^2+L^2)^2} \tag{8.6}$$

Where, $L = \frac{a.l}{c}$, $s_{11} = 6.10 \times 10^{-3}\ GPa^{-1}$, $s_{12} = -1.98 \times 10^{-3}\ GPa^{-1}$, $s_{13} = -2.39 \times 10^{-3}\ GPa^{-1}$, $s_{33} = -7.20 \times 10^{-3}\ GPa^{-1}$, $s_{44} = 11.55 \times 10^{-3}\ GPa^{-1}$, $s_{66} = 10.49 \times 10^{-3}\ GPa^{-1}$, a=0.28337 nm, and c=0.29354 nm [187].

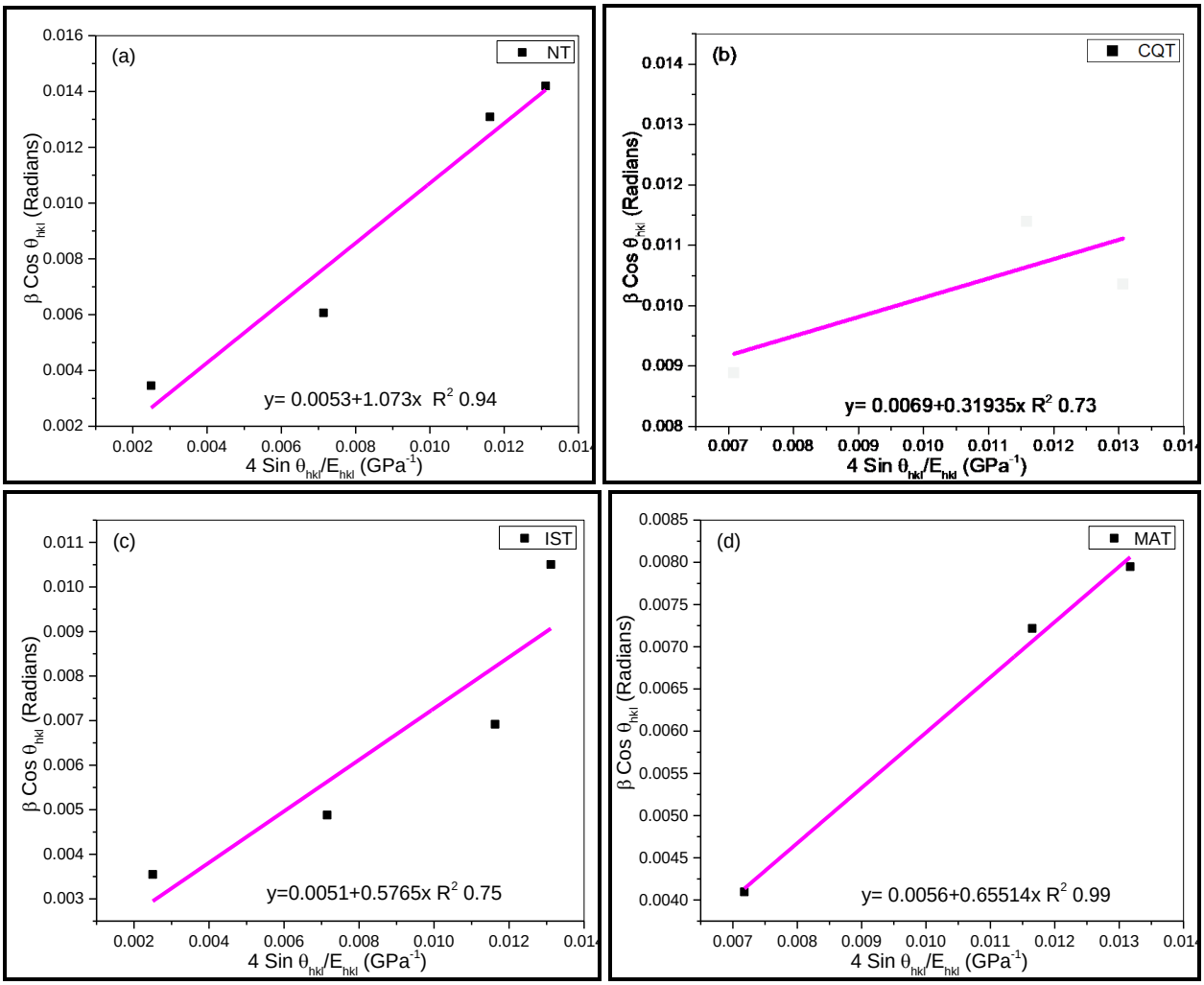

Figure 8.8 W-H equation plots of β cos θ versus 4 Sin θ /E for the XRD samples presented in Figure 8.4.

The slope and intercept of Figure 8.8 presents the value of stress and $K\lambda/D$ from slope and intercept of line fitted for USDM model. From the stress the strain in the system can also be calculated. The value of crystallite size, stress and strain is presented in Figure 8.4. Further, Figure 8.9 presents the plot fitted from USEDM model. The calculations from slope and intercept provide the calculations of strain energy and crystallite size. From strain energy calculations, stress and strain was also calculated. Figure 8.4 presents the different values of stress, strain etc. calculated

from different models. The lattice strain of MAT 300M steel was lower than other steel samples. This could be due to the presence of thick plate/lath of martensite compared to other conditions.

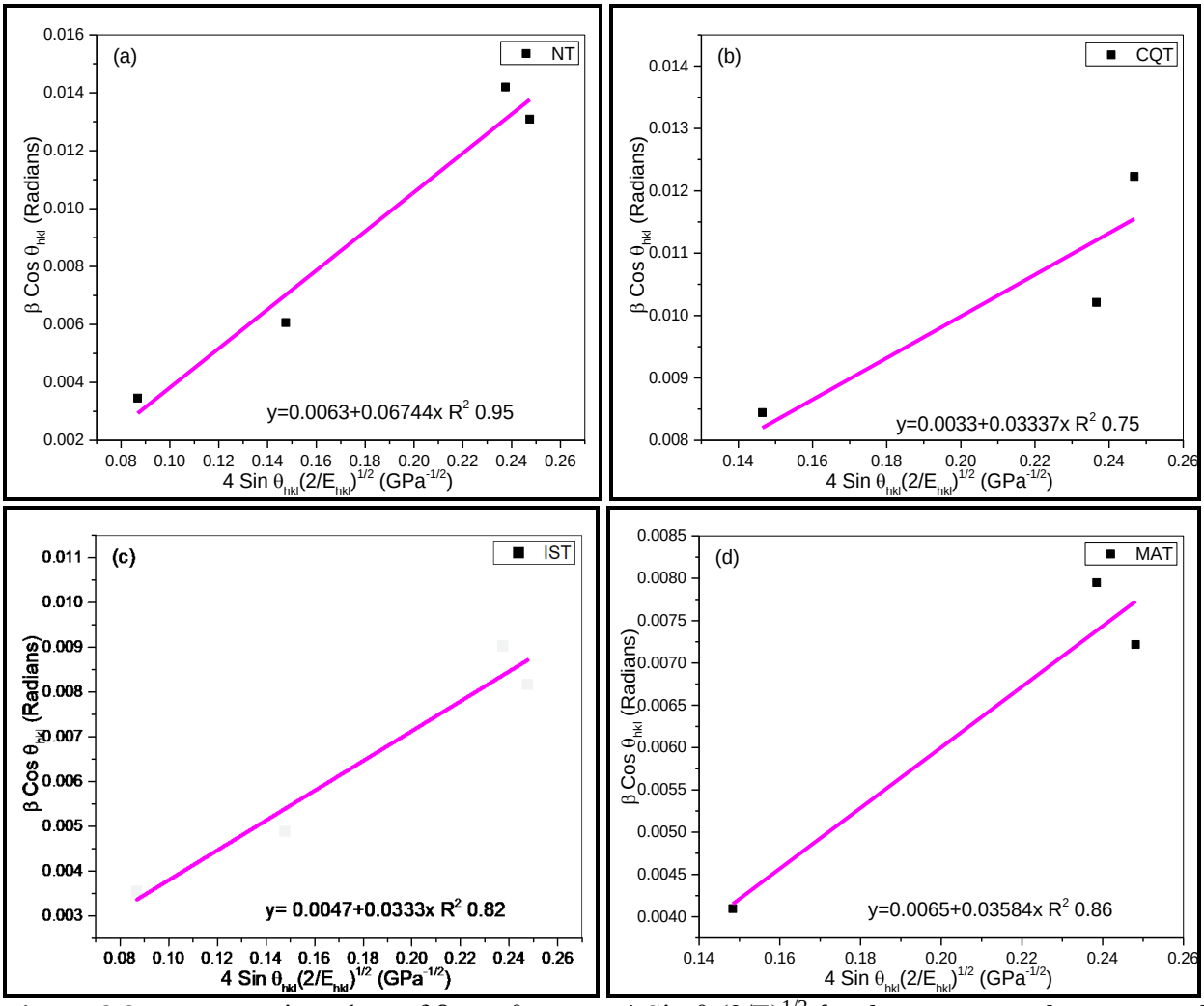

Figure 8.9 W-H equation plots of β cos θ versus 4 Sin θ $(2/E)^{1/2}$ for the XRD samples presented in Figure 8.4.

Table 8.4 Williamson-Hall analysis of different heat treated 300M steels.

Attribute	Scherrer	USM		USDM			USEDM			
	D (nm)	ε×10^{-3}	D (nm)	σ (GPa)	D (nm)	ε× 10^{-3}	U × 10^{3} (kJ/m^{-3})	D (nm)	ε× 10^{-3}	σ (GPa)
NT	23.3424	8.51	20.819	1.073	29.068	3.545	4.5482	24.454	5.482	1.659216
CQT	36.6809	4.52	18.125	0.3195	22.327	1.056	1.1136	46.685	2.713	0.820997
IST	20.0077	3.47	45.312	0.5765	30.208	2.862	1.1089	32.779	3.318	0.668401
MAT	39.5025	2.97	32.779	0.6551	27.511	3.252	1.2845	23.702	3.571	0.719384

Figure 8.5 presents the dislocation density of 300M steels using different models. USDM and

USEDM models provided the closest fit to the experimental data. Dislocation density of MAT heat treated samples was superior to other heat-treated specimen.

Figure 8.5 Dislocation density ($\times 10^{15}$ m^2) of 300M steel using different models.

Attribute	Scherrer	USM	USDM	USEDM
NT	1.835304	2.307192	1.18351	1.67225
CQT	0.743222	3.044094	2.005942	0.458826
IST	2.498053	0.487055	1.095874	0.930713
MAT	0.64084	0.930713	1.321284	1.78011

8.4 MECHANICAL PROPERTIES

Figure 8.10 presents the engineering stress-strain curves of different heat treated 300M steel. Further, Table 8.6 presents the mechanical properties of NT, CQT, IST and MAT 300M steel. For NT condition, % elongation and % reduction in area (% RA) was higher than the other steel formulations. However, hardness, yield strength (YS), and ultimate tensile strength (UTS) of NT sample was inferior to other steel formulations.

The best combination of mechanical properties was achieved by the IST heat treated 300M steel. IST steel exhibit comparatively better mechanical properties in terms of % elongation, % RA, impact energy with marginal loss in YS and UTS. It is attributed to a good combination of hard martensite, tough bainite and soft retailed austenite microstructure of IST 300M steel. Heat-treatment of 300M steel refined the grain size of bainite, martensite and retained austenite. The microstructure refinement was higher for CQT and MAT heat treated 300M steels. The higher refinement in the microstructure increases the grain boundaries in the microstructure. Grain boundaries act as a barrier to the dislocations and increase the resistance to deformation and increase the YS and UTS of steel.

Table 8.6 Mechanical properties of 300M steel after different heat-treatment conditions.

Heat No.	Hardness (HRC)	0.02%YS (MPa)	UTS (MPa)	Elongation (%)	Area Reduction (%RA)	Impact Energy (J)
NT	24	616	871	23	56	18
CQT	57	1744	2036	9	27	20
IST	56	1605	1890	14	35	24
MAT	59	1568	2256	8	10	14

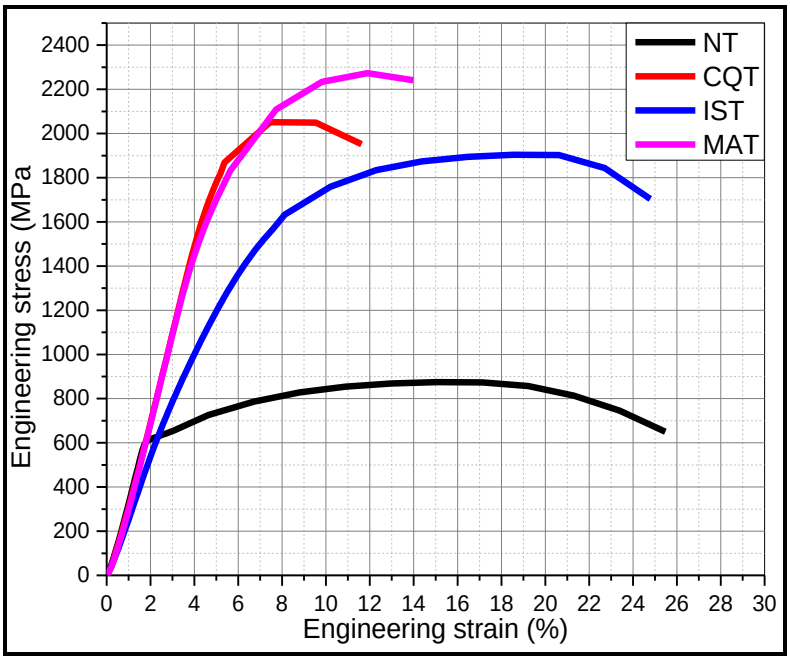

Figure 8.10 Engineering stress-strain curves of different heat treated 300M steel.

8.5 FRACTOGRAPHY

Figure 8.11 presents the SEM analysis of tensile fracture surfaces. SEM analysis revealed dimple type structure indicating the ductile fracture. For NT condition fine dimple like structures was observed (Figure 8.11a). The small dimples observed for NT 300M steel could be the resultant of the localized deformation of grain boundaries while the size of the final dimple is dependent upon the grain boundary deformation of the 300M steel. Dimple size and shape is ruled by the dislocation density and microvoids that are nucleated in the steel. Higher dislocation densities increase the resistance of material to deformation and decrease the size of the dimples and reduce the ductility of the steel. The dimples in MAT and CQT steels are shallow and wide indicating reduced ductility of the steels as shown in Figure 8.11b and Figure 8.11d. Further, the shape of the dimple is primarily governed by the internal stress and dislocation density of the steels.

Figure 8.12 presents the SEM images of impact fractographs of various heat-treated conditions. The fracture is mainly of ductile nature with the formation of microvoids. NT steel clearly indicates the formation of shear fractures and vein type fractures. Shear fractures are the resultant of the shear force acting on the steel sample due to impact.

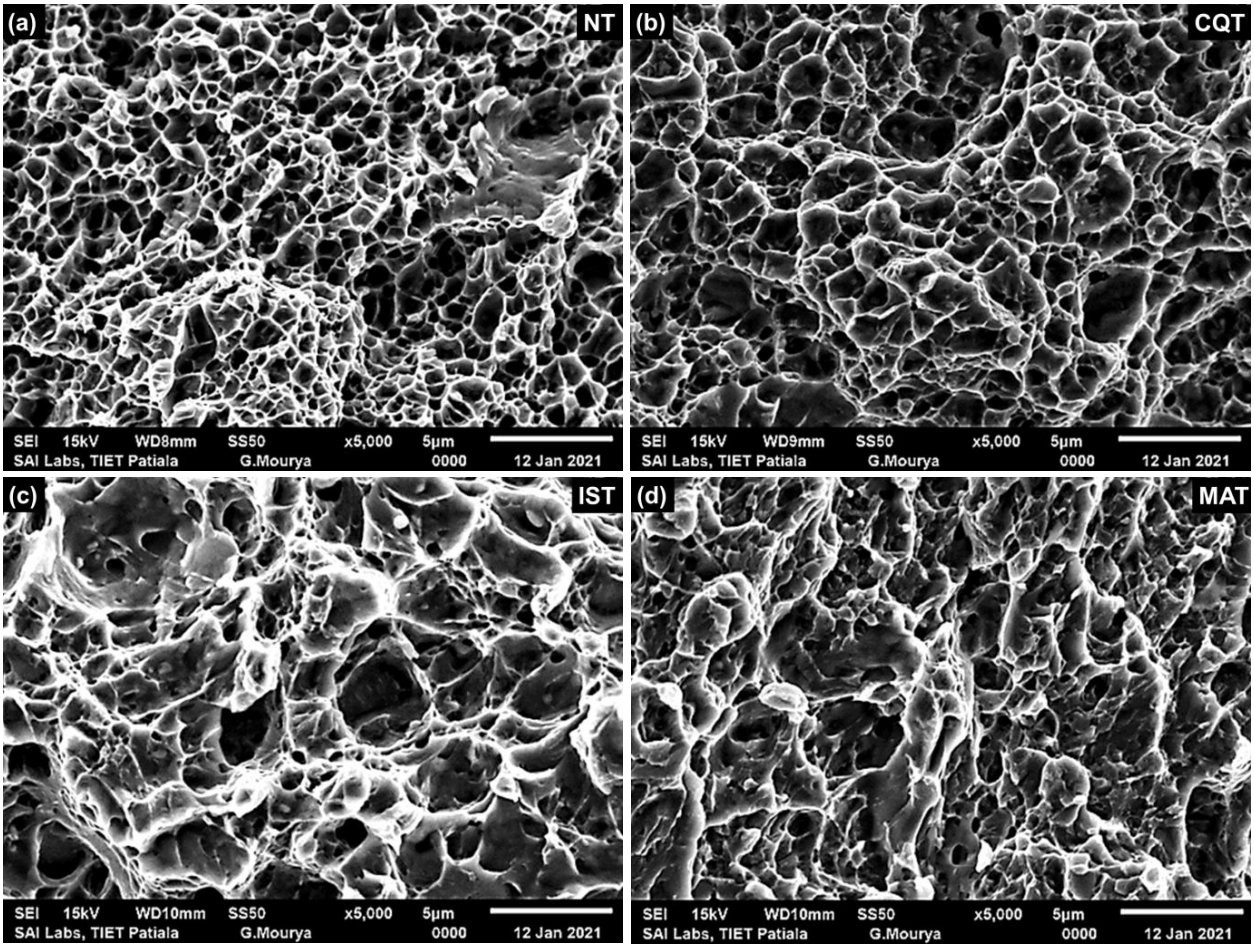

Figure 8.11 Tensile fractographs of 300M steel with various heat-treated condition (a) NT (b) CQT (c) IST and (d) MAT.

Further, vein type structure is an indicative of the failure of the material due to the amorphous nature of the grain boundaries (Figure 8.12a). Large sized dimples are observed for CQT, IST, and MAT 300M steels as shown in Figure 8.12(b–d). The fracture results observed in the study compliment the fracture characteristics of 300M steels. For 300M steel, higher dislocation density increases the resistance to deformation and thus improves the toughness of the 300M steels. Microvoids nucleate at the grain boundaries and increase the impact strength of the steel. NT condition shows the greater number of shear fracture and dimples which support the higher ductility and impact energy findings. CQT and MAT fractographs show the mixed dimples and cleavage type features. While the IST condition exhibits the deep and large dimples.

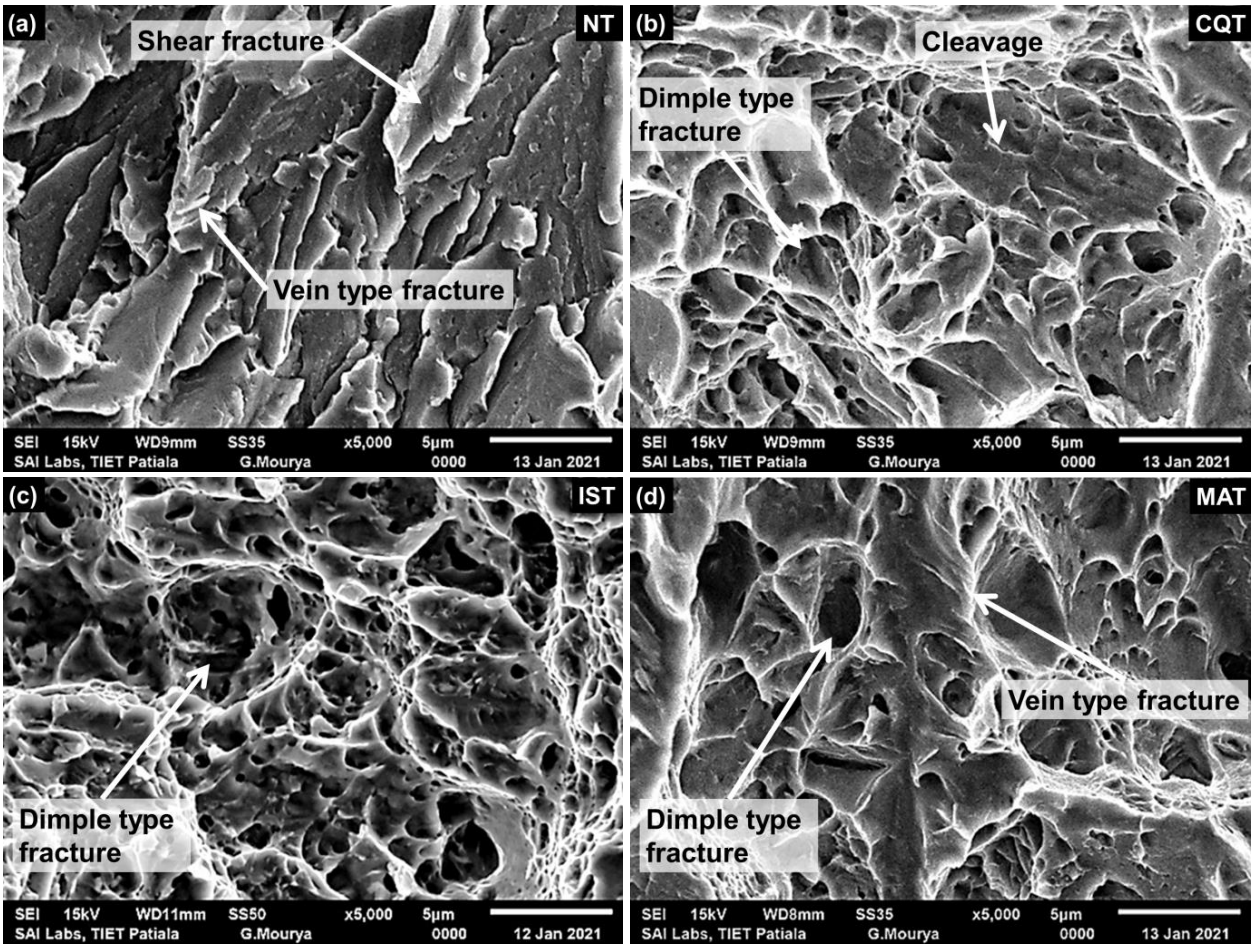

Figure 8.12 Impact fractographs of 300M steel with various heat-treated condition (a) NT (b) CQT (c) IST and (d) MAT.

CHAPTER 9
CONCLUSIONS

OVERVIEW

This chapter presents the major conclusions drawn from the present study. Different grades of ultra-high strength steels (UHSS) with variation in compositions were developed for different engineering applications. The conclusions drawn from the studied steels viz. AMS-4340 steels, 10.7CrMoVNbN steels, AISI321 steels, C250 steels, and 300M steels have been presented in this chapter. The chapter also discusses the future scope of work.

9.1 AMS 4340 STEEL

- The designated chemical composition as per the specification of AMS-4340 is achieved in all the developed ESR heats whereas, the least elemental segregation is observed for the ESR heat E4.
- Macrostructure evaluation revealed the presence of hydrogen flakes in ESR heats E1, E2, and E3, whereas, no hydrogen flakes are observed in ESR heat E4. Microstructure characterization revealed that the hardening and tempering of the ESR heats refined the microstructure.
- Ultrasonic testing revealed that no internal defects are observed for the ESR heat E4.
- ESR heat E4 achieved the best combination of mechanical properties. Thus, the proposed route used here for ESR heat E4 can be used as an alternate path to manufacture AMS-4340 UHSS without the use of vacuum induction melting and vacuum arc remelting process.
- The processing route suggested is more economical than the method currently used (VIM+VAR) for the manufacturing of UHSS.

9.2 10.7CrMoVNbN STEEL

- 10.7CrMoVNbN steel was given different thermo-mechanical treatments where the presence of delta-ferrite was monitored. The δ-ferrite concentration decreased from Heat 1 to Heat 4. The volume fraction of δ-ferrite for Heat 3 and Heat 4 was lower than 2% which was within the acceptable limit.
- Cr_{eq} values and Multiple multi-directional forging are controlling factors for delta-ferrite in this high strength and creep resistant martensitic steel. In Heat 3 and Heat 4, the chromium and other ferrite formers are kept at the lowest permissible level of the standard specification. When chromium equivalent is restricted to less than 12, δ-ferrite content was minimized in this grade of heat resistant steel.
- FESEM-EDS analysis revealed the formation of carbides in the tempered martensite matrix. Mainly two types of precipitates viz. NbMoC, and NbC were observed. The size of NbMoC precipitates was larger (5–10 μm) whereas the size of NbC precipitates was smaller than 2 μm.
- Microhardness analysis confirmed the presence of tempered martensite matrix, delta-ferrite phase, and different carbides.

- Mechanical properties of 10.7CrMoVNbN steel (Heat 1, Heat 2, Heat3, and Heat 4) exhibited that Heats having lower delta-ferrite showed improved mechanical properties. $Cr_{eq} \leq 12$ (Heat 3 and Heat 4) showed a marginal improvement in YS, UTS, % elongation, and % RA whereas, a significant improvement in impact strength was observed.
- Heat 4 with Cr_{eq} of 11.59 showed the best improvement in the mechanical properties. Further, the δ-ferrite content of Heat 4 was 0.3% which is much lower than the permissible limit of 2%. Hence, Heat 4 fulfilled the material specifications specified by industries.

9.3 AISI-321 STEELS

- Addition of boron to the AISI 321 steels increased the precipitate count in the steels. The precipitates were largely in the size range of 1-10μm^2. The precipitate count was higher for as-rolled and solution annealed condition as compared to the forged condition both for TB1 and TB30 steels.
- Optical micrographs revealed a uniform distribution of precipitates in the austenite matrix. The precipitates were largely located on the grain boundaries. Further, addition of boron to the steel refined the microstructure. Finest grain size was observed for rolled condition both for TB1 and TB30 steels.
- FESEM-EDS analysis revealed that TB1 steel comprised of austenite grains along with the precipitates of nitride (TiN) and carbonitride (TiCN). Whereas, for TB30 steel the precipitates of nitride (TiN) and carbonitride (TiCN) along with precipitates Fe_2B and Cr_2B were also observed. Fe_2B and Cr_2B precipitates are stable and provide improved yield strength stability of TB30 steels.
- Boron addition in TB30 steel improved the YS and UTS of the AISI 321 steel with a marginal loss in ductility. SA and ST TB30 steel exhibited best mechanical properties both at room and elevated temperatures. YS to UTS ratio of TB30 steel was lower both at room temperature and elevated temperature. This indicated that rolled and solution annealed TB30 steel is more suitable material to replace the inlet and outlet water tubes of VVER type nuclear reactor.
- Sensitization study also shows that TB30 steel under SA and ST condition are highly stable. TB30 steel under SA and ST condition are less prone to sensitization and provide superior

mechanical properties and improved corrosion resistance. Hence, these steels are more suitable for use in inlet and outlet water tubed of VVER type nuclear reactor.

9.4 C250 STEELS

- The microstructure of C250 steel in solution annealed condition comprises of the lath martensite along with the presence of prior austenite, while SA+ aged and SA+ coldworked+ aged conditions demonstrate the fine lath of martensite, retained austenite along with precipitates of Ni_3Ti and Fe_2Mo. Further, cold working improved the refinement in grain size.
- XRD analysis of C250 maraging steel predicted the presence of iron-nickel martensite.
- It is observed that hardness, YS and UTS increased drastically after ageing (T4) compared to solution annealed condition (T0). It is due to the presence of large numbers of precipitates and conversion of retained austenite/prior austenite grains into martensite. T14 and T18 steels presented the best combination of mechanical properties, thus can be used for the automobile and aerospace applications.
- Tensile and impact fractographs revealed the ductile type of fracture. With an increase in cold working, the dimples became shallow and smaller in size depicting the transition of failure mode from ductile to brittle.
- Cost estimation study revealed that cold drawing as an alternate method and provided a significant saving in the fabrication of fasteners over the conventional hot rolled method.

9.5 300M STEELS

- Optical micrographs revealed that 300M steel comprises a mixture of parallel laths of martensite, cross arranged white bundles of bainite and small quantities of retained austenite. The refinement of IST, and MAT 300M steels was higher than the other steel samples. Further, SEM analysis revealed that IST 300M steel exhibits moderate amount of retained austenite, sufficient amount of bainite and large amount of martensite.
- XRD analysis of 300M steel indicates the formation of martensite peaks. The crystallite size resulting from USM, USDM, and USEDM models of W–H method are almost accurate and provide a close comparison.

- The best combination of mechanical properties was achieved by the IST heat treated 300M steel. IST steel exhibit comparatively better mechanical properties in terms of % elongation, % RA, impact energy with marginal loss in YS and UTS.
- Fractrography analysis revealed a dimple like structure indicating ductile failure of 300M steels. The tensile fractrographs of NT specimen indicated the formation of fine and uniform dimple structure indicating higher ductility. Further, impact fractrographs showed a mixture of dimples, cleavage and vein type of failure. Fractrographs of IST 300M steel showed uniform dimple structure indicating the higher ductility and impact energy.

9.6 FUTURE SCOPE

This section presents the future scope of the present study:

- For AMS-4340 steels following studies may be conducted in future:

(i) High strain rate mechanical properties and strain hardenability study for ballistic resistance application.

(ii) Advanced characterization such as HR-TEM, EBSD and XRD etc. for in-depth analysis to develop structure-properties-performance correlation.

- For 10.7CrMoVNbN steel following studies may be conducted in future:

(i) Simulation study on chemical composition and thermomechanical process optimization to achieve negligible/nil delta-ferrite.

(ii) Creep and corrosion study with respect to delta-ferrite at identical conditions being experienced by steam turbines.

(iii) Advanced characterization such as HR-TEM, EBSD and XRD etc. for in-depth analysis to develop structure-properties-performance correlation.

- For AISI-321 steel following studies may be conducted in future:

(i) Boron (B) plays a crucial role in determining the final microstructure and properties. Boron content can be varied from 5 PPM to 2 % to study the effect on strengthening mechanism and mechanical properties. Design of experiment (DOE) may be used to optimize the boron level to obtain better results.

(ii) Creep and corrosion study with respect to boron content variation at identical conditions being experienced in nuclear reactors and similar applications.

(iii) Advanced characterization such as HR-TEM, EBSD and XRD etc. for in-depth analysis to develop structure-properties-performance correlation.

- For C250 steel following studies may be conducted in future:

(i) Simulation study on cold deformation and heat-treatment optimization.

(ii) Advanced characterization such as HR-TEM, EBSD and XRD etc. for in-depth analysis to develop structure-properties-performance correlation.

(iii) Cost reduction study between suggested routes and currently used at industrial scale.

- For 300M steel following studies may be conducted in future:

(i) High strain rate mechanical properties and strain hardenability study for ballistic resistance application.

(ii) Advanced characterization such as HR-TEM, EBSD and XRD etc. for in-depth analysis to develop structure-properties-performance correlation.

(iii) Comparative study of ballistic performance between AMS-4340 and AISI 300M (modified AMS 4340 steel).

REFERENCES

[1] Nanda T, Singh V, Singh V. Third generation of advanced high-strength steels : Processing routes and properties. Proc Inst Mech Eng Part L J Mater Des Appl 2019;233:209–38. doi:10.1177/1464420716664198.

[2] Meng Q, Li J, Wang J, Zhang Z, Zhang L. Effect of water quenching process on microstructure and tensile properties of low alloy cold rolled dual-phase steel. Mater Des 2009;30:2379–85. doi:10.1016/j.matdes.2008.10.026.

[3] Saleh MH, Priestner R. Retained austenite in dual-phase silicon steels and its effect on mechanical properties. J Mater Process Technol 2001;113:587–93. doi:10.1016/S0924-0136(01)00638-0.

[4] KUZIAK R, KAWALLA R, WAENGLER S. Advanced high strength steels for automotive industry. Arch Civ Mech Eng 2008;8:103–17. doi:10.1016/S1644-9665(12)60197-6.

[5] Shi C bin, Huang Y, Zhang J xiao, Li J, Zheng X. Review on desulfurization in electroslag remelting. Int J Miner Metall Mater 2021;28:18–29. doi:10.1007/s12613-020-2075-3.

[6] Pickering EJ. Macrosegregation in Steel Ingots: The Applicability of Modelling and Characterisation Techniques. ISIJ Int 2013;53:935–49. doi:10.2355/isijinternational.53.935.

[7] Liu Y, Zhang Z, Li G, Wang Q, Wang L, Li B. The Structural Evolution and Segregation in a Dual Alloy Ingot Processed by Electroslag Remelting. Metals (Basel) 2016;6:325–36. doi:10.3390/met6120325.

[8] Toshiba Thermal Power System Business in India.pdf n.d.

[9] Corporation T. High Performance Coal Fired Thermal Power Plant Achievement and R & D for Future 2010.

[10] Fujitsuka S, Executive T, Systems E, Company S, Corporation T. Toshiba ' s high-efficiency and low emission technology in thermal power 2017.

[11] Tao X, Li C, Han L, Gu J. Microstructure evolution and mechanical properties of X12CrMoWVNbN10-1-1 steel during quenching and tempering process. J Mater Res Technol 2016;5:45–57. doi:10.1016/j.jmrt.2015.06.001.

[12] Niessen F, Tiedje NS, Hald J. Kinetics modeling of delta-ferrite formation and retainment during casting of supermartensitic stainless steel. Mater Des 2017;118:138–45. doi:10.1016/j.matdes.2017.01.026.

[13] Wang P, Lu SP, Xiao NM, Li DZ, Li YY. Effect of delta-ferrite on impact properties of low carbon 13Cr – 4Ni martensitic stainless steel. Mater Sci Eng A 2010;527:3210–6. doi:10.1016/j.msea.2010.01.085.

[14] Carrouge D, Bhadeshia HKDH, Woollin P. Effect of d -ferrite on impact properties of supermartensitic stainless steel heat affected zones. Sci Technol Weld Join 2004;9:377–89. doi:10.1179/136217104225021823.

[15] Liu Y, Sun J, Li J, Jiang B, Zhang C. Investigation of forging process for eliminating delta-ferrites in USC unites last stage blades steel 10Cr12Ni3Mo2VN. Procedia Eng

2017;207:1797–802. doi:10.1016/j.proeng.2017.10.941.

[16] Agrawal SK, Chauhan A, Mishra A. The VVERs at KudanKulam. Nucl Eng Des 2006;236:812–35. doi:10.1016/j.nucengdes.2005.09.030.

[17] Chen K, Rui S yuan, Wang F, Dong J xin, Yao Z hao. Microstructure and homogenization process of as-cast GH4169D alloy for novel turbine disk. Int J Miner Metall Mater 2019;26:889–900. doi:10.1007/s12613-019-1802-0.

[18] Moura V, Kina AY, Tavares SSM, Lima LD, Mainier FB. Influence of stabilization heat-treatments on microstructure , hardness and intergranular corrosion resistance of the AISI 321 stainless steel. J Mater Sci 2008;43:536–40. doi:10.1007/s10853-007-1785-5.

[19] Rosenberg SJ, Darr JH. Stabilization of austenitic stainless steel. J Res Natl Bur Stand (1934) 1948;40:321–38. doi:10.6028/jres.040.024.

[20] Pardo A, Merino MC, Coy AE, Viejo F, Carboneras M, Arrabal R. Influence of Ti , C and N concentration on the intergranular corrosion behaviour of AISI 316Ti and 321 stainless steels. Acta Mater 2007;55:2239–51. doi:10.1016/j.actamat.2006.11.021.

[21] Hafez S, Eissa MM, Elshazly RM, Fawkhry MK El, Saeed A. Modified Boron-Titanium Austenitic Stainless-Steel Alloys for Power Reactors. Int J Eng Technol Manag Res 2018;5:87–95. doi:10.5281/zenodo.1313100.

[22] L. Karlsson, H.O. Andren HN. Grain Boundary Segregation in An Austenitic Stainless Steel Containing Boron- An Atom-Probe Study. Scr Mater 1982;16:297–302.

[23] Robinson FPA, Scurr WG. The Effect of Boron on the Corrosion Resistance of Austenitic Stainless Steel. Corrosion 1977;33:408–17.

[24] Bai J, Cui Y, Wang J, Dong N, Qurashi MS, Wei H, et al. Effect of boron addition on the precipitation behavior of S31254. Metals (Basel) 2018;8:1–10. doi:10.3390/met8070497.

[25] Varin RA, Tangri K. The Effect of Boron and Thermomechanical Treatment on the Properties of Ultafine-grained Type 316 Stainless Steel 1985;72:177–90.

[26] Yao XX. On the grain boundary hardening in a B-bearing 304 austenitic stainless steel. Mater Sci Eng A 1999;271:353–9. doi:10.1016/s0921-5093(99)00280-4.

[27] Laha K, Kyono J, Kishimoto S, Shinya N. Beneficial effect of B segregation on creep cavitation in a type 347 austenitic stainless steel. Scr Mater 2005;52:675–8. doi:10.1016/j.scriptamat.2004.11.016.

[28] Padilha AF, Rios PR. Decomposition of austenite in austenitic stainless steels. ISIJ Int 2002;42:325–7. doi:10.2355/isijinternational.42.325.

[29] Won CH, Jang JH, Kim SD, Moon J, Ha HY, Kang JY, et al. Effect of annealing on mechanical properties and microstructure evolution of borated stainless steels. J Nucl Mater 2019;515:206–14. doi:10.1016/j.jnucmat.2018.12.039.

[30] Sharma M, Ortlepp I, Bleck W. Boron in Heat-Treatable Steels: A Review. Steel Res Int 2019;90:1–28. doi:10.1002/srin.201900133.

[31] Guo WS and Z. Maraging steels- Modelling of microstructure, properties and applications. Woodhead Publishing Limited,; 2009.

[32] Chakravarthi KVA, Koundinya NTBN, Murty SVSN, Rao BN. Microstructure , properties and hot workability of M300 grade maraging steel. Def Technol 2018;14:51–8. doi:10.1016/j.dt.2017.09.001.

[33] Sun L, Simm TH, Martin TL, Mcadam S, Galvin DR, Perkins KM, et al. A novel ultra-high strength maraging steel with balanced ductility and creep resistance achieved by nanoscale b -NiAl and Laves phase precipitates. Acta Mater 2018;149:285–301. doi:10.1016/j.actamat.2018.02.044.

[34] Garrison WM. Ultrahigh-Strength Steels for Aerospace Applications. J Met 1990;42:20–4.

[35] Ding Z, Li B, Liang SY. Phase transformation and residual stress of Maraging C250 steel during grinding. Mater Lett 2015;154:37–9. doi:10.1016/j.matlet.2015.04.040.

[36] Ding Z, Sun G, Jiang X, Liang SY. Cubic boron nitride wheel topography effects on phase transformation of maraging C250 steel and grinding surface quality. Int J Adv Manuf Technol 2020;108:2881–93. doi:10.1007/s00170-020-05586-2.

[37] Aerospace Material Specification, AMS 6512C; 1991, Warrendale, PA, SAE. n.d.

[38] Aerospace Material Specification, AMS 6520C; 1995, Warrendale, PA, SAE. n.d.

[39] Lee IK, Chou CP, Cheng CM, Kuo IC. Effect of heat-treatment on microstructures of flow formed C-250 maraging steel. Mater Sci Technol 2003;19:1595–602. doi:10.1179/026708303225008095.

[40] Jha AK, Sreekumar K, Tharian T, Sinha PP. Process optimization for high fracture toughness of maraging steel rings formed by mandrel forging. J Manuf Process 2010;12:38–44. doi:10.1016/j.jmapro.2010.01.007.

[41] Sinha PP, Tharian KT, Sreekumar K, Nagarajan K V, Sarma DS. Effect of aging on microstructure and mechanical properties of cobalt free 18 % Ni (250 grade) maraging steel. Mater Sci Technol 1998;14:1–9. doi:10.1179/mst.1998.14.1.1.

[42] Tewari R, Mazumder S, Batra IS, Dey GK, Banerjee S. Precipitation in 18 Wt% Ni Maraging Steel of Grade 350. Acta Mater 2000;48:1187–200.

[43] Marcisz J, Adamczyk M, Garbarz B. Optimisation of Mechanical Properties of 18 % Ni350 Grade Maraging Steel Using Novel Heat-treatment. Arch Metall Mater 2017;62:73–84. doi:10.1515/amm-2017-0010.

[44] Marcisz J, Stepien J. Short Time Ageing of M350 Maraging Steel With and Without Plastic Deformation. Arch Metall Mater 2014;59:513–20. doi:10.2478/amm-2014-0085.

[45] Viswanathan UK, Dey GK, Asundi MK. Precipitation Hardening in 350 Grade Maraging Steel. Metall Trans A 1993;24:2429–42.

[46] Sha W, Cerezo A, Smith GDW. Phase chemistry and precipitation reactions in maraging steels: Part IV. Discussion and conclusions. Metall Trans A 1993;24:1251–6. doi:10.1007/BF02668193.

[47] Mukhopadhyay CK, Rajkumar K V., Jayakumar T, Raj B. Study of tensile deformation behaviour of M250 grade maraging steel using acoustic emission. J Mater Sci 2010;45:1371–84. doi:10.1007/s10853-009-4095-2.

[48] Liu F, Lin X, Shi J, Zhang Y, Bian P, Li X, et al. Effect of microstructure on the Charpy

impact properties of directed energy deposition 300M steel. Addit Manuf 2019;29. doi:10.1016/j.addma.2019.100795.

[49] Liu F, Lin X, Song M, Yang H, Song K, Guo P, et al. Effect of tempering temperature on microstructure and mechanical properties of laser solid formed 300M steel. J Alloys Compd 2016;689:225–32. doi:10.1016/j.jallcom.2016.07.276.

[50] Skubisz P, Sinczak J. Properties of direct-quenched aircraft forged component made of ultrahigh-strength steel 300M. Aircr Eng Aerosp Technol 2018. doi:10.1108/AEAT-12-2015-0253.

[51] He X, Yang X, Zhang G, Li J, Hu H. Quenching microstructure and properties of 300M ultra-high strength steel electron beam welded joints. Mater Des 2012;40:386–91. doi:10.1016/j.matdes.2012.04.010.

[52] Liu F, Zhang W, Lin X, Huang C, Liu F, Huang W, et al. Effect of isothermal temperature on bainite transformation, microstructure and mechanical properties of LSFed 300M steel. Mater Today Commun 2020;25. doi:10.1016/j.mtcomm.2020.101452.

[53] Tomita Y. Development of fracture toughness of ultrahigh strength, medium carbon, low alloy steels for aerospace applications. Int Mater Rev 2000;45:27–37. doi:10.1179/095066000771048791.

[54] Khan SA, Bhadeshia HKDH. The bainite transformation in chemically heterogeneous 300M high-strength steel. Metall Trans A 1990;21:859–75. doi:10.1007/BF02656570.

[55] Tomita Y, Okawa T. Effect of Modified Heat-treatment on Mechanical Properties of 300M Steel 1995;11:245–51. doi:10.2514/6.1975-802.

[56] Luo J, Li MQ, Liu YG, Sun HM. The deformation behavior in isothermal compression of 300M ultrahigh-strength steel. Mater Sci Eng A 2012;534:314–22. doi:10.1016/j.msea.2011.11.075.

[57] Liu YG, Li MQ. Characteristics of martensite transformed from deformed austenite with various states of ultrahigh strength 300 M steel. Mater Charact 2018;144:490–7. doi:10.1016/j.matchar.2018.07.037.

[58] Zhang H, Johansson B, Ahuja R, Vitos L. First-principles study of solid-solution hardening in steel alloys. Comput Mater Sci 2012;55:269–72. doi:10.1016/j.commatsci.2011.12.020.

[59] Calcagnotto M, Ponge D, Raabe D. Effect of grain refinement to 1μm on strength and toughness of dual-phase steels. Mater Sci Eng A 2010;527:7832–40. doi:10.1016/j.msea.2010.08.062.

[60] Avner SH. Introduction to Physical Metallury. 1974.

[61] Matlock DK, Speer JG, Moor E De, Gibbs PJ. Recent developments in advanced high strength sheet steels for automotive applications: an overview. JESTECH 2012;15:1–12.

[62] Matlock DK, Speer JG. Processing opportunities for new advanced high-strength sheet steels. Mater Manuf Process 2010;25:7–13. doi:10.1080/10426910903158272.

[63] Sharma S, Nanda T, Adhikary M, Venugopalan T, Kumar BR. A simulation study of pearlite-to-austenite transformation kinetics in rapidly heated hot-rolled low carbon steel. Mater Des 2016;107:65–73. doi:10.1016/j.matdes.2016.06.025.

[64] Singh AK, Wanhill RJH, Eswara NP. Lightweight Ballistic Armours for Aero-Vehicle Protection. Aerosp. Mater. Mater. Technol. Indian Inst. Met. Ser., Springer; 2017, p. 541–57. doi:https://doi.org/10.1007/978-981-10-2143-5_25.

[65] Majumdar A, Sadhukhan S. Improvement in properties of Ni-Cr-Mo-V steel by process control. Int J Mater Metall Eng 2016;10:743–52.

[66] Thorvaldsson T, Dunlop GL. Effect of stabilizing additions on precipitation reactions in austenitic stainless steel. Met Sci 1982;16:184–90.

[67] Thorvaldsson T, Dunlop GL. Precipitation reactions in Ti-stabilized austenitic stainless steel. Met Sci 1980;14:513–8.

[68] Mohan Raj AP, Selvakumar N, Narayanasamy R, Kailasanathan C. Experimental investigation on workability and strain hardening behaviour of Fe-C-Mn sintered composites with different percentage of carbon and manganese content. Mater Des 2013;49:791–801. doi:10.1016/j.matdes.2013.02.002.

[69] Choudhury IA, El-Baradie MA. Machinability of nickel-base super alloys: A general review. J Mater Process Technol 1998;300:278–84. doi:10.1016/s0924-0136(97)00429-9.

[70] Lal S, Upadhyaya GS. Effect of phosphorus and silicon addition on the sintered properties of 316L austenitic stainless steel and its composites containing 4 vol % yttria. J Mater Sci 1989;24:3069–75. doi:10.1007/BF01139020.

[71] Bhattacharya D. Effect of Sulfur and Zirconium on the Machinability and Mechanical Properties of Aisi 1045 Steels. Metall Trans A, Phys Metall Mater Sci 1981;12 A:973–85. doi:10.1007/BF02643478.

[72] Au LTY, Chau JLH, Ariso CT, Yeung KL. Preparation of supported Sil-1, TS-1 and VS-1 membranes: Effects of Ti and V metal ions on the membrane synthesis and permeation properties. J Memb Sci 2001;183:269–91. doi:10.1016/S0376-7388(00)00598-6.

[73] Parameswaran P, Godwin Antony A, Dinesh S, Radhakrishnan K. Experimental study on mechanical and corrosion characteristics of nab alloy with the addition of chromium. Mater Today Proc 2018;5:8089–94. doi:10.1016/j.matpr.2017.11.495.

[74] Jinlong L, Tongxiang L, Chen W. Surface enriched molybdenum enhancing the corrosion resistance of 316L stainless steel. Mater Lett 2016;171:38–41. doi:10.1016/j.matlet.2016.01.153.

[75] Reed RP. Nitrogen in austenitic stainless steels. Jom 1989;41:16–21. doi:10.1007/BF03220991.

[76] De Lima HMLF, Tavares SSM, Martins M, Araújo WS. The effect of copper addition on the corrosion resistance of cast duplex stainless steel. J Mater Res Technol 2019;8:2107–19. doi:10.1016/j.jmrt.2019.01.018.

[77] Shi S, Xu A, Fan J, Wei H. Study of cobalt-free, Fe-based alloy powder used for sealing surfaces of nuclear valves by laser cladding. Nucl Eng Des 2012;245:8–12. doi:10.1016/j.nucengdes.2012.01.015.

[78] Johnson WH. On Some Remarkable Changes Produced in Iron and Steel by the Action of Hydrogen and Acids. Proc R Soc London 1874;23:168–79. doi:10.1098/rspl.1874.0024.

[79] Garr CR, Troiano AR. Flaking of Heavy Alloy Steel Sections. J Met 1957:445–9.

[80] Lai GY, Wood WE, Clark RA, Zackay VF, Parker ER. Effect of Austenitizing Temperature on the Microstructure and Mechanical Properties of As-Quenched 4340 Steel. Met Trans 1974;5:1663–70. doi:10.1007/BF02646340.

[81] Choudhury A. State of the Art of Superalloy Production for Aerospace and Other Application Using VIM/VAR or VIM/ESR. ISIJ Int 1992;32:563–74. doi:10.2355/isijinternational.32.563.

[82] Fruehan RJ. A review of hydrogen flaking and its prevention. Iron Steelmak 1997;24:61–9.

[83] Voronenko BI. Hydrogen and flakes in steel. Met Sci Heat Treat 1997;39:462–70. doi:10.1007/BF02469113.

[84] Ifergane S, Eliaz N, Stern N, Kogan E, Shemesh G, Sheinkopf H, et al. The effect of manufacturing processes on the fatique lifetime of aeronautical bolts. Eng Fail Anal 2001;8:227–35. doi:10.1016/S1350-6307(00)00013-3.

[85] Dimitriu S. Causes for flakes appearance : Preventing ways and removing methods. Metall. Metall., 2002, p. 13–24.

[86] Mirzaev DA, Vorob'ev NI, Tokovi OK, Shaburov D V., Fominykh EA. On the problem of hydrogen removal during heat-treatment of large forgings. Russ Metall 2006;2006:38–41. doi:10.1134/S0036029506010071.

[87] Ćwiek J. Prevention methods against hydrogen degradation of steel. J Achiev Mater Manuf Eng 2010;43:214–21. doi:10.2478/v10077-009-0001-5.

[88] Sk MH, Overfelt RA, Haney RL, Fergus JW. Hydrogen embrittlement of 4340 steel due to condensation during vaporized hydrogen peroxide treatment. Mater Sci Eng A 2011;528:3639–45. doi:10.1016/j.msea.2011.01.100.

[89] Tartaglia JM, Hayrynen KL. A comparison of fatigue properties of austempered versus quenched and tempered 4340 steel. J Mater Eng Perform 2012;21:1008–24. doi:10.1007/s11665-011-9951-y.

[90] Sun S Da, Liu Q, Brandt M, Luzin V, Cottam R, Janardhana M, et al. Effect of laser clad repair on the fatigue behaviour of ultra-high strength AISI 4340 steel. Mater Sci Eng A 2014;606:46–57. doi:10.1016/j.msea.2014.03.077.

[91] Vrbek K, Lamut J, Marolt M, Knap M. Changes in hydrogen content during steelmaking. Arch Metall Mater 2015;60:295–9. doi:10.1515/amm-2015-0047.

[92] Arh B, Podgornik B, Burja J. ELECTROSLAG REMELTING : A PROCESS OVERVIEW. Mater Technol 2016;50:971–9. doi:10.17222/mit.2016.108.

[93] Ali M, Eissa M, Faramawy H El, Porter D, Kömi J, El-Shahat MF, et al. Electroslag Refining of CrNiMoWMnV Ultrahigh-Strength Steel. J Miner Mater Charact Eng 2017;05:385–407. doi:10.4236/jmmce.2017.56032.

[94] Konopel LA, Polyanskii AM, Polyanskii VA, Yakovlev YA. NEW METROLOGICAL SUPPORT FOR MEASUREMENTS OF THE CONCENTRATION OF HYDROGEN IN SOLID SAMPLES. Meas Tech 2018;60:46–50. doi:10.1007/s11018-018-1343-3.

[95] Steneholm K, Andersson NAI, Tilliander A, Jönsson PG. The role of process control on the

steel cleanliness. Ironmak Steelmak 2018;45:114–24. doi:10.1080/03019233.2016.1245917.

[96] AlSumait A, Li Y, Weaser M, Niji K, Battel G, Toal R, et al. A Comparison of the Fatigue Life of Shot-Peened 4340M Steel with 100, 200, and 300% Coverage. J Mater Eng Perform 2019;28:1780–9. doi:10.1007/s11665-019-03891-w.

[97] Ghazali S, Algarni M, Bai Y, Choi Y. A study on the plasticity and fracture of the AISI 4340 steel alloy under different loading conditions and considering heat-treatment effects. Int J Fract 2020;225:69–87. doi:10.1007/s10704-020-00466-y.

[98] Laliberté-Riverin S, Bellemare J, Sirois F, Brochu M. Internal hydrogen embrittlement of pre-cracked, cadmium-plated AISI 4340 high strength steel with sustained load tests and incremental step-loading tests. Eng Fract Mech 2020;223:106773. doi:10.1016/j.engfracmech.2019.106773.

[99] Parvinzadeh M, Sattarpanah Karganroudi S, Omidi N, Barka N, Khalifa M. A novel investigation into edge effect reduction of 4340 steel spur gear during induction hardening process. Int J Adv Manuf Technol 2021;113:605–19. doi:10.1007/s00170-021-06639-w.

[100] Hättestrand M, Andrén HO. Influence of strain on precipitation reactions during creep of an advanced 9% chromium steel. Acta Mater 2001;49:2123–8. doi:10.1016/S1359-6454(01)00135-5.

[101] Masuyama F. History of Power Plants and Progress in Heat Resistant Steels. ISIJ Int 2001;41:612–25.

[102] Ennis PJ, CZYRSKA-FILEMONOWICZ A. Recent advances in creep-resistant steels for power plant applications. Sadhana 2003;28:709–30.

[103] Kaybyshev RO, Skorobogatykh VN, Shchenkova IA. New Martensitic Steels for Fossil Power Plant : Creep Resistance. Phys Met Metallogr 2010;109:186–200. doi:10.1134/S0031918X10020110.

[104] Takasawa K, Miki K. Development of High- and Intermediate-Pressure Steam Turbine Rotors for Efficient Fossil Power Generation Technology. JSW Tech Rev 2011;20:15–22.

[105] Martorano MA, Tavares CF, Padilha AF. Predicting delta-ferrite content in stainless steel castings. ISIJ Int 2012;52:1054–65. doi:10.2355/isijinternational.52.1054.

[106] Prat O, Garcia J, Rojas D, Sauthoff G, Inden G. The role of Laves phase on microstructure evolution and creep strength of novel 9%Cr heat resistant steels. Intermetallics 2013;32:362–72. doi:10.1016/j.intermet.2012.08.016.

[107] Abe F. Research and Development of Heat-Resistant Materials for Advanced USC Power Plants with Steam Temperatures of 700 °C and Above. Engineering 2015;1:211–24. doi:10.15302/J-ENG-2015031.

[108] Nair A, Kumanan S. Newer Materials for Supercritical Power Plant Components – A Manufacturability Study. Proc. Int. Conf. Adv. Prod. Ind. Eng., 2015, p. 326–31.

[109] Liu Y, Sun J, Li J, Jiang B, Zhang C. Investigation of forging process for eliminating delta-ferrites in USC unites last stage blades steel 10Cr12Ni3Mo2VN. Procedia Eng 2017;207:1797–802. doi:10.1016/j.proeng.2017.10.941.

[110] Singh J, Nath SK. Dissolution of delta-ferrite through cyclic treatment and its influence on the hydro abrasive erosion and mechanisms. Tribol Int 2021;161:107056. doi:10.1016/j.triboint.2021.107056.

[111] Karlsson L, Andrén H-O, Nordén H. GRAIN BOUNDARY SEGREGATION IN AN AUSTENITIC STAINLESS STEEL CONTAINING BORON - AN ATOM-PROBE STUDY. Scr Metall 1982;16:297–302.

[112] Herman JC, Donnay B, Leroy V. Precipitation Kinetics of Microalloying Additions during Hot-rolling of HSLA Steels. ISIJ Int 1992;32:779–85. doi:10.2355/isijinternational.32.779.

[113] Yao XX. On the grain boundary hardening in a B-bearing 304 austenitic stainless steel. Mater Sci Eng A 1999;271:353–9.

[114] Min KS, Lee SC, Nam SW. Effects of TiC and Cr 23 C 6 Carbides on Creep-Fatigue Properties in AISI 321 Stainless Steel. Mater Trans 2002;43:2808–12.

[115] Min KS, Kim KJ, Nam SW. Investigation of the effect of the types and densities of grain boundary carbides on grain boundary cavitation resistance of AISI 321 stainless steel under creep – fatigue interaction. J Alloys Compd 2004;370:223–9. doi:10.1016/j.jallcom.2003.09.129.

[116] Laha K, Kyono J, Sasaki T, Shinya N. Effect of additions of Ti , B and Ce on microstructural stability , creep strength and creep damage in austenitic stainless steel. Mater Sci Technol 2005;21:1309–17. doi:10.1179/174328405X62305.

[117] Lima AS, Nascimento AM, Abreu HFG, De Lima-Neto P. Sensitization evaluation of the austenitic stainless steel AISI 304L, 316L, 321 and 347. J Mater Sci 2005;40:139–44. doi:10.1007/s10853-005-5699-9.

[118] Zaky IAF, El-bitar TA. Effect of Nb , Ti and cold deformation on microstructure and mechanical properties of austenitic stainless steels. Mater Sci Eng A 2010;527:3662–9. doi:10.1016/j.msea.2010.02.064.

[119] Nikulin I, Kaibyshev R, Skorobogatykh V. High-temperature Characteristic of Stainless Steel. 15th Int Conf Strength Mater J Phys Conf Ser 2010;240:012071. doi:10.1088/1742-6596/240/1/012071.

[120] Han Y, Shi J, Xu L, Cao WQ, Dong H. Effect of hot rolling temperature on grain size and precipitation hardening in a Ti-microalloyed low-carbon martensitic steel. Mater Sci Eng A 2012;553:192–9. doi:10.1016/j.msea.2012.06.015.

[121] Han Y, Shi J, Xu L, Cao WQ, Dong H. Effects of Ti addition and reheating quenching on grain refinement and mechanical properties in low carbon medium manganese martensitic steel. Mater Des 2012;34:427–34. doi:10.1016/j.matdes.2011.08.015.

[122] Green G, Higginson R, Hogg S, Spindler S, Hamm C, Najorka J. Analysis of ferrite formed in 321 grade austenitic stainless steel. Mater Sci Technol 2015;31:418–25. doi:10.1179/1743284714Y.0000000564.

[123] Liu J, Han JT, Liu YL. Study on Microstructure and Property of High Boron Alloyed Stainless Steel Composite Plate Containing Titanium. Adv Mater Res 2015;1095:193–8. doi:10.4028/www.scientific.net/amr.1095.193.

[124] Ghazani MS, Eghbali B. Characterization of the hot deformation microstructure of AISI 321 austenitic stainless steel. Mater Sci Eng A 2018;730:380–90. doi:10.1016/j.msea.2018.06.025.

[125] Jambor M, Nový F, Bokůvka O, Trško L, Oravcová M. Influence of structure sensitising of the AlSi 316Ti austenitic stainless steel on the ultra-high cycle fatigue properties. MATEC Web Conf 2018;157:1–11. doi:10.1051/matecconf/201815705011.

[126] Hichem S, Abderrazak C, Djeghlal MEA, Omar A, Montagne A, Alberto M, et al. Corrosion and tribocorrosion behaviours of AISI 321, AISI 431 and FDMA borided and non-borided steels. Mater Res Express 2019;6. doi:10.1088/2053-1591/ab4e4b.

[127] James MN, Matthews L, Hattingh DG. Weld solidification cracking in a 304L stainless steel water tank. Eng Fail Anal 2020;115:104614. doi:10.1016/j.engfailanal.2020.104614.

[128] Li W, Chen H, Li C, Huang W, Chen J, Zuo L, et al. Microstructure and tensile properties of AISI 321 stainless steel with aluminizing and annealing treatment. Mater Des 2021;205:109729. doi:10.1016/j.matdes.2021.109729.

[129] Vasudevan VK, Kim SJ, Wayman CM. Precipitation reactions and strengthening behavior in 18 Wt Pct nickel maraging steels. Metall Trans A, Phys Metall Mater Sci 1990;21 A:2655–68. doi:10.1007/BF02646061.

[130] Guo Z, Sha W, Li D. Quantification of phase transformation kinetics of 18 wt.% Ni C250 maraging steel. Mater Sci Eng A 2004;373:10–20. doi:10.1016/j.msea.2004.01.040.

[131] Guo Z, Sha W. Quantification of precipitate fraction in Al-Si-Cu alloys. Mater Sci Eng A 2005;392:449–52. doi:10.1016/j.msea.2004.09.020.

[132] Arabi H, Divandari M, Hosseini AHM. THE EFFECT OF Ti CONTENTS ON THE AMOUNTS OF INCLUSIONS FORMATION AND MECHANICAL PROPERTIES OF C300 HIGH STRENGTH STEEL. Iran J Mater Sci Eng 2006;3:1–8.

[133] Mukhopadhyay CK, Rajkumar K V., Jayakumar T, Raj B. Study of tensile deformation behaviour of M250 grade maraging steel using acoustic emission. J Mater Sci 2010;45:1371–84. doi:10.1007/s10853-009-4095-2.

[134] Galindo-Nava EI, Rivera-Díaz-Del-Castillo PEJ. A model for the microstructure behaviour and strength evolution in lath martensite. Acta Mater 2015;98:81–93. doi:10.1016/j.actamat.2015.07.018.

[135] Tian J, Wang W, Shahzad MB, Yan W, Shan Y, Jiang Z, et al. A New Maraging Stainless Steel with Excellent–Toughness–Corrosion Synergy. Materials (Basel) 2017;10:1–11. doi:10.3390/ma10111293.

[136] Saastamoinen A, Kaijalainen A, Porter D, Suikkanen P, Yang JR, Tsai YT. The effect of finish rolling temperature and tempering on the microstructure, mechanical properties and dislocation density of direct-quenched steel. Mater Charact 2018;139:1–10. doi:10.1016/j.matchar.2018.02.026.

[137] Shamsdini SAR, Pirgazi H, Ghoncheh MH, Sanjari M, Amirkhiz BS, Kestens L, et al. A relationship between the build and texture orientation in tensile loading of the additively manufactured maraging steels. Addit Manuf 2021;41:101954. doi:10.1016/j.addma.2021.101954.

[138] Khan SA, Bhadeshia HKDH. The bainite transformation in chemically heterogeneous 300M high-strength steel. Metall Trans A 1990;21:859–75. doi:10.1007/BF02656570.

[139] Tomita Y, Okawa T. Effect of modified heat-treatment on mechanical properties of 300M steel. Mater Sci Technol 1995;11:245–51. doi:10.1179/026708395790164805.

[140] Tomita Y. Development of fracture toughness of ultrahigh strength, medium carbon, low alloy steels for aerospace applications. Int Mater Rev 2000;45:27–37. doi:10.1179/095066000771048791.

[141] Luo Y, Peng J min, Wang H bin, Wu X chun. Effect of tempering on microstructure and mechanical properties of a non-quenched bainitic steel. Mater Sci Eng A 2010;527:3433–7. doi:10.1016/j.msea.2010.02.010.

[142] He X, Yang X, Zhang G, Li J, Hu H. Quenching microstructure and properties of 300M ultra-high strength steel electron beam welded joints. Mater Des 2012;40:386–91. doi:10.1016/j.matdes.2012.04.010.

[143] Luo J, Li MQ, Liu YG, Sun HM. The deformation behavior in isothermal compression of 300M ultrahigh-strength steel. Mater Sci Eng A 2012;534:314–22. doi:10.1016/j.msea.2011.11.075.

[144] Zhao R, Liu T, Zhao X. Effect of Q-P-T process on the microstructure and mechanicalproperties of 300M steel. Mater Sci Forum 2013;749:287–93. doi:10.4028/www.scientific.net/MSF.749.287.

[145] Liu F, Lin X, Song M, Yang H, Song K, Guo P, et al. Effect of tempering temperature on microstructure and mechanical properties of laser solid formed 300M steel. J Alloys Compd 2016;689:225–32. doi:10.1016/j.jallcom.2016.07.276.

[146] Skubisz P, Sinczak J. Properties of direct-quenched aircraft forged component made of ultrahigh-strength steel 300M. Aircr Eng Aerosp Technol 2018;90:713–9. doi:10.1108/AEAT-12-2015-0253.

[147] Liu F, Lin X, Shi J, Zhang Y, Bian P, Li X, et al. Effect of microstructure on the Charpy impact properties of directed energy deposition 300M steel. Addit Manuf 2019;29:100795. doi:10.1016/j.addma.2019.100795.

[148] Liu F, Zhang W, Lin X, Huang C, Liu F, Huang W, et al. Effect of isothermal temperature on bainite transformation, microstructure and mechanical properties of LSFed 300M steel. Mater Today Commun 2020;25:101452. doi:10.1016/j.mtcomm.2020.101452.

[149] Liu F, Zhang W, Lin X, Huang C, Wang Z, Liu F, et al. Achieving superior ductility for laser directed energy deposition 300 M steel through isothermal bainitic transformation. J Manuf Process 2020;60:426–34. doi:10.1016/j.jmapro.2020.10.077.

[150] Dang J, Zhang H, An Q, Lian G, Li Y, Wang H, et al. Surface integrity and wear behavior of 300M steel subjected to ultrasonic surface rolling process. Surf Coatings Technol 2021. doi:10.1016/j.surfcoat.2021.127380.

[151] ASTM A604/A604M-07. (2012) Standard Test Method for Macroetch Testing of Consumable Electrode Remelted Steel Bars and Billets n.d. doi:10.1520/A0604.

[152] ASTM A370 − 15. (2012) Standard Test Methods and Definitions for Mechanical Testing

of Steel Products n.d. doi:10.1520/A0370-15.2.

[153] AMS2315A, Determination of Free Ferrite Content 1980:1–4.

[154] JIS Z2241: 2011, Method of tensile test for metallic materials n.d.

[155] JIS Z2242: 2005, Method for charpy pendulum Impact test for metallic materials n.d.

[156] JIS Z2243: 2008, Brinell hardness test-test method n.d.

[157] ASM Handbook Volume 9: Metallography and Microstructures, ASM International (2004) 1- 1183. n.d.

[158] ASTM E8/E8M - 15a. Standard test methods for tension testing of metallic materials. ASTM, ASTM International, West Conshohocken, PA; 2015. doi:10.1520/E0008.

[159] ASTM E 23-12c. Standard test methods for notched bar impact testing of metallic materials. ASTM International, West Conshohocken, PA; 2012. doi:10.1520/E0023-12C.2.

[160] ASTM E112-13, (2013) Standard Test Methods for Determining Average Grain Size. n.d. doi:10.1520/E0112-10.

[161] ASTM A-262. Standard Practices for Detecting Susceptibility to Intergranular Attack in Austenitic Stainless Steels. 2015. doi:10.1520/A0262-15.

[162] ASTM E-21. Standard Test Methods for Elevated Temperature Tension Tests of Metallic Materials 1. vol. i. ASTM International, West Conshohocken, PA; 2017. doi:10.1520/E0021-09.2.

[163] Flemings MC, Barone R V., Brody HD. INVESTIGATION OF SOLIDIFICATION OF HIGH STRENGTH STEEL CASTINGS. Department of Metallurgy, Massachusetts Institute of Technology, Cambridge: 1967.

[164] Hoyle G. Electroslag processes, Principle and Practice. Applied Science Publishers LTD, England; 1983.

[165] Sabih A, Wanjara P, Nemes J. Characterization of Internal Voids and Cracks in Cold Heading of Dual Phase Steel. ISIJ Int 2005;45:1179–86.

[166] Reed RC. The Superalloys: Fundamentals and Applications. Cambridge University Press, 2006; 2006.

[167] Lowe EM, Hogg A. Aplication of ESR to alloy steel forgings. Proccedings Conf. Electroslag refining, Iron Steel Inst., Sheffield: 1973, p. 68.

[168] ASTM E45-13, (2013) Standard Test Methods for Determining the Inclusion Content of Steel n.d. doi:10.1520/E0045-13.2.

[169] Briickmann G, Scholz H. Vacuum Arc Metal Processing. Handb. Vac. Arc Sci. Technol. Fundam. Appl., Elsevier; 1996, p. 552–89.

[170] Scholz H, Biebricher U, Franz H, Paderni A, Bettoni P. http://www.asogroupsteel.com/wp-content/uploads/2014/05/var-and-esr-processes.pdf. STATE ART VAR ESR Process – A Comp 2014:1–12.

[171] JIS Z2320-1: 2007, Non destructive testing-Magnetic particle testing-part 1: General principles n.d.

[172] JIS Z2320-2: 2007, Non destructive testing-Magnetic particle testing-Part 2: Detection media n.d.

[173] JIS Z2320-3: 2007, Non destructive testing-Magnetic particle testing-Part3: Equipment n.d.

[174] AMS2315A, Determination of Free Ferrite Content, (1980) 1–4 n.d.

[175] Green HW, Borch RS. The homologous temperature dependence of creep. Rev Phys Appliquée 1988;23:709–10. doi:10.1051/rphysap:01988002304070900.

[176] AMS2759/4C. Heat-treatment Austenitic Corrosion-Resistant Steel Parts 2008:1–7.

[177] L. Karlsson, H.O. Andren HN. Grain Bundary Segregation of Boron: An Experimental and Theortical Study. J Phys 1986:257–62.

[178] Faulkner RG. Non-equilibrium grain-boundary segregation in austenitic alloys. J Mater Sci 1981;16:373–83. doi:10.1007/BF00738626.

[179] Williams TM, Stoneham AM, Harries DR. The segregation of boron to grain boundaries in solution-treated Type 316 austenitic stainless steel. Met Sci 1976;10:14–9. doi:10.1179/030634576790431471.

[180] Harries DR, Marwick AD. Non-equilibrium segregation in metals and alloys. Philos Trans R Soc London Ser A, Math Phys Sci 1980;295:197–207. doi:10.1098/rsta.1980.0100.

[181] Salhi H, Chilali A, Djeghlal MEA, Omar A, Montagne A, Mejias A, et al. Indentation creep and tribological characterization of AISI 321, AISI 431 and FDMA borided and non-borided steels. Mater Res Express 2019;6:096409. doi:10.1088/2053-1591/ab2c98.

[182] Rebak RB. Alloy Selection for Accident Tolerant Fuel Cladding in Commercial Light Water Reactors. Metall Mater Trans E 2015;2:197–207. doi:10.1007/s40553-015-0057-6.

[183] Gupta A, Singla G, Pandey OP. Effect of synthesis parameters on structural and thermal properties of NbC/C nano composite synthesized via in-situ carburization reduction route at low temperature. Ceram Int 2016;42:13024–34. doi:10.1016/j.ceramint.2016.05.081.

[184] Williamson GK, Smallman RE. III . Dislocation densities in some annealed and cold-worked metals from measurements on the X-ray debye- scherrer spectrum. Philos Mag A J Theor Exp Appl Phys 1956;1:1:34–46. doi:10.1080/14786435608238074.

[185] Liu F, Zhang W, Lin X, Huang C, Wang Z, Liu F, et al. Achieving superior ductility for laser directed energy deposition 300 M steel through isothermal bainitic transformation. J Manuf Process 2020;60:426–34. doi:10.1016/j.jmapro.2020.10.077.

[186] Jian-Min Z, Yan Z, Ke-Wei X, Vincentc J. Young's modulus surface and Poisson's ratio curve for tetragonal crystals. Chinese Phys B 2008;17:1565–73.

[187] Souissi M, Numakura H. Elastic Properties of Fe–C and Fe–N Martensites. ISIJ Int 2015;55:1512–21.